1998

Skin dose from radiotherapy x-rays

Martin Jonathan Butson
University of Wollongong

SKIN DOSE FROM RADIOTHERAPY X-RAYS

A thesis submitted in fulfilment of the

requirements for the award of the degree

DOCTOR OF PHILOSOPHY

from

UNIVERSITY OF WOLLONGONG

by

MARTIN JONATHAN BUTSON (BSc hons)

ENGINEERING PHYSICS

1998

Abstract

The near surface build up characteristics of photon and electron beams used for radiotherapy treatment of cancer patients have been studied. For the measurement of skin dose various detectors were developed. The Attix parallel plate ionisation chamber was used as the benchmark chamber for in phantom dose build up measurements. Extrapolation of thermoluminescent dosimeters readings were employed to produce in-vivo results, within the first 0.1cm of tissue. A metal oxide semiconductor field effect transistor (MOSFET) system provided on line integral dosimetry. Radiochromic film was employed as an off-axis skin dose measurement.

Neodymium Iron Boron rare earth lanthanide magnets were tested for their ability to remove electron contamination from photon beams produced by a linear accelerator. Results show a reduced surface and build up dose. For a 20cm x 20cm field size at 100cm source surface distance (SSD) using a 0.6cm perspex block tray, percentage surface dose is 18% and 32% with and without the magnetic field applied respectively at 6MV. A helium/air replacement system has been developed which enhances the skin sparing properties of megavoltage photon beams by replacing 25cm of air above the phantom with helium. By combining the magnetic and helium devices the percentage surface dose is 9% of maximum. This is due to the elimination of low energy electron contamination normally generated in the air column.

Monte Carlo simulations were performed in the build up region. Using experimental and Monte Carlo generated data as input, a model has been developed to predict central axis build up dose for 6MV photons. This is performed by separating dose components produced by i) photons scattered by the phantom and ii) electron contamination. Dose deposition changes depend on field size, source surface distance (SSD), angle of incidence, beam modifying devices (block trays, blocks and wedges) and patient geometry. The model accounts for these variables.

Preface

The clinical imperative

When cancer patients are treated with radiation therapy, various skin reactions have been noticed. Early stage effects include erythema and in some cases desquamation. Occasionally late effects such as Telangectasia may occur. The lowest skin dose is not always the treatment aim. In some cases a high dose to the skin region is required to prevent a near surface recurrence.

In any event because tissue complication probability in the form of a deliterious skin reaction is proportional to skin dose, the ability to predict, measure and control patient skin dose is an important first step in the process of total patient skin management. The radiobiological links between skin dose and skin reactions are discussed in section 1.2.

New detectors

The accurate measurement of dose in the x-ray build up region is a challenge due to the high dose gradient (typically change in dose of 20% of maximum per millimetre near the surface). A dose gradient rivalled only in the beams penumbral region. Suitable detectors require good spatial resolution. Two new detectors are developed and tested in this report, radiochromic film and metal oxide semiconductor field effect transistors (MOSFET's). MOSFET's are shown to possess characteristics which makes them suitable as on-line, in-vivo dosimeters. Radiochromic film can produce a quantitative dose map over a selected region. The methodology of these detectors is discussed, along with tradiational parallel plate ionisation chambers and thermoluminescent dosimeters.

Clinical data

The data measured using the detectors described in sections 2.3 - 2.6 is outlined in chapter 3 for a 6MV x-ray beam produced by a medical linear accelerator. Build up data for high skin dose modalities such as electrons and orthovoltage x-rays are included in chapter 5.

The computer model

Computer generated treatment plans are produced for each cancer patient, prior to treatment with radiotherapy x-rays. Each treatment plan usually consists of an isodose distribution overlayed on a patient axial cross section. The plan provides reasonably accurate dose distributions for the tumour and the surrounding tissue. The dose plan does not provide details of the dose to the patients skin. This report provides a calculation technique to accurately predict dose in the build up region discussed in section 4.1.

Reduction of dose

It is well known that megavoltage x-ray beams such as those produced by a linear accelerator provide lower skin dose and hence less patient skin reaction than other low energy machines. This thesis describes methods to enhance the skin sparing properties of the machines by further reducing the skin dose with the use of a magnetic electron sweeper and a helium bag system as discussed in section 3.9-3.10.

Internationally refereed publications directly related to this work which the author has published during the course of this thesis include the following :

Butson M J, Wong T P Y, Kron T , Mathur J N, Clubb B, Metcalfe P E 1994 Surface doses from combined electron/photon fields in radiotherapy. *Aust. Phys. Eng. Sci. Med.* **17** 14-22

Butson M J, Mathur J N, MetcalfeP E 1995 Dose characteristics of a Therapax 300kVp orthovoltage machine *Aust. Phys. Eng. Sci. Med.* **18** 133-138

Butson M J, Rosenfeld A, Mathur J N, Carolan M G, Wong T P Y, Metcalfe P E 1996 A new radiotherapy surface dose detector : the MOSFET. *Med. Phys.* **23** 655 -658

Butson M J, Mathur J N, Metcalfe P E 1996 Radiochromic film as a radiotherapy surface dose detector *Phys. Med. Biol.* **41** 1073-1078

Butson M J, Wong T P Y, Law A, Law M, Mathur J N, Metcalfe P E 1996 Magnetic repulsion of linear accelerator contaminates *Med. Phys.* **23** 953-955

Butson M J, Mathur J N, Perez M, Metcalfe P E 1996 6MV X-ray dose in the build up region: Empirical model and the incident angle effect *Aust. Phys. Eng. Sci. Med.* **19** 74-82

Butson MJ, Mathur J N, Metcalfe P E 1996 Surface dose equivalent square field size corrections. *Aust. Phys. Eng. Sci. Med.* **19** 194-196

Butson MJ, Mathur J N, Metcalfe P E 1997 Skin dose from radiotherapy x-ray beams : the influence of energy *Aust. Rad.* **41** 58-60

Butson MJ, Mathur J N, Metcalfe 1996 Effect of block trays on skin dose in radiotherapy *Aust. Phys. Eng. Sci. Med.* **19** 248-251

Butson M J, Yu P K N, Kan M, Carolan M G, Young E, Mathur J N, Metcalfe P E 1997 Skin dose reductions by a clinically viable magnetic deflector *Aust. Phys. Eng. Sci. Med.* **20** 183-187

Butson M J, Yu P K N, Metcalfe P E 1998 Effects of ambient light and readout source lights on radiochromic film. *Phys Med Biol* **43** 2407-2412

Butson M J , Yu P K N, Metcalfe P E 1998 Measurement of off-axis and peripheral skin dose using radiochromic film *Phys. Med. Biol.* **43** 247-2650

Associated papers in this area which the candidate has had significant input into include :

Kron T, Butson M, Hunt F, Denham J 1996 TLD extrapolation for skin dose determination in vivo *Radiotherapy and Oncology* **41** 119-123

Hunt F, Butson M 1996 Effect of beam incident angle on breast surface dose *The Radiographer* **43** 13-17

Parts of this work have also been published and presented by or on behalf of the author at the following conferences.

Butson M J, Perez M, Mathur J N, Metcalfe P E Prediction of near surface dose from x-rays used for radiotherapy patient treatment : The incident angle effect ACPSEM conference Perth Australia (1994)

Butson M J, Mathur J N, Metcalfe P E Skin dosimetry and skin effects in radiotherapy Experimental Radiation Oncology Syposium Sydney Australia (1995)

Butson M J, Metcalfe P E Patient skin dose from radiotherapy x-ray beams COMP Vancouver Canada (1996)

Kron T, Butson M J, Ostwald P, Metcalfe P E TLD extrapolation methods AAPM Los Angeles U.S.A (1994)

Kron T, Butson M J , Hunt F, Denham J In vivo - skin dose measurements on breast patients using TLD extrapolation ESTRO Vienna Austria (1996)

Pyiranatna N, Butson M J, Metcalfe P E De-contamination of a 6MV clinical x-ray beam AIR Bathurst Australia (1996)

Butson M J, Mathur J N, Carolan M G, Metcalfe P E Radiotherapy : How to save your skin EPSMH Canberra Australia (1996)

Carolan M G, Butson M J, Metcalfe P E Contribution to surface dose from air scatter in megavoltage photon beams EPSMH Canberra Australia (1996)

Butson M J, Metcalfe P E, Mathur J N Skin dosimetry in low LET radiation ERO symposium Wollongong Australia (1997)

Butson M J, Mathur J N, Metcalfe P E Advances in radiotherapy skin dosimetry and planning WCMP Nice France (1997)

Acknowledgements

Assoc. Prof Peter Metcalfe's close supervision and tireless help with this project is sincerely appreciated. Dr Jagdish Mathur has provided excellent project supervision and excellent lectureship in physics during my undergraduate and postgraduate days, for this I will always be thankful. I am grateful for their encouragement, help and friendship. Thanks to Martin Carolan for assistance with MOSFET results and Monte Carlo simulations.

Thanks is also given for financial assistance to the Hong Kong Polytechnic University for a grant which enabled manufacture of the magnetic deflector.

Finally to my wife, Elisa and son Ethan. Both have been very patient and loving with me during this time consuming and difficult challenge. This thesis is dedicated to them.

Table of Contents

Figures and tables

Symbols and abbreviations

Symbols

A	atomic mass
D	absorbed dose
d_{max}	depth of maximum dose
dW	solid angle
E_k	kinetic energy of electron
$\bar{E}_{tr}$	average energy transferred
$\bar{E}_{ab}$	average energy absorbed
h	Plank's constant
I_o	initial intensity (optical etc)
I_t	transmitted intensity
L_D	cut-off linear collision stopping power
m_o	rest mass of electron
N	number of photons
N_A	Avagadro's number
N_e	number of electrons per gram (electron density)
P_{eff}	effective point of measurement
μ	linear attenuation coefficient
μ/ρ	mass attenuation coefficient
μ_{coh}	coherent attenuation coefficient
μ_t	photoelectric attenuation coefficient
μ_s	Compton attenuation coefficient
μ_k	pair production attenuation coefficient
ρ	mass density
σ	total Compton cross section
υ	frequency

Abbreviations

CAX	central axis
cGy	centi-Gray
Co-60	Cobalt 60
CT	computed tomography
%D	percentage dose
GE	General Electric
Gy	Gray
keV	kilo-electronvolt
LET	linear energy transfer or restricted linear collision stopping power
linac	linear accelerator
MeV	mega-electronvolt
MOSFET	metal oxide semiconductor field effect transistor
OD	optical density
RFA	radiation field analyser
SSD	source to surface (skin) distance
TLD	thermoluminescent dosimetry/dosimeter

Chapter 1 Introduction

1.1 Dose build up

Depth dose

Megavoltage photon beams exhibit a dose build up effect within the first few centimetres of tissue followed by their characteristic attenuation as they travel through matter. This is shown in figure 1.1 which represents a 6MV x-ray beam incident on a water phantom. The absorbed dose is maximum at a certain depth beyond the surface which is called D_{max}. This is normally the point where relative dose is normalised to, so that

$$\%D\left(d_{ref},f,S,E\right)=\frac{D\left(d_{ref},f,S,E\right)}{D\left(d_{\max},f,S,E\right)}\times 100. \qquad 1\text{-}1$$

where D_{ref} is the dose at reference depth d_{ref}, f is the source skin distance, S is the field size and E is the beam energy. The percentage dose build up produces a 'skin sparing' effect which is highly dependent on beam parameters such as energy and field size. Most treatments are performed with megavoltage beams because deep tumours are treated to an effective dose whilst skin dose remains acceptably low.

Interactions

Dose deposited in the skin and subcutaneous tissue can be broadly considered to be effected by seven main dominant variables. These are shown in figure 1.2 as being :-

i) electron + contamination produced by x-ray collisions within the treatment head and/or beam modifying devices such as block trays

---

+ Interactions may also include some positrons.

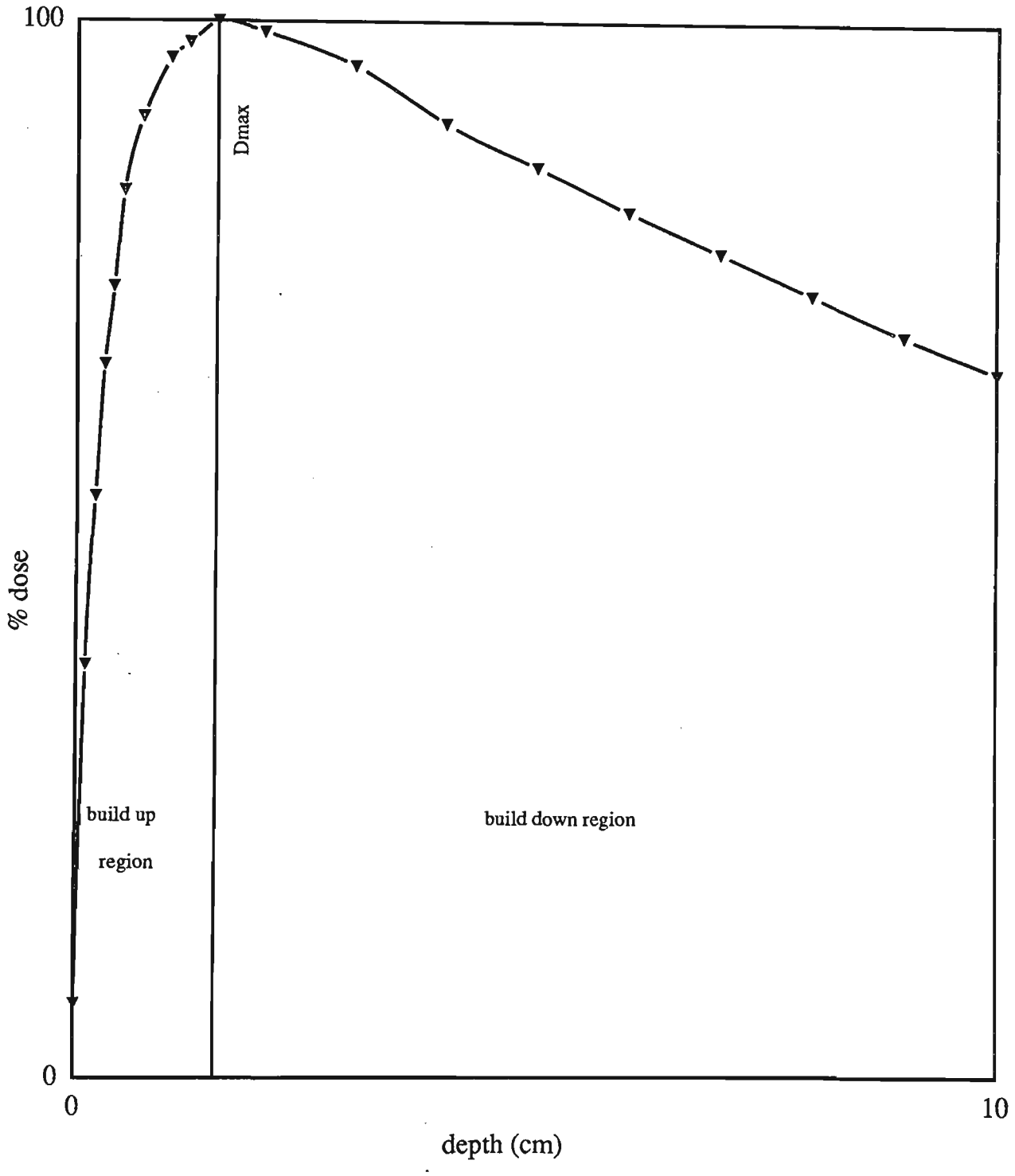

Figure 1.1 : Percentage depth dose characteristics for a megavoltage photon beam. Two distinct regions are observed, the dose build up region and the dose fall off region. This thesis involves measurement and analysis in the build up region.

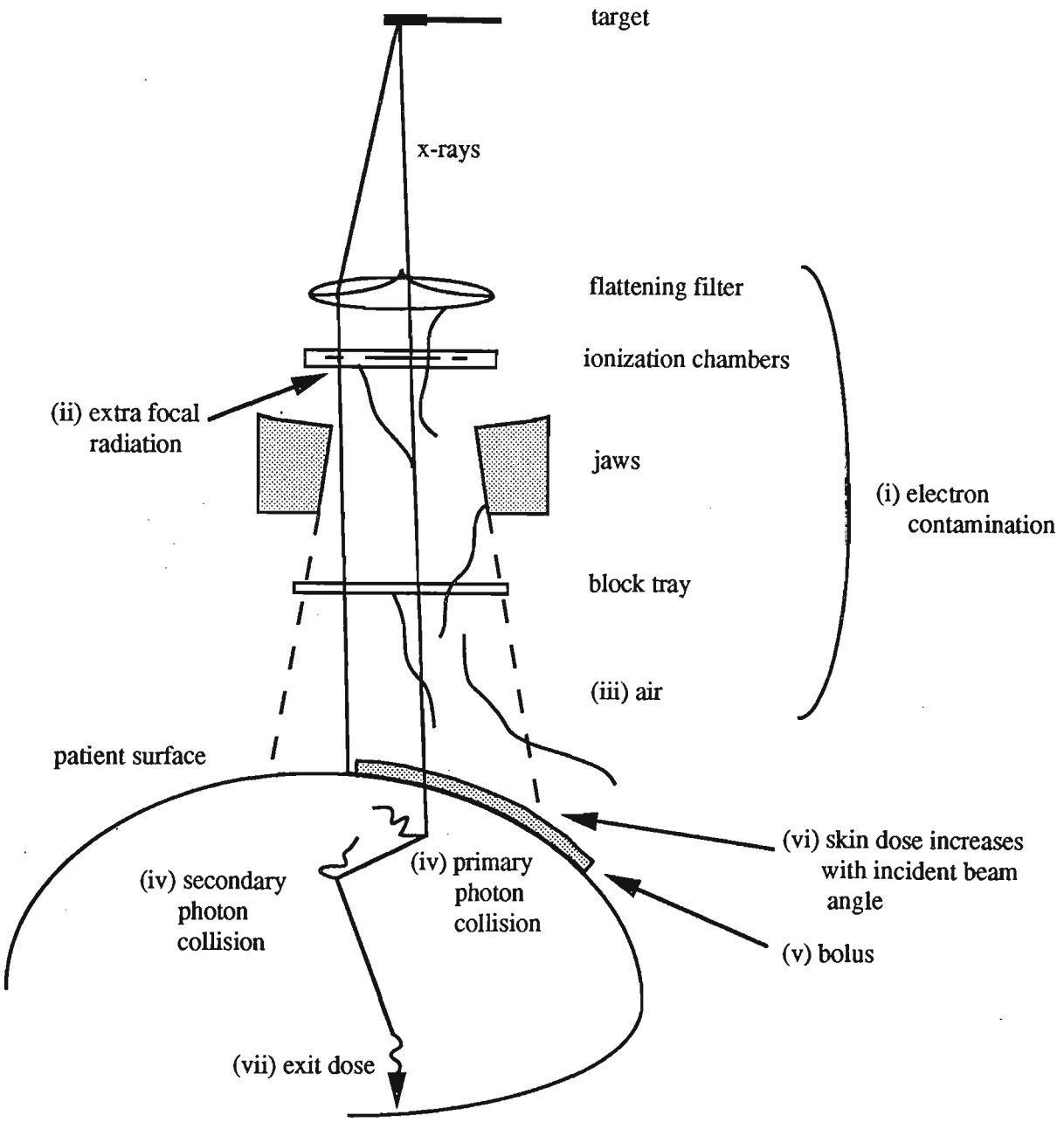

Figure 1.2 : Sites which can produce dose deposition in the build up region for a radiotherapy linear accelerator. These regions include the production of electron contamination outside the phantom and in-phantom photon interactions.

ii) extra focal radiation from flattening filter and collimators

iii) electron contamination produced by photon interactions in the air column

iv) primary and secondary (back scatter), in patient photon collisions which generate electrons

v) build up material (bolus) placed on the patient's skin causing extra dose build up

vi) incident beam angle

vii) exiting primary and scatter photon interactions with electrons (exit dose)

i) Electrons generated in the treatment head

A quantitative description of the intensity of contamination electrons produced by different components in the treatment head is difficult. Each machine has its own design with the internal placement and shape of each device varying. This is expected to produce an array of energy spectra for the contamination electrons. Nilsson (1985) produced an expression to model the relative lateral distribution of surface dose due to electrons emanating from materials in the beams path. The use of Monte Carlo techniques would be another approach. The MCNP and EGS4 methods were used in this thesis. A relatively new code which employs geometry routines that enable the use of EGS4 to simulate treatment head geometries known as BEAM (Rogers et al 1995) would perhaps have been the most suitable Monte Carlo resource for this investigation.

ii) Extra focal radiation

Some scattered photons are generated when primary photons interact to produce contamination electrons. The secondary photons produced from these devices are known as 'extra focal' radiation. This is sometimes quantitatively labelled as collimator scatter however other components are also involved such as the flattening filter.

iii) Electrons generated in air

Though the mean free path for photons is significant in air there is still a small probability that some photons will interact within the air column, and thus produce contamination electrons. The range of these electrons is relatively short in tissue so this adds to the surface/build up dose. One would also expect that as the x-ray beam energy increases the energy of the generated electrons would increase so that there penetrating power increases. By assuming that the relative skin dose (absorbed dose/ D_{max} dose) was produced by Compton recoil electrons scattered in the medium, (neglecting multiple scatter), Howarth (1985) calculated a quantitative measure for the relative skin dose from the air generated component of ionising radiation. Measurement and simulation of these components have been performed.

iv) In patient build up interactions

As photons (primary or scattered secondary) traverse tissue there is a probability that they will interact (eg. Compton) causing charged particle scatter. The charged particle energy entering successive regions increases with depth until approximately the maximum longitudinal range of the secondary electrons is reached (Metcalfe et al 1997). The number of electrons crossing each boundary continues to increase until eventually it is balanced by secondary electrons running out of energy and by attenuation of the photon fluence. This is known as the site of transient charged particle equilibrium. A schematic of the phenomena is shown in figure 1.3. Also shown in figure 1.4 are Monte Carlo generated electron tracks at an air-tissue interface which clearly show the in phantom build up effect.

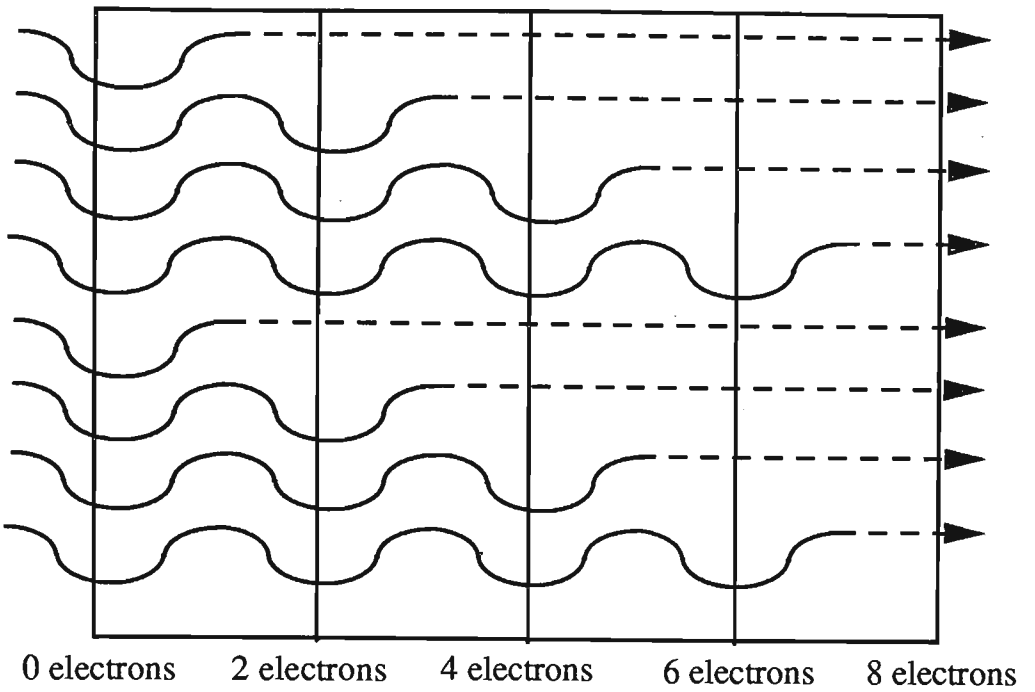

Figure 1.3 : Schematic representation of longitudinal electron disequilibrium. This feature of high energy photon beams produces the dose build up effect.

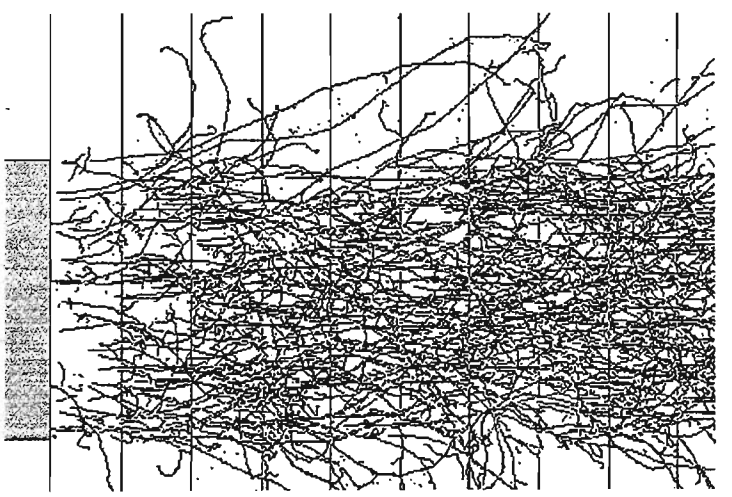

Figure 1.4 : Graphical representation of the build up effect generated by Monte Carlo simulation of a megavoltage photon beam. Shown are the electron tracks generated by interactions within the phantom. A smaller percentage of electrons are generated and deposit dose in the air/phantom interface region which produces the build up effect (Metcalfe et al 1997).

v) Bolus

In some cases the surface dose is increased by purposeful placement of build up material on the skin to bring the maximum dose to the skin surface. This material is called Bolus. In some cases the skin dose is increased by unwanted build up materials, such as immobilisation masks, within the treatment beam. In these cases the skin dose can be reduced by cutting away the area within the treatment field.

vi) Angle of incidence

Changes in the beam angle of incidence inherently increase the dose to the skin. In essence, the beam passes through a larger radiological distance for the same depth in skin and thus deposits an increased absorbed dose in this region as shown by figure 1.5. The area within each pear shaped region represents a qualitative assessment of the deposition zone of dose in the build up region from a series of discrete high energy photons interacting at points near the surface. These may be loosely described as pictures representing dose spread arrays (Mackie et al 1984, Dupont et al 1994, Ostwald 1997) or differential pencil beams (Mohan et al 1985). A larger percentage of the area covers the initial entrance region as the beams angle of incidence increases causing the increase in dose in the build up region. Note, this explaination does not include reduction in planar fluence through the skin with increasing angle of incidence.

vii) Exit dose

Exit dose contributions to skin dose depends heavily on the extent of previous attenuation or the thickness of tissue already traversed. A lack of backscatter material on the exit side of a patient produces a reduced dose in this region compared to full backscatter conditions. The exit dose is still significant however, and is usually about 85% of the exit dose if full back scatter were present (Kron et al 1996).

This thesis involves the measurement, modelling and reduction of skin and build up dose from megavoltage photon beams used to treat radiotherapy cancer patients. Skin dose from orthovoltage x-rays and megavoltage electron beams has also been addressed in the appendices.

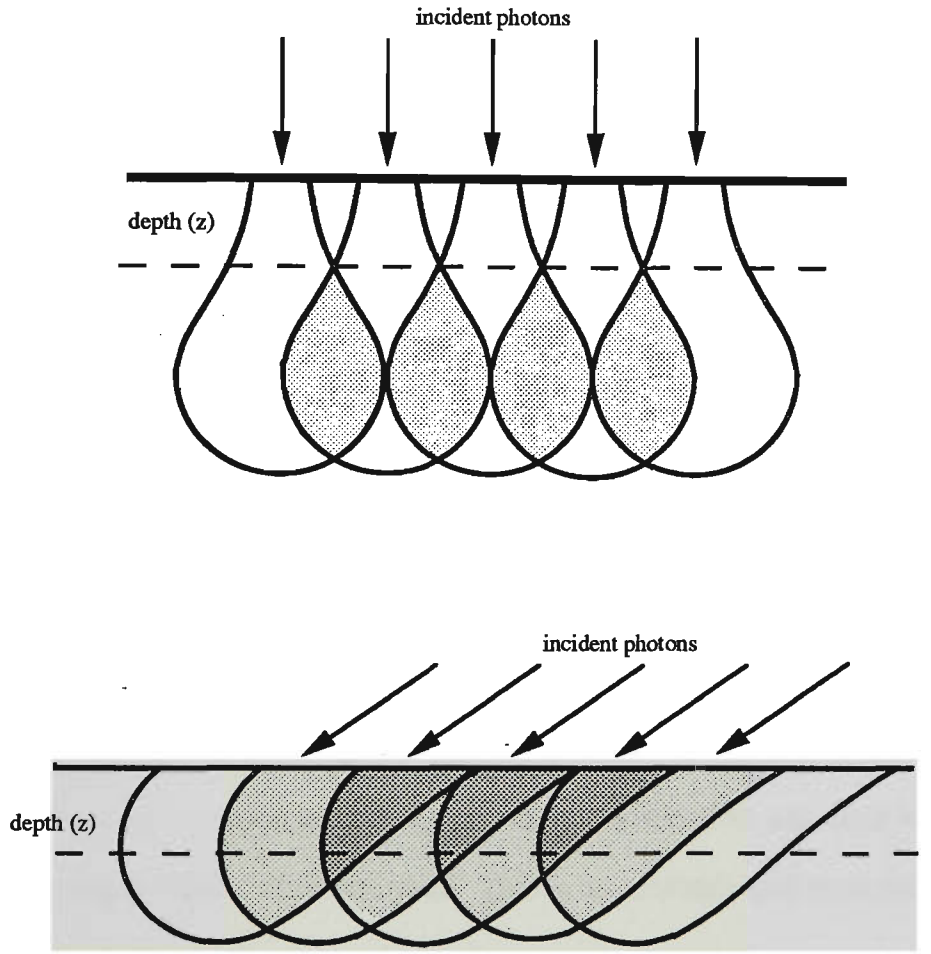

Figure 1.5 : Qualitative analysis of the enhanced dose effect due to beam angle of incidence. Each pear shaped region represents dose deposition for incident photons. As the beam angle of incidence increases, a larger quantity of the dose deposition moves closer to the surface.

1.2 Skin radiobiology and radiation damage

Layers of skin

The skin has two main layers (strata) as shown in figure 1.6, the epidermis and the dermis. In the epidermis the most inner layer called the basal layer repeatedly produces new cells in such a way as to push the older cells towards the surface. The depth to the basal layer from the surface can vary in different parts of the body. The average depth is approximately 0.07mm (Williams et al 1989). As the cells approach the surface they undergo some biological changes until they appear on the most outer layer as dead cells called the stratum cornium. The radiation damage to the skin is considered to be due to the destruction of the basal layer and the vascular dermis. Reddening of the skin (erythema) is assumed to be partly caused by the inflammation of the basal layer and partly due to direct effects on blood vessels due to radiation induced damage (Turesson et al 1989). Erythema is classified as an early effect. An early effect is classified as a reaction that occurs during or immediately proceeding irradiation. A late effect is that which is evident some length of time after radiation exposure. Early responding tissues are generally regarded as showing an effect in less than one year while late responding tissues show effects after one year. This is an arbitrary and non-universal time cut off.

The dermis which contains blood capillaries, sweat glands, sebaceous glands, nerve endings and hair follicles extends down from 1 to 4mm. This layer is prone to late reactions from radiation damage. Telangectasia, dry and atrophic skin, alopecia and pigmentation are some of the late effects. Clinical studies have shown that these effects especially telangiectasia can increase in severity for at least 15 years following radiotherapy and the progression is strongly dose dependent (Turesson et al 1989). The mechanisms behind telangectasia are still not entirely understood. Factors could be a deficiency in regenerated capillaries, or damage to the smooth muscle cells of the precapillary sphincters which fail in function (Turesson et al 1989). Below this region

is the subcutaneous tissue. This layer can be the site of near surface recurrence (Yip et al 85).

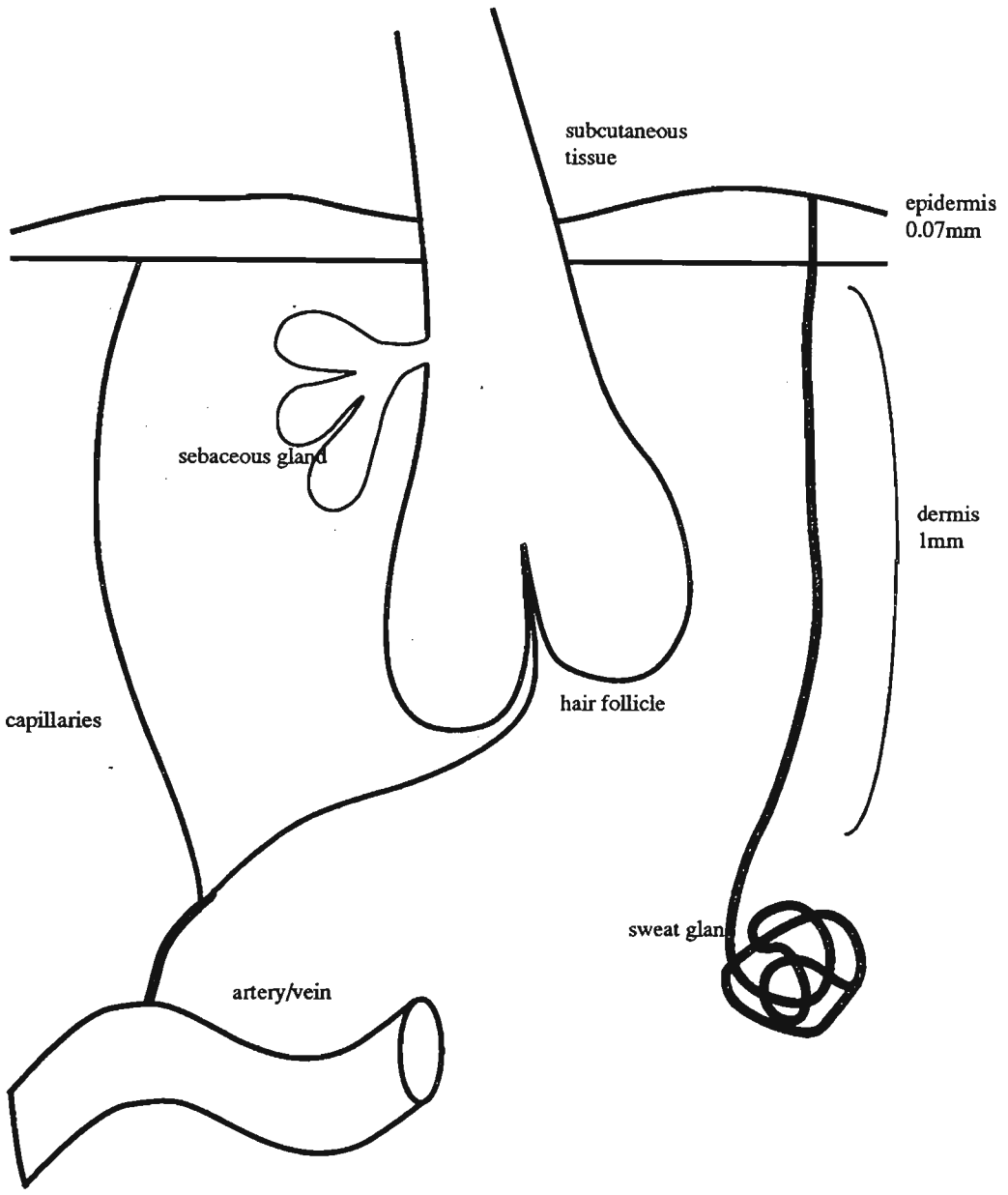

Figure 1.6 : Schematic of human skin. The basal layer lies at the base of the epidermis (0.07mm) and is the site of new skin production. Within the dermal layer lies hair follicles, capillaries and the sebaceous glands. Below this region is the subcutaneous tissue which has sweat glands, veins and arteries.

Radiotherapy and normal cell death.

During a course of radiotherapy the tumour volume is irradiated. Unfortunately a volume of normal tissue is also irradiated. The healthy skin is one organ which receives a dose on each occasion with sometimes serious complications. As with tumours, normal tissue is also affected by radiation. Radiation injury has both transient and permanent impacts on renewing populations of tissues. Two such impacts on cell production and renewal are mitotic delay and mitotic death. Mitotic delay occurs in the G2 phase of the cell cycle after irradiation. Following this delay, mitotic death may occur to transit cells. This can occur up to five divisions after irradiation and is dependent on dose (Thompson et al 1996).

The first sign of radiation injury to skin is evident as reddening, otherwise known as erythema. An acute erythema will occur a few hours after irradiation when the dose level is above 5Gy. This initial erythema will disappear but will reappear one to two weeks into a treatment regimen. Following these reactions, denudation can occur due to a continued loss of mature cells from the surface with a lack of production of new cells from the basal cell layer. The severity of the response depends on many factors including, dose, time, area of skin irradiated and skin site. Shown in table 1.1 is an assay of skin reactions and target cell population (Lippincott 1992).

Late reactions can also occur from months to years after irradiation. The epidermis is repaired by stem cell regeneration and migration from unirradiated parts. However this can be retarded by long term ulceration arising from severe acute desquamation or from injury to the dermal layer and subcutaneous tissue.

Table 1.1 : Clinical skin reactions to radiotherapy

Skin Reaction	Cell Population
Erythema	Capillaries and stroma
Hair (Alopecia)	Follicular clonogens
Pigmentation changes	Melanoblasts
Necrosis	Epidermal clonogens
Explants and cultures	Fibroblasts and keratinocytes
Telangectasia	Vasculature
Contraction, atrophy / Fibrosis	Dermal Components
Deformities	Epithelial/stromal

The five R's of radiotherapy

The effect of radiotherapy on cells has been summarised by Withers (1975) as the four R's of Radiotherapy. Steel (1989) included an additional R. The five R's are summarised as follows:

Repair

This consists of the repair capacity for both normal and cancerous cells and the non repairable cellular injury. The capacity for repair is determinable in vivo by comparison of single doses to several doses given in fractions which achieve the same biological effect. The repair capacity varies with cell type.

Reoxygenation

For x-rays it has been clearly seen that during fractionated radiotherapy the oxygen content of a tumour improves (Withers 1975). Fractionated schedules allow the tumour

to reoxygenate cells after radiation. This is necessary to optimise tumour cell kill. If time is allowed for reoxygenation cells are more sensitive to radiation and the tumour control will be achieved more effectively.

Redistribution of cells

The radiosensitivity of cells depends on their phase in the cell cycle. Consequently, if cells are in their most sensitive phase during treatment, the tumour control will improve. Thus if treatment is given by fractionation the majority of cells should be irradiated in their most sensitive phase at some time during treatment.

Regeneration

Regeneration refers to continued growth of tissues and in some cases accelerated growth of tumours. The rate of repopulation (otherwise known as proliferation) varies dramatically with the type of normal tissue or tumour involved.

In future, treatment fractionation regimens may be tailored to account for the individual tumour growth or regeneration of normal tissue such as skin cells. This is still the subject of further investigation and discussion.

Radiosensitivity

This factor accounts for the inherent differences in how different tumour types, or different tumours of the same type respond to radiation. Normal tissue shows variation in radiosensitivity also.

Skin complication probabilities

In order to control a tumour, all clonogens need to be destroyed. Poisson statistics show that the probability of tumour control occurring increases with dose (Metcalfe et al 1997). This probability is defined as the tumour control probability (TCP). This probability also varies with tumour treatment schedule, size, density and stage.

Normal tissue complication probability (NTCP) is the probability of a complication occurring in normal tissue. Unlike TCP, for NTCP not all the cells have to be killed to cause a complication. The serial structure model is one way of explaining this observation where a loss of critical sub-elements in the tissue chain can cause significant damage (Kallman 1995).

It would appear to be beneficial to calculate NTCP's versus dose for skin and subcutaneous tissue. Then by assessing build up dose before treatment the NTCP for the skin of each patient can be estimated. If the NTCP is too high then action may be considered to reduce skin dose via a modification of some technical aspect of the regimen.

Calculating NTCP's

Calculation of the probability of complications follows a similar mathematical procedure as calculation of tumour control probabilities. To preserve the skin we need to restrict the absorbed dose level to remain below the 'kick off' dose at which point skin complications increase. Consider tissue with a survival probability of S. The probability of death is then 1-S. If the tissue contains N cells then the probability of the entire tissue region not surviving is

$$P = (1 - S)^N \qquad 1\text{-}2$$

S is determined from the linear quadratic(LQ) model of cell survival such that

$$S = e^{-(\alpha d+\beta d^2)} \quad . \qquad 1\text{-}3$$

By allowing for proliferation

$$S = e^{-(nd(\alpha+\beta d)-\gamma(T-T_k))} \qquad \text{(Fowler 1989)} \qquad 1\text{-}4$$

where n is the number of fractions, d is the dose per fraction, T is the time of overall regimen duration (days), T_k is the 'kick off' time. The terms α and β are fitting parameters which are loosely related to single hit kills and multiple hit kills respectively. Note : $\gamma = \ln 2/T_p$ where T_p is the potential doubling time of clonogens when cell loss is not considered.

This model assumes a constant exponential growth independent of tumour volume. This is the currently "most used" approximation although it is likely that a more complex relation (eg. Gorpertzian) may be more exact (Newcomb et al 1993). It is felt that this model does not adequately model skin cell death as the rapid nature of skin cell death and replacement is not accounted for by this work (Hamilton et al 1996).

Repair of skin tissue can in part be introduced by including the rate of Elkind repair which is described by the first order rate constant μ (h^{-1}) or half time of repair $t_{1/2}$(h) where $\mu=\ln 2/t_{1/2}$. The effect of total treatment time is then expressed by the rate constant γ.

If complete Elkind repair is assumed, (time between fractions is $\geq$ 24h) the effect to skin and probability of effect can be modelled such that (Turesson et al 1989):-

$$Effect = -\ln S.F. = \alpha Nd + \beta Nd^2 - \gamma(T - T_0) \qquad 1\text{-}5$$

and

$$\therefore P_{effect} = 1 - \exp(\ln k - \alpha Nd + \beta Nd^2 - \gamma(T - T_0))^k \qquad 1\text{-}6$$

$$\therefore P_{effect} \approx \exp(-\exp(\ln k - \alpha Nd + \beta Nd^2 - \gamma(T - T_0))) \qquad 1\text{-}7$$

where S.F. is the surviving fraction of the target cells and P_{effect} is the probability of the effect, N is the number of fractions, T is the overall treatment time, T_0 is the time lag in days and k is the number of tissue rescuing units initially at risk.

NTCP is shown in figure 1.7. with varying values for dose per fraction. All other parameters are held constant to show how NTCP can be effected by dose per fraction. Other values are consistent with empirical parameters for 50% erythema as quoted in table 1.2. Successful radiotherapy relies on the NTCP versus dose curve being located to the right of the TCP versus dose curve. Thus the TCP is high while the NTCP is low. Table 1.2 gives values quoted by Turesson et al (1989) of suitable parameter values required to match dose for reactions of 50%-Erythema, desquamation and Telangectasia. These values are from direct analysis of patient results. It should be noted however that the values for radiobiological modeling are considered variable and can change on a patient to patient basis.

Skin damage

Turesson et al (1989) have performed comprehensive clinical studies of skin damage and the radiobiological effects on skin from radiotherapy. Their studies have included the influence of dose per fraction, inter fraction interval and duration of rest periods on

the response of acutely early and late reacting normal tissue. Skin reactions for 50% erythema (where the skin doubles in redness as measured by a reflectometer), desquamation and telangectasia were measured to varying degrees. Patient results were then compared to the NTCP results using the complete Elkind repair model from equation 1.6). Figures 1.8a and 1.8b show clinical results for 50% erythema and telangectasia at the quoted dose per fraction and number of fractions. NTCP curves are fitted to the data. Dose levels for these reactions are quite high. However for some patients this can be an achievable range with their treatment regimen. In these cases, early prediction of clinical skin damage could be used to reassess the treatment technique by changing beam parameters in an attempt to limit skin dose to an acceptable level. However it should be noted that the NTCP may apply to the radiotherapy treatment population on average, but to use NTCP values for individual response may be inaccurate unless an individuals response is measureable by an assay (Thames and Hendry 1987).

Table 1.2 : Skin complication probability parameters

Parameter	Erythema	Desquamation	Telangectasia
lnk	4.81	5.57	4.59
α	0.095	0.102	0.084
β	0.00127	0.0091	0.0206
μ	-	-	0.19
$t_{1/2}$	-	-	3.6
γ	-	-	0.042
T_p	-	-	17

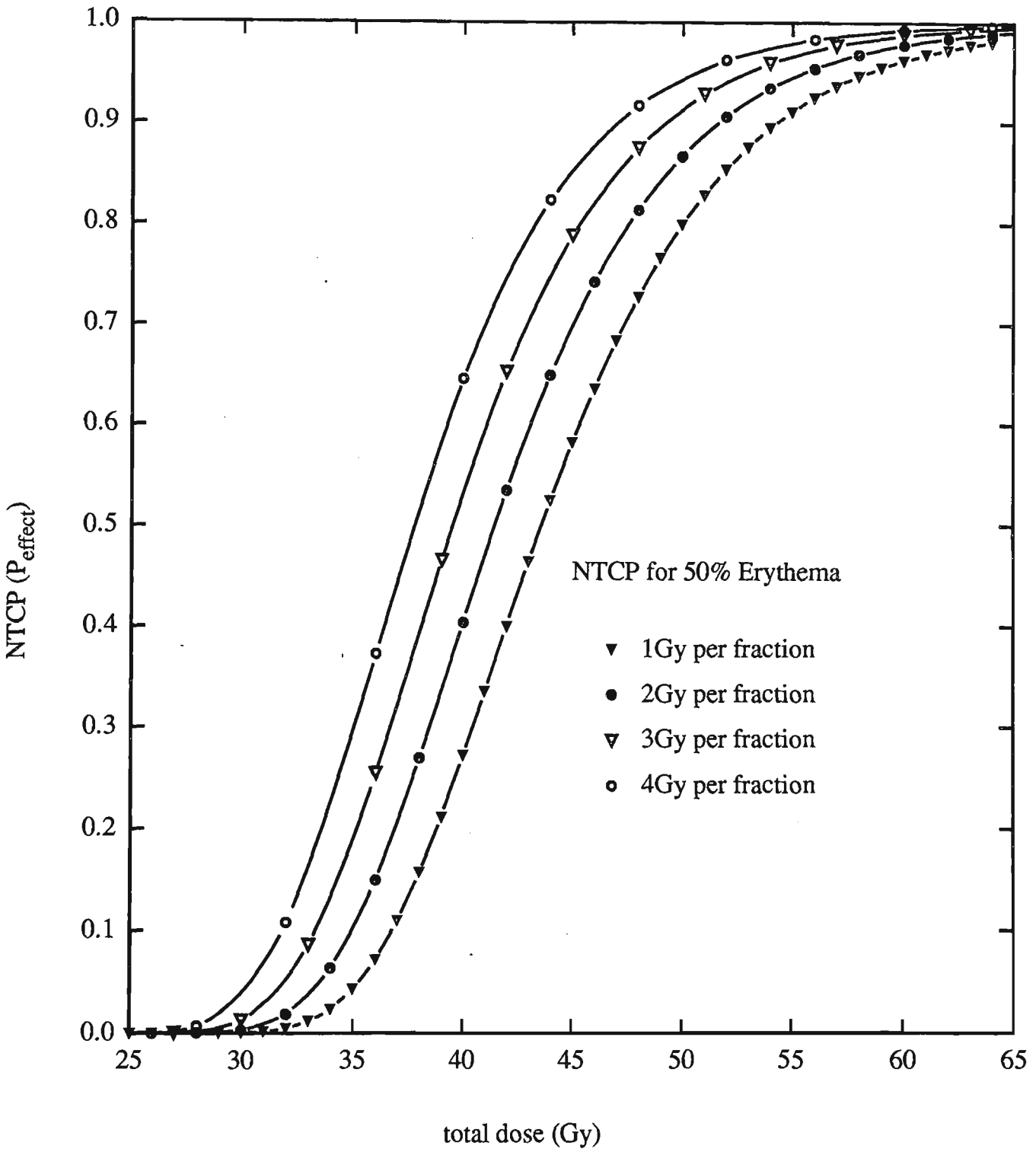

Figure 1.7 : Normal tissue complication probabilities for 50% erythema with typical treatment regimens ranging from 1Gy to 4Gy per fraction.

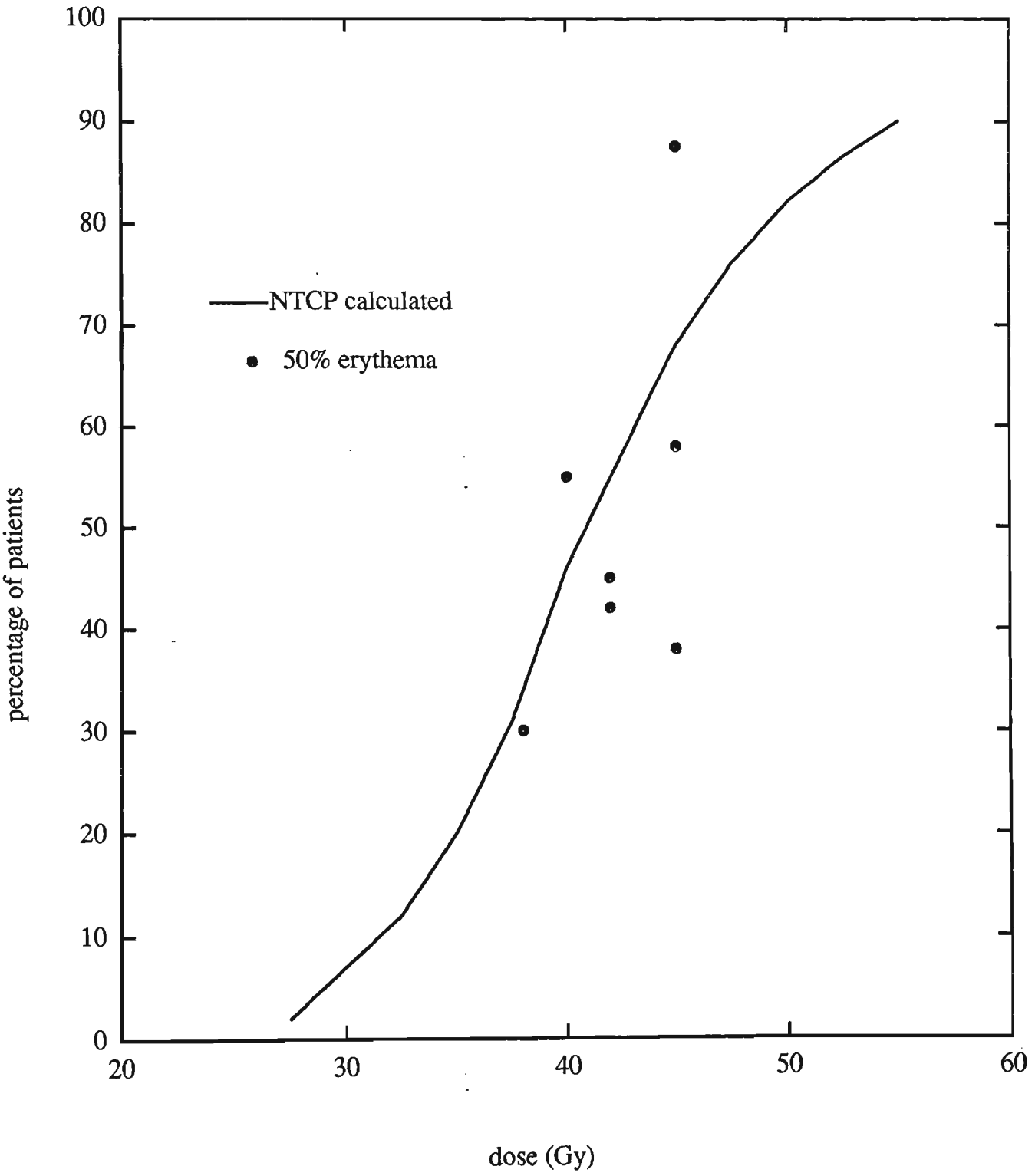

Figure 1.8a : Clinically measured normal tissue complication probabilities for 50% erythema at a 2Gy per fraction regimen.

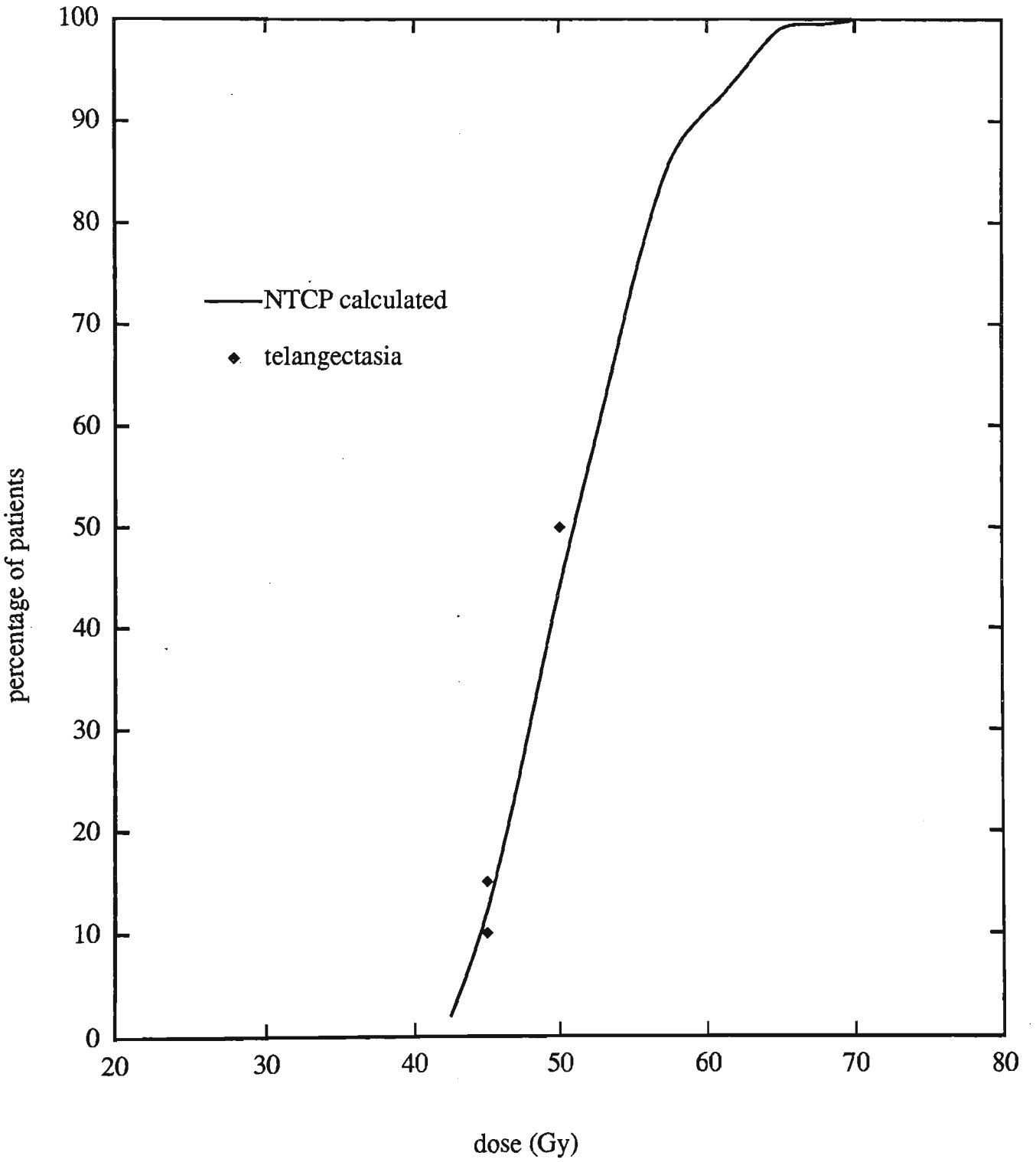

Figure 1.8b : Clinically measured normal tissue complication probabilities for telangectasia at a 2Gy per fraction regimen.

1.3 Photon interactions

Attenuation coefficients

A characteristic of the interaction of photon radiation with matter is that each individual photon is absorbed or scattered from the incident beam in a single event. The photon number removed ΔB is proportional to the thickness travelled through Δx and the initial photon number B, ie.

$$\Delta B = -\mu B \Delta x \quad , \qquad 1\text{-}8$$

where μ is a constant of proportionality called the attenuation coefficient. In this case, upon integrating 1.8, then

$$B = B_0 e^{-\mu x}. \qquad 1\text{-}9$$

The attenuation coefficient is related to the probability of interaction per atom, ie. the atomic cross section σ_a is given by,

$$\sigma_a = \frac{\mu A}{N_A \rho} \qquad 1\text{-}10$$

where A is the mass number and N_A is Avogadro's number (6.022×10^{23} mol^{-1}).

Table 1.3 gives a summary of most photon interaction processes with matter (Siegbahn 67).

Table 1.3 : Table of radiation interaction processes

Process	Type of interaction	Other names	Approximate energy range of maximum importance	Approximate variation with Z
Photo electric Effect	with bound atomic electrons (all energy given to electron)		Dominates at low (1keV to 500keV) Cross section decreases as E increases.	Z^5
Scattering from electrons				
Coherent electrons	with bound atomic resonance	Rayleigh , Electron small angles scattering	<1MeV and greatest at Z^3	Z^2
	with free electrons	Thomson scattering	Independent of energy	Z
Incoherent	with bound atomic electrons		<1MeV least at small angles	Z
	with free electrons	Compton scattering	Dominates in region of 1MeV Decreases as E increases	Z
Nuclear photo effect	with nucleus as a whole emitting gamma or particle	particle production Nuclear photodisintegration	Above threshold, has broad maximum range of 10-30 MeV	
Nuclear Scattering				
Coherent	with material as a whole. Dependant on	Nuclear resonance nuclear energy levels	Narrow resonance maximum scattering at low energies. Broad max` in energy range of 10-30MeV.	Z^2/A^2
Incoherent	with individual Nucleons	Nuclear Compton scattering	$\lambda <<$ nuclear radius ie >100MeV	Z^4/A^2
Interaction with a Coulomb field.				
Pair production	in coulomb field of nucleus	Elastic pair production	Threshold about 1MeV Dominates at high E ie E> 5MeV and increases as E increases	Z^2
Pair production	in coulomb field of electron	Triplet production Inelastic pair prod/n	Threshold at 2MeV Increases as E increases	Z
Delbruck scattering	in coulomb field of nucleus	Nuclear potential scattering	Real max> imaginary below 3MeV. Both increase as E increases	Z^4

In the energy range of superficial to megavoltage clinical x-ray beams, ie. nominally less than 20MeV, interactions of photons with matter are mainly due to three processes. These being:- i) photoelectric absorption, ii) Compton scattering and iii) pair production

As the above mentioned processes are energy dependent and would all effect the beam, we find that the total attenuation coefficient or cross section is approximated by the sum of all interactions. For therapeutic photon energies, this consists of absorption and scattering such that

$\mu = \tau$ (photoelectric)+ σ (Compton) + κ (pair production),

$$\Delta B = -(\tau + \sigma + \kappa) B \Delta x. \qquad 1\text{-}11$$

Photoelectric effect

With a photoelectric interaction, the photon transfers all of its energy to a bound electron and the kinetic energy of the electron is given by Einstein's photoelectric equation,

$$T_{max} = h\nu - \phi \qquad 1\text{-}12$$

where, $h\nu$ is the initial photon energy, ϕ is the electron binding energy (work function) and $T_{max} = \frac{1}{2} m v^2$ which is the maximum kinetic energy of the ejected electron.

The atom is left in an excited state and will emit characteristic radiation and auger electrons in its transition back to the ground state. The energy deposited in a photoelectric event in tissue can be assumed to be absorbed at the point where the photon interacted.

Compton scattering

When considering scattering theory of photons by electrons it is usually a satisfactory approximation to consider the electrons as free particles (McGervey 1983). If scattering is considered as in figure 1.9, relativistic equations derived from the conservation of energy and momentum can be formulated. The change in wavelength of a photon ($\Delta\lambda$) is given by

$$\frac{c}{\nu'} - \frac{c}{\nu} = \lambda' - \lambda = \frac{h}{mc(1-\cos\theta)} \quad . \qquad 1\text{-}13$$

where λ is the wavelength of the incident photon, λ' is the wavelength of the scattered photon, m is the mass of the electron and θ is the angle of scattering for the photon.

Rearranging gives

$$h\nu' = \frac{h\nu}{1+\alpha(1-\cos\theta)} \quad . \qquad 1\text{-}14$$

where α is the ratio of the energy of the photon to the rest energy of the electron.

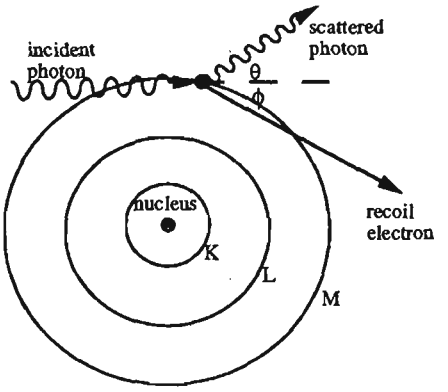

Figure 1.9 : Compton interaction processes with an m-shell electron. The photon is scattered and a recoil electron produced.

The kinetic energy (T) for the recoil electron is given by

$$T = h\nu \frac{\alpha(1-\cos\theta)}{1+\alpha(1-\cos\theta)} \qquad 1\text{-}15$$

and the scattering angle of the electron is given by

$$\cot\phi = (1+\alpha)\tan\frac{1}{2}\theta \ . \qquad 1\text{-}16$$

Klein and Nishina (1929) carried out a quantum mechanical treatment to obtain the Compton scattering cross section using the Dirac equation for the electron. Let the intensity of the scattered photons at angle θ and distance r from the scattering electron be I and incident energy of the photon be I_0 then,

$$I = \frac{I_0}{r^2}\left(\frac{h\nu'}{h\nu}\frac{d\sigma}{d\Omega}\right) \qquad 1\text{-}17$$

where $d\sigma$ is the cross section per electron for the number of photons scattered into solid angle $d\Omega$ in direction θ. This gives the differential cross section per unit solid angle obtained by Klein and Nishina as

$$\frac{d\sigma}{d\Omega} = \frac{r_o^{\,2}}{2}\left(\frac{1}{(1+\alpha(1-\cos\theta))^2}\left(1+\cos^2\theta+\frac{\alpha^2(1-\cos\theta)^2}{1+\alpha(1-\cos\theta)}\right)\right) \qquad 1\text{-}18$$

where r_0 is the classical electron radius and $\alpha = h\nu/mc^2$. This reduces to the classical Thomson scattering equation, for low energy photons when $\alpha << 1$.

$$\frac{d\sigma}{d\Omega} = \frac{1}{2}r_0^{\,2}(1+\cos^2\theta) \qquad 1\text{-}19$$

Pair production

The production of a positive and negative electron pair is a process which can take place in the vicinity of the field of a atom or an electron. Absorption of photons through the mechanism of pair production can occur when the energy of an incident photon is greater than twice the rest mass of an electron, ie. 2 x 0.511 MeV = 1.022 MeV(Johns and Cunningham 1983). During pair production interactions, a photon has its energy converted to an electron-positron pair. The positron so produced interacts with matter by ionising and exciting atoms through the same processes as electrons, thus losing energy and being brought to rest. At this point the positron combines with an electron in an annihilation process producing two 0.511 MeV photons.

Importance of each interaction process

It has been shown in the previous section that the probability of each interaction occurring varies with the incident photon energy $h\upsilon$, and the atomic number Z of the absorber. Figure 1.10 shows the relative proportion of the three main interaction processes plotted against energy, taking place in water. Compton interactions are the main process at therapeutic energies. Results are graphed using relative percentage data for interactions from Johns and Cunningham (1983).

Mean free path

The mean free path of photons in matter is given by the reciprocal of the linear attenuation coefficient. It represents the average distance a photon will travel before interacting. There will be a statistical variance around the mean value which normally follows a Gaussian shape. Figure 1.11 shows the mean free paths for photons in water, fat, muscle and bone. Relatively large distances are travelled before interactions take place on average. For photons in water at 6MeV the mean free path is approximately 40cm.

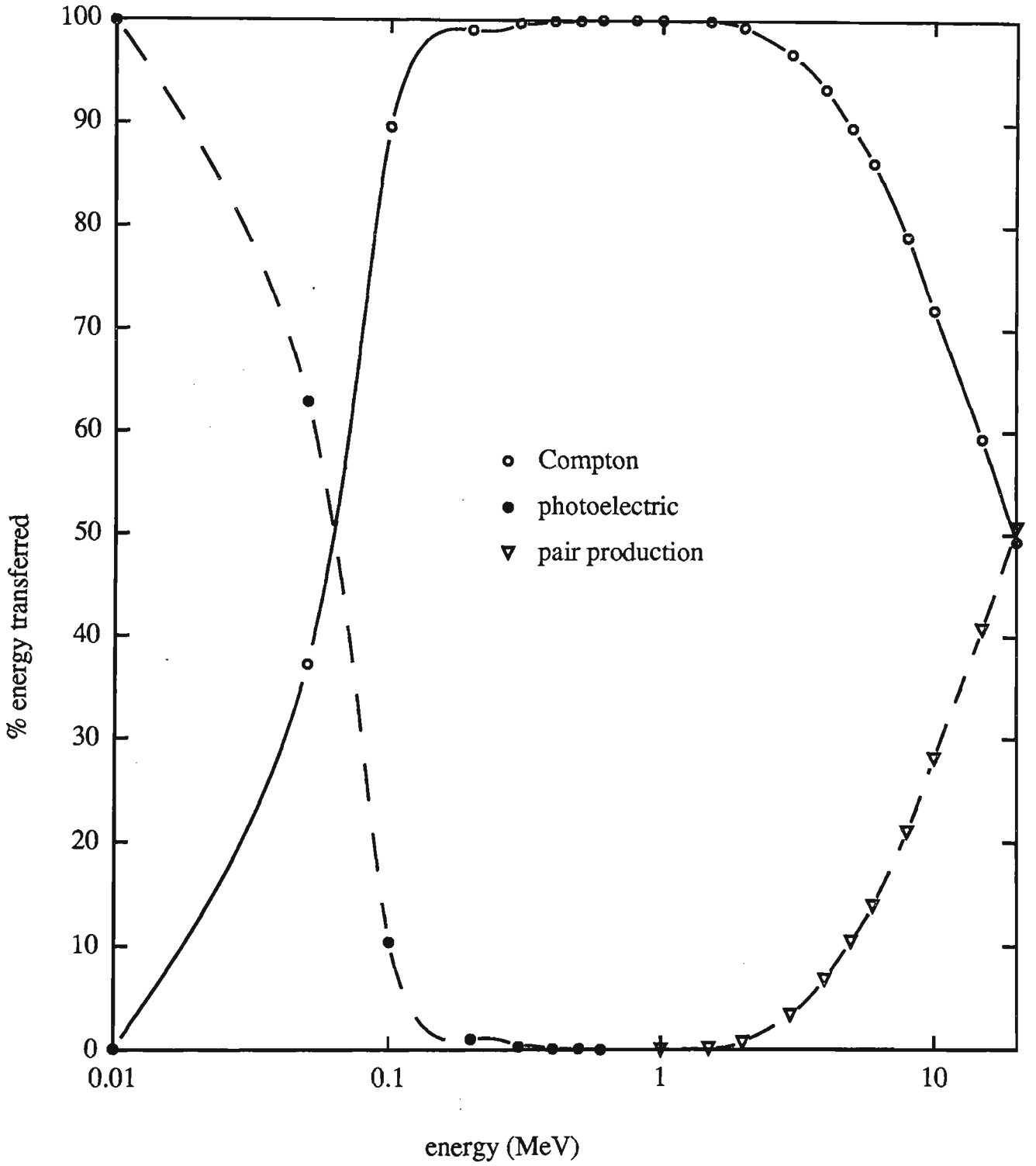

Figure 1.10 : Percentage contributions of photoelectric, Compton and pair production for photons at various energies. At clinical photon energies, Compton interactions are the main process.

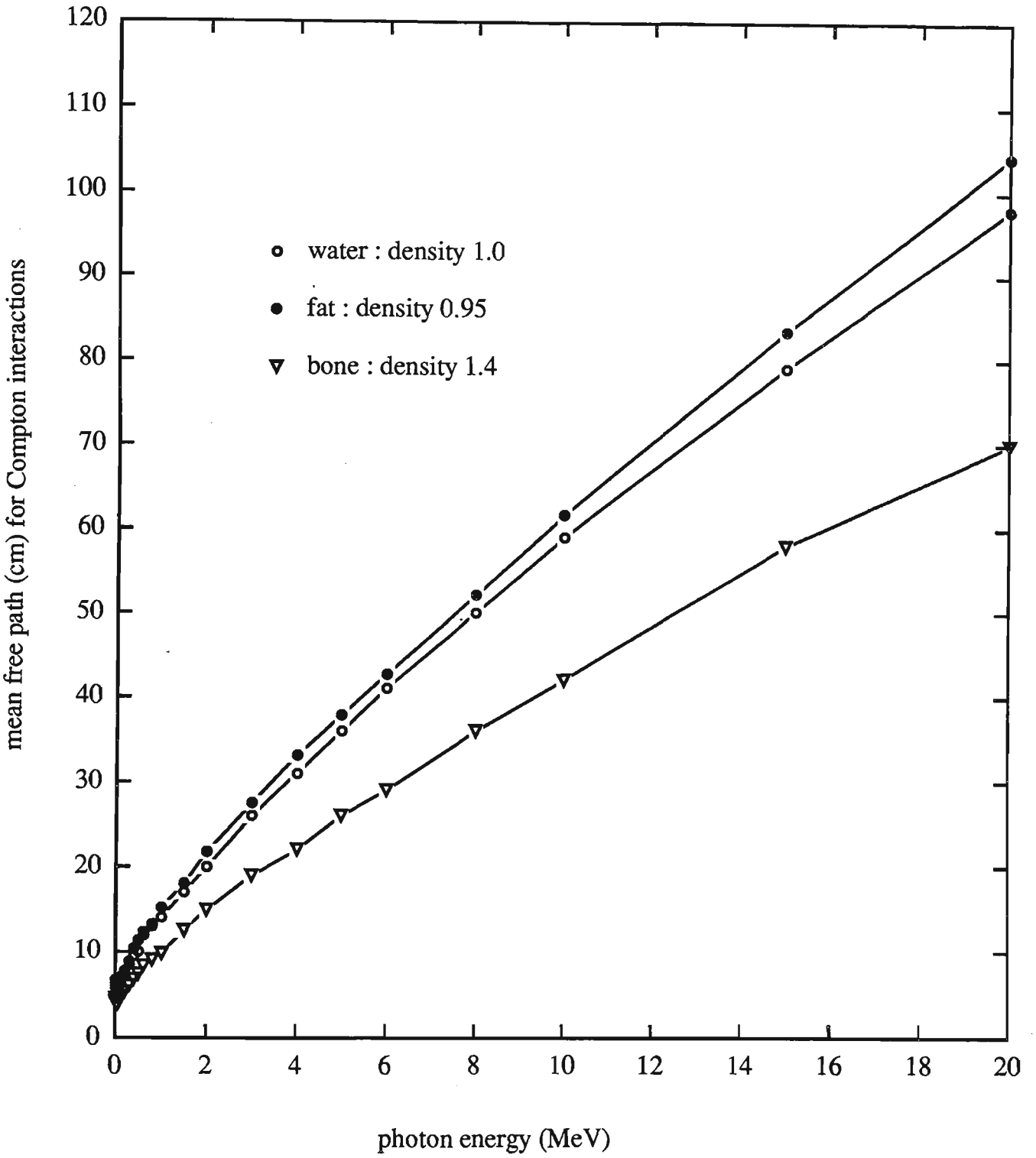

Figure 1.11 : Mean free path of photons in water, fat and bone. The average energy for a 6MV clinical photon spectrum is approximately 2MeV, for which the mean free path in water is approximately 20cm.

At 2MeV (approximately the mean energy for a 6MV spectrum) the mean free path is approximately 20cm in water. This would be approximately 170 metres in air.

Radiological depth

The radiological depth is found from the electron density of the traversed material along the beams path. It is the equivalent depth in water required to attenuate the photon beam by the same amount as in the medium. If P is a point in the medium at position r_p and the line from the source to P intersects the medium at r_0 then the radiological depth at P is given by

$$d_p' = \int_{r_0}^{r_p} \rho_e^w(r')dr' \qquad 1\text{-}20$$

The physical depth R_p is simply r_o-r_p. When deriving radiological depths in the build u region the electron density of the skin and subcutaneous tissue should be taken into accoun Skin can be considered to have a density close to water density as shown by table 1.4 Results show average values for each material as quoted by Woodard et al 1986. Variation in density for skin and subcutaneous tissue are noted however they are considered not large nor predictable enough to warrant a correction factor in build up dose calculations.

Table 1.4 : Mass and electron densities of tissue in the build up region

	Density (g/cm)	Elec./g (x 10^{21})	Elec./cm^3 (x10^{21})	Relative elec./g	Relative elec.cm^3
water	1.00	3.343	3.343	1.000	1.000
skin	1.09	3.306	3.604	0.989	1.078
adipose	0.95	3.347	3.180	1.001	0.951
muscle	1.04	3.312	3.444	0.991	1.030

1.4 Electron interactions

Photon beams produce secondary electrons which deposit energy throughout the medium. Electron beams are also used for clinical treatments. The electrons travel on an irregular path as they deposit their energy, until all kinetic energy is expended or they are absorbed. These properties can be quantified by i) the electron stopping power and ii) electron scattering power.

Stopping power.

Electron stopping power is dependent on two main processes : i) the electron may lose energy via ionisation or excitation of other electrons (collisional stopping power) ii) the electron may lose energy from production of bremsstrahlung photons (radiative stopping power). Collisional stopping power may include energy lost to delta rays which are also called knock-on electrons. These rays are the tracks produced by the once bound electrons which suffered a violent collision. If the incoming charged particle is an electron and a delta ray is produced then the process is called Moller scattering. If a positron causes the delta ray production the process is called Bhahba scattering. The total kinetic energy of the positron can be lost during Bhahba scattering as the particles can be distinguished. Only half of the incident kinetic energy of an electron can be lost in Moller scattering as the electrons are indistinguishable.

Collisional stopping power.

The electron loses most of its kinetic energy through excitation and ionisation of atoms and molecules. Excitation or ionisation occurs depending on the proximity of the passing electron to the atom or its energy. That is, a close pass will transfer more energy often resulting in an ionisational process and a distant pass will more often only supply enough energy for a bound electron to be elevated to a higher state causing

excitation. The energy lost by the electron per unit path length due to excitation and ionisation is called the linear collisional stopping power, S_{coll}.

Radiative stopping power

When an electron passes close to a nucleus, it is decelerated and as a result, deflected by the electrostatic force between the nucleus and itself. The energy lost is converted into a photon and called a bremsstrahlung event. The energy lost (or converted into the photon) during this bremsstrahlung event is called the radiative stopping power S_{rad}.

The total stopping power is the sum of these two processes and is called the total linear stopping power, $S_{tot} = S_{coll} + S_{rad}$. The radiative stopping power at clinical energies remains a relatively small component of the total being only 0.7% at 1 MeV and 8.4% at 10MeV.

Electron scattering power

Elastic scattering of electrons is due to electromagnetic interactions with other electrons and nuclei. This continually deflects the incident electron from its current path.

Statistical prediction of the net angular deflections of the electron is possible as the deflections are independent of each encounter. According to Fermi-Eyges theory, when crossing a material of thickness Δz the electrons have an approximately Gaussian distribution of angles through which they are deflected (Klevenhagen 1985). The Gaussian distribution has a standard deviation σ_θ given by the root mean square angular deviation

$$\sigma_\theta = \sqrt{\frac{d\theta^2}{dz}\Delta z} \qquad 1\text{-}21$$

where $d\theta^2/dz^2$ is the linear scattering power and θ^2 is the mean square angle of deflection. The scattering power decreases with increasing electron energy (Werner et al 1982, Andreo 1985).

1.4 Range of electrons in matter

An electron is deviated off a straight line in collisions with atomic electrons. An electron can lose up to one half of its energy in a single inelastic collision. This value is such, because of the indistinguishable nature of electrons. A loss of all the energy from one electron to another is equivalent to no energy loss at all with the target electron replacing the incident one and vice versa.

The fact that energy lost by electrons in their interactions is random means that there is a probability that a very high energy electron will be stopped within a relatively short distance (McGervey 1983) whilst a lower energy electron could travel further into the material. However mean ranges for electrons at a given energy can be defined. This range for low energy (up to 30keV) is proportional to E^2 whilst at high energies (>1MeV) the range is proportional to E (Siegbahn 1963).

High energy electrons

A simple relation to calculate the maximum extrapolated range of electrons above the energy of 0.6 MeV in gm/cm^2 is

$$R_e = 0.526\frac{E}{MeV} - 0.094 \qquad \text{(Siegbahn 1963).} \qquad 1\text{-}22$$

Table 1.5 shows the theoretical maximum range of electrons of energy 6, 9, 12, 16 and 20 MeV. These are the beam energies available for treatment purposes on the Varian Clinac 2100C.

Table 1.5 : Range of electrons in water and air.

Electron energy (MeV)	Range in water (cm)	Range in air (cm)
6	3.06	255
9	4.64	390
12	6.22	520
16	8.32	690
20	10.43	870

Low energy contamination electrons

The typical range for lower energy electrons can be calculated by the use of the photon spectrum produced by the accelerator and the total mass stopping powers of materials. Figure 1.12 shows the energy range relationship for low energy electrons as quoted by Khan et al (1984).

By examining the 6MV photon spectrum shown in figure 1.13 (Mohan 1985), the average energy of the 6MV beam can be estimated by taking the mean of the spectral components (found to be 1.5MeV). The energy transferable to an electron in a Compton scattering event is given by

$$E_k = h\nu\left(\frac{\alpha(1-\cos\beta)}{1+\alpha(1-\cos\beta)}\right) \qquad 1\text{-}23$$

where α = 0.511MeV for electrons and β is the scattering angle. Maximum energy is transferred when we have a 180° forward scattering, hence

$$E_k = 1.5\times\frac{0.511\times 2}{(1+2\times 0.511)} = 0.758MeV$$

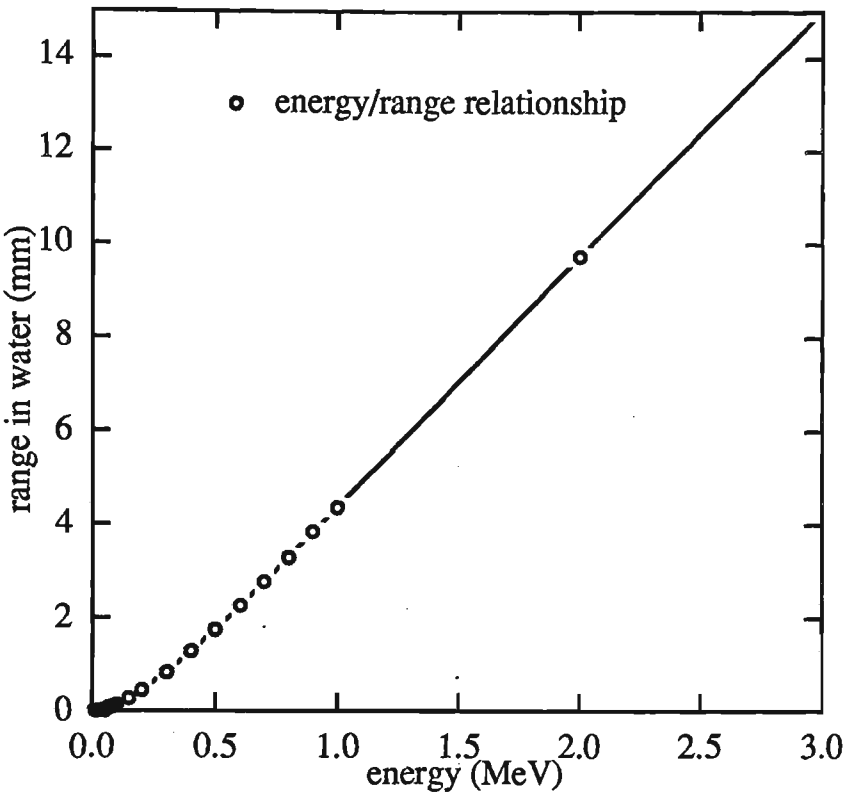

Figure 1.12 : Energy/range relationship for low energy electrons.

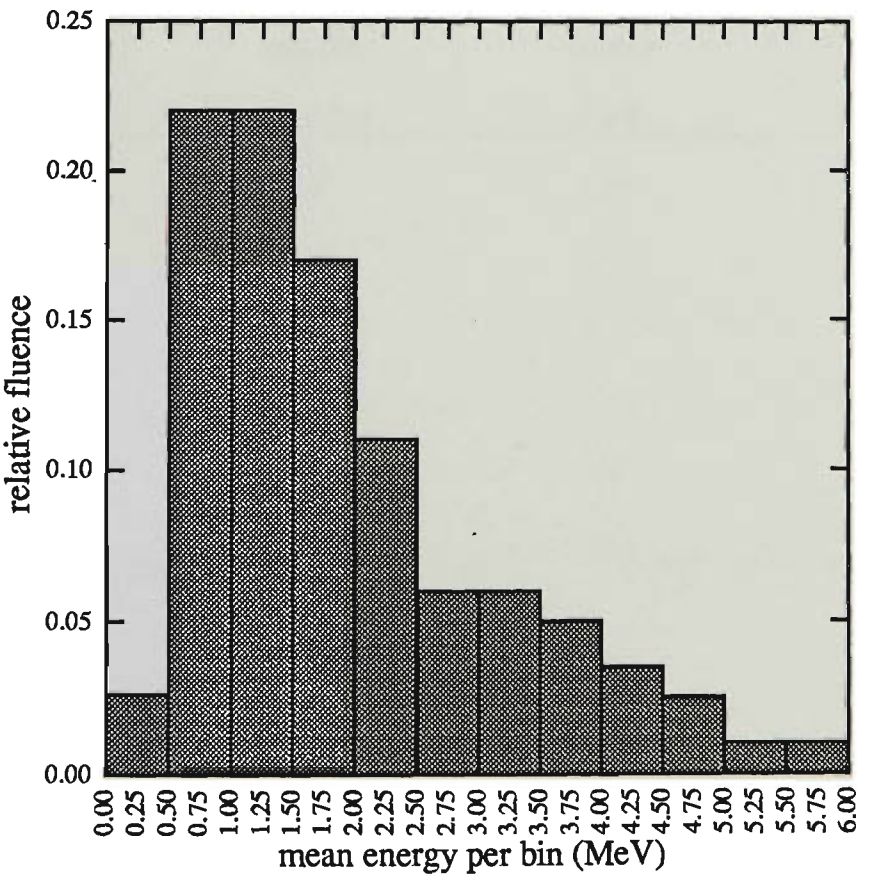

Figure 1.13 : Linear accelerator , 6MV photon spectrum determined by Monte Carlo. The mean energy is approximately 1.5MeV. (Adapted from Mohan et al 1985).

which gives a maximum kinetic energy for the electron in this collision of 0.76 MeV. This relates to a range of approximately 3.0mm in water.

There is a spectrum of incident photon energies and a range of scattering angles for the electrons in the collisions. So various ranges will occur. Also, not all electrons will scatter forward and many will scatter at different angles and will have less energy.

Table 1.6 shows the relative ranges for electrons scattered at various angles from various energy photons..

Table 1.6 : Scattering angles and ranges of electrons.

energy (MeV)	angle of electron (degrees)	energy of electron (MeV)	range of electron in water (mm)
1.5	45	0.195	0.1
1.5	90	0.51	1.7
1.5	180	0.76	3
6	45	0.78	3.1
6	90	2.0	10
6	180	3.0	15

1.6 Electrons in electromagnetic fields

Electrons in constant magnetic fields

Contamination electrons produced by clinical linear accelerators can be considered as medium energy relativistic particles. Relativistically the mass of an electron with kinetic energy E_k is given by

$$m = m_0 + \frac{E_k}{c^2}, \qquad 1\text{-}24$$

thus an electron with kinetic energy of 6MeV will have a relativistic mass of

$$m = m_0 + 12m_0 = 13m_0.$$

The radius of curvature (R) of an electron with charge e and momentum p within a magnetic field of strength B is given by

$$R = \frac{p}{eB}. \qquad 1\text{-}25$$

An expression which defines momentum in terms of kinetic energy is

$$p = \sqrt{\left(E_k\left(\frac{E_k}{c^2} + 2m_0\right)\right)}. \qquad 1\text{-}26$$

Upon substitution into 1-25 we can find the radius of curvature of an electron.

Figure 1.14 shows the radius of curvature as a function of energy for electrons in a uniform magnetic field. Our magnetic deflector produces magnetic fields up to 0.55

tesla near the poles with an average field strength at the central axis ranging from 0.08 to 0.35 Tesla for clinical radiotherapy field sizes.

One limitation in using the radius of curvature for an electron in a magnetic field in a clinical situation is that the magnetic field strength is not homogeneous. A magnetic field used to sweep electron contamination out of a therapeutic beam would be ideally positioned on the linear accelerators treatment machine head. Thus the magnetic field would be generated across the field in a slice or section below the block tray. As an electron generated above this field travels towards the patient, the magnetic field strength applied would increase as it approaches the poles and decrease again after passing by. This would produce a deflected path of flight. Thus a deflection angle would be a more appropriate measure of the magnetic deflectors ability to sweep electrons away from the patient's skin surface. Experimental results are discussed in chapter 4, where the deflection angles generated by a NeFeB magnetic deflector to produce such an effect are discussed.

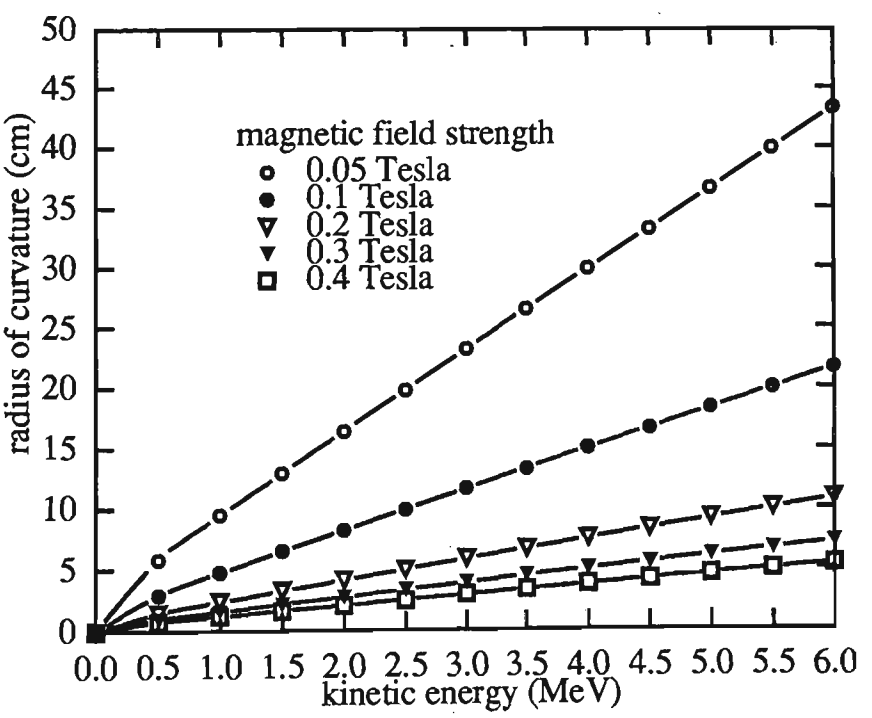

Figure 1.14 : Radius of curvature for electrons in a uniform magnetic field. the radius of curvature increases with electron energy and with decreasing magnet field strength.

Chapter 2 Materials and methods

2.1 Current dose planning

Assessment of skin dose during radiotherapy has to this point been limited by the accuracy of currently available planning systems. Our centre uses a General Electric Target series II planning station. The GE Target II uses a cubic approximation algorithm to calculate dose in the build up region for megavoltage photon beams (GE Target II physics manual 1996). This is performed by linear interpolation between the starting reference dose d_{ref} at the surface and d_{max} such that

$$d'_{ref} = d_{max} - \frac{\left(d_{max} - d_{ref}\right)^3}{d_{max}^{\ 2}} \quad . \qquad 2\text{-}1$$

The system allows the input of one initial starting point for surface dose and then fits a depth dose curve between this point and the dose at maximum. This is certainly not the case for all patient build up dose curves as shown in figure 2.1 which shows 3 build up curves measured using an Attix ionisation chamber for field sizes 5cm x 5cm, 15cm x 15cm and 40cm x 40cm compared to the cubic approximation

Differences of 10%, 12% and 45% of applied dose are encountered at the basal cell layer and 0%, 25%, 48% at the dermal layer when the calculation in 2-1 is applied. In the absence of a more elegant model, in-vivo dosimetry is performed to measure the skin dose on any one patient to determine the absorbed dose to this region. This process however is not an easy task due to the steep dose gradient in this region. Most current in-vivo dosimetry devices do not produce an accurate measure of epidermal dose due to their finite thickness which covers a significant distance across the steeply varying dose gradient.

The oversimplified calculation used by the Target series II planning system in the build up region leads to dose calculation errors. Hence a new build up dose planning calculation has been developed and reported in this thesis. The improvement and implementation of new skin dosimetry techniques have also been undertaken.

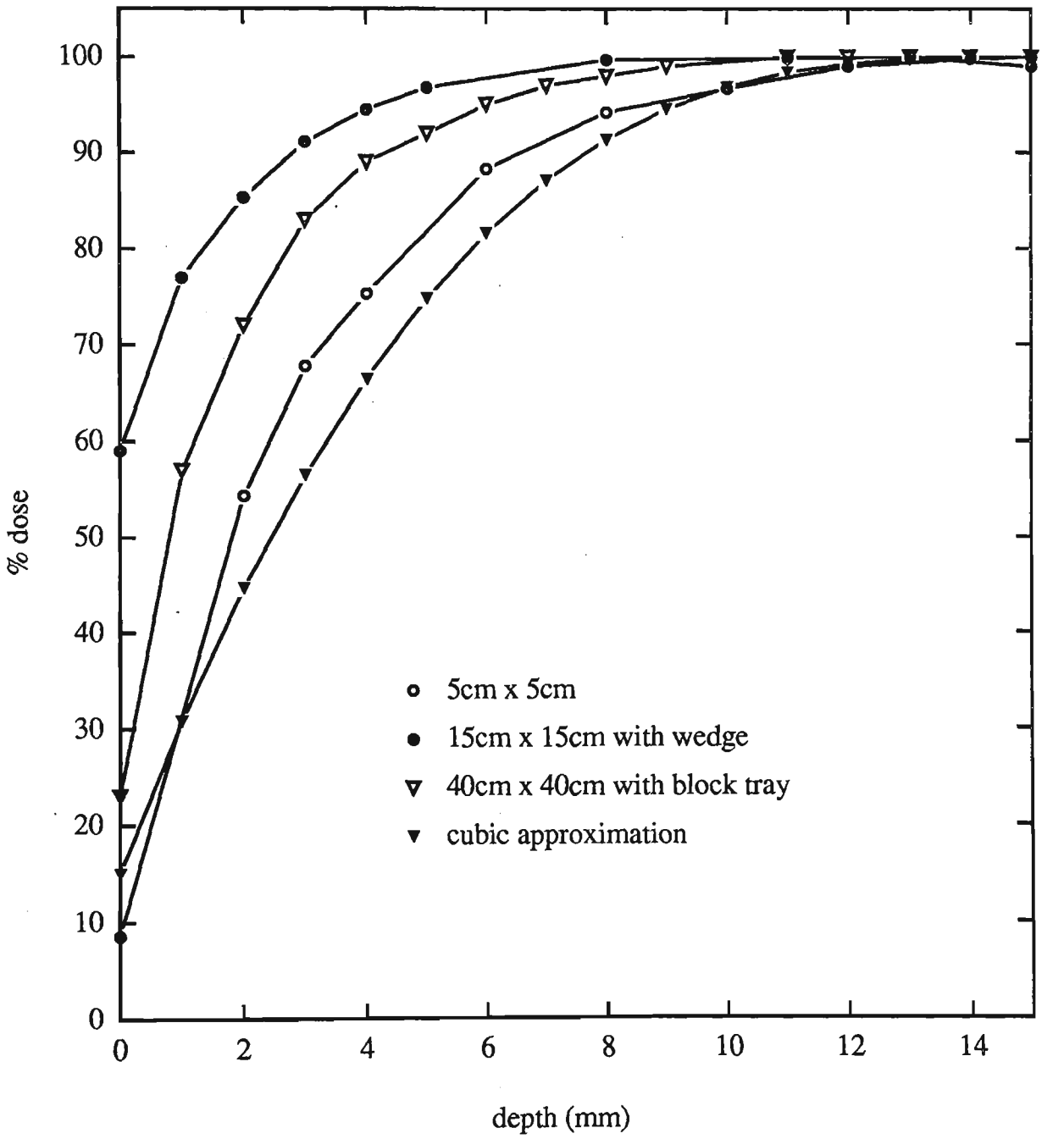

Figure 2.1 : Dose build up curves for 3 typical treatments and the cubic approximation used by the GE Target planing system. Large discrepancies in calculations are seen from experimental results for the cubic approximation.

2.2 Linear accelerators

A linear accelerator as the name implies is designed to accelerate charged particles (ie electrons, protons and heavy ions) to high energies through a linear tube (Khan 1992). A radiotherapy linear accelerator makes use of a wave guide to produce an electric field to accelerate electrons. This is performed using high frequency electromagnetic waves at approximately 3000 MHz. The radiotherapy machine almost exclusively used during this thesis was a Varian Clinac 2100C, as shown in figure 2.2.

Figure 2.3 gives an overview of the major components and auxiliary systems of a medical linear accelerator. The high energy accelerated electron beams themselves can be used for treatment. Alternatively they can be made to strike a target and produce x-rays for treatment (Metcalfe et al 1997).

Working principles

DC power is supplied to the modulator which includes a switch tube (a hydrogen thyraton) and a pulse forming network. These pulses are injected simultaneously into the klystron and the electron gun. The klystron is a microwave producing device. The klystron consists of an electron tube which supplies amplified microwave power to the waveguide. When an electron travelling at high velocity is incident on an electric field opposing its motion, the kinetic energy of the electron can be transferred to the electric field. This energy in the klystron is then emitted in the form of amplified microwaves in the microwave cavities. The klystron uses a resonant microwave cavity which generally has a cylindrical or rectangular cross section which is several centimetres in diameter and length. Wave resonance (which is related to the cavity length) is the condition under which these microwave cavities work. The Clinac 2100C utilises multiple cavity resonators which act as bunching and catching cavities.

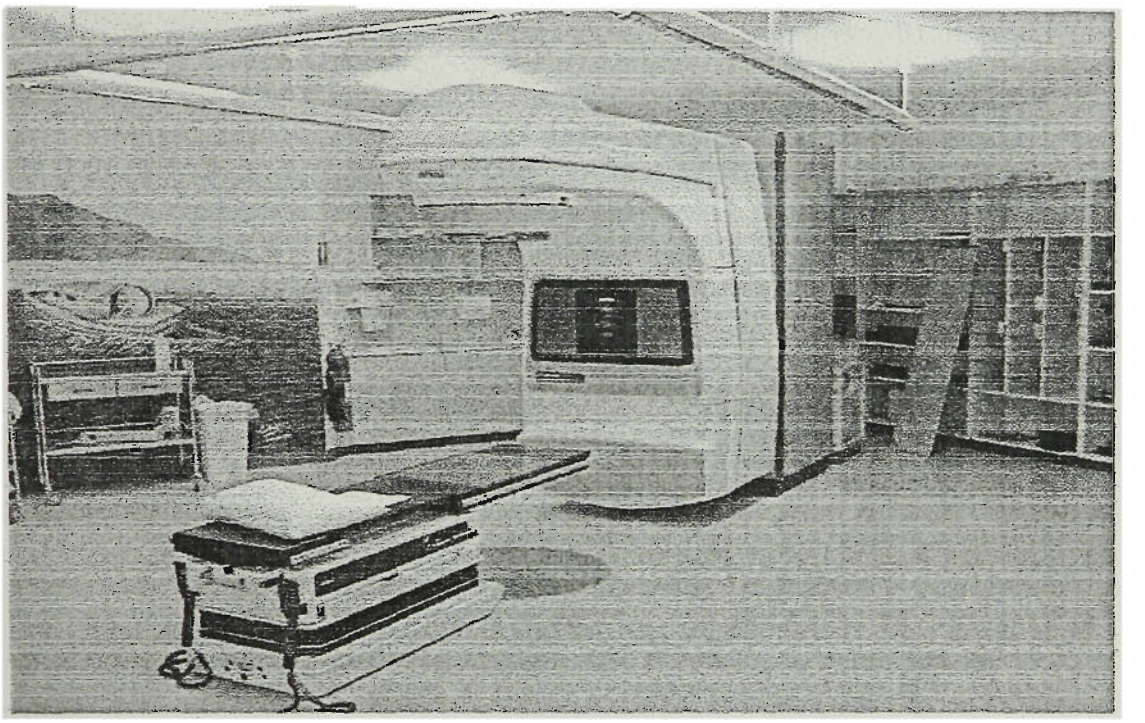

Figure 2.2 : Photograph of a Varian 2100C linear accelerator

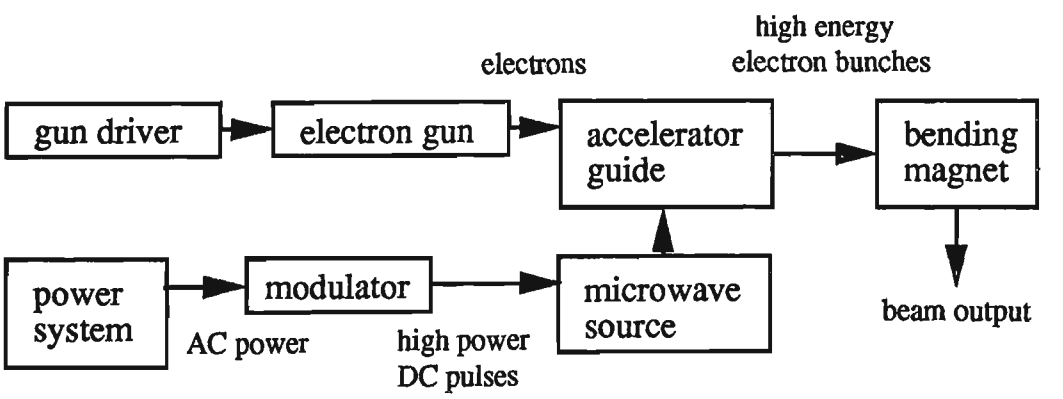

Figure 2.3 : Major components and auxiliary systems for a medical linear accelerator.

The electrons in the buncher are accelerated from the cathode and interact with an alternating electric field between the cavity walls produced by a small microwave oscillator. This interaction produces a variety of speeds to the electrons causing the electrons to bunch. This process is called velocity modulation. The catcher utilises the deceleration of the electrons to produce energy in the transfer process mentioned above to produce microwaves.

In turn the pulsed microwaves from the klystron are delivered to the accelerator tube/ wave guide along with the electrons produced by the electron gun. The accelerating device consists of a copper tube whose interior is divided by copper diaphragms (microwave cavities) of varying spacing and aperture. Copper is used as it has a high electrical conductivity at the operating frequency and this results in low power loss when the microwaves are reflected off the walls. This chamber is held close to vacuum. The electrons are initially injected into the accelerator tube from the gun with an energy of approximately 50keV and they gain energy from interaction with the electromagnetic field of the microwaves and thus are accelerated along the tube.

In the accelerator/wave guide, the microwaves produced in the klystron are used to accelerate the electrons. As the microwaves are travelling much faster than the electrons within a tube, this means the electrons aren't in 'contact' long enough with the microwaves to absorb energy. So to slow down the microwaves, cavities are used which give the microwaves a phase velocity matching the electrons, these being the copper diaphragms in the tube. The electrons are quickly accelerated up to velocities close to the speed of light as they move down the guide.

The Varian Clinac 2100C uses a standing wave accelerator system in which the microwaves are reflected along the guide thus producing standing waves within the guide. This is in contrast to travelling wave accelerators in which none of the power is reflected. A circulator, (which is a directional coupler designed to introduce resonant

frequency power) is used to feed microwave power into the guide while ensuring reflected power is diverted to a water load, thus avoiding damaging the klystron. When the cavities are moved to the side of the accelerating structure away from the electron central axis the structure can further be shortened and is then referred to as a side coupled wave guide. These are the most common devices used in medical linear accelerators because of their compactness allowing the gantry to be shortened.

The high energy electrons exit the tube via a window in the form of a pencil beam of the order of a few millimetres in diameter. This beam is then bent with the use of a beam transport system to a suitable angle. The beam transport system consists of bending magnets and focusing coils. The Varian Clinac 2100C accelerator guide is mounted horizontally (due to the length of the accelerating tube). In theory a 90° bend only is required to redirect the beam in the patients direction. But this linac uses a 270° bending magnet as it appears to provide superior steering and energy stability compared to the 90° bend. An achromatic magnet is used to bend the beam. The magnets are made with energy slits designed to remove electrons which do not fall within the chosen energy range and thus the required curvature of radius. Variations in energy of greater than 5% of the required peak energy is a typical value for removal from the beam.

Photon beams and their production

In the Bremsstrahlung process an electron loses kinetic energy and in doing so creates one or more photons (Weidner 1980). When the electrons hit a target made from high atomic number (Z) material, Bremsstrahlung photons are produced. The Varian Clinac 2100C uses a tungsten target.

The high energy electrons experience an electromagnetic force from the atoms and are thus deflected as they pass. Classical electromagnetic theory predicts that when a

charged particle is accelerated it will radiate electromagnetic energy and quantum mechanics predicts that this energy will be quantised. Thus we have an equation using energy conservation for the energy produced by the acceleration as

$$E_{K_1} - E_{K_2} = h\nu \qquad 2\text{-}2$$

where E_{K_1} is the kinetic energy of the incident electron, E_{k_2} is the kinetic energy of the electron after the interaction and $h\nu$ is the energy difference represented as a photon emitted.

Photons produced have a spectrum of energies with the largest being produced by a collision in which the electron is entirely stopped such that $E_{k_2} = 0$, therefore $E_{T_1} = h\nu_{\max}$ or the energy of incident electron (units eV) and can be written as

$$E_{K_1} = \frac{hc}{\lambda_{\min}}. \qquad 2\text{-}3$$

The average photon energy of the beam is approximately one third of the maximum energy.

Electron beams

Electrons are accelerated down the tube as described earlier in clusters with a thin pencil like shape. Instead of striking a target as with photon beams, the electrons strike an electron scattering filter which spreads out the beam into a near uniform electron fluence across the treatment field. This scattering foil is usually made from thin lead foil so that the majority of electrons are scattered. A small amount of bremsstrahlung (usually less than 5%) is produced by electron interactions with collimators and other material in the beam path.

The accelerators treatment head consists of various devices to guide, steer or shape the electron/photon beam. These being the target, scattering foil, flattening filter, ion chamber, fixed and moveable collimators made of tungsten as shown in figure 1.2.

2.3 Ionisation chambers

Bragg-Gray cavity theory

Bragg-Gray cavity theory can be used to determine the dose in a medium directly from ion chamber measurements. According to Bragg-Gray theory (Khan 1983), the ionization produced in a gas filled cavity in a medium is related to the energy absorbed in the surrounding medium. When the cavity is infinitesimally small, the Bragg-Gray relationship is satisfied, such that

$$D_{med} = J_g \frac{\omega}{e} \left(\frac{S}{\rho} \right)_{gas}^{med} \qquad 2\text{-}4$$

where D_{med} is the absorbed dose in the medium, J_g is the ionisation charge per unit mass within the cavity, $\left(\frac{S}{\rho}\right)_{gas}^{med}$ is the weighted mean ratio of the mass stopping power of the medium to that of the gas for electrons crossing the cavity, $\frac{\omega}{e}$ is the average energy absorbed per unit charge of ionization produced.

Electrons passing through a medium interact through Coulomb interactions with the atoms of that medium. Processes such as elastic and inelastic collisions with nuclei and electrons take place. In those processes, kinetic energy is converted into other forms of energy such as production of photons, atomic excitation of the medium and redistribution of energy among the emerging particles (elastic collisions). In a medium such as water and tissue (low atomic number), electrons predominantly lose energy from ionisation events with atomic electrons. Thus as the beam of electrons passes through the medium, the energy is continually decreased until the point where electrons reach thermal energies and are then captured by the atom.

The stopping power is defined as the energy loss of a charged particle per unit length of a medium in which it is travelling. To determine the stopping power ratio's, it is first necessary to determine a weighted mean of the stopping power ratios for the electron spectrum set in motion by the x-ray spectrum incident on the material.

Spencer and Attix (Spencer et al 1955) formulated a stopping power ratio to approximate an air filled cavity in a water medium given by

$$\frac{L}{\rho} = \frac{\int_{\Delta}^{E} \phi(E) \frac{L}{\rho}(E) dE}{\int_{\Delta}^{E} \phi(E) dE} \qquad 2\text{-}5$$

where $\phi(E)$ is the distribution of electron fluence in energy, $\frac{L}{\rho}$ is the restricted mass collision stopping power and Δ is the cut-off energy.

The cut off energy is introduced to account for the secondary electron energy transfer. Below Δ it is assumed that the energy transfer is dissipated at a site near the site of release. Thus the integration is performed to obtain the energy deposited in the cavity by the primary electrons (those generated by initial x-rays). This gives us the Spencer-Attix formulation of the Bragg-Gray cavity theory as

$$D_{med} = J_g \frac{\omega}{e} \left(\frac{L}{\rho} \right)_{gas}^{med} \qquad 2\text{-}6$$

$\left(\frac{L}{\rho}\right)_{gas}^{med}$ is the average restricted mass collisional stopping power ratio (between the medium in question and the gas of the chamber) of the electron spectrum set in motion in the material by the incident photon spectrum.

Determination of J_g

If the volume of the chamber or mass of air in the chamber/cavity is known accurately then J_g can be determined. However if it is difficult to determine the volume to the desired accuracy, you can determine J_g with the use of a calibration beam such as Cobalt-60 gamma rays.

If the gas is air and the chamber is made from material, m, then the dose D_m to the centre of a homogeneous mass of the same material, m, can be calculated by the Spencer-Attix formulation as

$$D_m = MN_c\left(\frac{\omega}{e}\right)\left(\frac{\mu_{en}}{\rho}\right)_{air}^{m} A_m \qquad 2\text{-}7$$

where M is the charge measured in coulombs, N_C is usually measured using a Cobalt-60 beam as a calibration factor. $\frac{\omega}{e}$ for air =33.85J/C (0.873 rad/R), $\left(\frac{\mu_{en}}{\rho}\right)_{air}^{m}$ is the ratio of weighted mean mass energy absorption coefficient of material m, to that of air. A_m is a displacement factor and is the ratio of photon energy fluence at the centre of the mass to that of air at the same point (AAPM 1983, IAEA 1987).

Also from Spencer-Attix we get

$$D_m = J_{air}\left(\frac{\omega}{e}\right)\left(\frac{L}{\rho}\right)_{air}^{m} A_2 \qquad 2\text{-}8$$

where A_2 is a ratio factor in the electron fluence for the chamber being filled with material m to that of air.

Thus comparing these two quantities gives

$$J_{air} = MN_c \frac{A_m}{A_2} \left(\frac{\mu_{en}}{\rho} \right)_{air}^{m} \left(\frac{L}{\rho} \right)_{m}^{air} \quad . \qquad 2\text{-}9$$

This can be expanded to introduce a more realistic situation where the walls of the chamber are material w and the buildup cap material c. Letting α equal the fraction of cavity ionisation from wall generated electrons and $(1-\alpha)$ be that from the buildup cap then

$$J_{air} = MN_c \frac{A_m}{A_2} \left(\left(\frac{\mu_{en}}{\rho} \right)_{air}^{w} \left(\frac{L}{\rho} \right)_{w}^{air} \alpha + (1-\alpha) \left(\frac{\mu_{en}}{\rho} \right)_{air}^{c} \left(\frac{L}{\rho} \right)_{c}^{air} \right) \qquad 2\text{-}10$$

which can be written as

$$J_{air} = MN_c A_c A_\alpha \qquad 2\text{-}11$$

where $A_c = A_m/A_2$ and A_α is the bracketed quantity in equation 2.10. Thus we have all the components necessary to determine the dose received by the chamber by finding the charge collected.

Markus parallel plate chamber

One key feature of the Markus chamber is that its small diameter enables measurement of small field sizes. The Markus electron chamber is shown in figure 2.4. The Markus chamber is water proof, so that it can be used in solid and liquid water phantoms.

The active volume of the Markus type 329 chamber is $0.055cm^3$. It consists of a cylindrical body made from perspex in which the cylindrical measuring volume (diameter 6mm, height 2mm) is embedded flush to the surface. The chamber window consists of a polyethylene disc covered with a graphite layer with weight of 2.3

mg/cm^2. The collector is made from perspex with a graphite layer and has an effective diameter of 5.4mm. This enables small radiation field sizes to be measured. Both window and collector have fixed position. The collector is surrounded by a guard ring which is grounded. The chamber is an open air filled chamber which means almost instantaneous equilibrium with barometric pressure and temperature occurs.

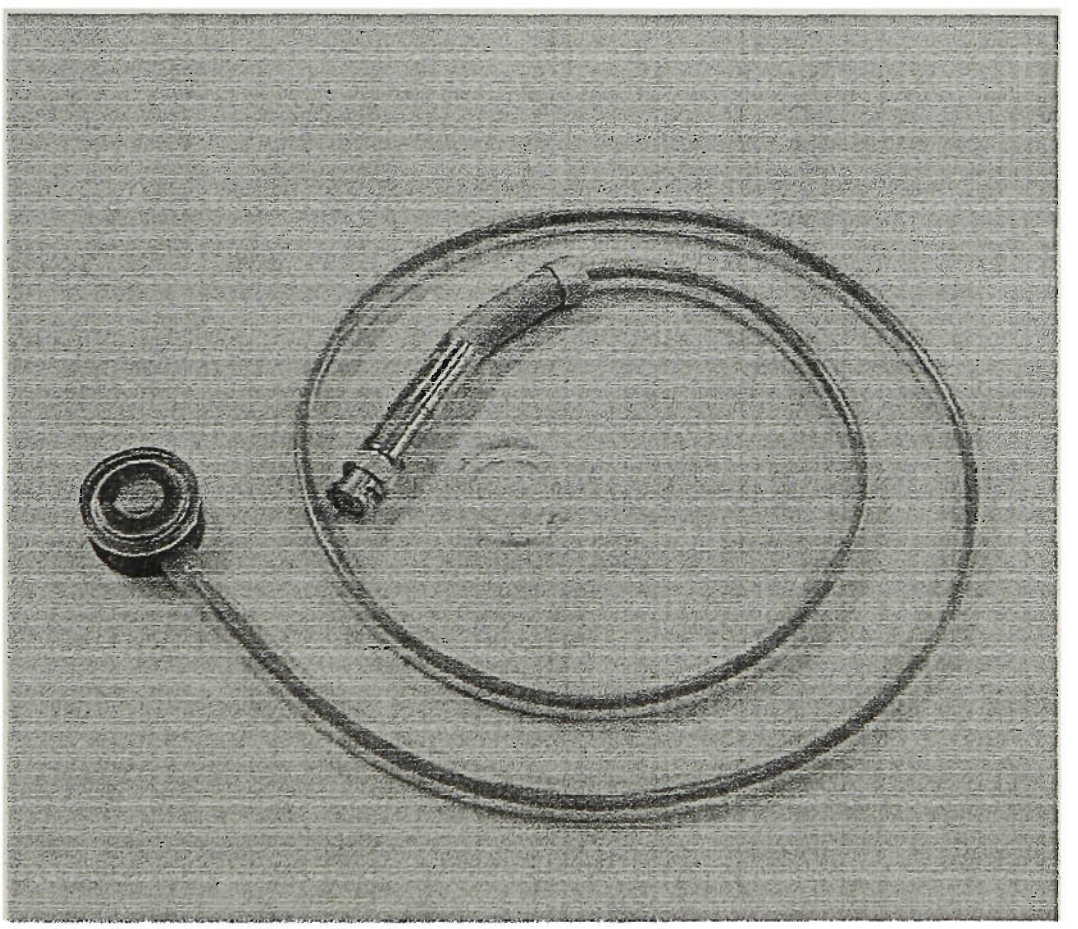

Figure 2.4 : Picture of the Markus parallel plate ionisation chamber.

Rawlinson corrections

The Markus chamber and other fixed plate separation ionisation chambers generally over respond in the build up region and other regions of electron disequilibrium due to the contribution to chamber signal from electrons produced in the side walls.

A paper by Rawlinson (1992) discusses how these effects can be corrected by chamber design. The design features of an ion chamber to minimise the level of side wall scatter are listed below .

i) the diameter of the wall (made from unit density material) needs to be at least 25 times the electrode separation of the chamber. This stipulation can be relaxed if the walls are angled or made from low density material (Rawlinson 1992)

ii) a flange upstream of the walls should be avoided unless its diameter is greater than the wall diameter

iii) the ion chamber should include a guard ring. The guard ring helps produce a homogeneous electric field across the collector and collects side scatter electrons but no current is added to the signal

iv) a thin collector electrode plate (to minimise the polarity effect) , a thin entrance window and it should be made from tissue equivalent material

If these parameters can't be optimised then there will be either an over response or under response of the specific chamber. The Markus chamber has been tested and found to produce an over response. This over response is dependent on depth in material.

Velkley et al (1975) formulated an empirical correction to the over response of the Markus chamber in which electrode separation was considered as the major chamber geometrical factor influencing the correction. However the proximity of the side walls was not taken into account and this caused incorrect results under certain conditions. That is when side wall electrons significantly add to charge collected.

Gerbi et al (1990) extended the formulation to account for the distance between the edge of the collector and side wall but did not take into account the size of the collector electrode and again under certain chamber geometry's this can be inaccurate.

Rawlinson extended the Velkley formula further to account for the collector and guard electrode size and side wall height and angle so that the Markus results can be corrected once the beam energy, depth in the material of measurement and geometry of the chamber is known.

The equation is

$$P(d,E) = P'(d,E,G) - \zeta(d,E,G) \qquad 2\text{-}12$$

where E is the beam energy, d is the depth in the phantom and G is the geometry

Here P and P' are the true and measured percentage depth doses and ζ is the correction factor.

ζ is depth (d) dependent and is given by the formula

$$\zeta(d) = \zeta(0)e^{-\alpha d/d_{max}} \qquad 2\text{-}13$$

where α=4.0±0.8 and d_{max} is taken as 15mm and 30mm for 6MV and 18MV beams respectively. $\zeta(0)$ is given as

$$\zeta(0,E,G) = c(E)\left(\frac{s}{w}\right)\rho^{0.8} \qquad 2\text{-}14$$

where c(E) = 27% for 6MV and c(E) = 15% for 18MV photon beams, s is the electrode separation, w is the wall diameter, ρ is the density of the chamber walls.

Table 2.1 : The data required to calculate P(d, E) for the Markus chamber.

	parameter	data
wall	material	polymethylmethacrylate (PMMA)
	density (ρ)	1.17 g/cm^3
	diameter (w)	5.7mm
	angle	0
collector	material	graphited PMMA
	diameter	5.4mm
	electrode separation (s)	2.0mm
window	material	graphited polyethylene
	thickness	2.7mg/cm^2

Figure 2.5 shows the overresponse calculated for the Markus chamber at various depths for 6MV and 18MV. The calculation is for a 10cm x 10cm but it is expected that field size changes will not significantly effect the magnitude of electron scatter off the chamber side walls so these results are also used to correct for all other field sizes.

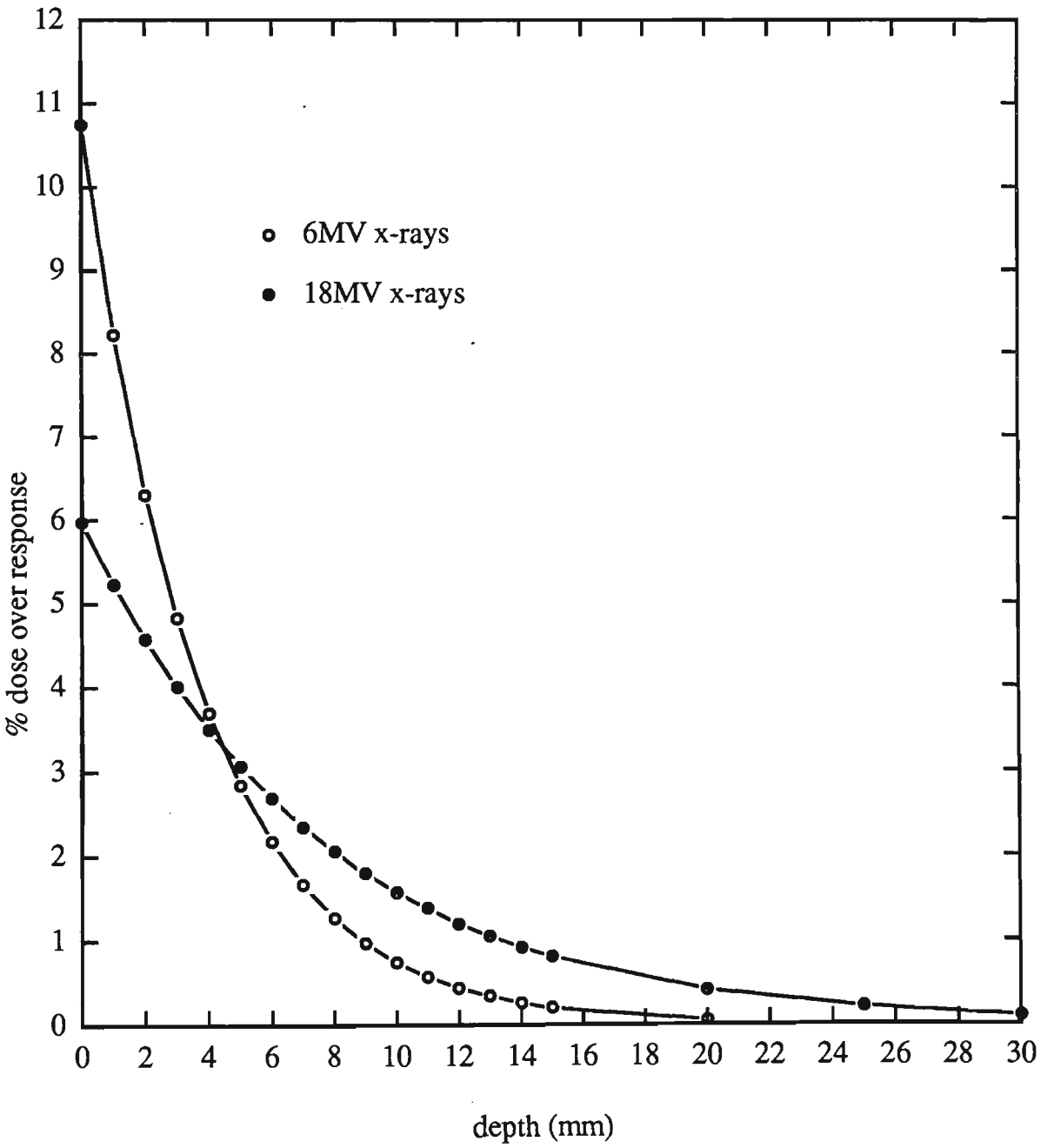

Figure 2.5 : Overestimation of dose in the build up region for the Markus chamber calculated using the Rawlinson correction method.

Attix parallel plate chamber

One key feature of the Attix chamber is that side wall correction is so small that it can be neglected. The Attix model 449 chamber is a plane parallel ionisation chamber with dimensions 6.0cm diameter and 1.4cm height, as shown in figure 2.6. The body is made from RMI solid water, model 457 and nylon screws. The chamber window consists of a 0.025mm thick, 4.8mg/cm^2 Kapton conductive film. The conducting surfaces are minimal thickness colloidal graphite. The air gap is 1mm giving an ion-collecting volume of approximately 0.127cm^3 which is vented to atmospheric temperature and pressure.

The guard ring diameter is 4.0cm and the collecting electrode is 1.27cm diameter. This gives a wide clearance across the guard and reduces the over response due to in scatter to less than 1% if Rawlinson's scatter correction calculation previously mentioned is applied. The Attix chamber with it's wide guard ring is the most ideal design commercially available for near surface doses as over response correction is not usually necessary. The wide diameter does however mean small fields have to be measured by other detectors.

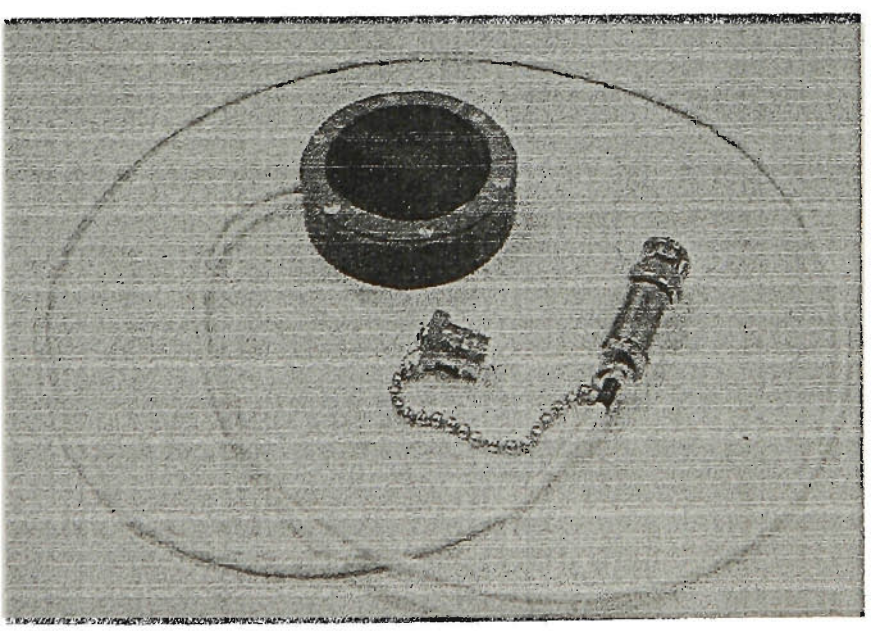

Figure 2.6 : Picture of the Attix parallel plate ionisation chamber.

2.4 Thermoluminescent dosimeters (TLD's)

Thermoluminescent dosimeters (TLD's) of different thickness can be used as extrapolation devices to estimate dose at different skin depths. They can also be placed on patients as in-vivo dosimeters.

Thermoluminescence is the emission of light by the application of heat. Some crystalline materials (when irradiated) store some energy in the crystal lattice. This energy is emitted in the visible light region when heated and is proportional to the level of radiation damage previously inflicted on them. Thus the light emitted from a crystal can be used to determine the radiation dose absorbed by it. This phenomenon is employed in TLD's. Lithium Fluoride doped with titanium and magnesium (LiF:Ti:Mg) is the predominant material used for TLD's in this thesis. With an effective atomic number of Z_{eff}=8.31, the energy response is closer to tissue than many other phosphors, (eg. $CaSO_4$ has a Z=14). The mass density is however rather high (ρ =2.65) when compared to most tissues.

Imperfections in the crystal lattice (which arise from the doping of various materials) provide energy traps for electrons in excited states within the material. The TLD is irradiated, providing energy to raise the electrons from the valance band to the conductor band or into higher excited states. Some of these electrons remain trapped while the others re-radiate the energy and go back to the ground state.

Upon heating the TLD at a constant rate we receive an output of light as a function of time. This is called a glow curve. An example of a glow curve is shown in figure 2.7. Different peaks relate to different trapped energy levels. Thus the area under the curve represents the measured radiation dose absorbed by it. Because the TLD's retain a small residual TL after annealing, a small background light level may need to be subtracted. Each TLD has its own sensitivity thus each chip must be individually

calibrated. With the TLD system used, the accuracy for each measurement is ± 5% (± 2SD based on the four chips used in each measurement; reproducibility is 3%) of the reading above 0.1Gy.

Extrapolation TLD's consist of three TLD's, front surface dimensions of 3.15mm x 3.15mm and of nominal thickness' , 0.14mm, 0.39mm and 0.89mm as shown by figure 2.8. They are Lithium Fluoride (LiF) crystals doped with Magnesium and Titanium from Harshaw Chemicals. The 0.14mm thick TLD's were Li^6 enriched chips (700 model) which increases their response to neutrons but does not effect their response under x-ray radiation. The 0.39mm and 0.89mm chips were made from the Li^7 isotope (600 model). The TLD's were read in a manual Victoreen model 2800M TLD reader in a two step read out cycle (pre heat anneal temp of 160°C for 10 seconds and read out temperature of 300°C for 10 seconds) after a 10 minute 100°C pre read anneal in a dedicated annealing oven. Extrapolation TLD's were used to verify surface dose results in phantom and in-vivo experiments.

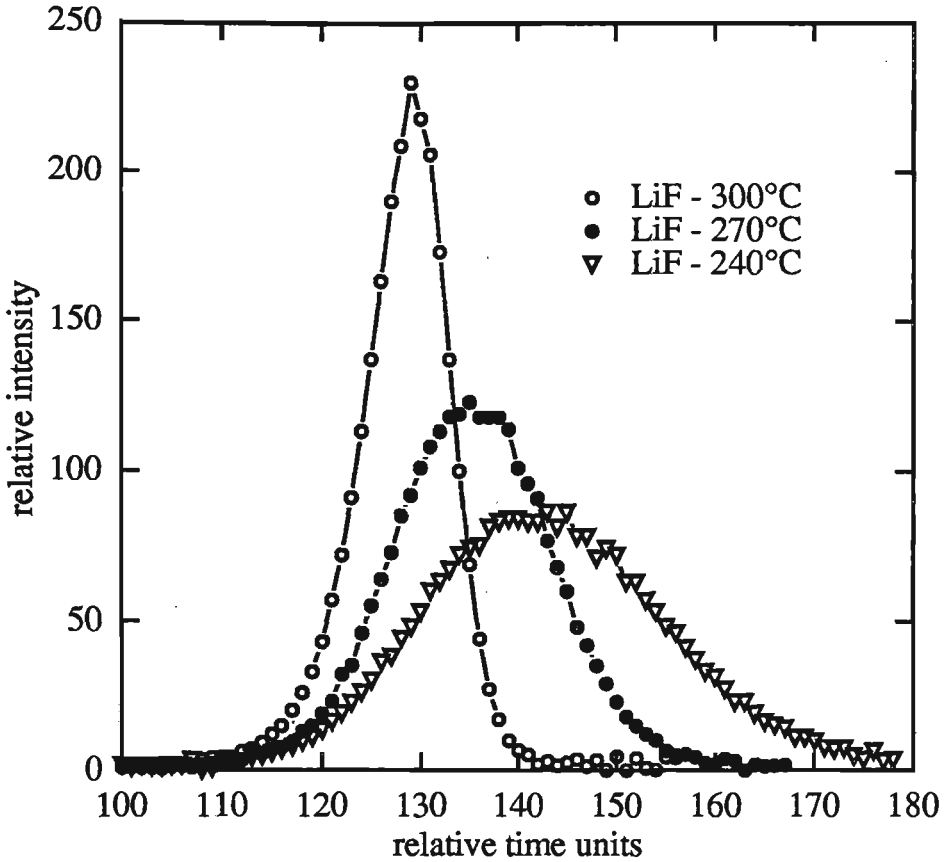

Figure 2.7 : Glow curves produced by LiF TLD's at different heating temperatures. A broadening of the glow curve is produced at lower heating temperatures.

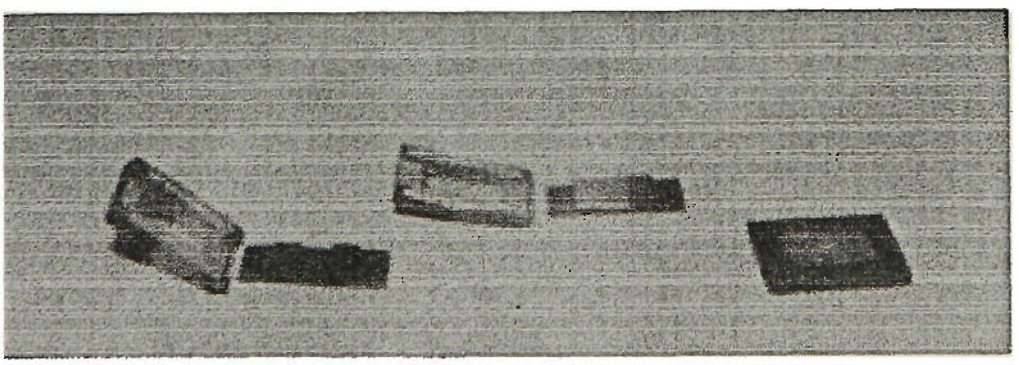

Figure 2.8 : Picture of the extrapolation TLD's and solid water holders.

2.5 Film dosimetry

Radiographic film

A radiographic 'emulsion' consists of a suspended silver halide (normally bromide) crystal layer in gelatine which is highly energy dependent to dose. Crystal size can vary but a relative measure of their size is about 0.01mm diameter. The size and degree of distribution of these grains is carefully controlled during the manufacture process. This produces the degree of contrast and sensitivity of the film. An x-ray film has a layer construction that is built up on a transparent central support of cellulose acetate. The film wrap can also lead to unwanted build up if skin dose measurements are to be attempted.

Radiographic emulsions can be classified into groups according to their sensitivity. Ordinary untreated photographic film emulsion is predominantly sensitive to ultra violet and blue light and only has a small response to longer wavelengths. Sensitizers can be added to the emulsion to increase the films wavelength range. X-ray emulsions normally consist of a double-coated emulsion of increased thickness and a very high silver bromide content.

The use of radiographic film for dosimetry in photon and electron beams is dependent on many factors including exposure techniques, processing, scanning and its high energy dependence as shown in figure 2.9 (Muench et al 1991). Silver in the film emulsion has an atomic number of 47 and a K absorption edge at 25.5keV (Johns and Cunningham 1983). Radiation is absorbed through the photoelectric process at lower energies.

Absorbed surface dose includes varying components of different energy photons as well as a wide energy spectrum of electron contamination. Radiographic film in surface and build up dose measurement is limited to 'qualitative work, however, a few direct measurements are included in results for direct comparisons. Its advantages include high spatial resolution, ease of set up and exposure, complete information from single exposure and the ability to take cumulative measurements from multiple field exposures.

The optical density (OD) of a film measures the degree of blackening and is defined as the log of the quotient of initial intensity (I_0) and transmitted intensity (I_t).

$$OD = \log I_0 / I_t \qquad 2\text{-}15$$

The measured optical density is a combination of the net optical density produced by the exposure and the fog optical density which is the films natural background. For maximum accuracy, films from the same batch should be used for calibration and experiments, and should be exposed and developed at the same time. They should be developed in a carefully controlled automatic processor to minimise the errors due to changes in processing environment conditions (Suchowerska et al 1997).

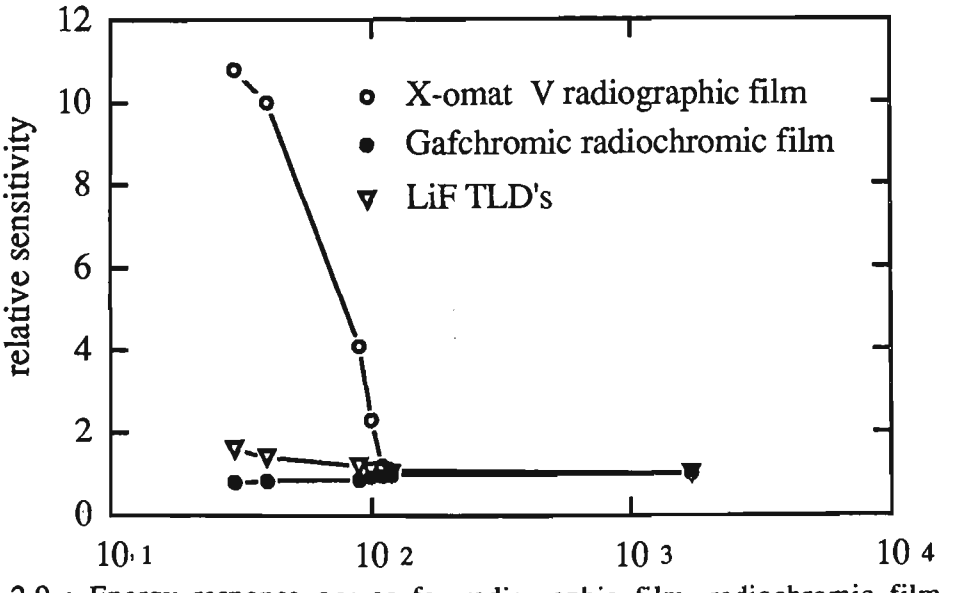

Figure 2.9 : Energy response curves for radiographic film, radiochromic film and LiF TLD's. Radiographic film has an extreme over response at low energies.

Radiochromic film

Radiochromic film has the potential for use as an in-vivo dosimeter to analyse off axis skin dose profiles. It is able to produce quantitative dose measurements over a large area. Radiochromic film works on the principle that ionising radiation activates a chemical reaction of colourless leuco dyes. The specific name of the film used as a radiation dosimeter here is Gafchromic film+. This consists of a thin film of hexa-hydroxyethyl pararosaniline leucocyanide dye coated onto a non-reactive base. The reaction process produces a blue coloured dye whose optical density is proportional to absorbed dose. Gafchromic film irradiated to various doses is shown in figure 2.10a on a white paper background to highlight the colour change associated with absorbed dose. Gafchromic film was manufactured in two forms, a single layer media which could be used for surface dose measurements and a double layer media in which two active layers are sandwiched between two plastic coatings and held together by a layer of glue. The active film layer in each is approximately 7μm thick (McLaughlin 1993) and the base is 100μm thick for the single layer media and is given the name MD-55-1. The double layer film is approximately 250μm thick which can be considered as two single layer devices stuck together by about 40um of glue. This film is given the name MD-55-2. A schematic of each film construction is shown in figure 2.10b. Gafchromic film exhibits the following general properties.

Dosimeter response

Gafchromic film is slightly ultraviolet (UV.) sensitive and thus for optimum results the film should be placed in a dark storage container between irradiation's. However the film will only degrade when exposed for long time periods in environmental UV. This occurs after a few hours of direct sunlight unlike radiographic film whose response is instantaneous.

+ ISP technologies, Nuclear Associates California, USA.

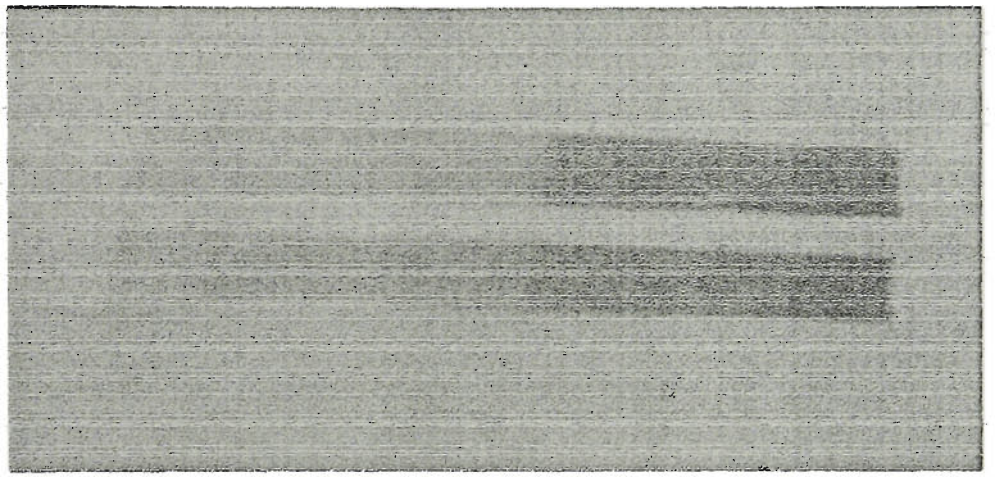

Figure 2.10a : Picture of Gafchromic film. The film does not require processing and turns blue immediately on irradiation.

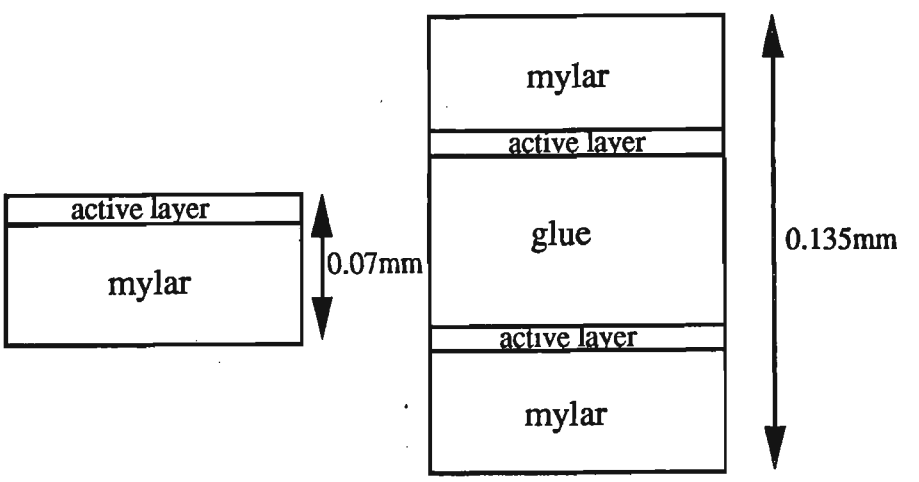

Figure 2.10b : Cross section schematic of MD-55-1 and MD-55-2 Gafchromic film.

Gafchromic film is relatively energy independent in its sensitivity response. Figure 2.9 shows a comparison of Gafchromic film to X-omat V radiographic film and LiF TLD's. A slight under response to lower energy is seen when normalised to 1 at 1710 keV. As monoenergetic beams are only attainable on synchrotrons, all measurements were taken on an orthovoltage and megavoltage x-ray machines. The energy quoted is the mean of the spectra, (eg. 1710keV refers to a 4MV peak).

The absorbency spectra for Gafchromic film is shown in figure 2.11. This was measured using a GE spectrometer scanning from 200nm to 900nm. The increase in absorbency (A) at 3 wavelengths are shown in figure 2.12. All are relatively linear in absorbency up to 30Gy.

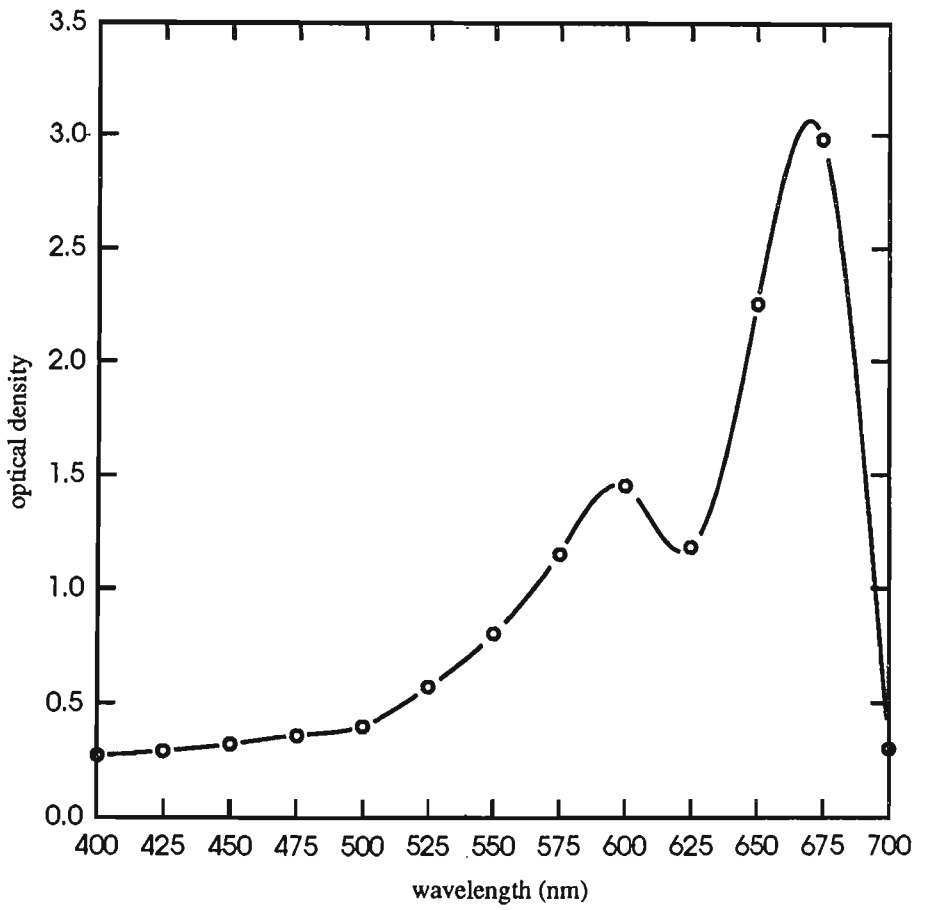

Figure 2.11 : Absorbency spectra for Gafchromic MD-55-1 film. Two main absorption peaks are found in the red region.

Post irradiation coloration

Figure 2.13 shows the post irradiation colouring of the film up to 10 days at constant temperature and humidity. A relatively large increase in coloration (at 600 nm which is consistent at all wavelengths) is seen over the first day but the film becomes relatively stable following this period. Thus for improved accuracy, the Gafchromic film should be read after a period of at least 1 day.

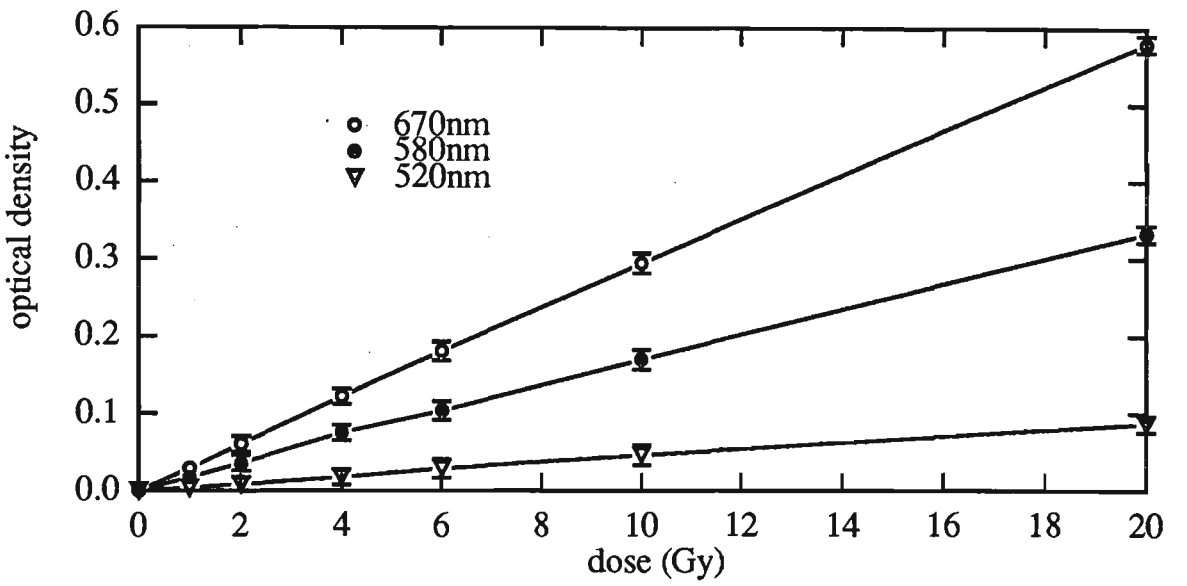

Figure 2.12 : Optical density/absorbed dose relationship for MD-55-1 gafchromic film at various wavelengths.

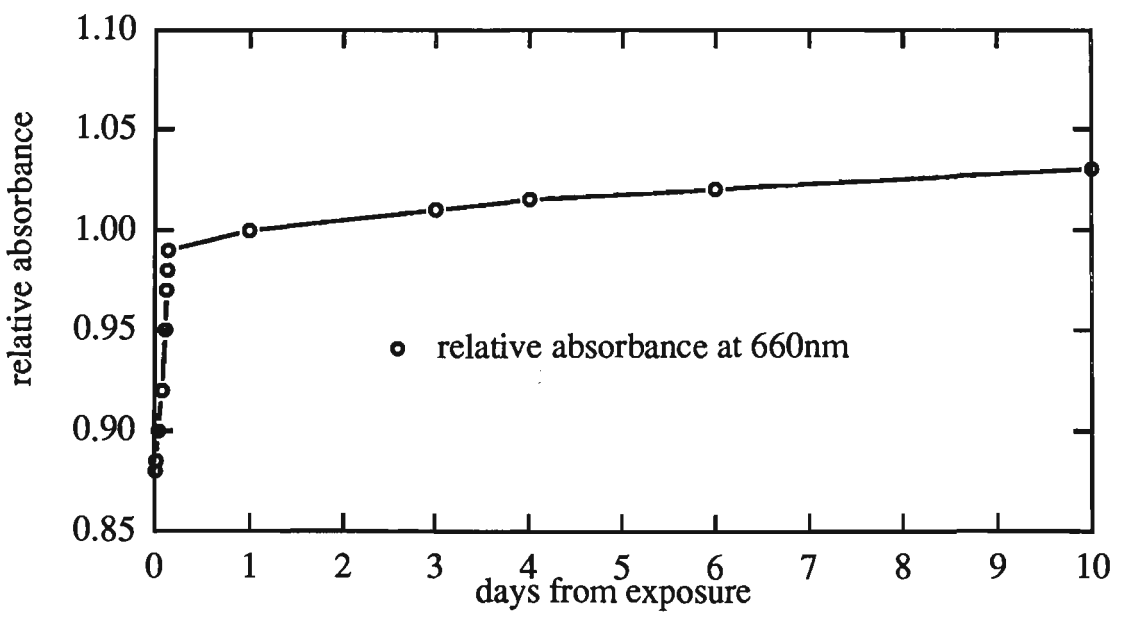

Figure 2.13 : Post irradiation coloration of MD-55-1 gafchromic film which shows a significant increase in coloration for a period of 5-6 hours after irradiation.

Experimental methods and readout system

i) Broad band frame grab

Gafchromic dosimetry media type MD-55-1 was used with the broad band frame grab system. The films were read after a two day delay from irradiation to reduce errors involved with post irradiation coloration (McLaughlin 1991). A set of calibration films covering experimental doses were produced with every set of measurements for comparison. Light transmittance was measured using a CCD camera. A broad band red light source with a 610-700nm band pass filter was used for illumination of the films. This was chosen due to the absorption spectra of the Gafchromic film. Results were analysed with a hardware/software package called JAVA[+]. The broad band frame grab equipment is shown in figure 2.14.

JAVA is an image analysis system generally used for astronomical image analysis purposes. It consists of a video digitising board and software for analysis. The system is calibrated using optical densities measured from an optical step wedge. Results can be analysed with a multitude of functions including pixel comparisons, along lines, in specific areas or over the whole film. Background subtraction is performed manually by using the transmittance value through our control film as our initial intensity I_0.

The spatial resolution of the system varied depending on the lens used on the CCD camera. For these experiments the resolution was set to approximately 20 lines per mm. Measurements in a darkened room or with fluorescent room lights on showed no perceptible difference.

The films were exposed perpendicular to the beam central axis at the entrance interface and at D_{max} for each beam.

[+] Jandel Scientific

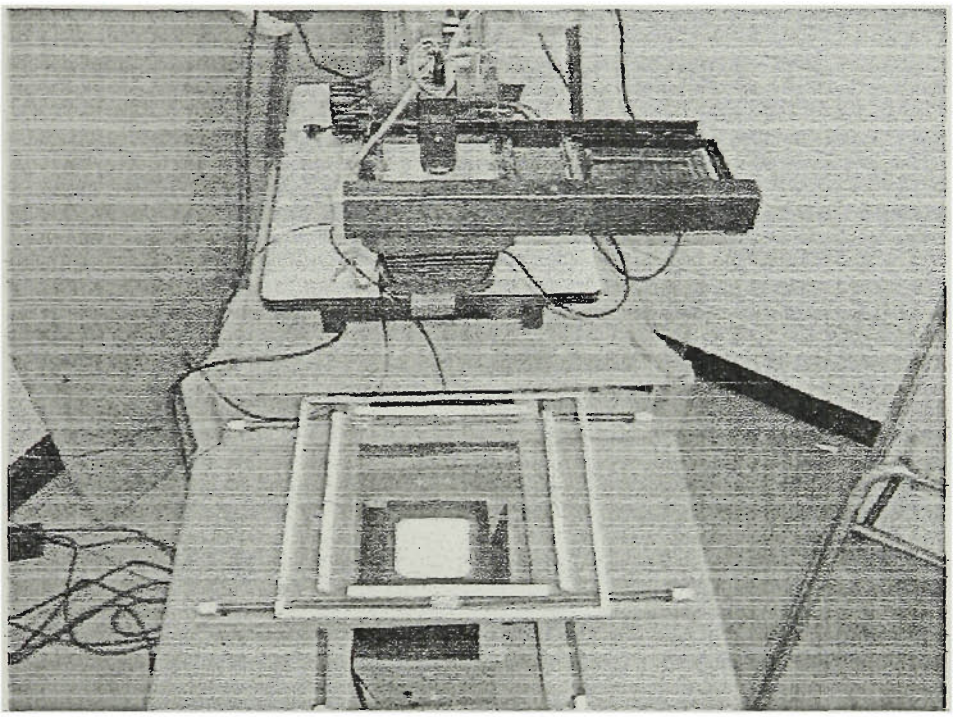

Figure 2.14 : Picture of the JAVA system.

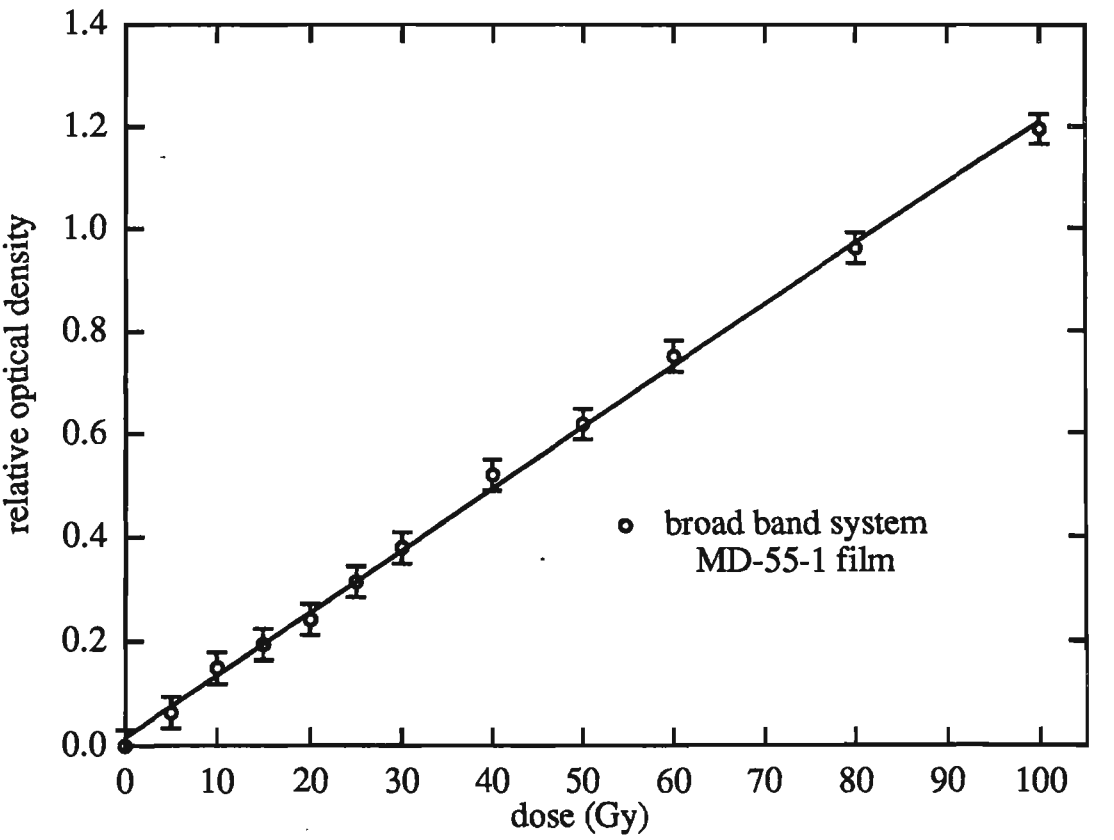

Figure 2.15 : Calibration curve for MD-55-1, Gafchromic film using the JAVA system. A relatively linear optical density to dose relationship is found.

The Gafchromic's sensitive layer is approximately 7μm thick. The depth of D_{max}, was obtained with an Attix chamber and varies slightly with field size. Measurements performed include central axis percentage surface dose plus profiles at the surface.

Figure 2.15 shows the broad band frame grab relative density units versus absorbed dose for the MD-55-1 Gafchromic film. The film was calibrated with 6MV x-rays at 100cm SSD and 10cm x 10cm field size. A relatively linear response was found using this system. The percentage error in measurements is shown on the graph as one standard deviation for 10 films. Films were irradiated to standard doses at D_{max} in a solid water stack phantom perpendicular to the beam direction.

ii) Narrow band LED scanning system

A narrow band high spatial resolution gafchromic film scanner was produced by the conversion of an infrared densitometer to also produce and detect in the red region. The infrared densitometer which we used was produced by Scanditronix and controlled by radiation field analyser (RFA300) software. This infrared densitometer consists of an attachable arm, which is placed together with a glass sheet over the Scanditronix RFA300 water dosimetry phantom. The infrared source is located below the glass sheet and is focused through a lens onto a detector positioned on the underside of the arm assembly. The film is placed on a glass sheet covering the water tank and scanning can be performed in the x-y plane with a resolution of ±0.1mm. The system was modified to introduce a red GaAlAs, 3000 mcd ultra bright LED in a clear plastic housing into the existing infrared source housing. The LED used has a maximum forward current rating of 50mA, and a forward voltage of 2.5V. The peak wavelength is 660nm according to manufacturers specifications. The red LED was mounted inside the scanning densitometers arm next to the infrared source and directed towards the lens focusing system. A switch and appropriate current limiting devices were installed to allow the selection of either infrared or red mode readout. The red LED was not

attached to a heat sink due to space restrictions and thus a warm up period of approximately 30 minutes is required to alleviate errors involved with dark current readings.

Figure 2.16 shows the scanner film relative density units versus absorbed dose for the Gafchromic MD-55-2 film. The film was calibrated with 6MV x-rays at 100cm SSD and 10cm x 10cm field size. The film was placed perpendicular to the beam axis during irradiation. A second order polynomial is fitted to the scanner density readout for a series of exposed calibration doses. This polynomial is then used for the determination of Gafchromic absorbed dose in subsequent experiments using the densities measured with the scanner. The shape of the non-linear response is assumed to be predominantly due to the conversion hardware/software already built in to the Scanditronix infrared system. The unit is calibrated to be linear with the infrared source and a radiographic AgBr film. This device was used to analyse films placed around curved patient surfaces for surface/skin dose analysis. THe differences seen with the two calibration curves are due to the bandwidths of the readout devices.

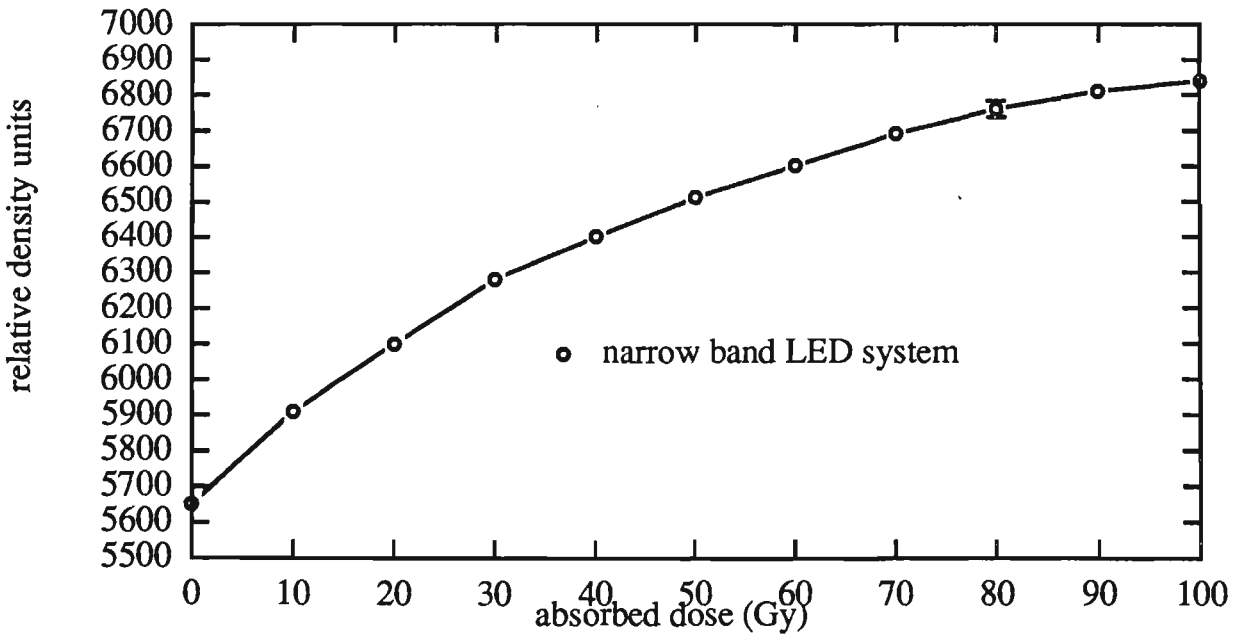

Figure 2.16 Calibration curve for MD-55-2, gafchromic film using the narrow band RFA-300 system. The calibration curve could be matched with a 2nd order polynomial function.

Impact of ambient and readout light sources on Gafchromic film

Due to the low radiation sensitivity of Gafchromic film, the effects of ambient light and source readout light on Gafchromic MD-55-2 film may influence the final measured results if the appropriate level of care and handling is not performed. Common light sources used to measure Gafchromic films optical density include, helium neon lasers, ultra bright diodes, incandescent and fluorescent white light sources. The effects of these light sources as well as ambient light sources are studied.

Readout light sources

Measurements were performed under four possible Gafchromic dosimetry light sources. These being i) helium neon laser ii) ultra bright LED iii) incandescent light iv) fluorescent light. Details of each source are given as follows :

i) A 1mW helium neon laser with wavelength of 632.8nm was used. The film was placed 3mm from the beams aperture for experiments. The diameter of the laser beam was approximately 1mm. Measurement of luminance was unable to be performed due to the band pass wavelength restriction (400nm -520nm) on the minolta/ air shields fluoro-lite meter 451 used.

ii) A red GaAlAs 3000mcd ultra bright LED in a clear plastic housing (peak wavelength 660nm according to manufacturers specifications) was used. The film was placed 3mm from the LED surface for experiments. As with helium neon laser, luminance was unable to be measured.

iii) A 60W incandescent light source with a plastic diffuser (0.3mm thickness) was used. The film was placed approximately 15cm from the light source on a clear glass sheet, thickness 5mm. Luminance from 400nm-520nm at this position was measured as 6.4 ± 1.0 mwcm^{-2}nm^{-1}.

iv) A 40W fluorescent light source was used, with and without a 3mm plastic diffuser. The film was placed approximately 15cm from the light source. Luminance from 400nm-520nm at this position was measured as 16.3 ± 1.7 mwcm^{-2}nm^{-1}.

In all instances, measurements were performed using two 1cm x 1cm square pieces of MD-55-2 Gafchromic film of batch number 941206. A control film of the same dimensions from the same piece of film was placed in a light tight envelope and used in all experiments as a standard for background readings. Colouration of the films was recorded periodically over a 175 hour period with a RFA300 densitometer converted to read Gafchromic film with a type ii) ultra bright red LED.

Gafchromic film should be handled either using soft gloves or tweezers to avoid finger prints and other contaminants which effect readout. By attaching a paper or plastic tab on the side of the film with sticky tape, it can be easily handled without touching the film. Gafchromic film is prone to scratching which can also effect the optical density readout. Care should be taken not to slide the film on surfaces with any force.

Ambient light sources

Experiments were performed under different ambient light sources and exposures. Sunlight, fluorescent light and incandescent light were tested for coloration effects on Gafchromic film.

i) Gafchromic film was placed in full and filtered sunlight during spring time (October) in Australia. Both full and filtered conditions were through a 0.5cm thick glass window with the filtered sunlight projected through 50% black plastic shade cloth. Luminance in the 400nm - 520nm waveband varied considerably due to climatic conditions and time during the day. For full sun conditions, luminance varied from 25 mwcm^{-2}nm^{-1} up

to 85 mwcm^{-2}nm^{-1} between the hours of 7:00am and 6:00pm. For filtered light conditions, the luminance varies between 5mwcm^{-2}nm^{-1} and 20mwcm^{-2}nm^{-1}.

ii) The film was exposed by two 40W fluorescent tubes at a distance of 1.5m. They were placed on top of a book shelf directly under the light source. Measurements were performed with the fluorescent lights uncovered and with a 3mm plastic diffuser over them. Luminance from 400nm-520nm at this position was measured as 0.64 ± 0.1 mw-cm-2-nm-1 for uncovered fluorescent lights and 0.59 ± 0.1 mwcm^{-2}nm^{-1} for covered lights.

iii) The film was exposed to a 60W incandescent light at a distance of 1.8m. The film was placed on top of a table directly under the light source. Measurements were performed with the incandescent lights uncovered and with a 3mm plastic diffuser over them. Luminance from 400nm-520nm at this position was measured as 0.085 ± 0.02 mwcm^{-2}nm^{-1}.

Results

Figure 2.17 shows the equivalent dose coloration of Gafchromic MD-55-2 film exposed to various types of light sources at close range as would be expected in typical densitometry systems. The equivalent dose was calculated by comparing the coloration of experimental films to a set of standard doses given by a 6MV x-ray beam produced by a medical linear accelerator. Results show a dramatic effect in coloration for fluorescent lights. Increases in coloration were also seen for helium neon lasers (approximately 7.5Gy equivalent dose for 175 hours of exposure), incandescent lights (approximately 5Gy equivalent dose for 175 hours) and ultra bright LED's (approximately 3Gy equivalent dose for 175 hours).

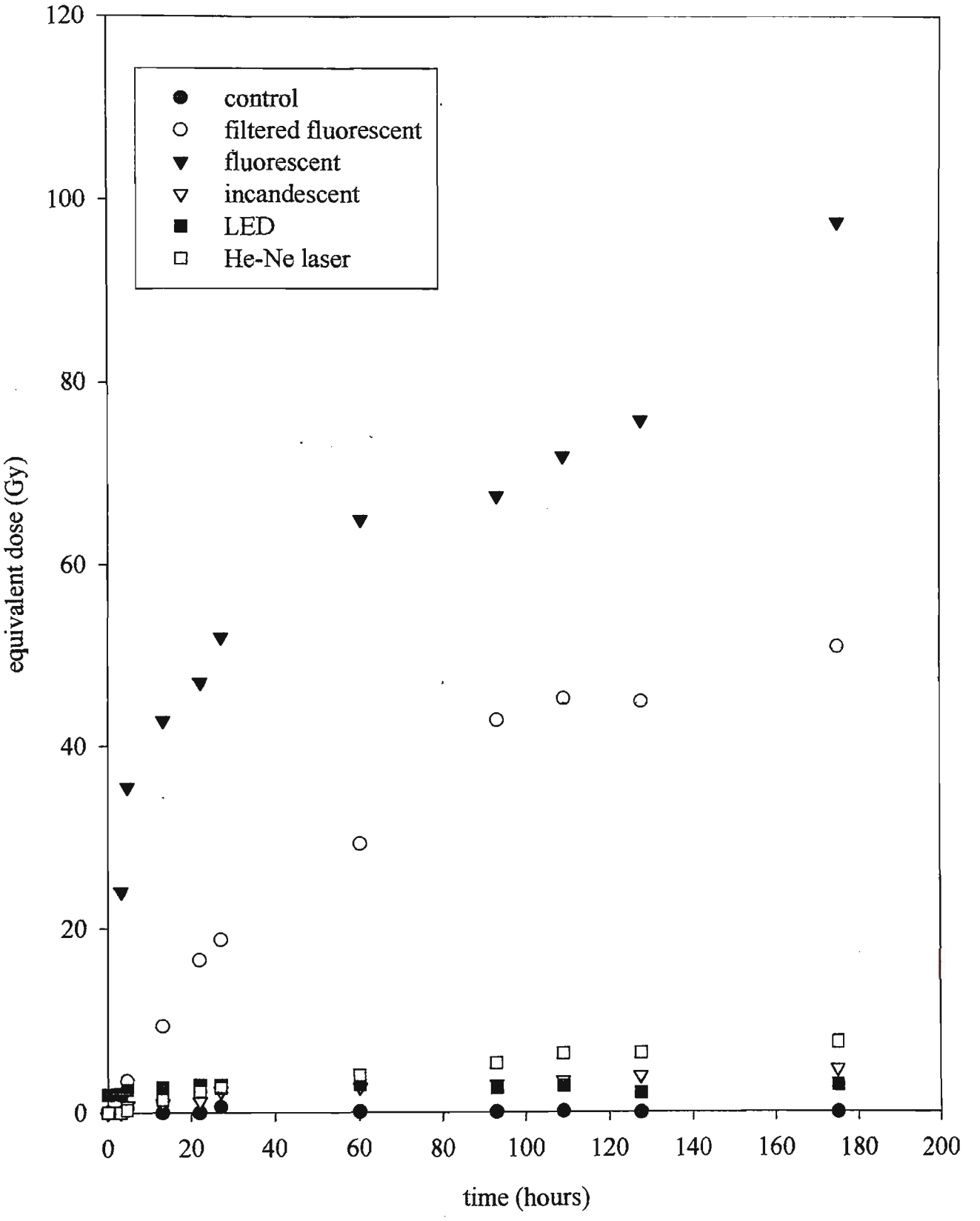

Figure 2.17 : Equivalent dose coloration of MD-55-2 Gafchromic film associated with exposure to various readout light sources.

Figure 2.18 shows a matrix plot for the coloration obtained by the laser light source in equivalent Gray. The laser produced a definite coloration within the beams aperture. A slight blurring and non-uniformity is seen around the beam which is assumed to be due to small alignment errors associated with each replacement of the film after densitometer readout.

Figure 2.19 shows the equivalent dose of ambient light sources. The largest effect was seen with direct sunlight accumulating approximately 50Gy equivalent dose from 175 hours of exposure. Fluorescent lights also produce a significant effect on coloration with approximately 20-30Gy equivalent dose after 175 hours. Ambient incandescent lights however produced a negligible effect on film coloration.

Discussion

Many types of light sources and readout systems have been used to measure radiochromic film dose response. These include incandescent and fluorescent light sources (Butson et al 1996, Stevens et al 1996), Helium neon lasers (Cheung et al 1997, Reinstein et al 1997) and ultra bright LED's (Carolan et al 1997). As shown by figures 2.17 and 2.18, the readout light source can seriously effect the measured optical density of the film. Fluorescent light sources even after 3 hours of exposure at close range can produce an equivalent dose of up to 20Gy, most likely due to their high ultra violet content. This equates to approximately 11cGy equivalent dose coloration per minute. Stevens et al (1996) have used a document scanner for evaluation of Gafchromic film. This devise exposes the film for a few seconds to fluorescent light. This produces a negligible coloration. However other devices which use a continuous illumination of fluorescent light should be avoided for film analysis. Relatively smaller but still distinguishable effect on coloration are seen using incandescent, LED's and helium neon lasers at close range.

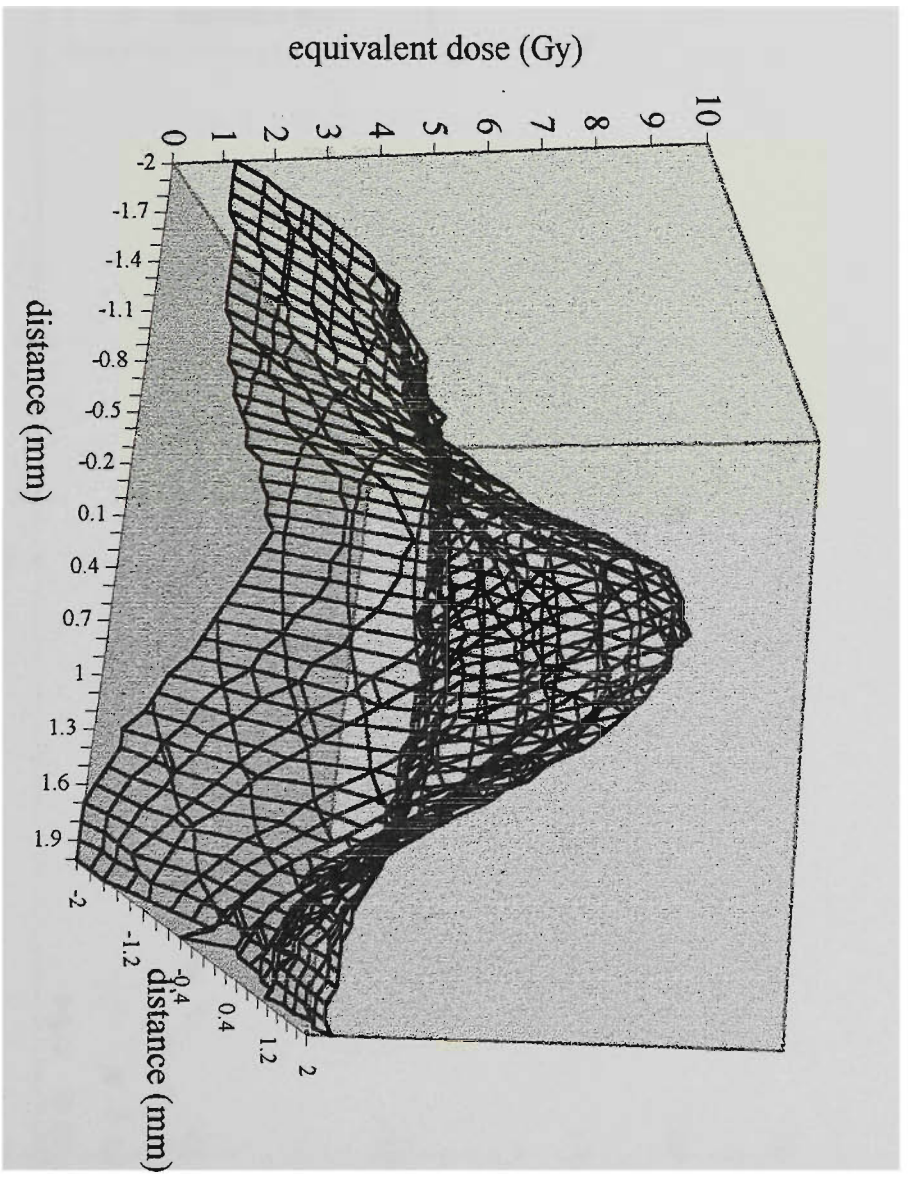

Figure 2.18 : Matrix plot of equivalent dose coloration of MD-55-2 Gafchromic film exposed to 632.8nm helium neon laser light.

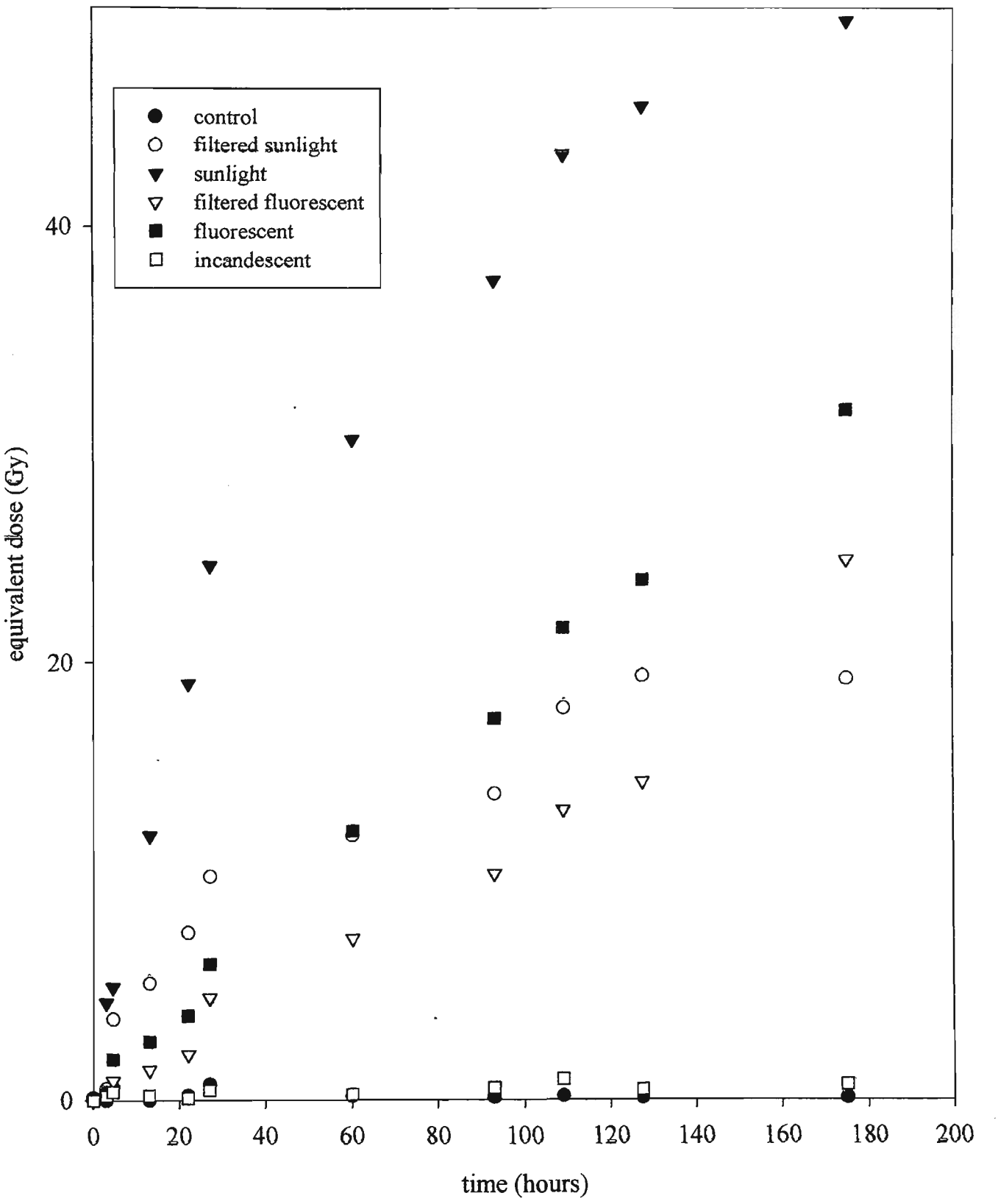

Figure 2.19 : Equivalent dose coloration of MD-55-2 Gafchromic film associated with exposure to various ambient light sources.

Equivalent dose coloration rates are approximately 1.7cGy/hr, 2.6cGy/hr and 4.3cGy/hr for LED's, incandescent and lasers respectively. The coloration would be negligibly small if the film was read and then placed back in a light proof envelope, however if unintentionally left under the light source for some time, spurious results could be obtained.

Fluorescent light sources have been investigated previously and shown to effect Gafchromic film due to its UV content (Meigooni et al 1996). Similar effects were observed where fluorescent light and filtered fluorescence was found to produce an equivalent dose coloration of approximately 18cGy/hr and 13cGy/hr respectively. Direct sunlight produced a more significant effect with an equivalent dose coloration of approximately 30cGy/hr and only 10cGy/hr for filtered sunlight which showed the high UV content of sunlight. Incandescent light sources do not produce significant UV rays and there is an associated negligible coloration of film. Time of fluorescent light exposure is the main consideration for clinical use of Gafchromic film. A normal patient treatment including set up time would be approximately 15-20 minutes. A film placed on the patient during a single fraction would therefore only receive an equivalent coloration of 4-6cGy if removed at the end of treatment.

In the case of a radiosurgical procedure, if the film was left attached to the patient for an estimated 1-2hours setup time, an equivalent coloration of 20-40cGy equivalent coloration would be seen. These values would be considered to lie within the error values associated with Gafchromic film evaluation.

The effect of ambient light could be significant in the case of accumulated dose measurement. For example if Gafchromic film is placed on a patients head cast and the film is left unprotected for a 5 week period, then up to 20Gy equivalent coloration could be seen. In this case, a small light proof envelope should be used to hold the film whilst remaining on the head cast.

Conclusions

Both readout light systems and ambient light can affect the coloration of Gafchromic film. Devices like document scanners which use fluorescent light for a few seconds will not produce significant coloration of Gafchromic film however other continuous light fluorescent sources should be avoided to reduce unwanted film coloration.

Temperature impacts on Gafchromic film

McLaughlin et al (1991) showed that there was a temperature dependence for optical density measurements associated during irradiation and readout spectroscopy. During irradiation an increase in temperature effects the evolution of the active layer and seems to act as a reaction enhancer by increasing the optical density at 660nm. This is shown in figure 2.20 where MD-55-2 film was irradiated to 30Gy at various temperatures ranging from 17°C to 40°C. This was achieved by placing the Gafchromic film on a heat pillow warmed in a microwave oven and allowed to slowly cool. Results show an approximate 5% increase in measured optical density from 17°C to 40°C. These results have implications when considering using Gafchromic film for in-vivo measurements inside head casts which when placed on a patient could heat to normal body temperature.

The temperature during film analysis is a major consideration for accuracy due to the temperature dependency on the absorption spectrum of Gafchromic film. Figure 2.21 (McLaughlin 1991) shows the shift of the Gafchromic films absorbency spectrum as temperature is varied. Depending on the wavelength of analysis a large change in optical density could be recorded with a change in temperature of the film. Temperature changes for film could be achieved by handling, where the film is heated (or cooled) by

fingers, changes in ambient room temperature (heaters or air conditioners) or by the heating of the readout system through normal electrical component heating.

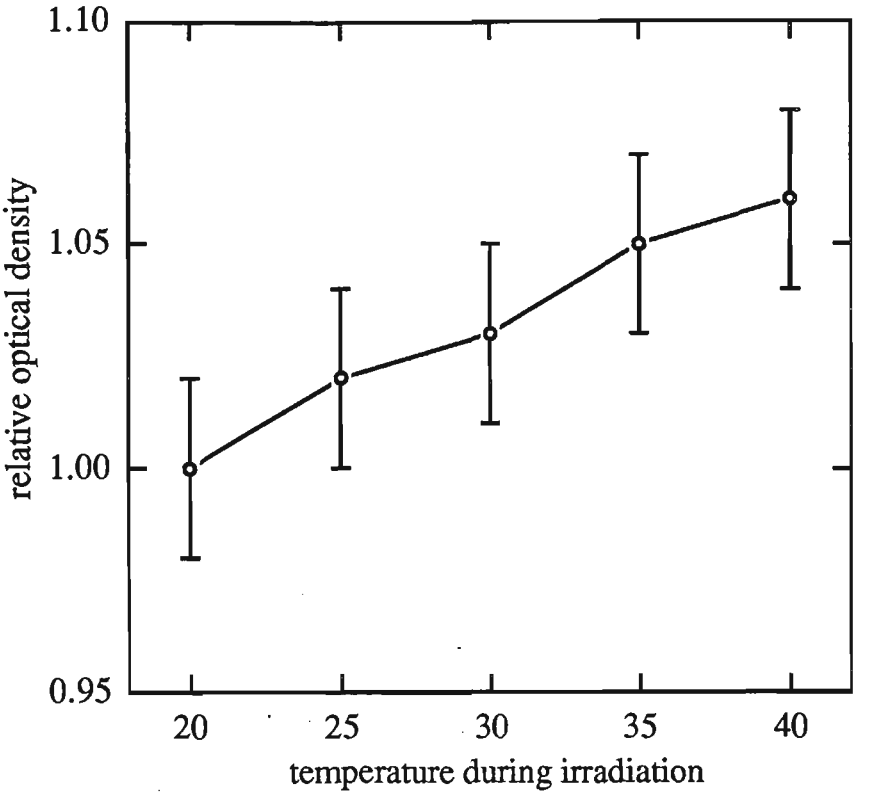

Figure 2.20 : Changes in optical density caused by different temperatures during irradiation of MD-55-2 Gafchromic film

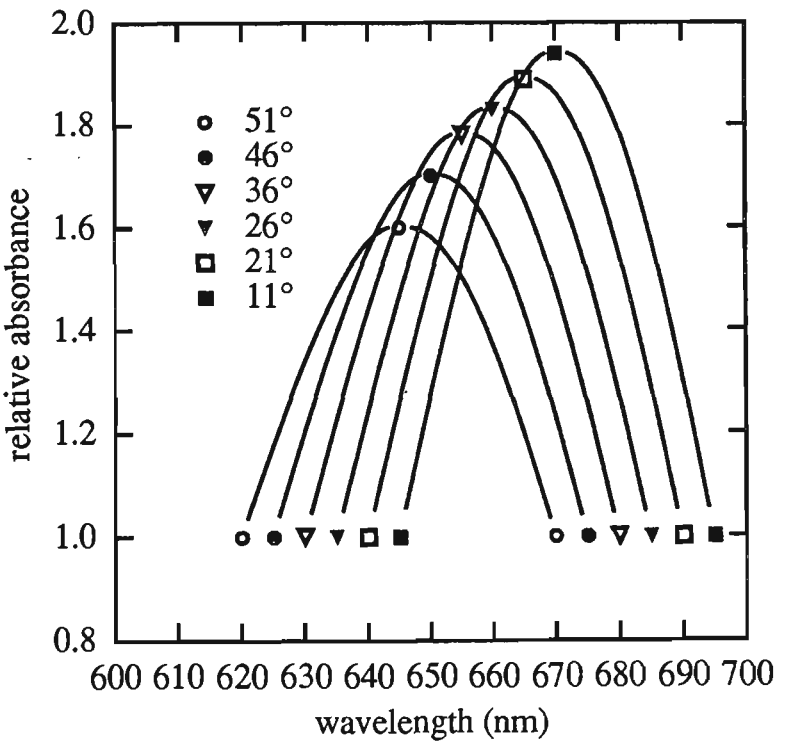

Figure 2.21 : Changes in the absorbency spectrum of Gafchromic film due to temperature variations. The peaks temporarily shift to shorter wavelengths with an increase in temperature. (Adaptabled from McLaughlin 1991).

Figure 2.22 shows the change in optical density at 660nm as a function of readout temperature using the Scanditronix RFA300 system. Temperature was measured using a Fluke thermistor. Due to this characteristic, the temperature around the densitometer is constantly checked during experimental analysis.

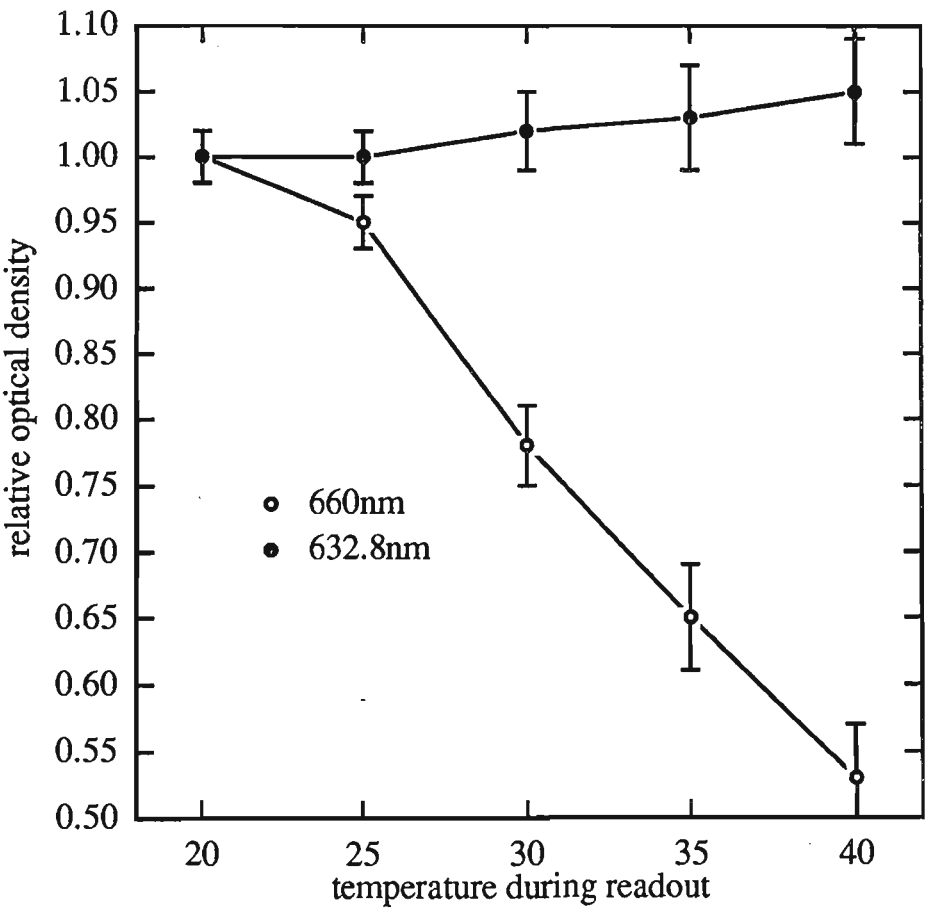

Figure 2.22 : Changes in optical density caused by variation in readout temperature for MD-55-2 Gafchromic film.

2.6 Metal oxide semiconductor field effect transistor (MOSFET)

MOSFET's can be used as online in-vivo skin dosimeters. MOSFET devices consist of a source (S), drain (D), gate (G) and a substrate (SB). This is shown schematically in figure 2.23.

The channel region consists of the semiconductor located under the gate which connects the source and drain. There is a direct relationship between current flowing in the channel and the applied voltage. MOSFET's can have two classifications depending on the conduction carrier types flowing in the channel. These being :

i) n-channel or electron conduction

ii) p-channel or hole conduction

They are also described by two mode types:

i) enhancement mode where the transistor is normally off, (if $V_g = 0$ then current = 0)

ii) depletion mode where the transistor is normally on

Operation for a n-channel enhancement mode MOSFET

If $V_g = 0$ (the gate voltage), the source-drain current is negligible. (A small amount of current will flow due to reverse saturation of the p-n junction). When $V_g > 0$ the hole carriers in the channel are depleted due to the positive gate charge field. However, this depletion acts as an insulator and the source drain current will still be negligible. When V_g becomes large enough (ie. $V_g = V_t$ which is the threshold voltage), a number of electrons will be attracted to the silicon oxide interface from the silicon source and drain regions. This will allow a current to flow between the source and drain. As V increases so does current flowing to the drain.

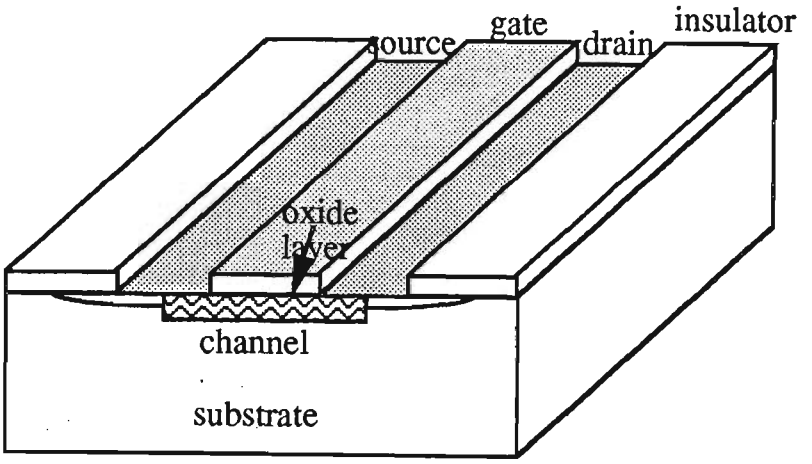

Figure 2.23 : Schematic representation of a MOSFET radiation dosimeter.

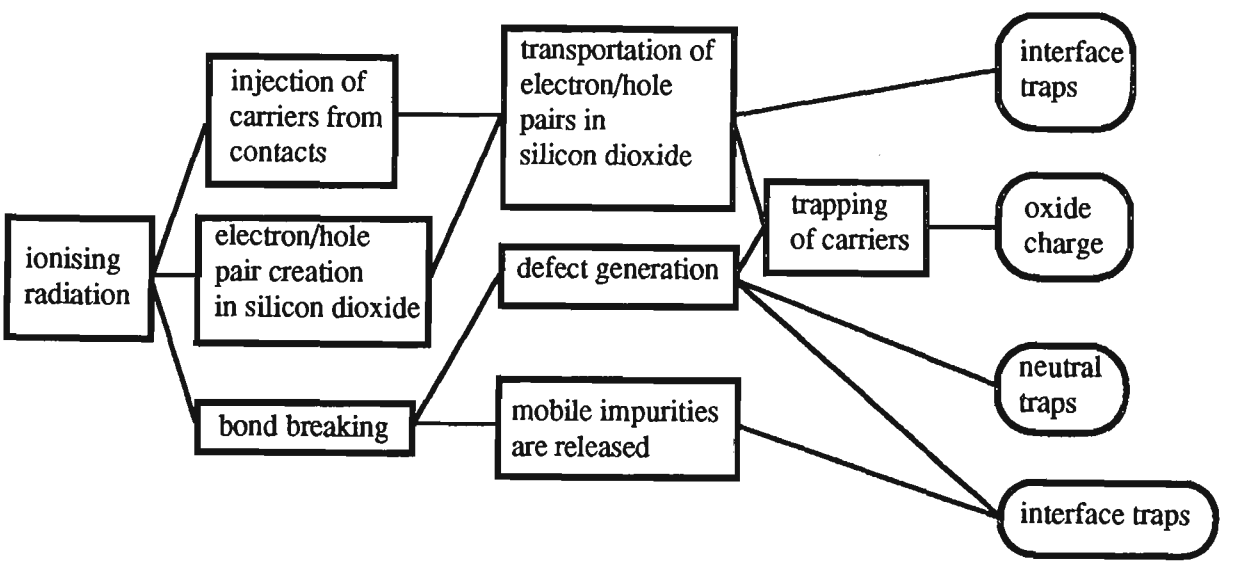

Figure 2.24 : Interaction processes within a MOSFET dosimeter produced from ionising radiation.

Ionising radiation affects

MOSFET's are effected by radiation and thus their performance parameters change. That is with a shift in the threshold voltage and a decrease in gain. The damage in the SiO_2 layer consists of three components :

i) a build up of trapped charge in the oxide

ii) an increase in the number of interface traps

iii) an increase in the number of bulk oxide traps

The process by which this happens is summarised in figure 2.24.

Principle of operation

On exposure, electron-hole pairs are formed in the SiO_2 oxide layer which is the active dosimetric volume. These holes migrate to the silicon oxide interface and are trapped. The trapped positive charges cause a shift in the threshold voltage. Because of this, a negative voltage must be applied to the gate to overcome the electric field of the trapped charges to achieve conduction.

The change in the threshold voltage, ΔV_t, is proportional to the radiation dose deposited and can be given by

$$\Delta V_t = \frac{eN_0 t_{ox}}{\varepsilon_{ox}\varepsilon_0} + g(t) \qquad 2\text{-}16$$

where g(t) = trapped charge leakage, N_0 = number of captured holes/cm^2 in the silicon oxide layer, t_{ox} = thickness of silicon oxide layer.

Experimental methods and circuit design

The experimental configuration for the MOSFET used in these experiments consisted of a n-type MOSFET device with the Nickel casing removed. This leaves the bare crystal intact and exposed as shown in figure 2.25. We refer to this state as uncovered. Only 200 microns of the surface area is the MOSFET active crystal thus producing a very small detector. During irradiation the MOSFET was connected with a 6V bias voltage to the drain supplied by a dc battery as shown in figure 2.26. Following irradiation , the bias voltage is removed and the voltage at V_{out} is measured.

The MOSFET was placed in a custom made solid water phantom holder through which a small hole was drilled to accommodate it. Small amounts of wax were placed around the uncovered MOSFET to fill any air cavities present around or below the exposed crystal. A small channel was drilled to accommodate the connecting wires from the battery/reader and MOSFET. The reader consisted of a 2540 Keithley electrometer operating in charge mode. During readout the potential difference between the MOSFET's gate and substrate was measured. This was performed before and after each irradiation. The difference in voltage potential is proportional to absorbed dose. The system is linear to within 1%. MOSFET's experience a decrease in potential difference across the gate and substrate after each irradiation and thus have a limited lifetime. At 6V bias voltage, the MOSFET's absorb approximately 50Gy before their response becomes non-linear. At this level of radiation they are permanently damaged and are discarded. Radiation doses were measured for field sizes ranging from 2cm x 2cm to 40cm x 40cm for open field and with various beam modifying devices such as block trays and wedges.

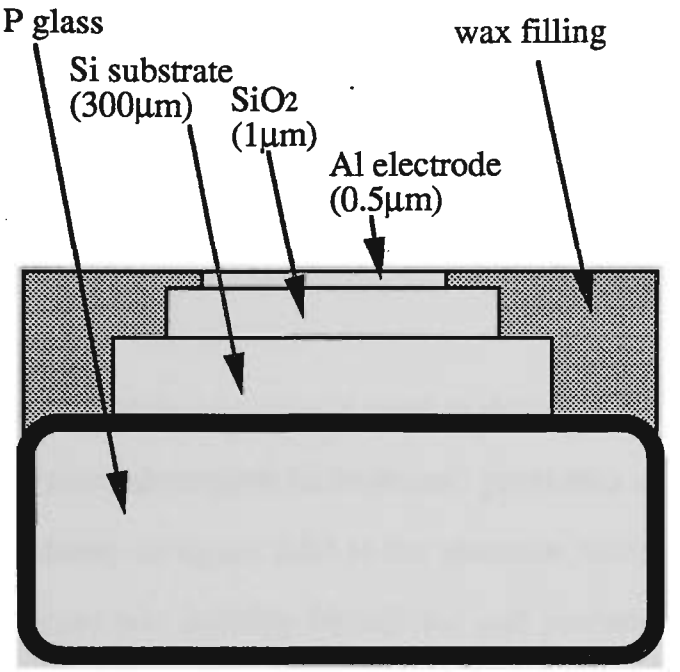

Figure 2.25 : Schematic representation of an uncovered MOSFET dosimeter used for surface dose measurements.

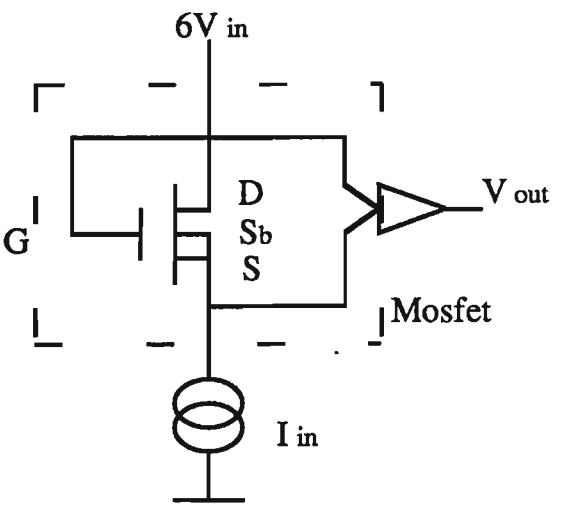

Figure 2.26 : Simplified circuit diagram for our clinical radiation dosimetry system.

2.7 Phantom materials

Solid water

In radiotherapy the term phantom is used to describe a material and structure which models the radiation absorption (attenuation) properties of body tissues. Solid water type WT/SR6 shown in figure 2.27 is the phantom material mainly used during this thesis. Solid water was initially formulated and produced by the Radiation Physics Department of St. Bartholomew's Hospital London EC/UK (Constantinou 1978, 1982). It consists of a solid epoxy resin based material with a composition as shown in table 2.2.

Table 2.2 : Composition of solid water (type WT/SR 6) : Percentage weight of component.

components	epoxy CB4	% by mass
	MY750 and 40 parts of hardener XD716.	80.48
	polyethylene.	10.00
	calcium carbonate.	5.77
	PMS (pheonolic microspheres)	3.75
elements	hydrogen	8.09
	carbon	67.22
	nitrogen	2.40
	oxygen	19.84
	calcium	2.32
	chloride	0.13

WT/SR 6 solid water's specific gravity is 1.015±0.002 (relative to distilled water at 22°C which has a density of 0.9978 g/cm^3). This slightly higher density of solid water was required in order to match the electron density of water (e/cm^3) and to make it

'volumetrically' equivalent to water so that x-ray transmission through each material would be the same on a cm per cm basis.

The electron density N_e of water is 3.35 x 10^{21} e/cm^3 (Khan 1984). From this a relative electron density ρ_e^w of a material can be quoted. Water being ρ_e^w=1.00, solid water has ρ_e^w= 1.00, perspex ρ_e^w=1.14 and polystyrene ρ_e^w=1.01. The effective atomic numbers Z_{eff} of these materials are :- water (Z_{eff} = 7.41), solid water (Z_{eff} = 7.54) , perspex (Z_{eff} = 6.46), polystyrene (Z_{eff} = 5.69). Table 2.3 gives results for relative transmission intensities through solid water type WT/SR 6 compared with water using x-ray, gamma ray and electron beams. The transmission values were recorded at 10cm for x-rays and at 3cm for electron beams.

Table 2.3 : Relative transmission values for solid water at various beam energies. Data adapted from White et al 1989)

Type of energy	SSD	I' (solid water)/I(water)
Co-60	80	1.001±0.001
4MV x-rays	80	1.002±0.002
10MV x-rays	100	1.002±0.002
12MeV electrons	100	1.031±0.010
15MeV electrons	100	1.028±0.008
20MeV electrons	100	1.037±0.003

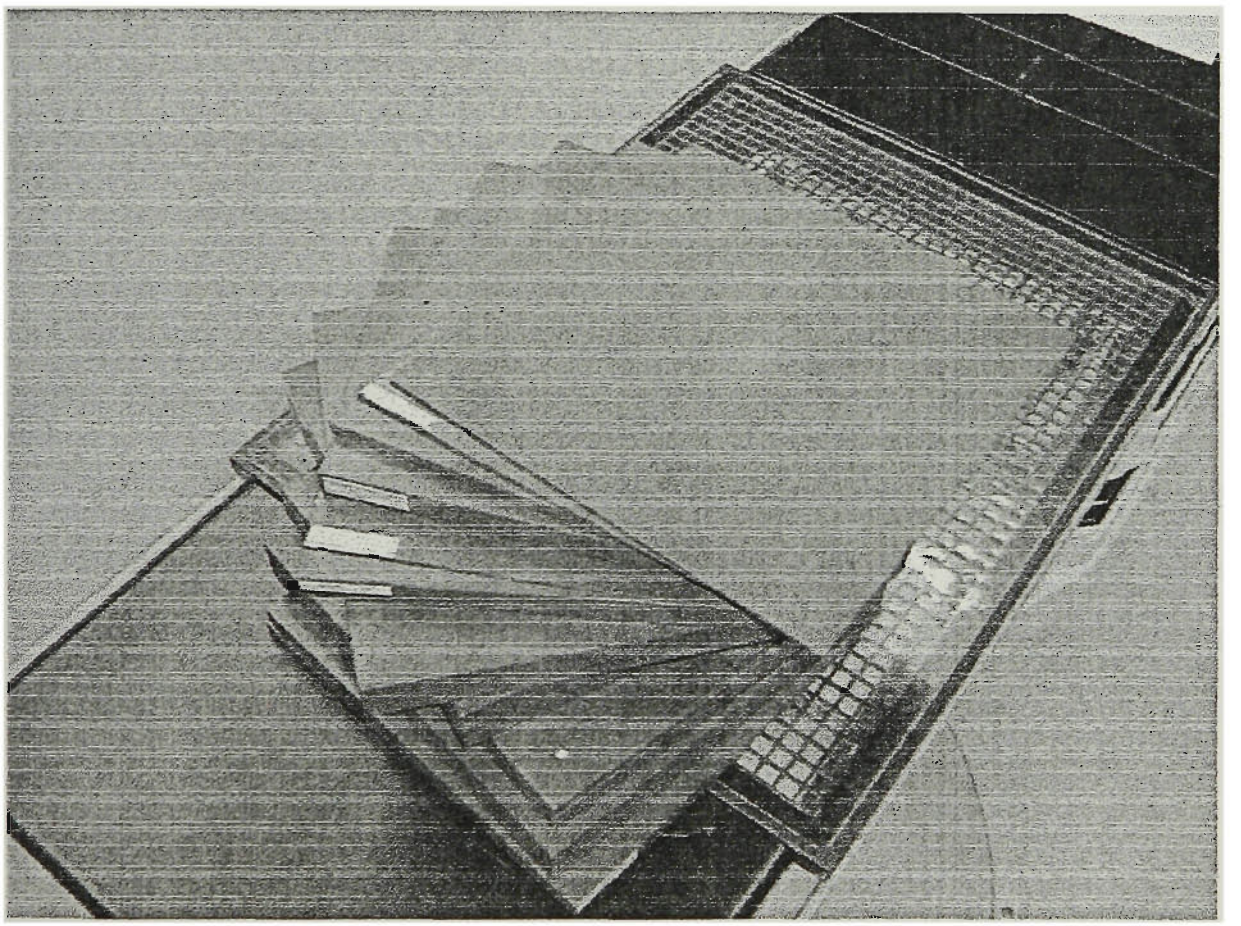

Figure 2.27 : Picture of solid water slab phantom used for the majority of data collection.

Block trays

Block trays are used to hold lead shielding in position during clinical treatment. All block trays are 30cm x 30cm to slot into the block tray holder. Four types of block trays have been investigated in detail. These being,

i) steel honey comb tray. Constructed from steel with a hexagonal pattern with 85% of surface area open

ii) solid perspex, 0.6cm thickness

iii) solid perspex, 1.0cm thickness

iv) solid lexan, 1.0cm thickness

All four block trays are shown in figure 2.28. The block tray holder is located 65.3cm from the source on the accessory mount of the Linac's treatment head. Blocks are constructed from either 100% lead or cerrobend material. They are usually mounted on top of the block tray although they may hang below the block tray.

Wedges

Wedges are made from steel and are designed to produce isodose lines at 10cm depth of angles 15°, 30°, 45° and 60° orthogonal to the beams central axis. The wedge accessory mount is located 55cm from the source. The wedges studied in this thesis were orthogonal wedges and are shown in figure 2.29.

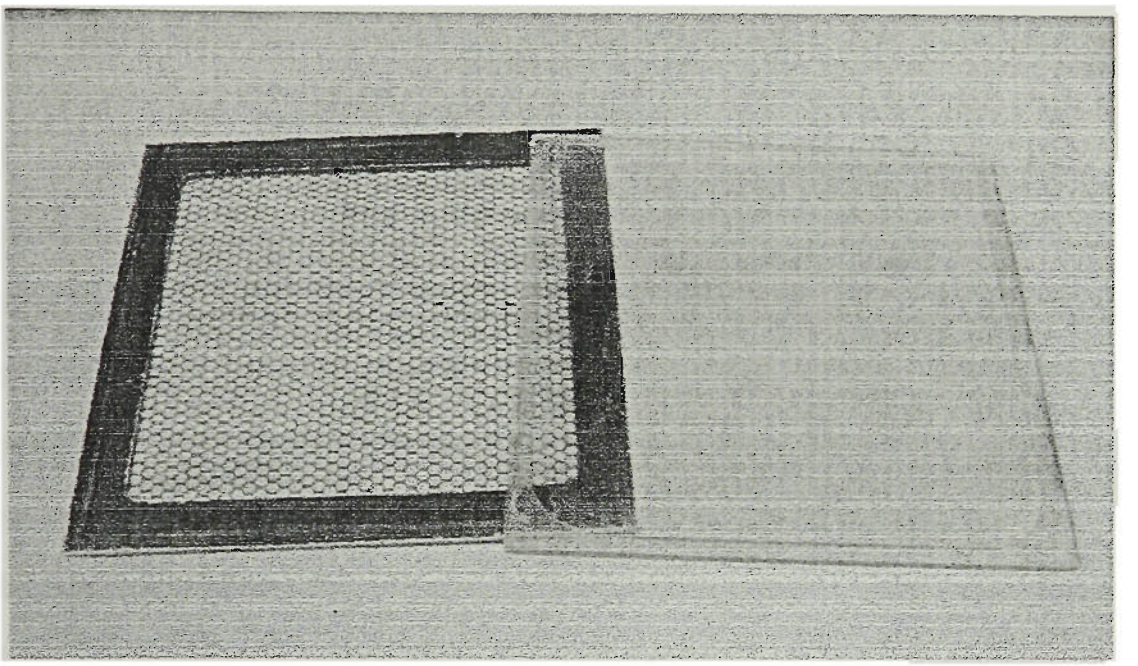

Figure 2.28 : Picture of the various block tray types used in experiments. They are used clinically for different treatment setups.

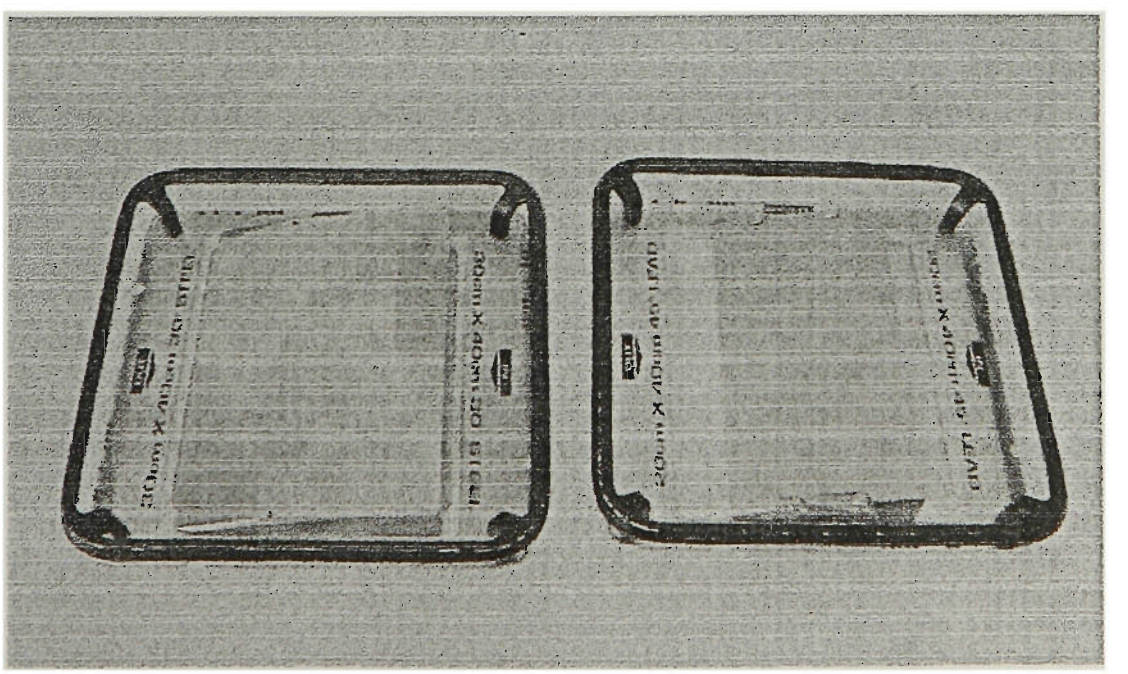

Figure 2.29 : Wedges used in radiotherapy treatment

Head casts

A transparent heat mould material, called 'uvex' is commonly used to make patients' immobilisation masks, as shown in figure 2.30 This material is made with 2 mm flat sheets of cellulose acetate which has a relative electron density of 1.146. Therefore the effective depth of a uvex sheet is 2.3mm. Elementary data for uvex supplied by the manufacturer is given in the table 2.4. As uvex is moulded to fit snugly around the patients head, additional material is added to the build up region. This material thickness changes the radiological depth to the skin surface. Thus larger skin doses are given due to the build up material. Investigations are performed to ascertain the degree of increase to skin dose with these materials.

Table 2.4 : Composition for uvex material

specific gravity	1.2
chemical composition	$C_{16}H_{26}O_{15}$
effective atomic number	7.05
relative electron density	1.146

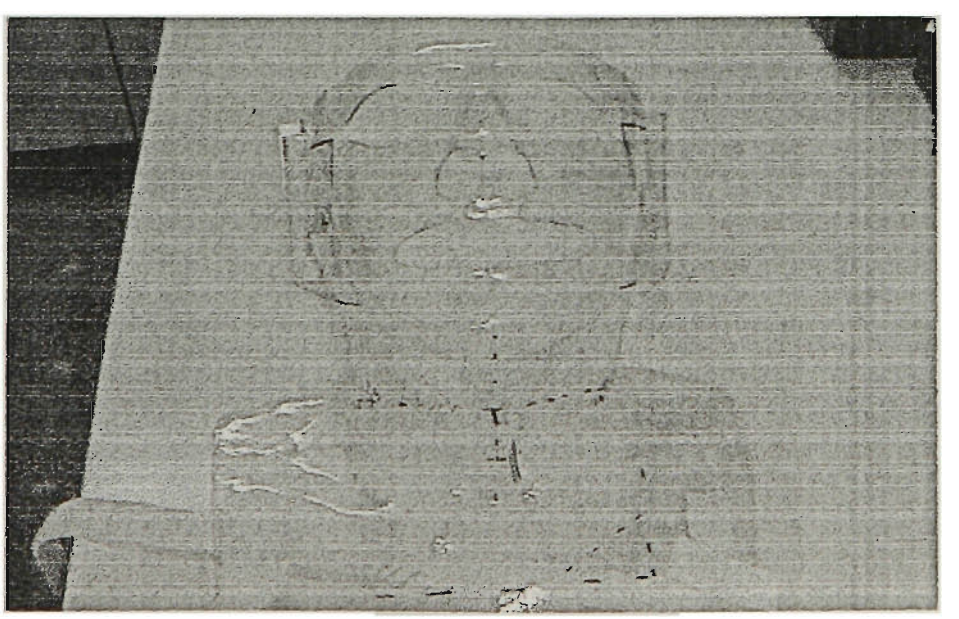

Figure 2.30 Uvex head cast material used clinically to accurately position patients during treatment.

2.8 Neodymium iron boron lanthanide magnetic deflector

A set of Neodymium Iron Boron (NdFeB) lanthanide ceramic magnets each of dimension 30cm x 5cm x 5cm were placed in a custom made holder to fit directly under the block tray holder on the accessory mount of the machines head as shown by figure 2.31.

Neodymium Iron Boron alloy rare earth permanent magnets have a magnetic field strength approximately 16 times greater than iron by weight thus producing a strong magnetic field from a small volume. The magnetic field strength was measured with a Hall effect probe. Field sizes up to 35cm x 35cm could be examined without interference from the supporting frame. The magnetic field will sweep contamination electrons away from the treatment field via the Lorentz force. It was important to map the path of the swept electrons to ensure their path or magnitude could not accidentally expose the patient in a non treatment zone.

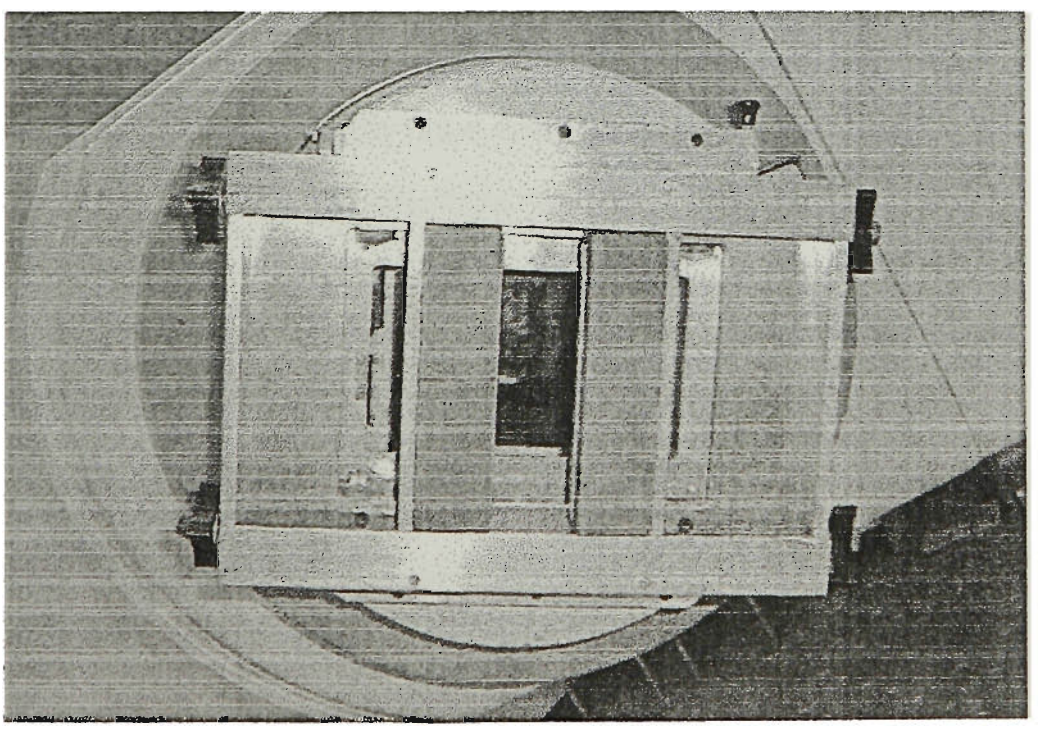

Figure 2.31 : Neodymium Iron Boron electron deflector mounted on the treatment head of the linear accelerator.

2.9 Monte Carlo techniques

Monte Carlo calculated are used in radiotherapy applications to simulate the interactions of x-rays and electrons in matter such as human tissue or equivalent mediums. Monte Carlo can directly simulate the physical processes which occur such as photoelectric effect, Compton scattering or pair production and the particle transport occurring from such interactions. Simulations of dose deposition in the build up region of megavoltage photon beams has been performed to analyse the photon in phantom component. Electron contamination has not been simulated using geometric sources of the electron contamination sites. This work has been performed elsewhere using the BEAM code (Rogers 1993).

Physical processes and assumptions

Photon transport

Monte Carlo models a photon beam as a large but finite number of discrete events. The mean free path of a photon in a medium is expressed as

$$\lambda = \frac{M}{N_A \rho \sigma_t} \qquad 2\text{-}17$$

where M = molecular weight of the medium, N_A = Avogadro's number, ρ = mass density of medium, σ= cross section per molecule.

The number of mean free paths N_λ between two points x_0 and x_1 is given by

$$N_\lambda = \int_{x_0}^{x_1} \frac{dx}{\lambda(x)} \qquad 2\text{-}18$$

The Monte Carlo code generally simulates a finite number of homogeneous region in which λ has a given value. Interaction processes modelled include, photoelectric effect, Compton effect, pair production, Thomson scattering, Rayleigh scattering, nuclear photoelectric effect and triplet production. The relative probabilities of each interaction are taken into account to produce the final interaction process.

Electron transport

A simple Monte Carlo approach to energy deposition of electrons is to use a total stopping power to determine the energy lost along an electron step, and a multiple scattering theory to define the scattering angle. This method assumes a continuous slowing down approximation in which the energy losses of the electrons are continuous. In reality, the energy loss per unit distance varies and the stopping power represents the average energy loss. This fluctuation is known as energy loss straggling and a correction can be incorporated to account for this.

A path length correction is also incorporated into the simulation to account for differences in distance and displacement for the travelling electron. This effect is small if the electron step size is small.

The electron gamma shower code (EGS4)

The EGS4 system contains two main components (Nelson et al 1985). These being the PEGS4 pre-processor and the EGS4 simulation code. PEGS4 creates data sets for each element, compound or mixture used in the simulation. This data is read by the HATCH routine in the EGS4 code. The user is responsible for writing the MAIN, HOWFAR and AUSGAB routines. These three components form the user code. MAIN includes such parameters as media type, particle parameters energy cut offs and simulation

geometry. Using HATCH to transfer data from PEGS4, MAIN repeatedly calls SHOWER to simulate particle transport. HOWFAR is used to determine the distance to the next medium boundary along the current path and AUSGAB is used to score the energy and other parameters of interest.

EGS4 electron transport and PRESTA

The EGS4 code groups small collisions together and large collisions are treated individually using differential cross-sections. The user can control the implementation of these two processes. AE represents the low energy threshold for discrete electron collisional losses (delta ray production) and can be set to the required level. AP represents the low energy threshold for discrete electron radiative losses (Bremsstrahlung) and can be set to the required level. For simulations at megavoltage therapeutic energies, energy cut-offs of 10keV for AP and 521keV for AE is sufficient for high accuracy without impractical time constraints. ECUT represents the charged particle low energy cut-off (energy deposited locally below this value) PCUT represents the photon low energy cut-off (energy deposited locally below this value).

Normally ECUT is chosen so that the range of the electron with energy ECUT is a small proportion of the minimum scoring region. PCUT is normally chosen to be a value similar to ECUT or less due to the photons attenuation properties. The values of ECUT and PCUT are set when the PEGS4 data is created however their values can be increased when the simulation is run.

ESTEP represents the maximum fraction of energy lost during each electron step due to continuous energy losses. The larger ESTEP, the fewer steps will be performed per electron. Using a high ESTEP value can underestimate the electron path length per step and the electron is transported further than in reality.

The parameter reduced electron step transport algorithm (PRESTA) is used to dynamically select the appropriate step length for quicker simulations without losing accuracy. It consists of a new path length correction based on Moliere multiple scattering theory, a lateral correlation algorithm (LCA) which accounts for lateral movement of electrons during larger ESTEP sizes and a boundary crossing algorithm (BCA) when multiple scattering theory is compromised crossing from one material into another. PRESTA in this situation reduces the electron step size near a boundary and then increases the size again after crossing.

Chapter 3 Results and discussion

3. 1 Ion chamber measurements

Rationale - Central axis input data is needed to be collected for use in the empirical model outlined in chapter 4.

Mini methods

Measurements were taken on the central axis of the x-ray beam in a flat solid water slab phantom. The chambers were connected via a triaxial cable to a Keithley electrometer at 300V bias voltage. The source surface distance (SSD) was kept to 100cm via the use of horizontal side wall lasers. To achieve a constant SSD thin solid water slabs were taken from underneath the chamber and placed on top so as to maintain a constant SSD. Results were measured for field sizes between 5cm x 5cm and 40cm x 40cm in 5cm increments.

Dose build-up curves

(i) Beam energy

A comparison of dose build up curves for energies, 1.25MeV gamma rays from a Cobalt-60 source, 4MV x-rays, 6MV x-rays, and 18MV x-rays is given in figure 3.1. All beams were measured with a 10cm x 10cm field size using an Attix ion chamber. The cobalt-60 beams SSD was 80cm and all others were 100cm.

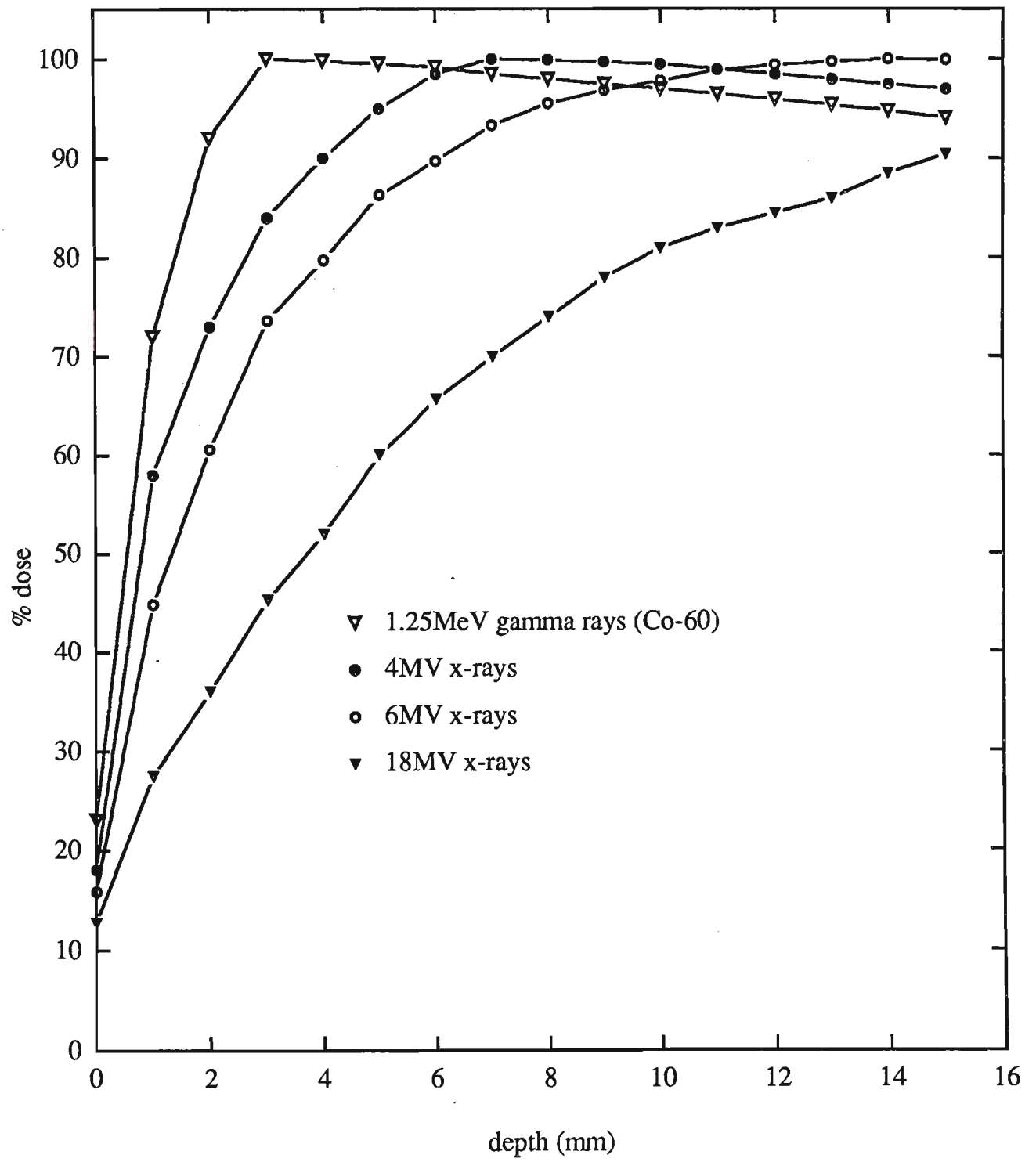

Figure 3.1 : Increases in energy extends the build up region for megavoltage photon beams. The position of d_{max} increases from 3mm for cobalt-60 up to 33mm for 18MV photons.

The build up depth for cobalt-60 was measured as 3mm. Three distinguishable features concerning dose build up characteristics are noticeable in this graph. The depth of maximum dose increases with energy. The position of d_{max} ranges from 3mm for cobalt-60 up to 33mm for 18MV x-rays. This is directly related to the effective range of the secondary electrons produced by the interaction of the primary x-rays. The mean energy of cobalt-60 is 1.25MeV. In a 180° forwardly scattered Compton interaction, the maximum kinetic energy of the released electron would be 0.632MeV. This corresponds to a range of 2.2mm in water. Similarly, the mean energy of a 18MV x-ray beam is approximately 6MeV. In the same reaction process the range of the scattered electron would be approximately 31mm. These values are closely related to the depth of d_{max} for these x-ray beam energies. Ranges were determined using a low energy range equation (Siegbahn 1963).

For a 10cm x 10cm field size surface dose was measured as 24% of maximum for cobalt-60 and decreases with increasing x-ray energy (eg. 14% for 18MV). This effect is due to a combination of changes due to photon phantom scatter and electron contamination generated by different sites above the phantom and will be discussed in more detail in the following sections. The increase in surface dose with lower energy (i.e. 4MV and 6MV) seems to be predominantly due to the increased production of low energy electron contamination from the air column directly above the patient. Finally the dose gradient from the surface through to d_{max} decreases with increasing energy. Within the first 1mm the dose gradients range is from 50%/mm to 15%/mm from cobalt-60 to 18MV x-rays. This is directly related to the range of secondary electrons produced within the phantom and their energy deposition. The data in this region is of importance especially in areas such as the treatment of breast and head/neck tumours where there is a requirement to keep the near surface dose reasonably high to reduce the risk of cancer recurrence in the superficial layer of skin.

(ii) Field size

Figure 3.2 demonstrates the percentage dose build up effect for 6MV x-ray open beams as field size is varied between 10cm x 10cm and 40cm x 40cm. Results are measured with the Attix chamber at 100cm SSD. Surface dose and dose build up increases with field size. Surface dose ranges from 16% of maximum at 10cm x 10 cm, to 42% of maximum at 40cm x 40cm field sizes respectively. As mentioned in chapter 1, two contributions to dose build up are photon interactions within the phantom and electron contamination due to photon interactions outside the phantom. As shown previously in figure 1.2 the flattening filters shape is concave rising to a point at the centre. This spreads the x-rays into a flat beam but also produces a spectrum of different energy contamination electrons across it. Contamination produced from the flattening filter and ionisation chambers in the accelerator head will inherently be in every beam from the smaller field sizes to the larger field sizes. Note that most contamination produced above the jaws will be stopped by the jaws when they are in a small field size configuration. However as the field size is increased three effects occur:

i) the upper surface of the jaws allows more contamination produced in areas of the flattening filter, mirror and ionisation chambers to pass through
ii) a greater surface area of the sides of the jaws presents itself to the beam. Extra focal photons in particular may interact with these surfaces causing electron contamination
iii) the air volume exposed to x-rays increases and therefore increases the probability of electron contamination being produced

Thus as field size is increased the near surface dose increases.

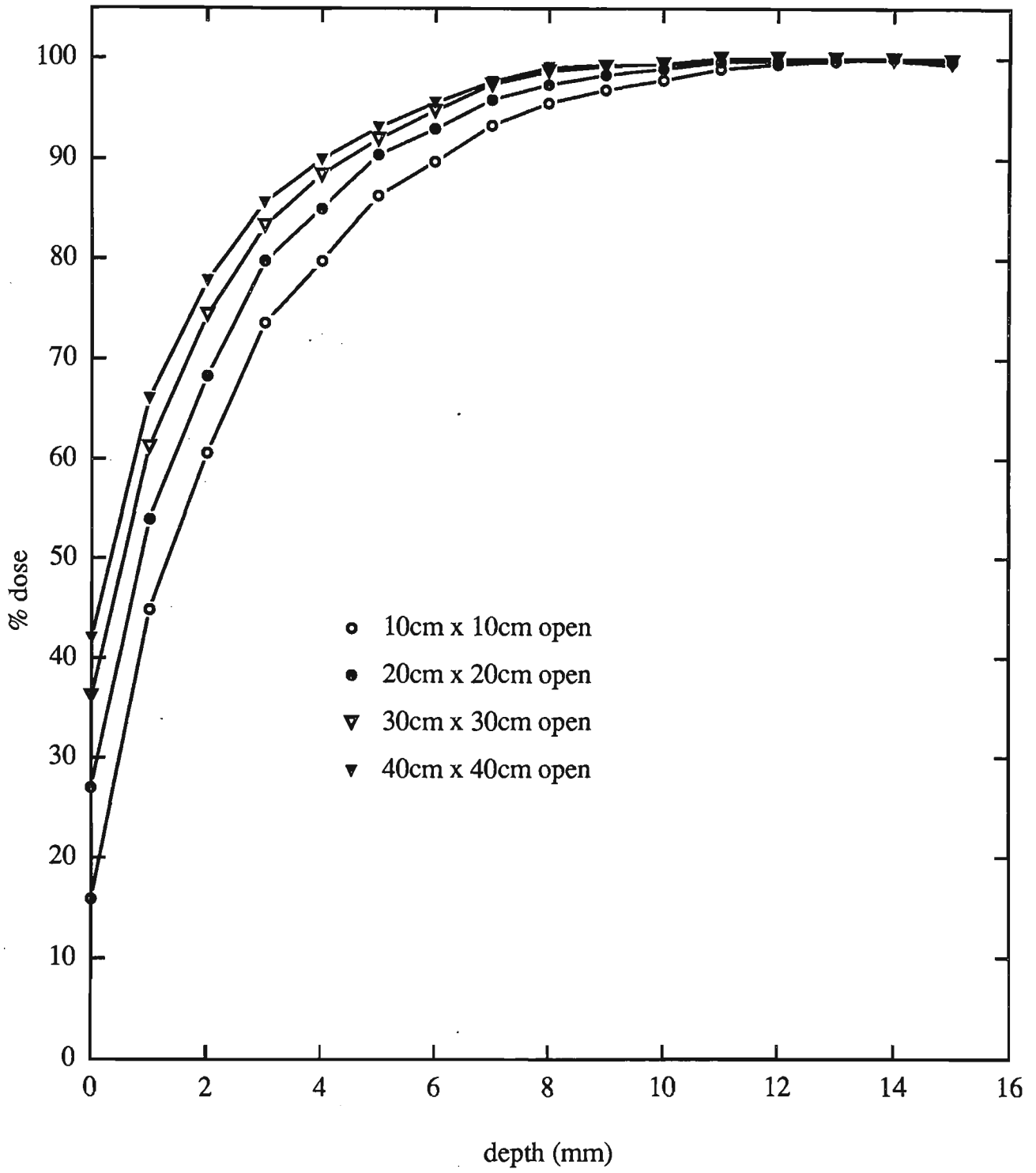

Figure 3.2 : Dose build up characteristics change significantly with field size. This is mainly due to the effects of electron contamination produced in the treatment head of the machine and within the air column above the phantom.

Another feature not easily distinguishable from figure 3.2 is that the position of d_{max} decreases with increasing field size. .This region has a small dose gradient and slight changes in dose deposition will effect the position of d_{max}. With the increase in field size a relative increase in the electron contamination component with a range capable of reaching near d_{max} is produced. This in turn deposits more dose just before the d_{max} position bringing the position of d_{max} closer to the surface. The position of d_{max} is 15mm for a 10cm x 10cm field. This reduces to 11mm for a 40cm x 40cm field.

(iii) Beam modifying devices

Beam modifying devices such as perspex block trays inherently change the dose build up region. Figure 3.3 shows the percentage dose build up for a 6MV beam with and without block trays in the beam for a 10cm x 10cm and 30cm x 30cm field respectively. Data for different block tray types, steel honeycomb and solid 6mm perspex are shown. Results show an increase in surface and build up dose with the introduction of both block trays, however perspex has a more significant effect. Surface doses normalised to D_{max} for the steel block tray ranged from 15.9% to 45.6% from 10 x 10cm to 40cm x 40cm. For perspex block trays, these values ranged from 17.8% to 57.4% from 10cm x 10cm to 40cm x 40cm field sizes.

Dose delivered to the surface and at 1mm depth are important sites in terms of skin reactions within the basal cell and dermal layer. Figure 3.4 demonstrates the increase in surface dose with field size for various types of block trays at 6MV. An important feature is that the steel honeycomb block tray has a small effect on the dose to the surface/basal cell layer. Increases in surface dose produced by the introduction of a 10mm perspex block tray range from 1% for a 5cm x 5cm field up to 21% for a 40cm x 40 cm field. Similar dose increases are seen at 1mm depth as shown in figure 3.5. At this depth, the increases range from 3% for a 5cm x 5cm field up to 17% at 40cm x 40cm field size.

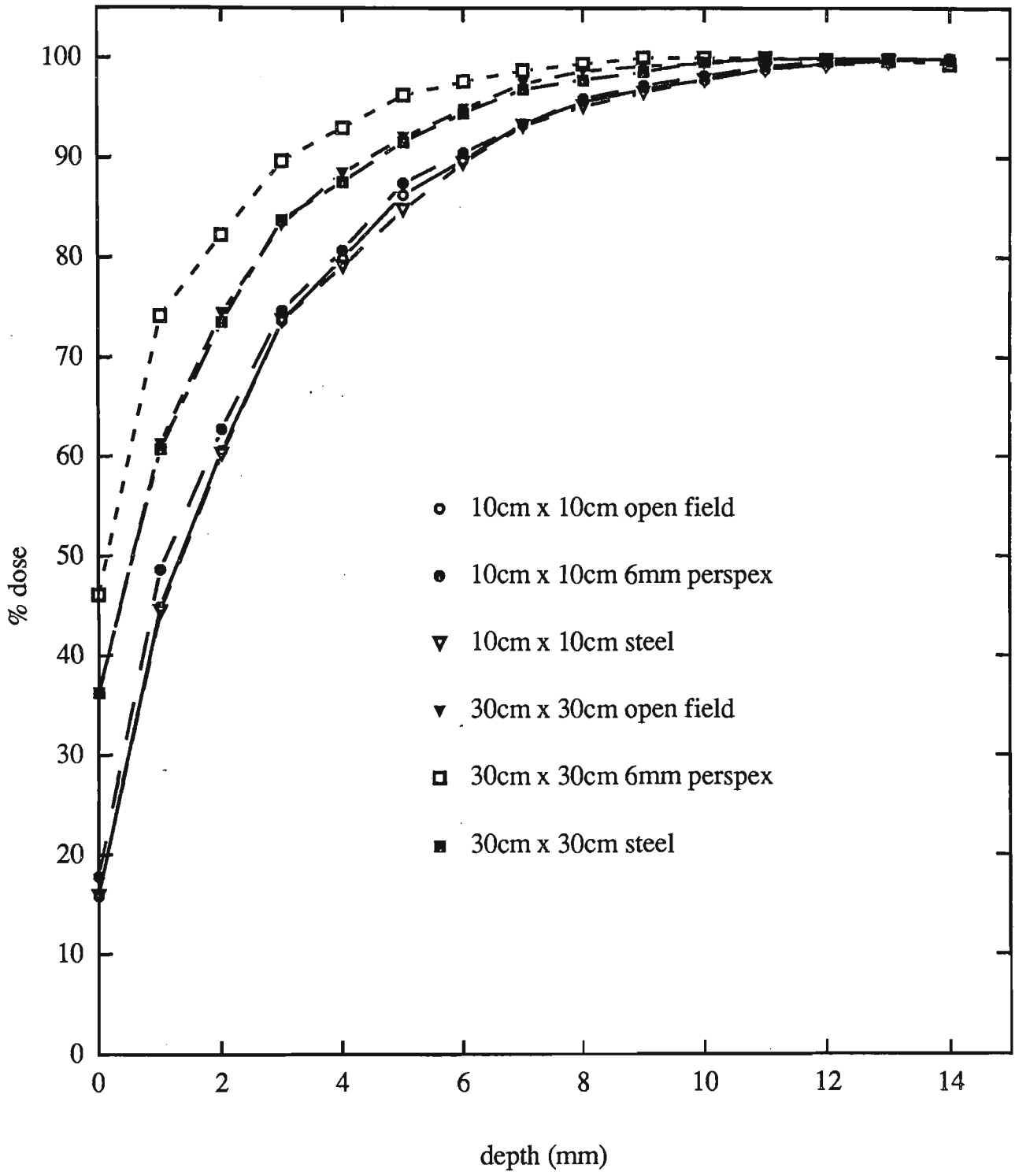

Figure 3.3 : Block trays can significantly increase the dose in the build up region due to the production of extra electron contamination. The effect is minimal for the steel honeycomb design block trays and largest for 6mm perspex trays.

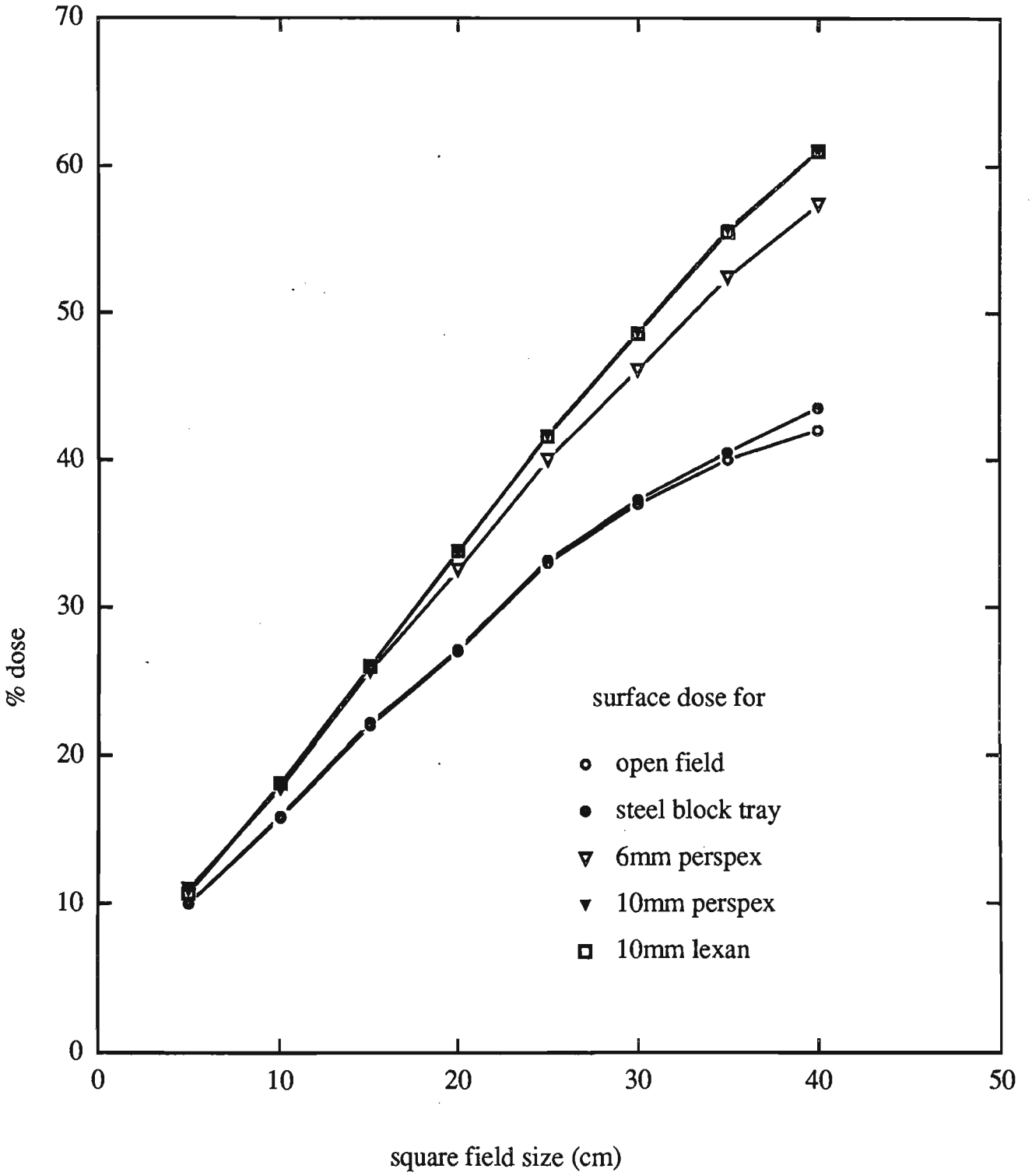

Figure 3.4 : Surface dose increases with field size and with the use of block trays. Increases from 10% at 5cm x 5cm field size up to 60% at 40cm x 40cm field size with a 10mm perspex block tray are seen.

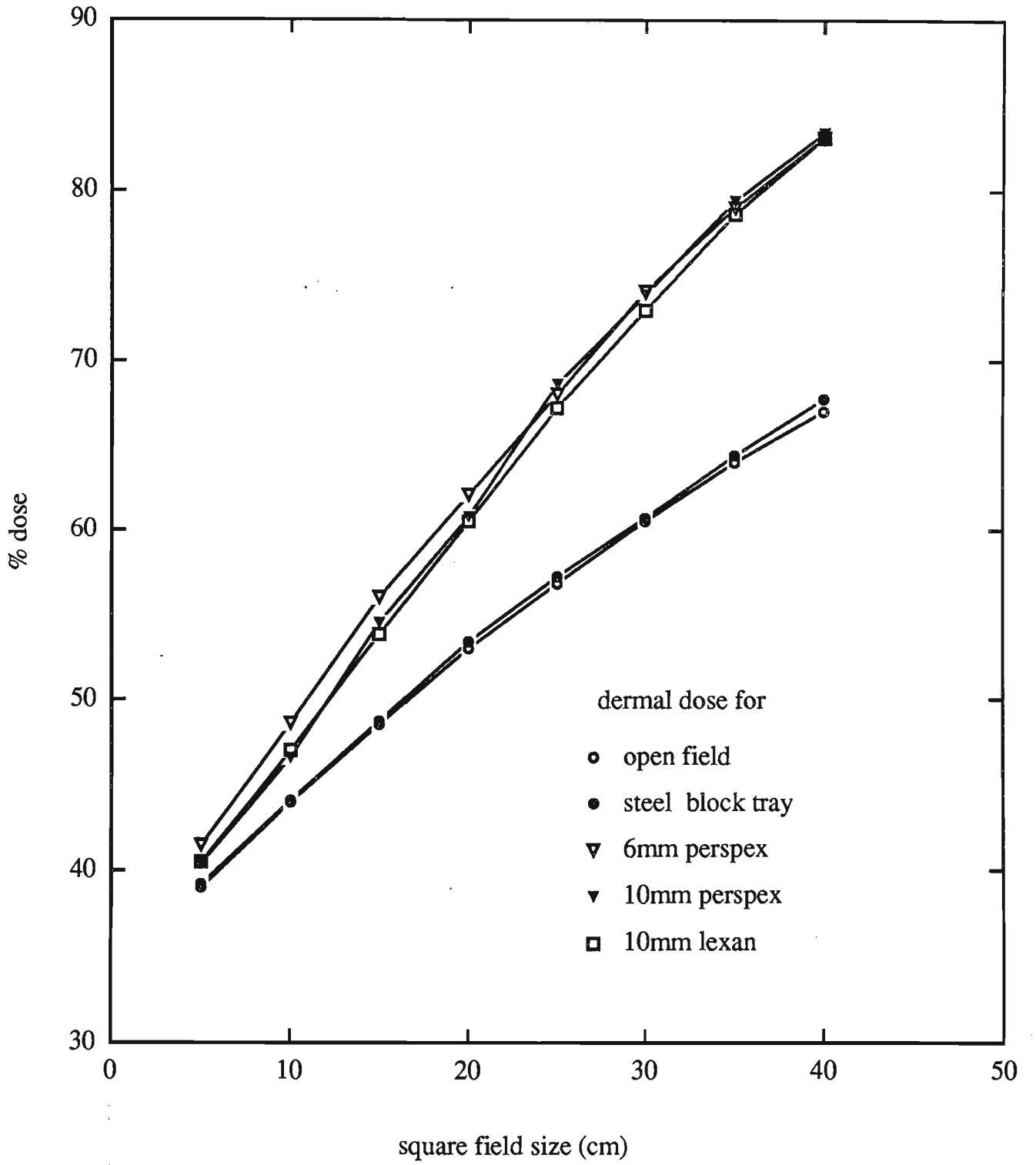

Figure 3.5 : Increases in dose are seen at 1mm depth which is in the dermal region with field size and the use of block trays. Increases from 40% at 5cm x 5cm field size up to 85% at 40cm x 40cm field size with a 10mm perspex block tray are seen.

Block trays absorb and produce electron contamination when exposed to x-ray radiation. Electron contamination produced within the head must pass through the block tray before reaching and interacting with the phantom. Low energy electrons will be absorbed and higher energy electrons will be attenuated to varying degrees. Electrons are also produced and scattered towards the phantom by the interactions of the x-rays. Changes in percentage dose build up due to the block tray were obtained by subtracting experimental open field results from the respective block tray results. Differences seen are due to the introduction of the beam modifying device.

Figure 3.6 shows the additional dose produced by the 6mm perspex block tray and the steel honeycomb tray at 10cm x 10cm and 30cm x 30cm field sizes. Results show an increase in contamination in the build up region from the introduction of the perspex block trays however a negligible effect was seen with the steel honeycomb tray. The steel honeycomb block tray has virtually no effect on the percentage dose in the build up region due to its open design with 85% of its surface area being open. The steel with a relatively high atomic number also acts to some degree as an electron filter with no measurable increase in electron production compared to its absorption. The perspex tray due to its low atomic number however produces a spectrum of electrons which deposit their dose at various depths. Comparison of the shape of the curves as field size changes give some indication of the homogeneity of electron energies produced and absorbed as field size increases. The shape is consistent with a peak somewhere between 0mm and 2 mm (recorded at 1mm) followed by a gradual drop off. The block tray is homogeneous and would produce similar contamination throughout its whole area. Thus the increase seen with field size is comparatively linear with field size increase.

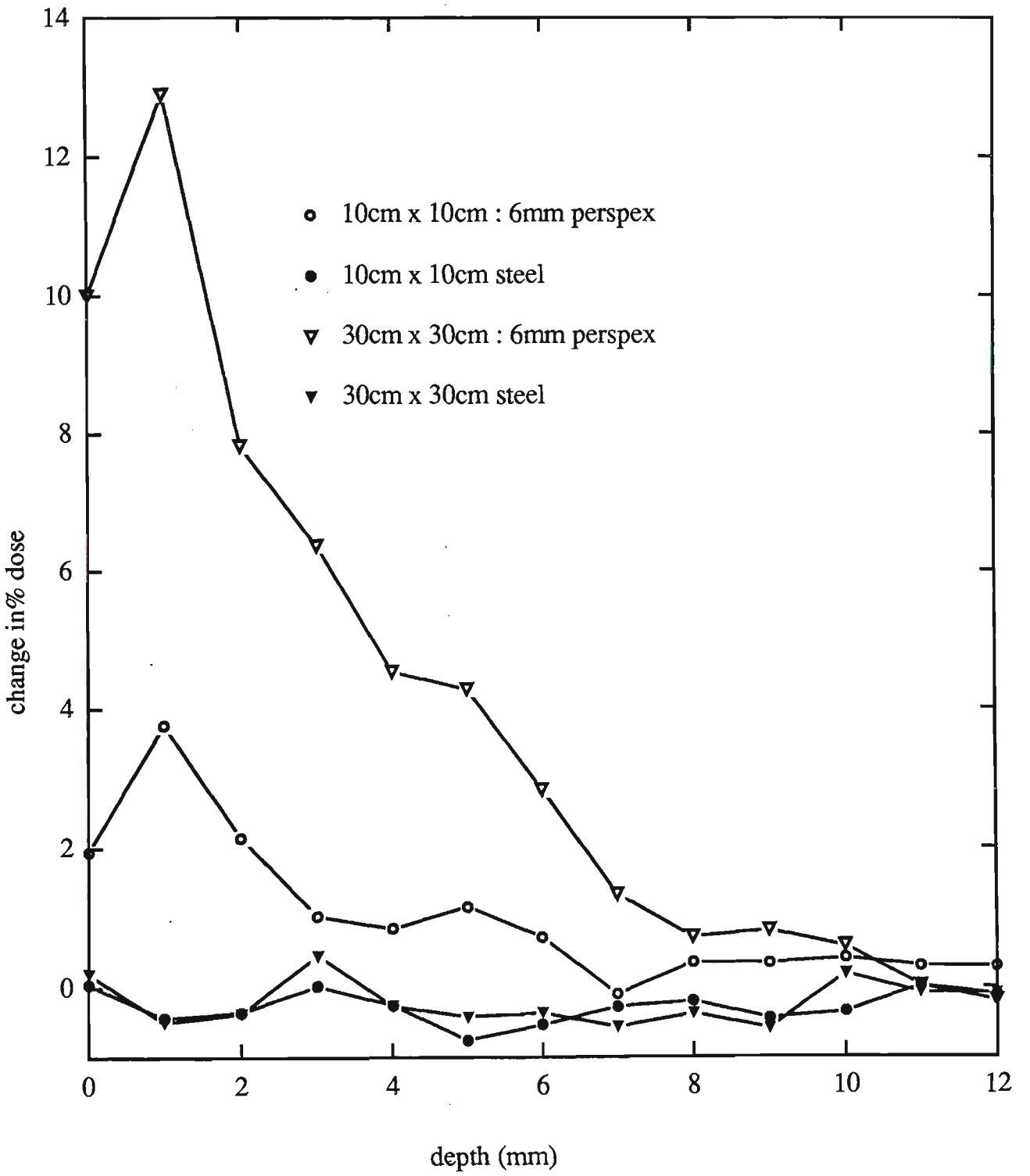

Figure 3.6 : Change in percentage dose seen with the introduction of a 6mm perspex block tray and a steel honeycomb tray in the build up region. Maximum change in build up dose is seen at 1mm depth.

Another commonly used beam modifying device is a physical wedge made from steel or lead. This is designed to skew the isodose curves of an x-ray beam and thus can be used to compensate for a patient's sloping external contour or to compensate for angled wedge pairs. These wedges are constructed from either steel or lead. The effect of placing a 15° wedge in a 6MV beam is shown in figure 3.7. Percentage dose build up curves for the central axis are shown for field sizes of 7cm x 7cm, 14cm x 14cm and 20cm x 20cm. Percentage surface doses were 10.8%, 17.1% and 22.6% respectively showing a decrease in percentage dose from open fields. Similar results are seen for other wedge angles up to 60° which is the largest attainable.

Figure 3.8 demonstrates the change in percentage surface dose across the wedge face for 15°, 30°, 45°, 60° wedges with a 5cm x 5cm field size normalised to 100% at d_{max} on the central axis. These results were measured using the Markus chamber with the Rawlinson correction applied to the results. The Markus chamber was used to increase spatial resolution in the profile. It is recognised that these penumbral results are not corrected due to the finite size of the Markus chamber (Metcalfe et al 97) however a correction was not applied as this was not the primary concern of this report. The predominant effect here is the elimination and production of new electron contamination by the 'secondary' x-rays produced by the wedge.

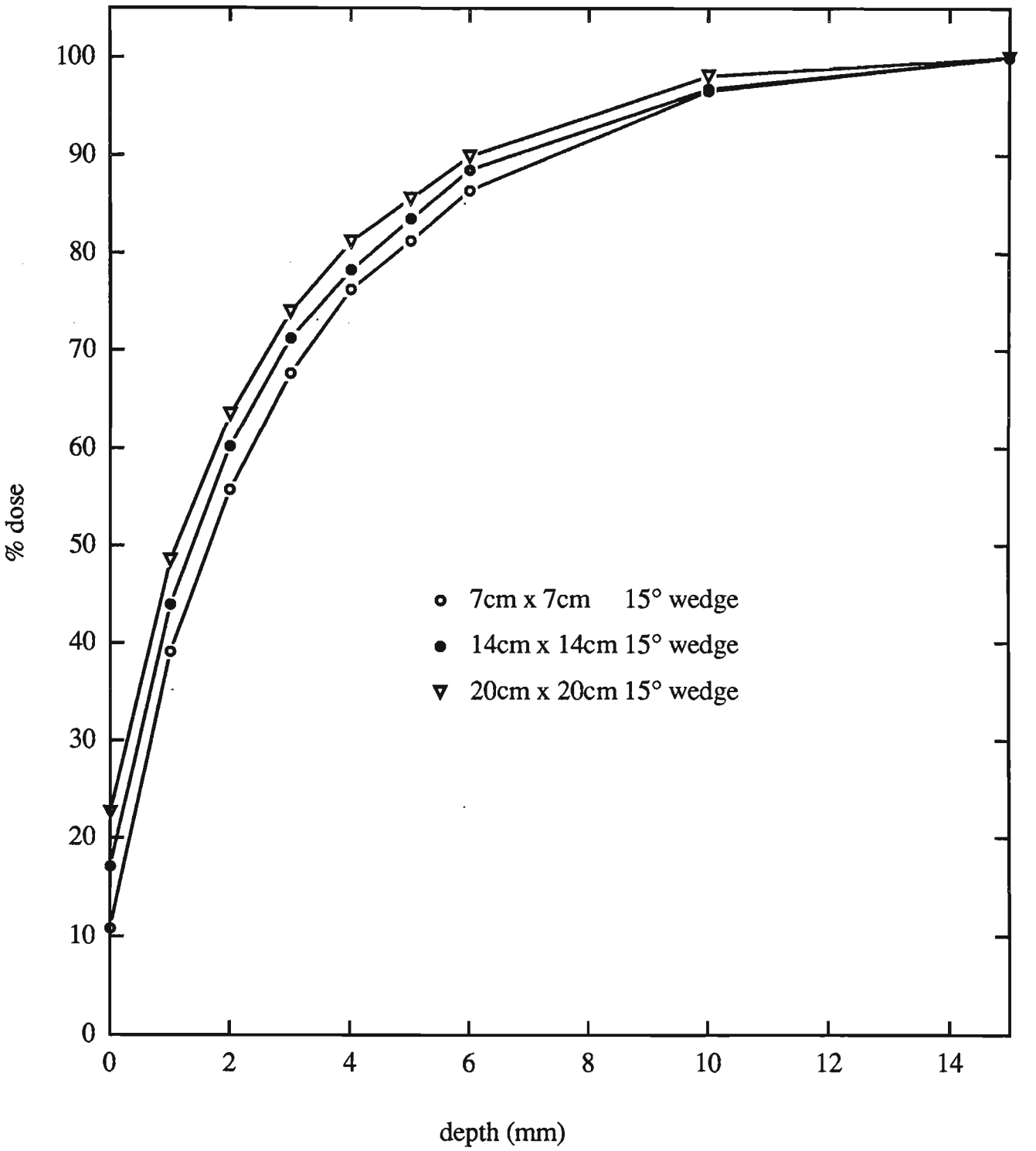

Figure 3.7 : Percentage build up dose with a 15° wedge. The wedge reduces the percentage dose in the build up region by partial removal of electron contamination produced in the treatment head of the accelerator.

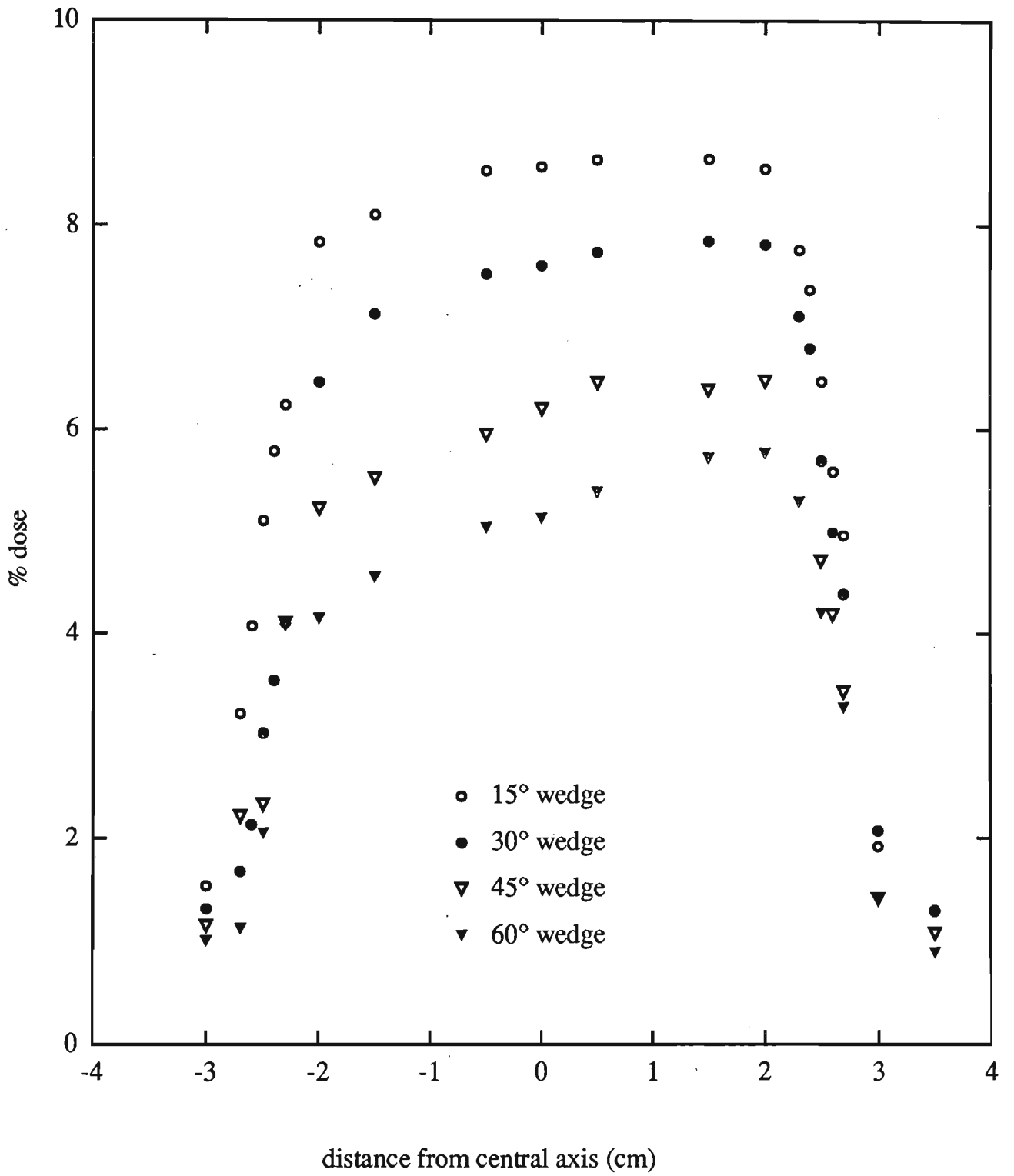

Figure 3.8 : Surface dose profiles across a field for a 15° wedge. Larger percentage surface doses are measured on the thin side of the wedge. (Normalised to 100% at dmax.)

Wedges produce a 'decontamination' effect or effectively reduce the percentage dose in the build up region compared to open fields. Figure 3.9 shows the 'decontamination' percentage dose which is the reductions in percentage dose produced by wedged beams. These were obtained by subtracting experimental open field results from the respective wedge field results. Results show a change in percentage surface dose of -1%, -4% and -4.5% for 7cm x 7cm , 14cm x 14cm and 20cm x 20cm field sizes respectively. As field size increases, a larger proportion of electron contamination is absorbed by the wedge as shown by the increase in decontamination with field size, especially in the region from 0-6mm depth. Results are quoted here only on the central axis but a difference in percentage doses over the profile as the amount of wedged material changes along the incident ray off axis was also observed. There are two possible reasons:

i) the hardening of the x-ray beam where lower energy photons are absorbed increasing the electron range

ii) the wedge absorbs electron contamination produced inside the treatment head

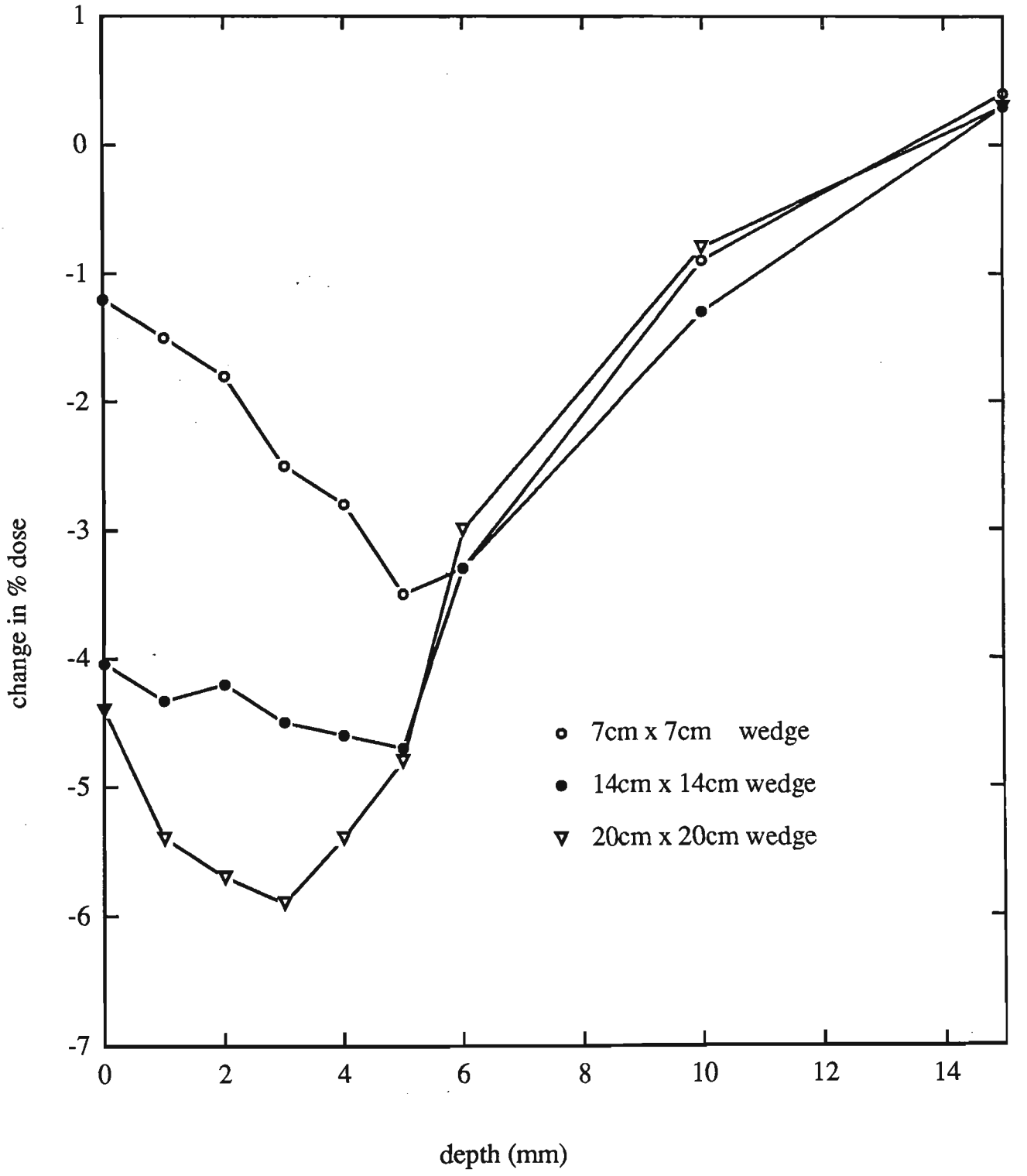

Figure 3.9 : Change in percentage dose seen with the introduction of a 15° wedge in the build up region. Maximum change in build up dose is seen at approximately 2-4mm depth.

3.2 Differentiation of photon in-phantom scatter and electron contamination.

Monte Carlo modelling

Contamination free dose calculations were performed by simulating beams incident on a water phantom using the EGS4 Monte Carlo dose calculation code. A 6MV beam spectrum which had been tested and matched our data in the depth dose region to within 2% at all depths was employed. The spectrum was originally generated from Mohan 1985. Monte Carlo dose calculations were performed on an IBM compatible PC using the EGS4 user code. The extension XYZDOS was utilised where parameters such as beam spectrum, phantom material and voxel size could be defined. Primary and back scatter dose was scored together. Voxel sizes were defined according to field size in each of the simulations, for example, 2cm x 2cm x 0.05cm for a 10cm x 10cm field size. Larger voxels were used for larger field sizes. Results quoted are the percentage doses at depth along a perpendicular line from the central axis at the surface and averaged over the voxel size used. PRESTA was employed and 20 million histories with E-step set at 1%, were scored in each case. Subtraction of Monte Carlo data from experimental data to produce the contamination components was considered reasonable and has been performed previously (Harper et al 91). However as beam data generated from Monte Carlo was to be subtracted from experimental data, careful validation of the results by other purely experimental methods were undertaken.

Figure 3.10 shows the percentage dose build up curves normalized to 100% at d_{max} for Monte Carlo EGS4, contamination free beams at 6MV energy using Mohan's spectrum (1985). Field sizes from 10cm x 10cm to 40cm x 40cm are shown. The position of dmax changes by about 1mm, but this is a low dose gradient and does not affect the normalisation. Voxels in each case were 0.5mm thick and had a surface area of approximately one quarter of the beam size

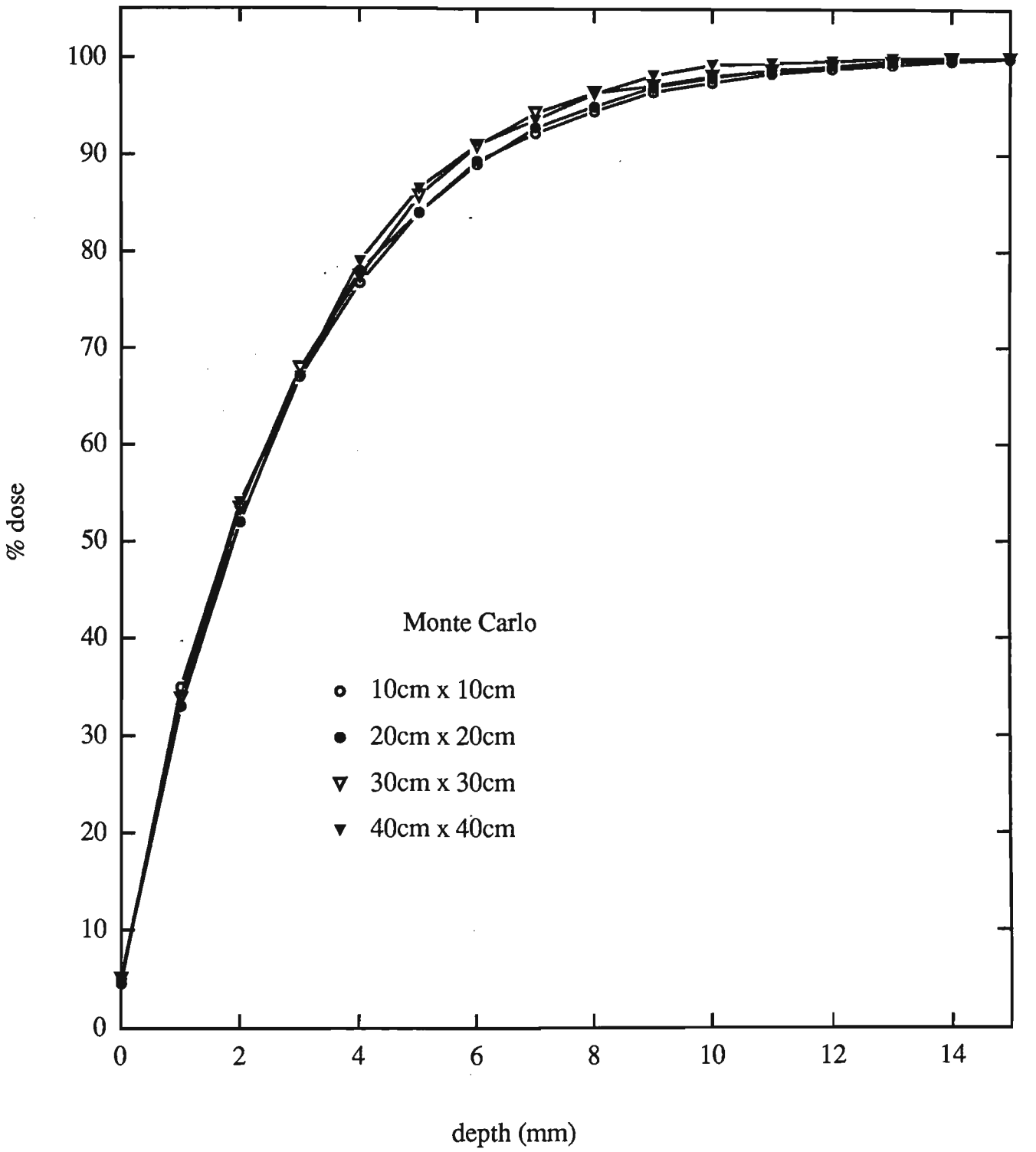

Figure 3.10 : Monte Carlo generated 'pure' photon beams using a 6MV spectrum to match our linear accelerators depth dose. Only small differences were seen in the build up dose as field size was varied from 10cm x 10cm up to 40cm x 40cm.

at central axis. Results show slight differences in percentage dose build up as field size is changed. Surface and near surface doses where comparatively similar for all field sizes. Statistical errors for Monte Carlo simulations where approximately ± 2%.

Figure 3.11 shows the electron contamination dose produced by open fields at various field sizes as derived from Monte Carlo and experimental results. The Monte Carlo in-phantom photon dose build up is subtracted from experimental results at field sizes between 10cm x 10cm and 40cm x 40cm to estimate the level of contamination produced inside the treatment head and the air column. Surface dose contributions normalised to D_{max} for electron contamination range from 11.4% to 37.4% for 10cm x 10cm to 40cm x 40cm field sizes respectively. The electron contamination is produced from x-ray interactions with material in the beams path outside of the phantom. From the surface, a steep reduction in contamination dose is seen to the levels of approximately 8% of D_{max} at 4mm depth. Close coincidence from 4mm to d_{max} for most field sizes is seen. There may be a small amount of dose included in the subtraction due to extra focal scattered photons. The random directional changes set for the incident photons in the Monte Carlo model may account for some but not all of this effect.

Extrapolation methods

TLD methods

Direct verification of electron contamination components was performed using two different methods. Firstly, electron contamination percentage dose was measured with the use of TLD extrapolation. A thin strip of glad wrap was used to suspend the extrapolation TLD's at the central axis of the beam at 100cm SSD to isolate them from any scatter material. Doses were measured within each TLD chip and results were

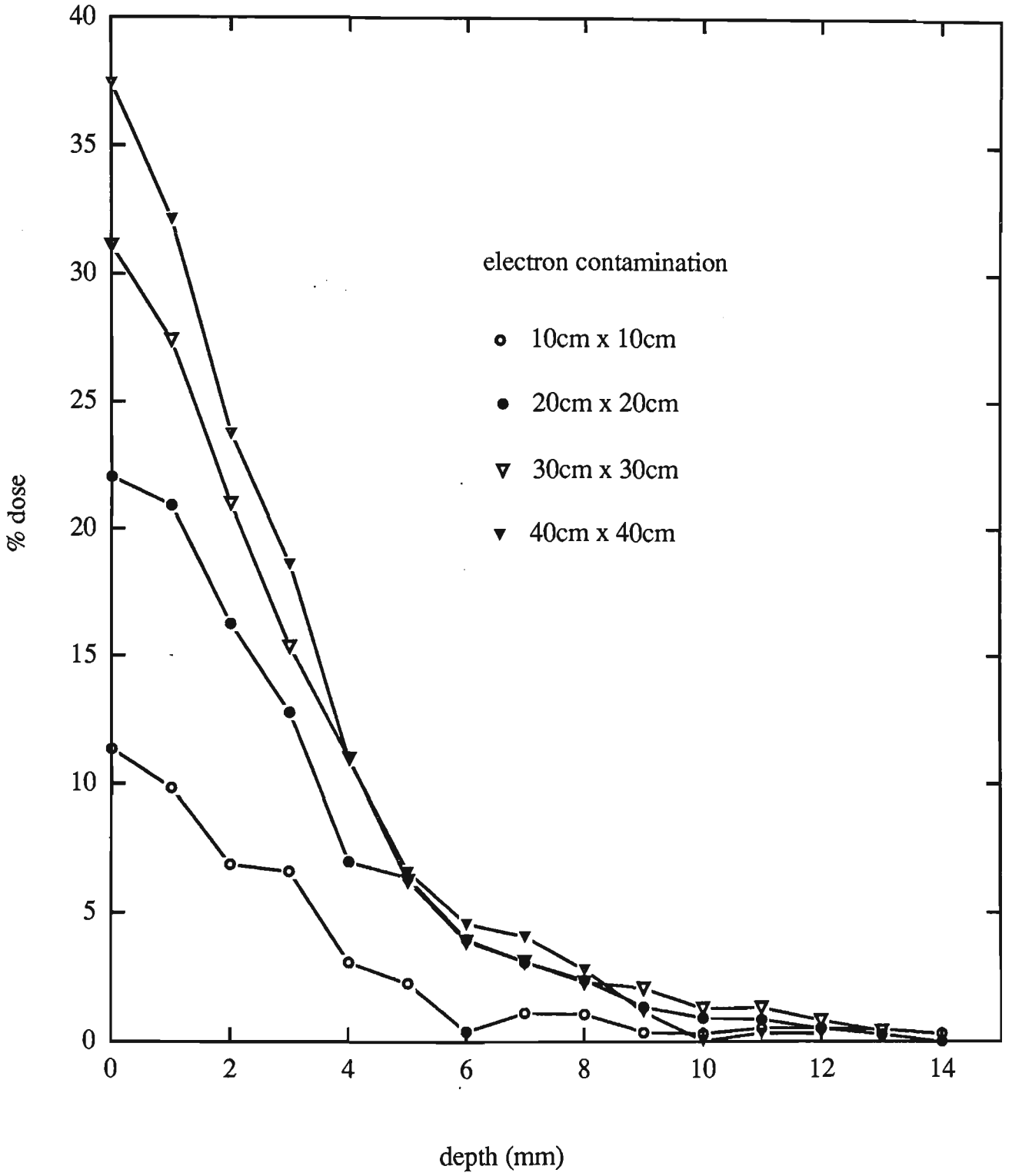

Figure 3.11 : Electron contamination produced by the treatment head and air column for open fields at 6MV energy. The contamination level at the surface constitute the majority of dose deposition.

extrapolated back to zero thickness to eliminate the scatter component produced within each TLD. Results were also measured with various thicknesses of plastic sheets below the TLD to enable extrapolation to zero thickness of supporting material.

Attix chamber

Secondly a comparative measure was used with the Attix chamber suspended in the beam without any other scatter material around it. Charge was measured starting from a small field size which covered the whole chamber. Results at depth were measured by placing pieces of cellulose acetate the same size as the chamber above it. Results at larger field sizes were then compared to the smaller field size results. Increases seen above the small field size results would be almost entirely due to electron contamination minus a small amount from scattered x-rays from outside the phantom and the chamber. However, as the dimension of the chamber remains constant ie. no more scattering medium, the increase due to scatter which occurs should result in a negligible increase in collection.

Figure 3.12 compares the variation in electron contamination measured using Monte Carlo methods and validated by suspended Attix chamber experimental procedures as mentioned above. Results are shown for the extra dose build up produced by increasing the field size from initially 10cm x 10cm, up to 30cm x 30cm and also from 10cm x 10cm up to 40cm x 40cm. Changes in surface dose contamination levels are 20%, 19% and 26%, 25% respectively for field size changes of 10cm x 10cm to 30cm x 30cm and 10cm x 10cm to 40cm x 40cm respectively.

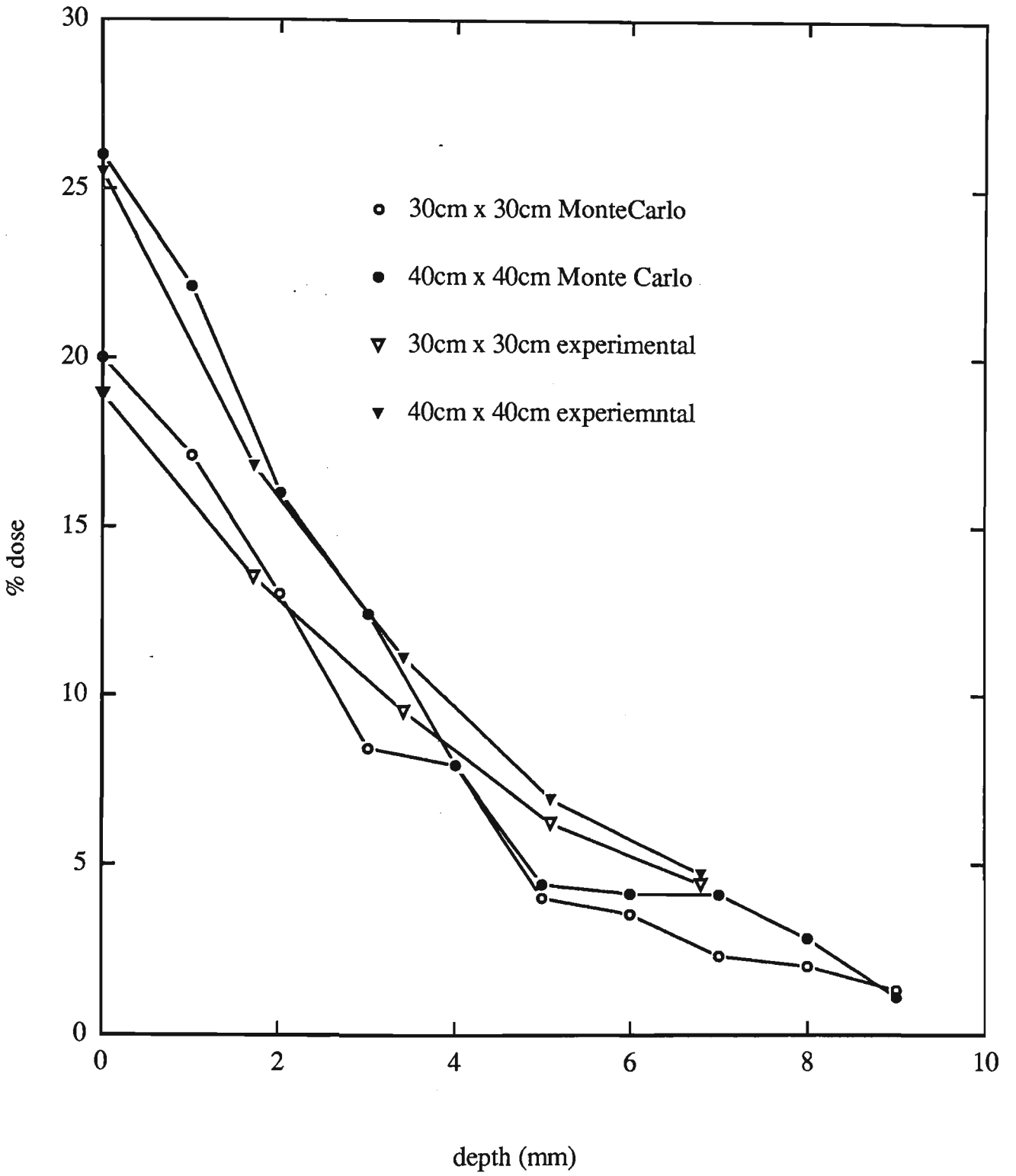

Figure 3.12 : Experimental verification of the electron contamination component of open field photon beams.

Suspended TLD extrapolation at the surface measuring electron contamination produced results of 29% ± 3% and 37% ±3% for 30cm x 30cm and 40cm x 40cm field sizes respectively showing close coincidence with Monte Carlo results. These two results, suspended TLD and chamber methods seem to validate the results obtained by subtraction of Monte Carlo simulated data from experimental data to obtain the electron contamination components.

3.3 Angle of incidence effect

Rationale - As beams often enter the patient at an oblique angle, the surface dose enhancement due to this effect was studied.

Chamber angular response

A detector with a low inherent angular response is required to avoid the chamber response adding to the true angular dose enhancement. The angular dependence of the Attix parallel plate ionisation chamber was tested in a cylindrical solid water slab phantom at a depth of 7.5cm. The chamber was placed at the centre of the cylinder. The beam was rotated through various angles of incidence to the chamber with the distance to the centre of the chamber remaining 7.5cm. Dose variation for the beam normalized to 100% at normal incidence was 2% between 0° and 75°. Corrections were applied for this slight over response. The Attix chamber results were compared to TLD extrapolation for verification and results showed a match within ± 2.5% over all data points collected for both Attix and TLD. Results reported are restricted to angles equal to or less than 75°.

Figure 3.13 shows the way in which results were taken and depth measured. The chamber was continually placed on the central axis of the beam at depth thus the position of the chamber followed the beams central axis as angle was varied. The depth quoted was the perpendicular depth (mm) or the thickness of solid water placed on top of the chamber. Results are quoted as perpendicular depth, instead of radiological depth along the beam ray (ie. $x\sec\theta$), as the former relates to the depth in a patient's skin and subcutaneous tissue. Thus giving a direct comparison to dose at depth in tissue. Results were measured for angles from 0° to 75° incidence. Angle of incidence is defined as the angle subtended by the beam from a normally incident beam perpendicular to the surface.

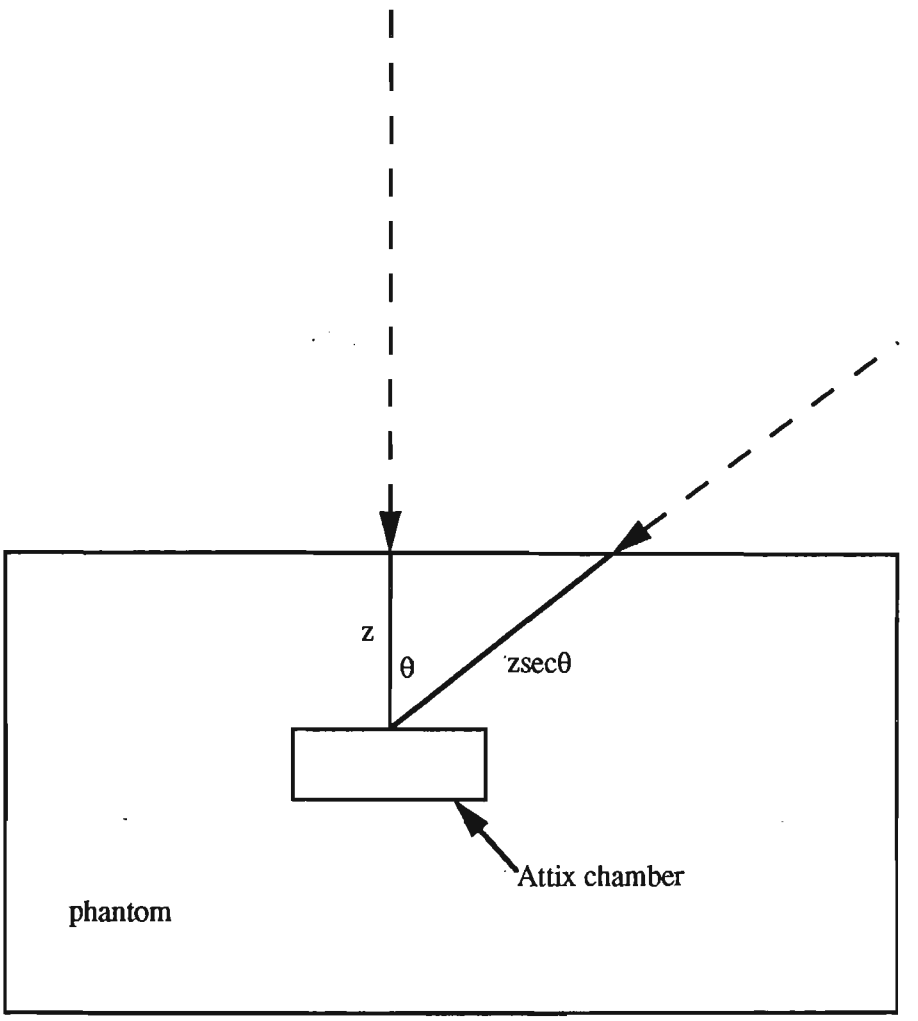

Figure 3.13 : Definition of experimental procedure for measurement of dose at varying beam angle of incidence. The chamber was continually placed on the central axis of the beam whilst depth was quoted as the perpendicular depth to the chamber.

Dose versus angle with energy

The majority of dose deposited on the patients skin is due to electron contamination at normal incidence from therapeutic radiotherapy (Biggs et al 1983, 1979, Fiorino et al 1992). At depth, the balance tips back towards phantom scatter, with this component eventually becoming the predominant dose depositor. At oblique incidence, the percentage dose results show a similar scenario but the in-phantom photon component at the surface and near surface increases due to the Compton scattering of tissue electrons. Figure 3.14 shows dose versus angle at the surface for different energies ranging from Cobalt-60 up to 18MV x-rays. Results are normalised to 100% at the surface for a 0° incident beam.

Results show that the angle of incidence effect decreases with increasing energy. This can be explained if the Klein-Nishina scattering theory is applied to Compton interactions. This theory predicts an increase in forward scattered photons with an increase in energy. Thus a greater percentage of photons would be forward scattered in higher energy beams. Hence, when a high energy beam is incident at an angle there is less probability that a side scattered photon will make its way back to the surface to create an electron to deposit dose. This in turn inhibits the increase in dose with beam angle for higher energy beams. Conversely at lower energies such as Cobalt-60 the production of side scattered photons is greater. This acts to increase the dose with an increase in incident beam angle.

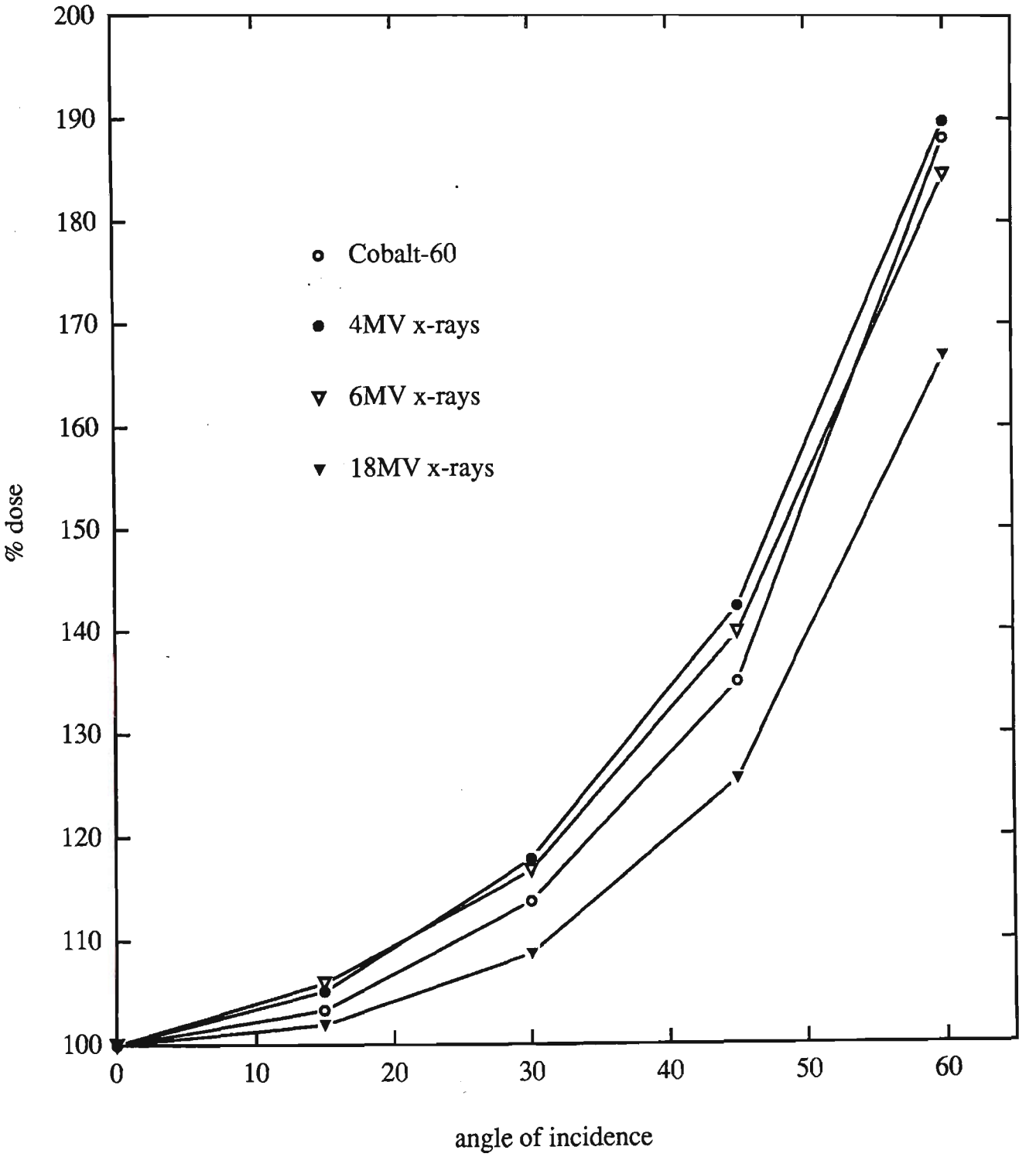

Figure 3.14 : Incident angle effect for various photon beam energies. With all energies, the percentage surface dose increases with incident beam angle.

Dose versus angle with field size

Figure 3.15 shows dose versus angle at the surface as measured by the Attix chamber in a solid water slab phantom for a 6MV x-ray beam with varying field sizes from 5cm x 5cm to 40cm x 40cm. Results are normalised to 100% at the surface for 0° incidence. The angular response on the Attix chamber at the surface here is assumed to be negligible. At the surface, the relative proportions of electron contamination, secondary photons and electrons are different to that of a depth of 7.5cm. However, the Attix chambers negligible front window thickness and solid water design, we feel makes it the most adequate detector for these measurements. Results show a non linear increase in dose with angle where the percentage dose increases more dramatically with larger angles. As field size increases, surface dose increases mainly due to the increase in electron contamination produced by more of the Flattening filter, ionisation chambers, collimators and air column being in the x-ray beam (Johns and Cunningham 1983, Khan 1984). Percentage surface dose for a 10cm x 10cm field size on a 6MV Clinac is 16% of D_{max} whereas for a 40cm x 40cm field size this increased to 42% of D_{max}. Dose at angle increased at every field size. Percentage dose (relative to 100% , 0° incidence) of 280% was seen for 10cm x 10cm field size at 75° whilst for 40cm x 40cm percentage dose of 157% was recorded at 75°.

The percentage dose increases for 10cm x 10cm, 20cm x 20cm, 30cm x 30cm and 40cm x 40cm fields relative to their own D_{max} values at the surface for 60° angle of incidence were 13.4%, 14.4%, 14.4% and 14.3% respectively giving a relatively constant increase in percentage dose independent of field size. Initial surface doses for normally incident beams ranged from 16% to 42% of D_{max} or 10cm x 10cm to 40cm x 40cm fields. Thus showing the larger proportional percentage increase at small field sizes where the angular effect becomes more substantial.

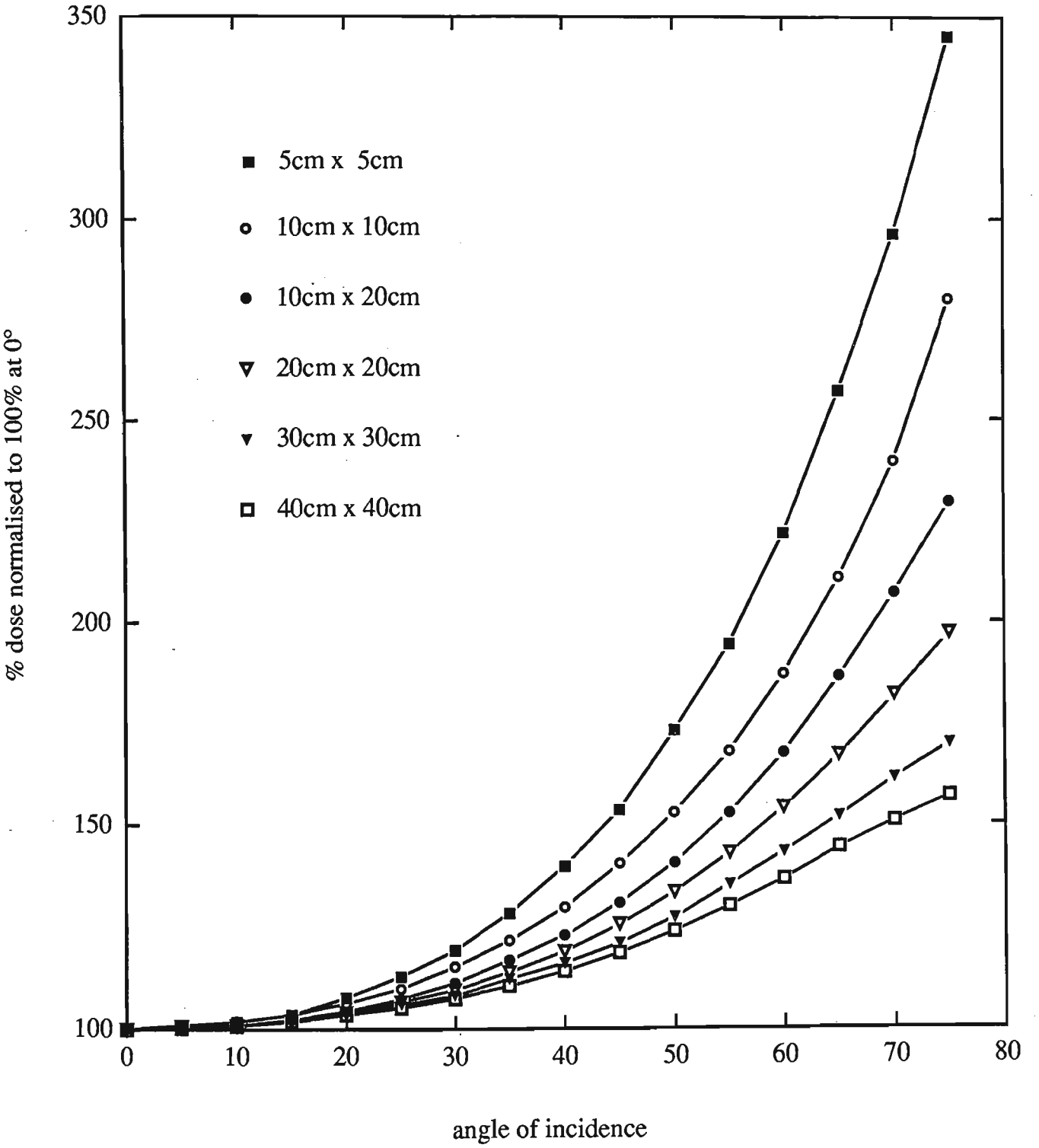

Figure 3.15 : Incident angle effect on surface dose for 6MV photons at various field sizes. Smaller fields produce a larger percentage increase in surface dose at oblique angles.

Dose versus angle with depth

Figure 3.16 shows the angular response at different depths in solid water and with overlying cellulose acetate and ORFIT head cast material. Data was measured with the Attix chamber in a 6MV x-ray 10cm x 10cm field size. Shown are results for surface, 1mm and 5mm solid water plus 2.3mm effective depth in cellulose acetate and 3mm ORFIT head cast materials. Normalised to 100% at 0° incidence, percentage dose results at 60° incidence are 185% at surface, 147% at 1mm, 112% at 5mm and 132%, 141% under Cellulose acetate and ORFIT head cast material respectively. The resultant percentage increase in dose at depth is much less substantial than at the surface. This is important to note for head cast material and the treatment of head/neck patients. In this region, large oblique angles exist on the patients surface due to the extreme curvature and shape of the patients head and neck. All angles between 0° and 90° would be seen. The patients skin dose will already be higher due to the 2.3mm of overlaying head cast material above them but there is not as substantial a percentage increase in dose due to the angular effect at this depth as at the surface.

Figure 3.17 shows the percentage depth dose build up curves for a 6MV beam at 100cm SSD 10cm x 10cm field size as angle is varied. Results are normalised to 100% at D_{max}. Results show an increase in percentage dose at the surface and in the dose build up region as angle is increased, note also a reduced depth of D_{max}. Percentage doses normalised to D_{max} at the surface for angles ranging from 0° to 60° were 16% to 29% respectively. This shows an almost doubling in percentage surface dose from 0° to 60° angle of incidence. Over this range of angles the position of D_{max} moved closer to the surface by 4mm from 14mm to 10mm. Figure 3.18 shows similar results as in figure 3.17 but for a 40cm x 40cm field size. Surface doses at angles ranging from 0° to 60° were 42% to 57% of D_{max} respectively. The position of D_{max} was reduced by 3mm from 12mm to 9mm at this field size.

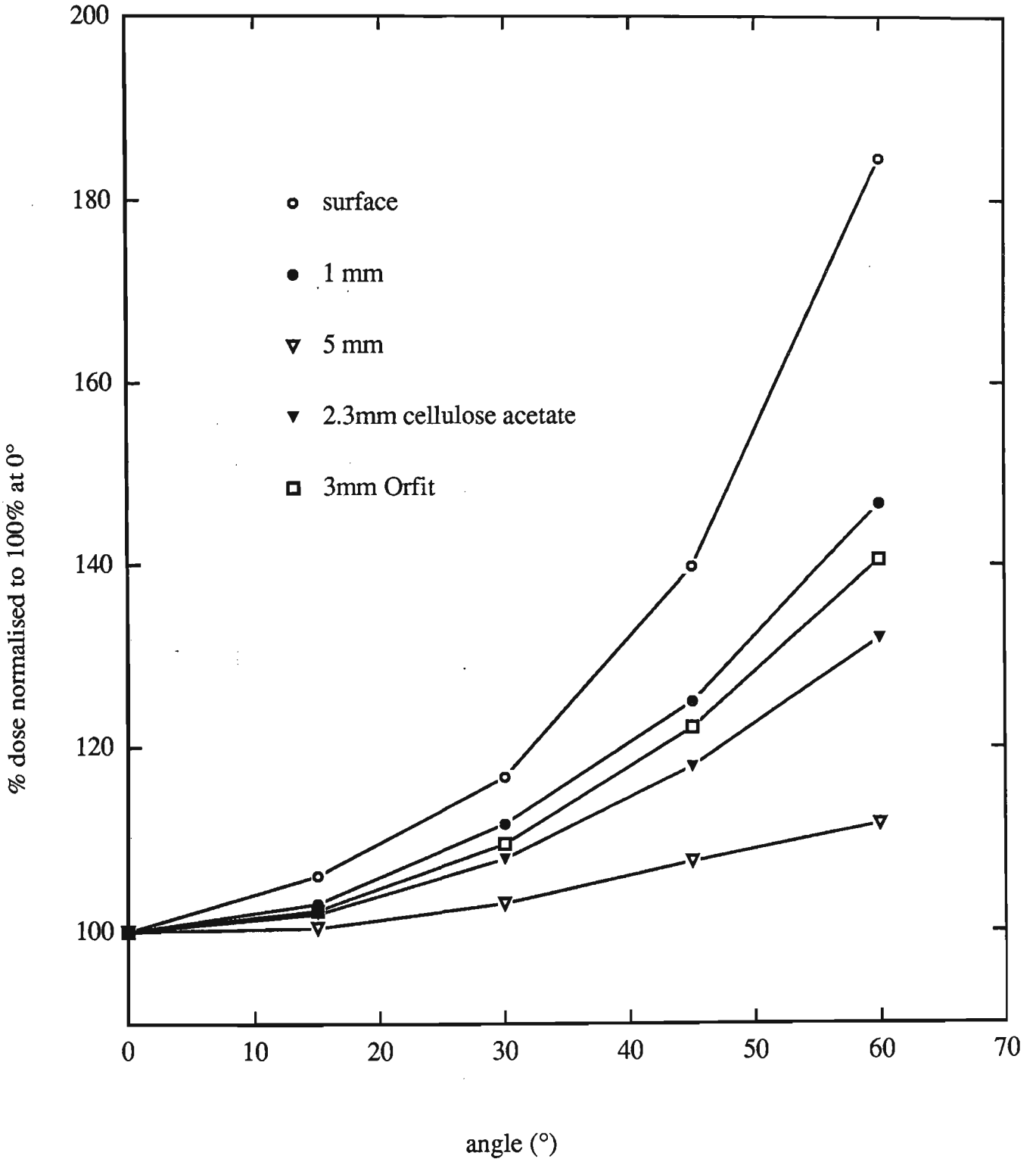

Figure 3.16 : Incident angle effect on dose at various depths for a 10cm x 10cm field size, 6MV photons. The percentage dose increases to a lesser extent at depth.

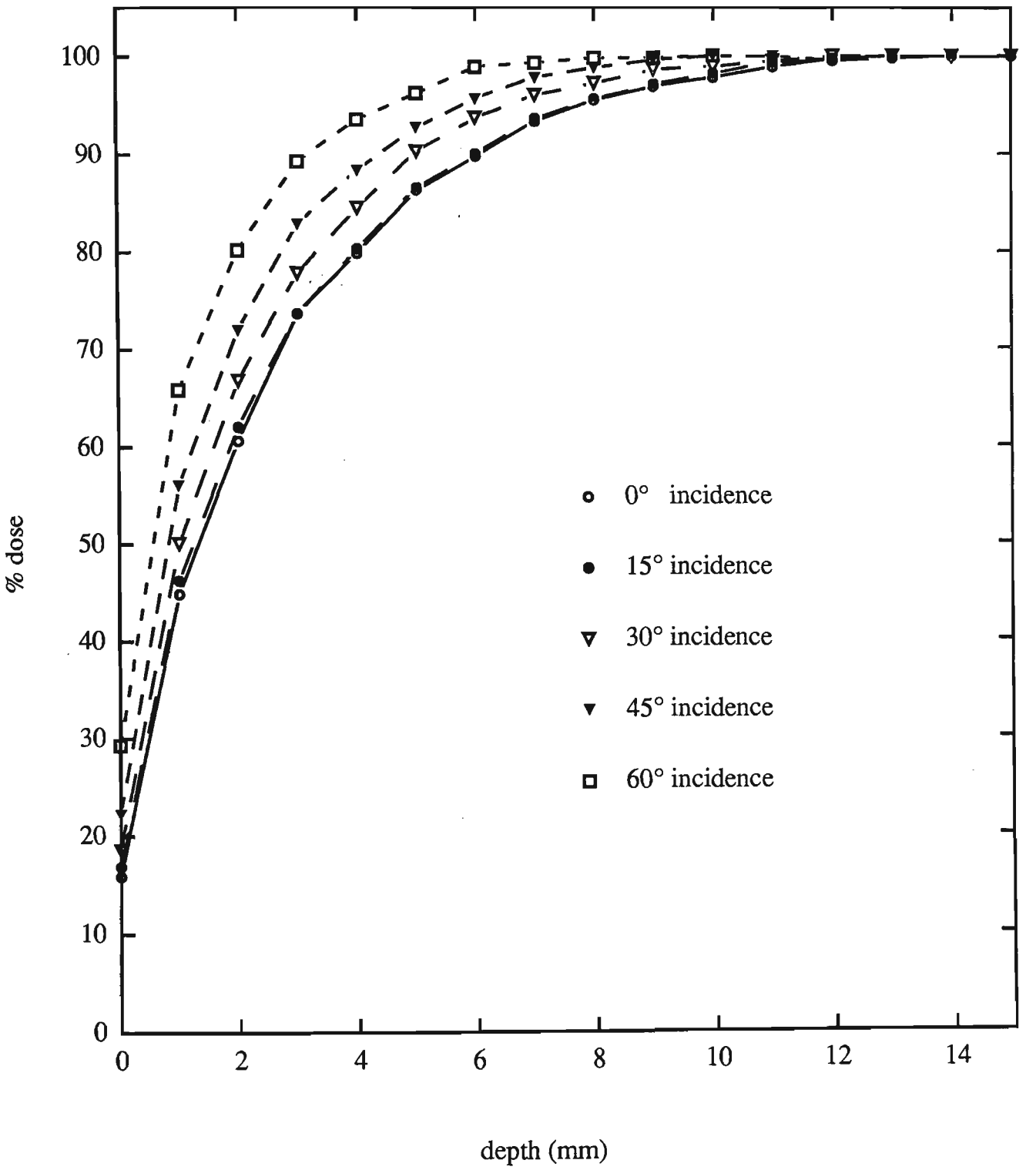

Figure 3.17 : Percentage dose build up for 6MV photons at 10cm x 10cm field size at various incident angles. Dose in the entire build up region increases with increasing angle of incidence.

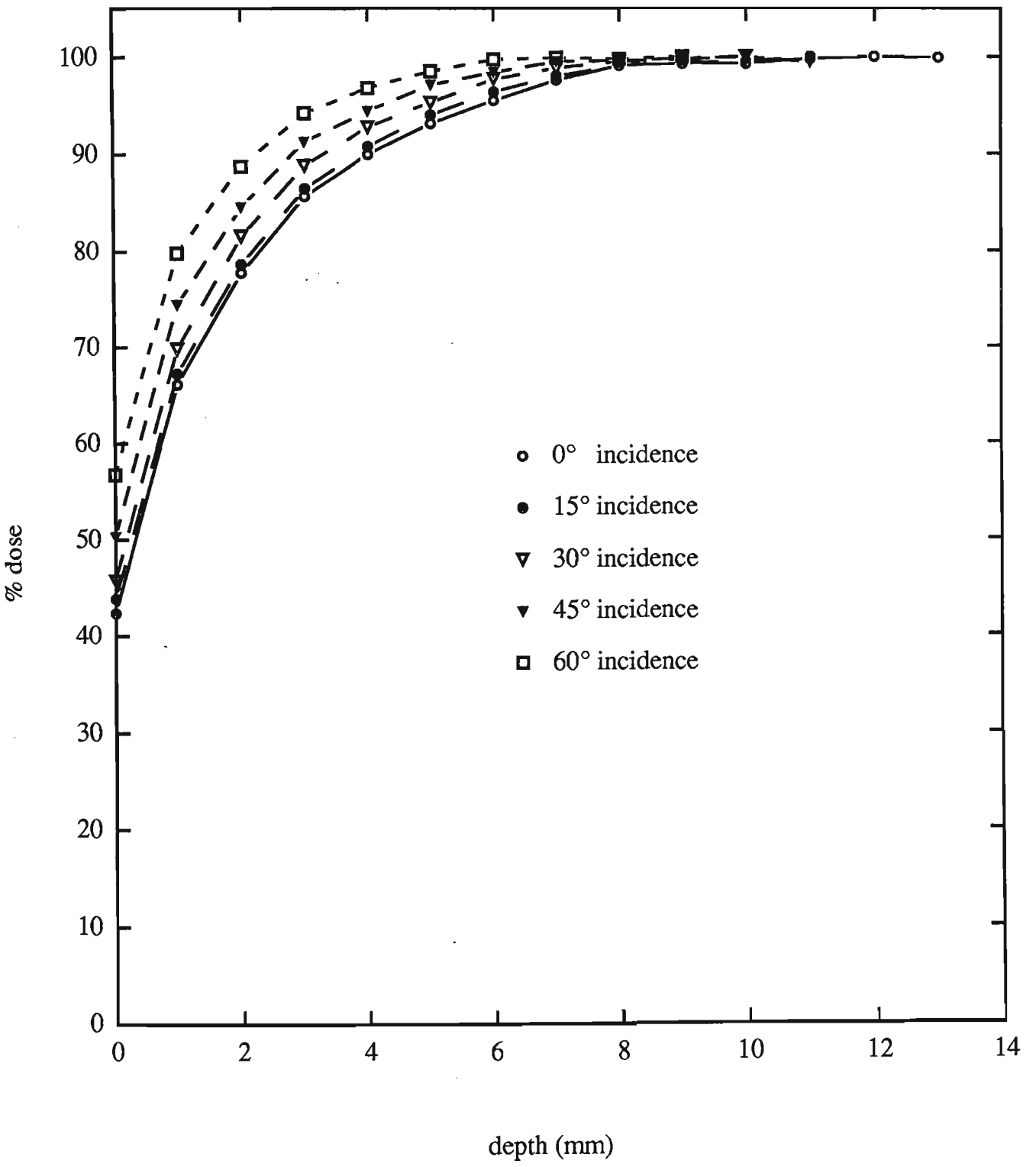

Figure 3.18 : Percentage dose build up for 6MV photons at 40cm x 40cm field size at various incident angles. Dose in the entire build up region increases with increasing angle of incidence.

By subtracting the percentage dose build up curve for a 0° angle of incidence beam from the oblique incidence beam the percentage dose build up increase due to angle of incidence is obtained. This is given in figure 3.19 for 6MV x-ray beams at oblique incidence for a 10cm x 10cm field size. The results show an increase in percentage difference from the surface to 1-2mm then a decrease up to approximately 12mm where the results align. Percentage dose differences at the surface ranging from 15° to 60 were 1% to 13.5% respectively. Figure 3.20 shows the differences at 40cm x 40cm field size. The results show a decrease from surface to a depth of approximately 10mm where the results align. Percentage differences in surface dose for angle ranging from 15° to 60 were 1.5% to 14.5%. These percentage differences at the surface are relatively field size independent but at depth differences vary with field size. The relative independence of field size on the angle of incidence effect points towards the negligible influence of electron contamination produced outside the phantom. To ascertain the validity of this assertion, Monte Carlo simulations of obliquely incident beams were performed. An x-ray beam with initial spectrum as described by Mohan et al (1985) was simulated to model a pure beam with no electron contamination at various angles of incidence.

Figure 3.21 shows the percentage dose build up for Monte Carlo simulations of a 10cm x 10cm field of 6MV x-rays were set incident with an angle of 0° and 45° respectively. The curves only represent photon in-phantom dose, ie. defined here as a pure beam where a pure beam has no contamination component produced outside the phantom. Dose due to primary and back scatter photons are combined to give results shown. Results show an increase in percentage dose in the build up region as angle of incidence is increased. Surface dose for the 0° beam was 4.5% whilst for the 45° beam it was 11%.

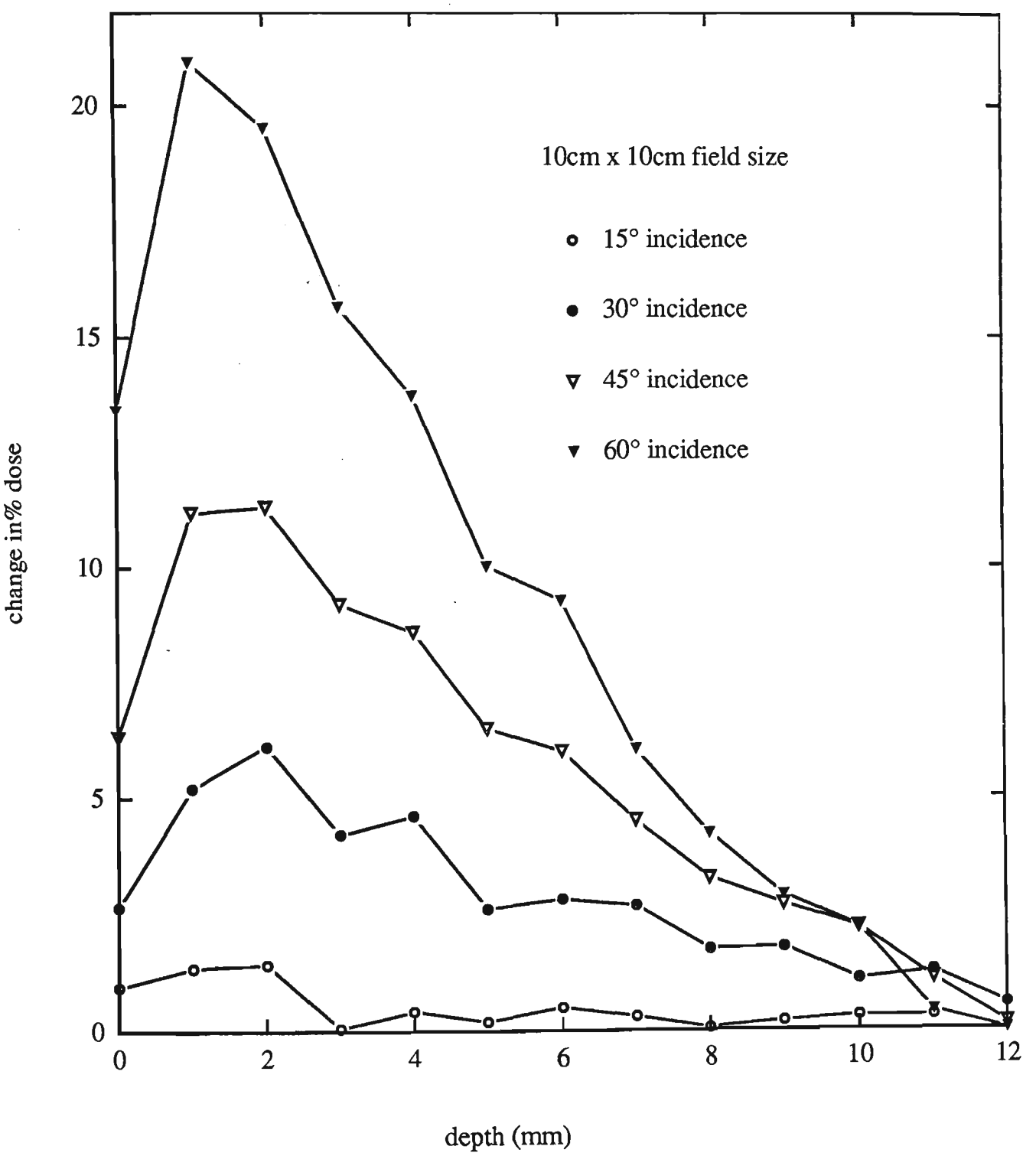

Figure 3.19 : Change in percentage dose in the build up region at 10cm x 10cm field size associated with the change in angle of incidence.

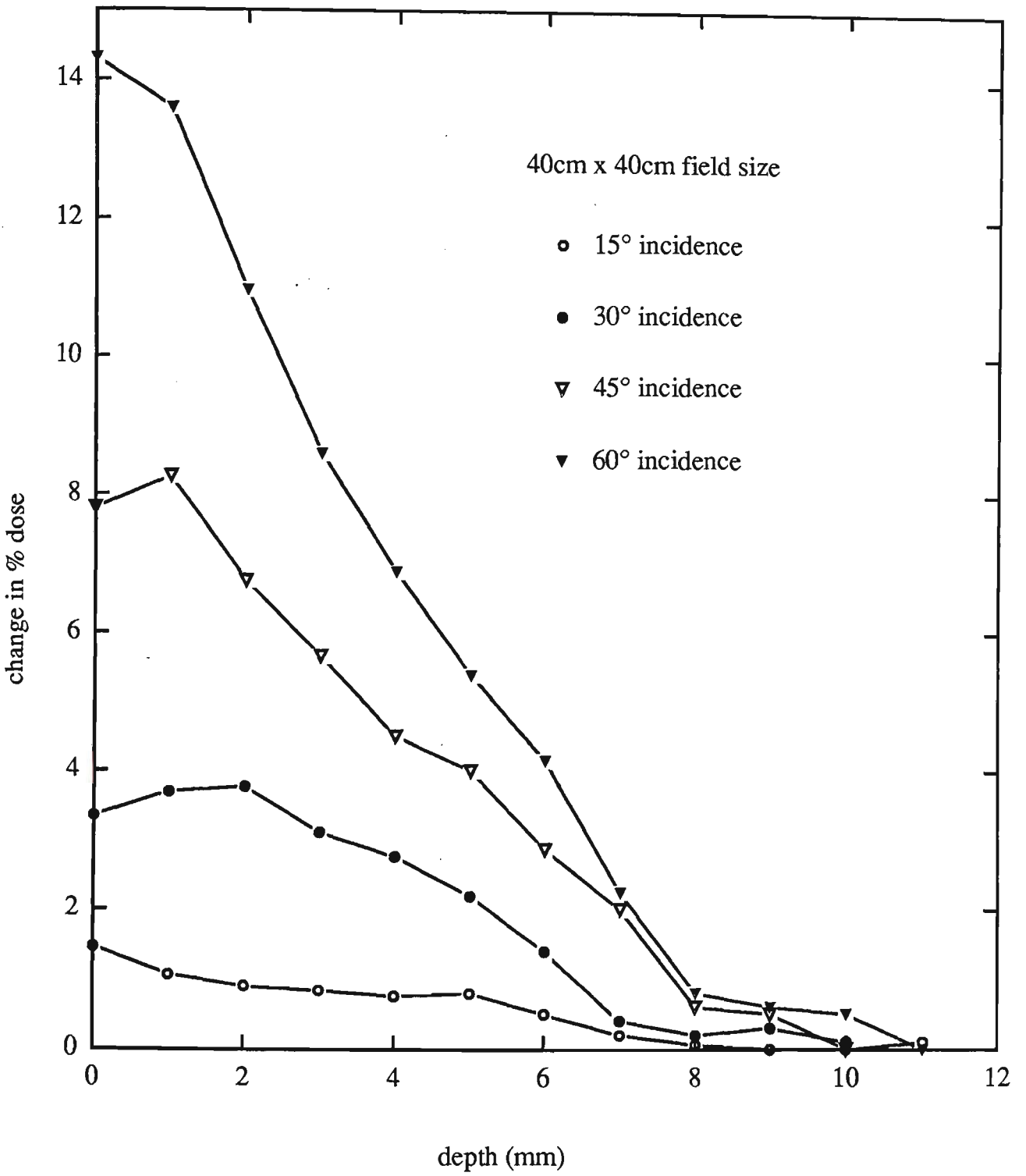

Figure 3.20 : Change in percentage dose in the build up region at 40cm x 40cm field size associated with the change in angle of incidence.

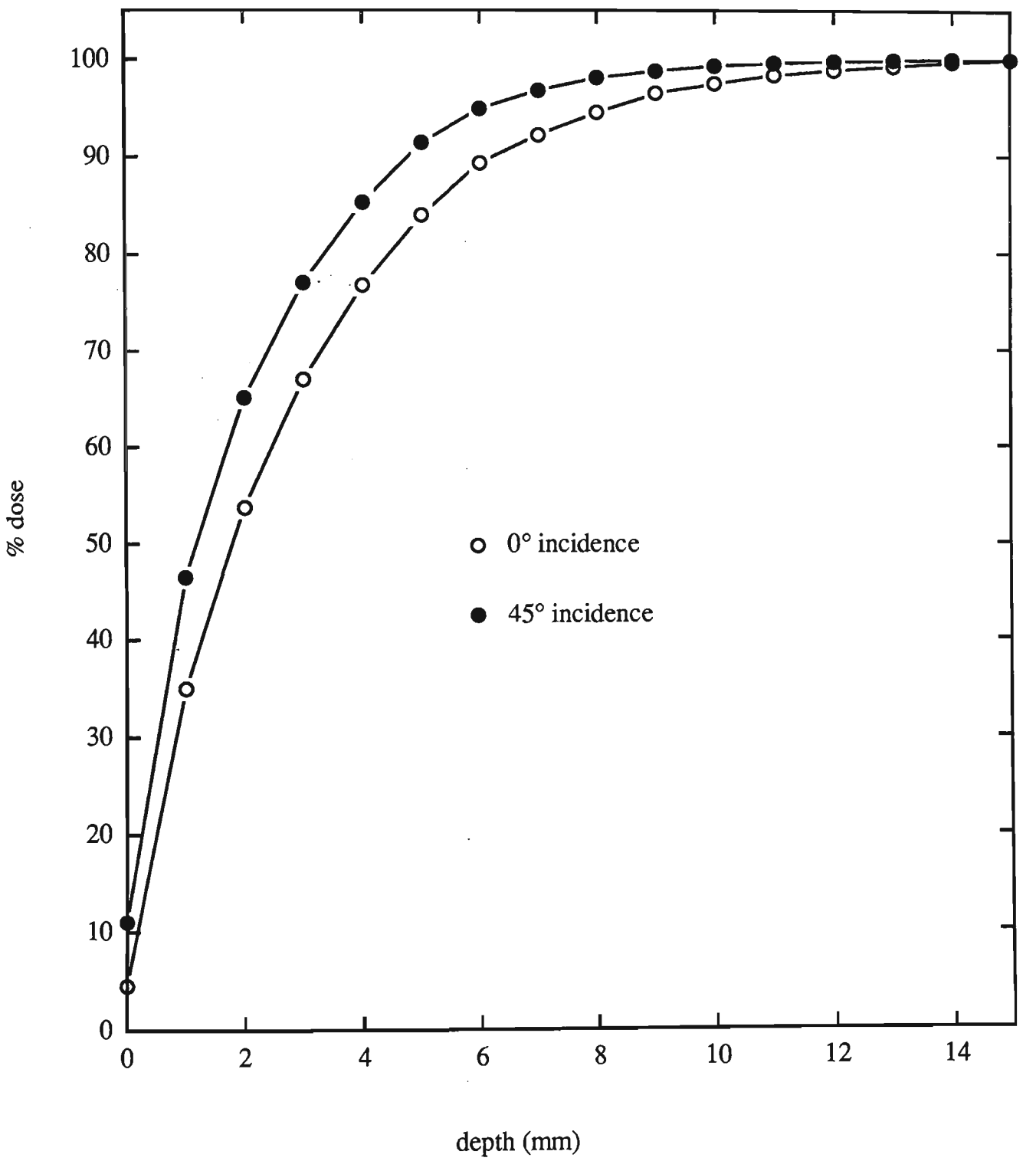

Figure 3.21 : Monte Carlo simulations of dose build up for a 6MV photon beam at 0° and 45° angle of incidence at 10cm x 10cm field size.

Figure 3.22 shows a comparison of the percentage dose differences between the Monte Carlo results and the experimental results at 0° and 45°. This was achieved by the subtraction of the 0° incident percentage dose build up from the 45° build up to produce the two curves shown. When the 0° percentage depth dose results were subtracted from the 45° results a close match was found to experimental results using the same parameters. This indicated that the increase in percentage dose in the build up region was mainly caused by electrons set in motion by in-phantom photon scatter effects and that electron contamination did not contribute significantly. Suggested reasons for this are as follows

i) the electron contamination component peaks at the surface and decreases in its contribution at depth due to absorption by the tissue. For a 10cm x 10cm field size the contribution to percentage dose is approximated 10% and falls to 2% at 5mm depth. This 2% is only a small fraction of dose deposited there and thus not effectively seen in results as compared to the change in dose due to in-phantom scatter effects.

ii) due to the dose deposition path of low energy electrons, the initial angle of incidence of the electron contamination is so broad and varied that it does not play a major role in altering dose with change in incident angle.

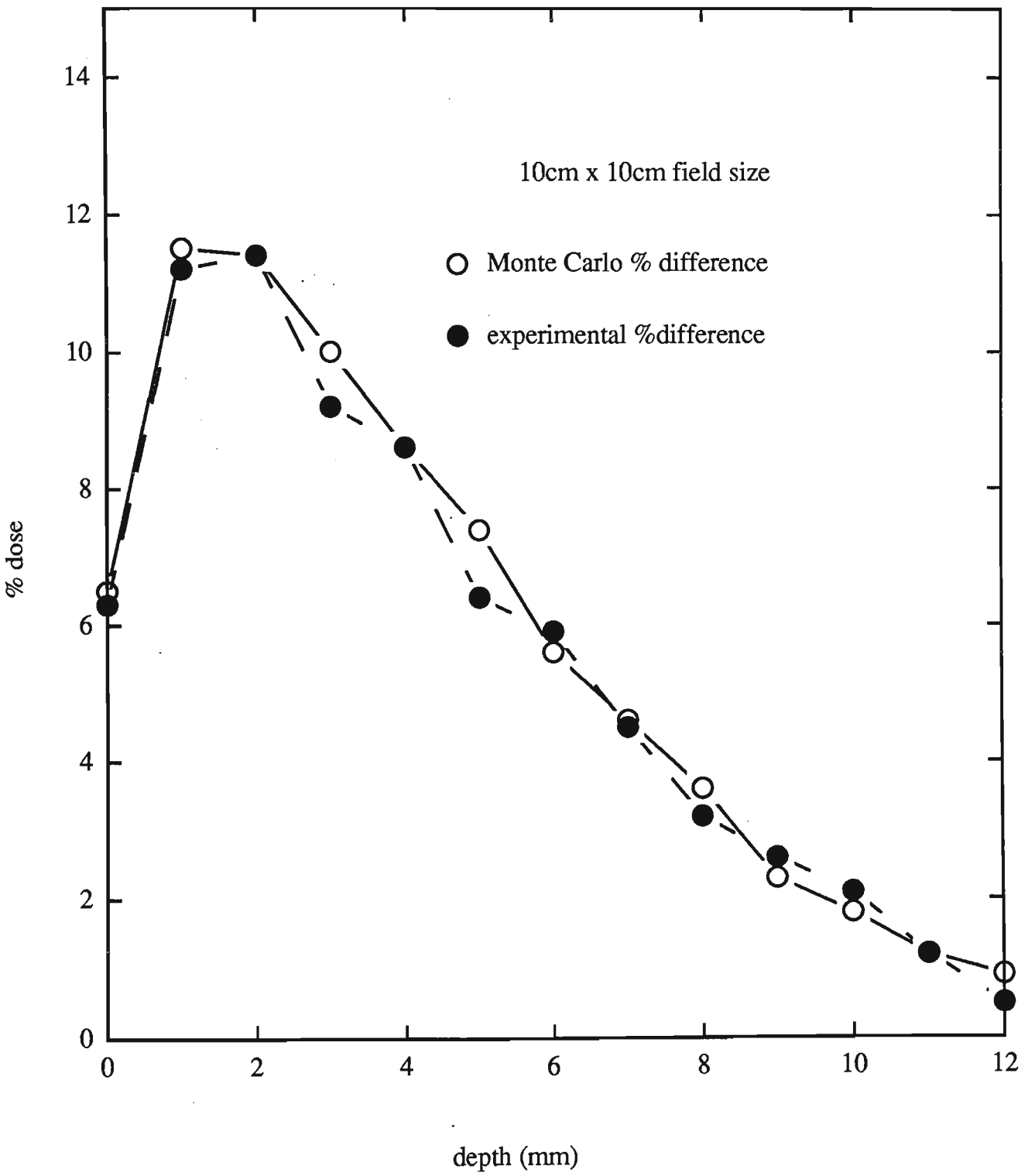

Figure 3.22 : Percentage dose differences measured between 0° and 45° angle of incidence, experimentally and with Monte Carlo generated results at 10cm x 10cm field size.

3.4 Source surface distance (SSD)

Radiotherapy treatments are not always performed at 100cm SSD. Isocentric treatments are often used. Isocentric treatments usually consist of several fields matched to a fixed centre of rotation (isocentre). Usually this point is located within the patient. Due to overlaying tissue this means the SSD may be typically less than 100cm eg. 80cm if there is 20cm of tissue between the isocentre and the patients skin surface.

Sometimes extended SSD treatments are used. These produce a larger field size than physically possible at 100cm SSD. Experiments have been performed to ascertain the SSD dependence of build up dose with variations in parameters such as field size and with the use of block trays. SSD's ranging from 80cm up to 120cm have been studied.

Figure 3.23 shows build up dose for a 10cm x 10cm field size (at the isocentric position) with varying SSD from 80cm up to 120cm. Only a slight difference is seen in all dose build up curves with the largest differences being near the surface which is approximately 2% when all beams are normalized to 100% at their respective D_{max} values. This is shown in figure 3.24. This result is similar in magnitude for all field sizes up to 40cm x 40cm for open fields. The fact that field size is quoted at the isocentre (ie. collimator jaws remain unchanged) would explain the closeness of the build up dose. The area inside the treatment head which produces and allows electron contamination to escape remains constant as the SSD is varied. Electron contamination is mostly produced by the photon interactions within the treatment head and the air column. Head produced electrons may be of relatively high energy (ie. range up to 15mm in water). Thus when these electrons are required to travel 10cm more or 10cm less in air, it will not change their range in the phantom by a sizeable amount. The inverse square law for radiation divergence is not exact for electrons due to the isotropic nature of their production but can be considered as a reasonable approximation for photons.

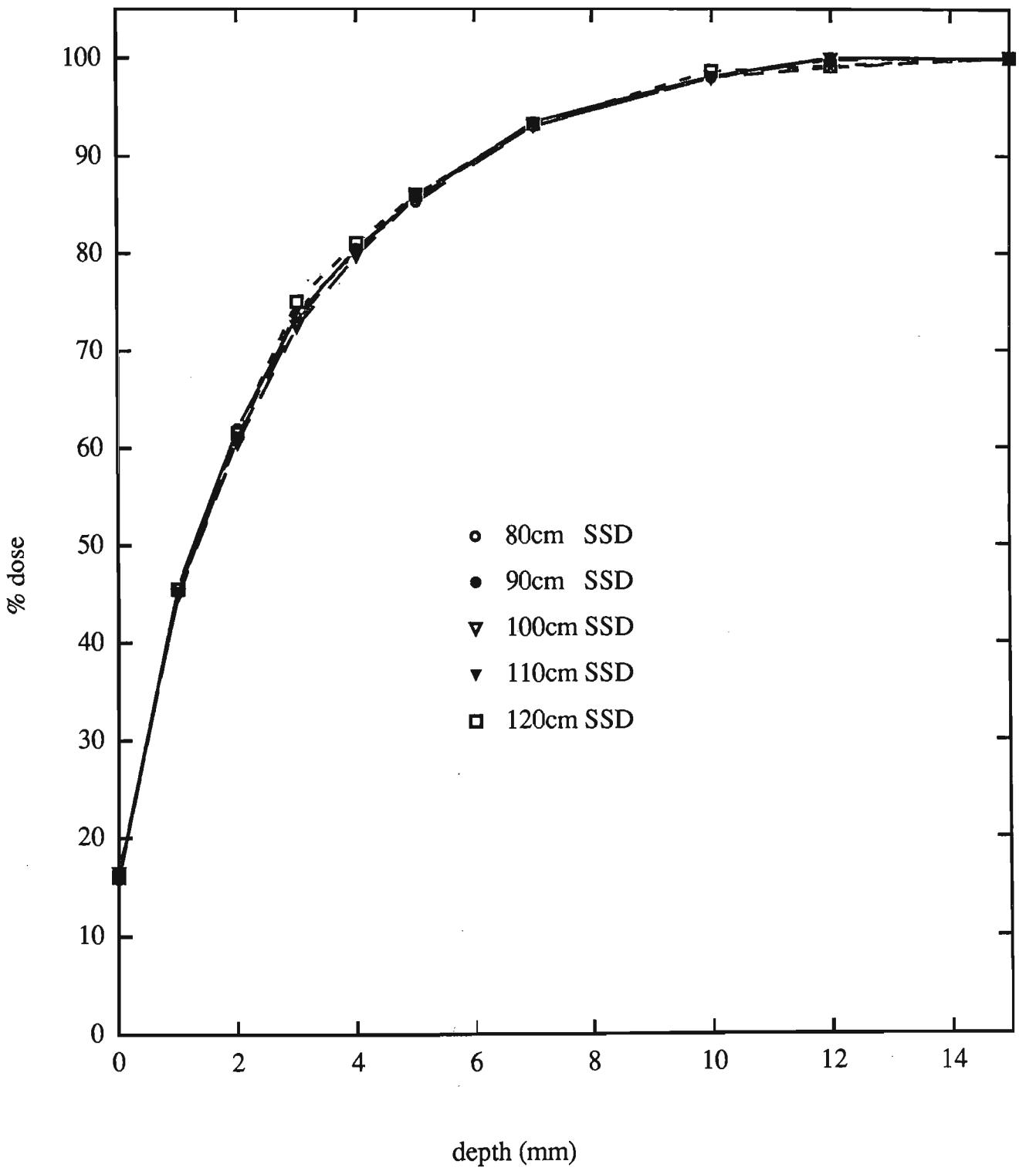

Figure 3.23 : Percentage dose build up for 6MV photons at 10cm x 10cm isocentric field size as SSD is varied form 80cm to 120cm. No significant difference in build up dose was measured.

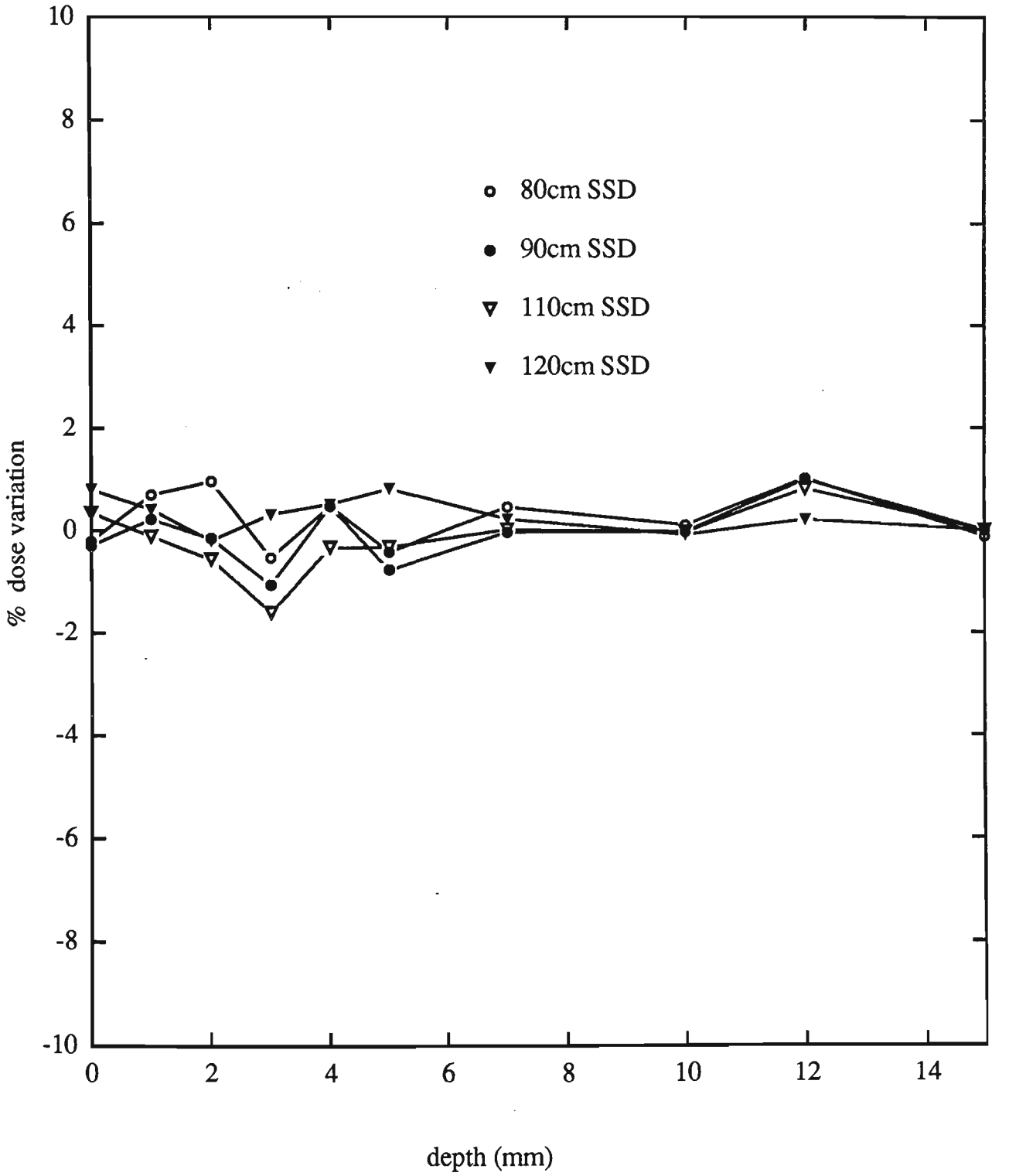

Figure 3.24 : Change in percentage dose compared to 100cm SSD results for a 10cm x 10cm field size.

The inverse square law for x-ray beams is not expected to produce a significant effect compared to electron contamination in build up dose for varying SSD treatments. The amount of electrons produced by the air column irradiated by the beam varies with SSD. As will be shown later the most significant air volume for the production of electron contamination is the last 20cm above the patient. Thus if the SSD is increased the volume of air irradiated increases which in turn will produce an increase in the production of low energy electron contamination. Similarly a smaller air column is irradiated for smaller SSD's. These differences are small, ie. for a 10cm x 10cm field only the outer 10% of the air volume will change with a SSD change of 10cm. It is shown experimentally by the closeness of build up dose for varying SSD's that these two effects produce a negligible impact on the build up dose relative to D_{max} for 6MV photons as they cancel each other out.

In contrast, with the introduction of block trays and blocks to the photon beam a considerable variation in build up dose is seen with varying SSD. Figure 3.25 shows build up dose for a 40cm x 40cm field size as a function of SSD which is varied from 80cm up to 120cm with a 6mm perspex block tray. Surface dose differences of 21% of maximum dose can be seen as SSD is varied from 80cm to 120cm. The variations are shown in figure 3.26 where dose differences for a 10cm x 10cm field is seen. These results point towards the measurable difference in low energy electron contamination produced by the perspex block tray being recorded at different SSD's. The 40cm x 40cm field size has a larger dose effect than the smaller fields eg. 10cm x 10cm as the volume of block tray irradiated is larger. As these electrons have a large angular distribution it is hypothesised that their dose contribution decreases quite considerably with increasing SSD.

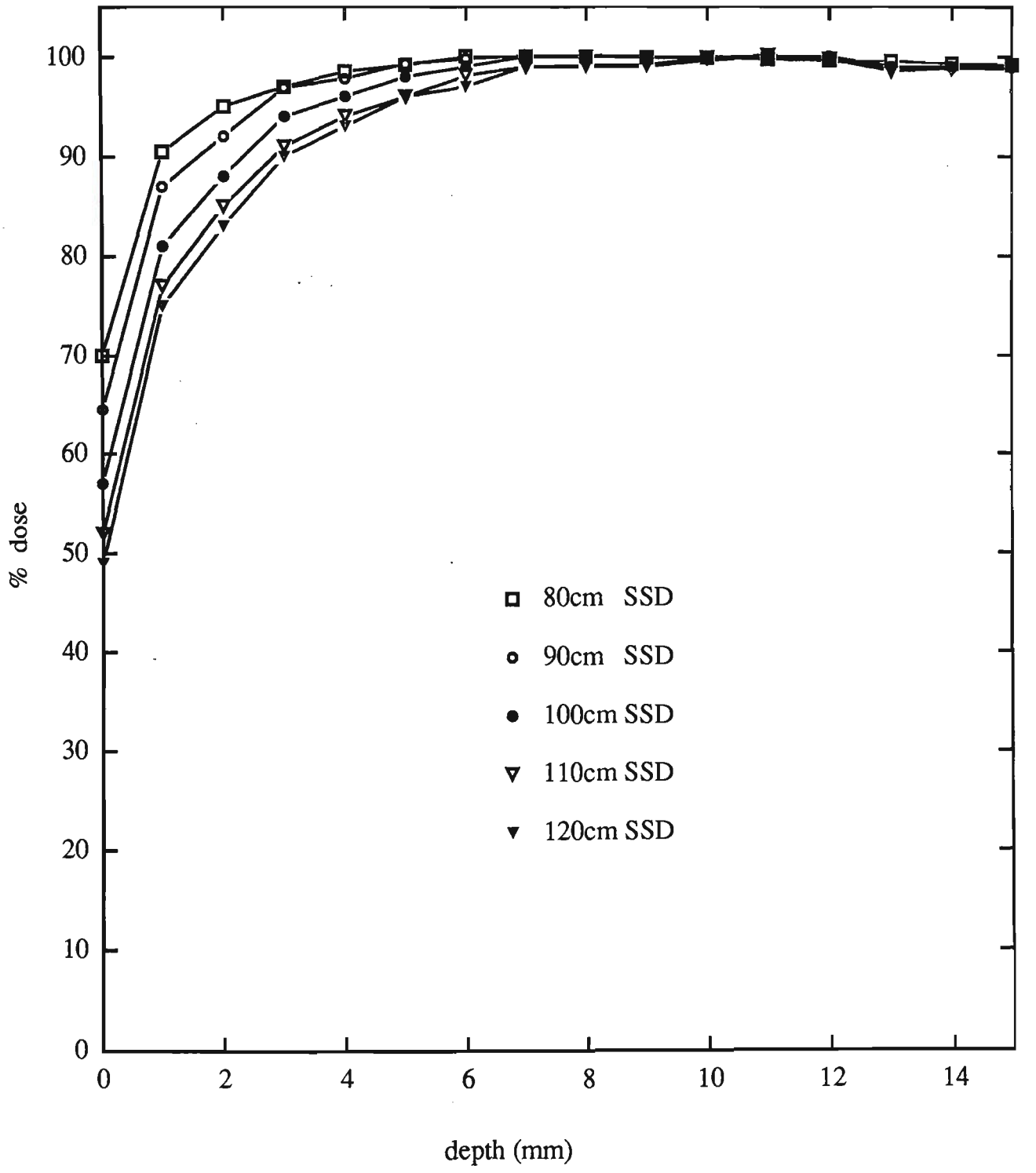

Figure 3.25 : Percentage dose build up for 6MV photons at 40cm x 40cm (for 100cm SSD) field size with a 6mm perspex block tray as SSD is varied form 80cm to 120cm. Large differences are seen due to the range and spread of electron contamination produced by the block tray.

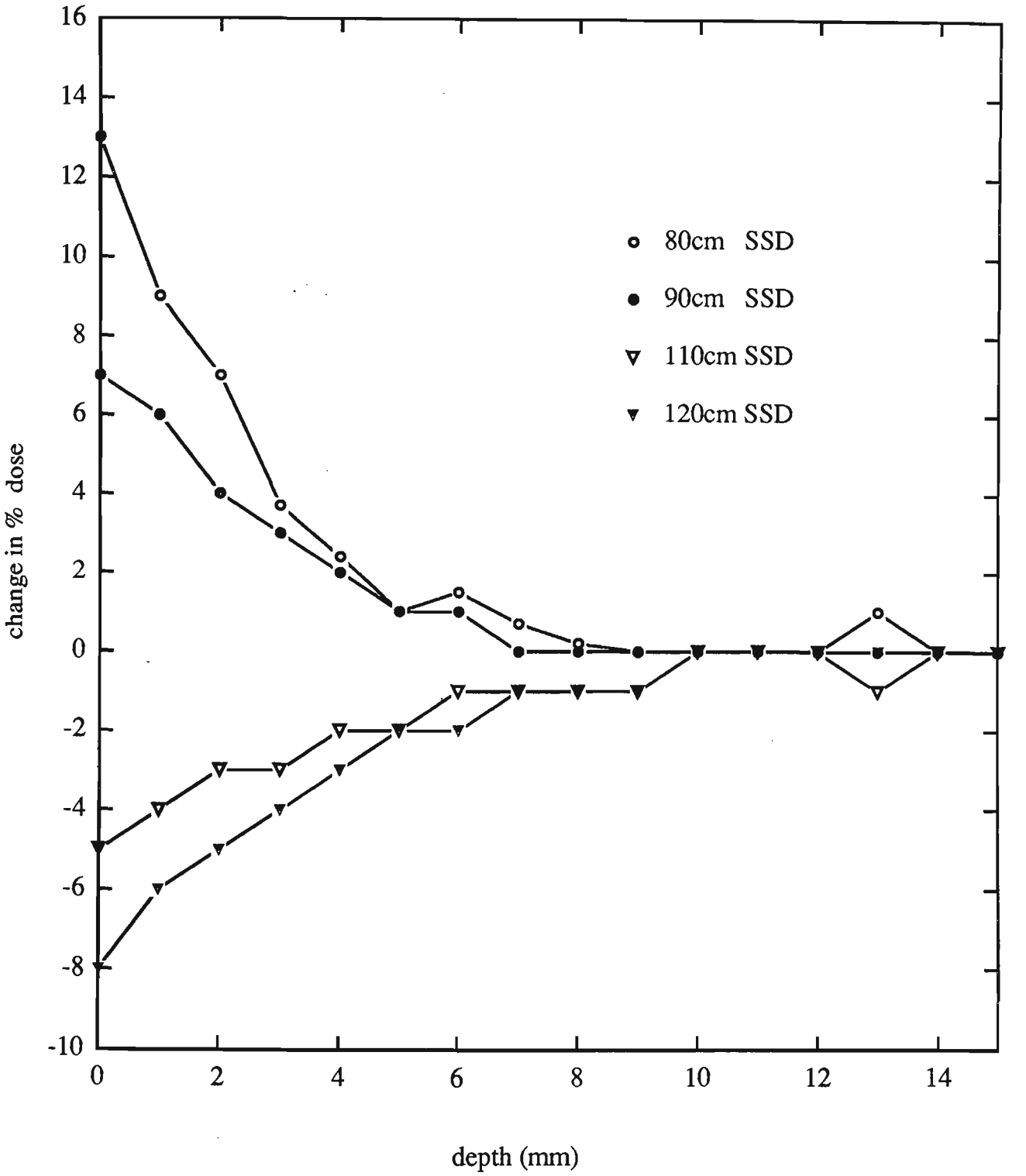

Figure 3.26 : Change in percentage dose compared to 100cm SSD results for a 40cm x 40cm field size.for a 6mm perspex block tray.

3.5 Patient geometry

Patient geometry can influence the amount of scatter material around a certain point , that could in turn influence the dose to that point. Geometry is also associated with changing angle of incidence and the source surface distance when dealing directly with patients. An example would be a breast treatment where a lack of scatter due to the patients geometry would be present. This is however offset in part with associated changes in angle of beam incidence around the curvature and a change in SSD at different positions in the field as well.

Lack of scatter

The effect of patient geometry or 'lack of scatter' was studied in the build up region and especially the first few millimetres for slab phantoms at 0° incidence. Experiments were performed by reducing the size of a rectangular phantom to remove the side scatter component of dose in the build up region. This was performed with a wood phantom that could be chopped into pieces as side scatter material. Solid water was placed over the chamber to simulate depth. The Attix chamber was used to measure surface and build up dose. Table 3.1 shows results for surface dose for a 10cm x 10cm and a 30cm x 30cm field size for various phantom sizes ranging from 30cm x 30cm to 5cm x 5cm. Negligible differences in dose were observed.

Table 3.1 : Phantom geometry effects on surface dose using Attix chamber.

phantom size (cm)	field size 10cm x 10cm (% of D_{max})	field size 30cm x 30cm (% of D_{max})
5	16 ±1	37±1
10	16	37
20	16	37
30	16	37

Lateral electron disequilibrium seems not to interfere with build up dose for the phantom sizes studied. The lack of side scatter also has a negligible effect on the dose deposition of electron contamination. In brief, the effect of patient geometry in terms of lack of scatter does not play a major role in the build up region when the phantom size is larger than 5cm x 5cm. The effect of incident angle and SSD play a much larger role in changing the build up dose.

Curvature

Experiments were performed on a cylindrical phantom (radius 7.5cm) where the lack of scatter is immediately next to the point of measurement. Extrapolation TLD's were used to measure surface dose with varying angles of incidence to ascertain if the curvature influences the surface dose and the incident angle effect measured earlier. Figure 3.27 shows the reduced surface dose associated with varying angles of incidence on the curved phantom compared to a flat phantom. A reduction in dose is seen at the surface by 2%-5% for a 10cm x 10cm field size when the angle of incidence becomes large. As previously discussed, the extra surface dose associated with the angle of incidence effect could be due to the increased 'upstream' phantom interactions depositing dose at the measurement site. In this case, the upstream position now has a

lack of scattering material which could effect the production of extra dose. Another possible explanation of these results is the direct lack of side scatter produced around the TLD's which were placed directly on top of the curved phantom. In most extrapolation TLD experiments, the TLD's are housed in a custom built solid water holder which has a flat surface and side walls to produce side scatter. This housing was not used in these experiments as it is thought that the flat surface design of the holders would effect the validity of the curvature experiments. In stating these results is is also known that the errors involved with these measurements are often larger than the differences seen. The influence of curvature has only been initially studied here. Future work will include a detailed study of all effective radius' of curvature both experimentally and with Monte Carlo simulations. At this stage no correction is made for the curvature effect in the model discucces in chapter 4.

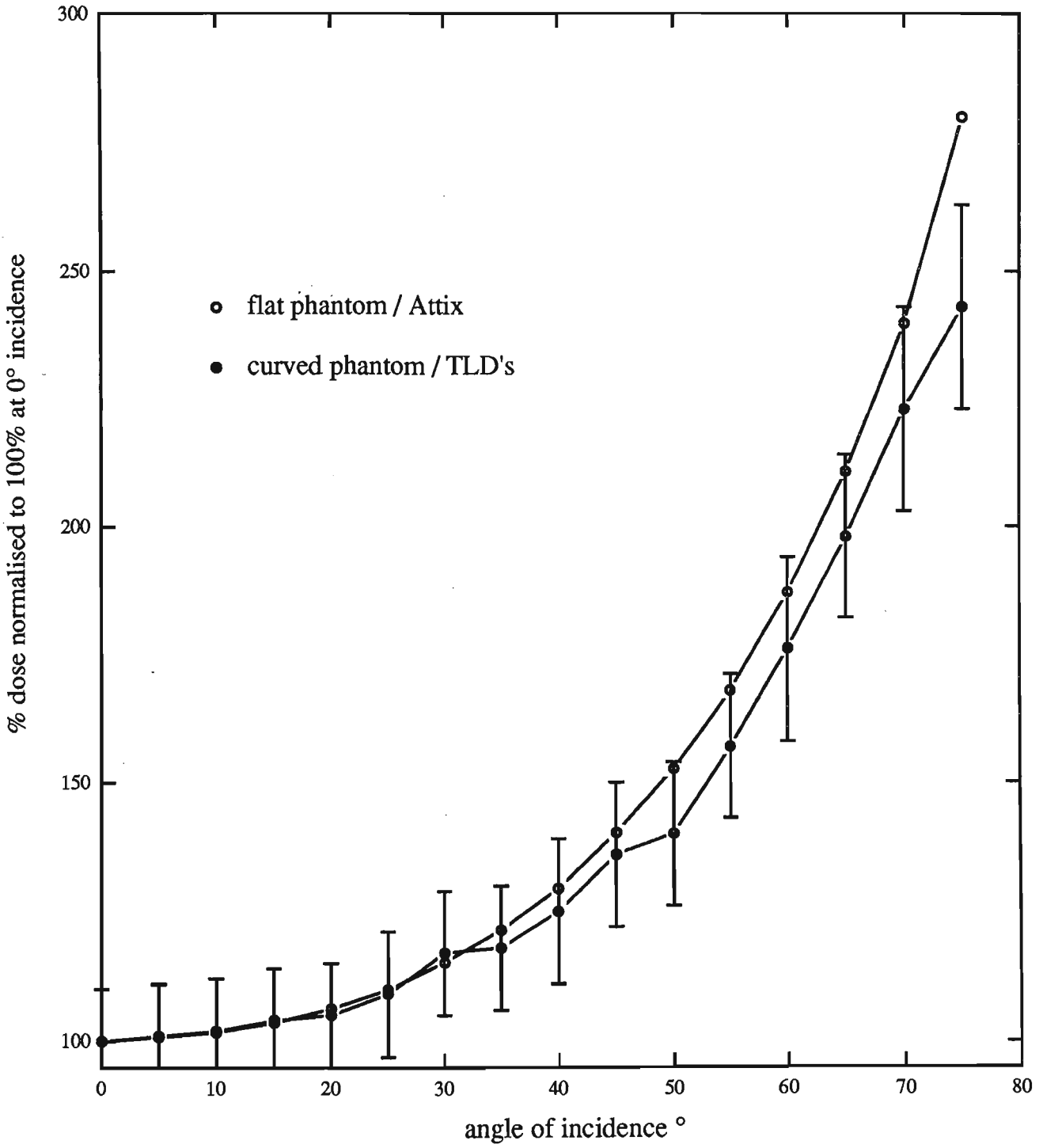

Figure 3.27 : Effects on surface dose for obliquely incident photon beams in a flat phantom and curved phantom configurations. The lack of side scatter in a curved surface phantom seems to reduce the incident angle effect.

3.6 Exit dose

Dose deposition to the skin can also originate from an opposing exiting beam. The dose delivered to the skin will depend on the radiological depth of the skin on the exit side as dose reduces with depth. The dose will be less at this point however due to lack of back scatter (Klein et al 1993). EGS4, Monte Carlo studies were performed to evaluate the effect of the lack of backscatter due to exiting beams to see the effect on skin dose. Simulations were performed using very thin voxels on the exiting side of the virtual phantom. A 10cm x 10cm field was simulated and a 5.025cm thick water phantom used with an air interface beyond it. Figure 3.27 shows the effect of the lack of backscatter for a 6MV spectrum. A reduction of approximately 15% is seen over the last few centimetres due to the lack of backscatter with an extra 5-10% decrease seen over the last 0.2mm which would reduce the dose to the basal cell layer. Kron et al (1995) have performed experimental measurements which have confirmed this reduction close to the exit surface for 6MV and 18MV x-ray beams. Their measurements were undertaken using black carbon loaded TLD's and an Attix ionisation chamber. They found the dose to the skin from an opposing beam is about 85% of the percentage depth dose at the specific radiological depth of the sight in question.

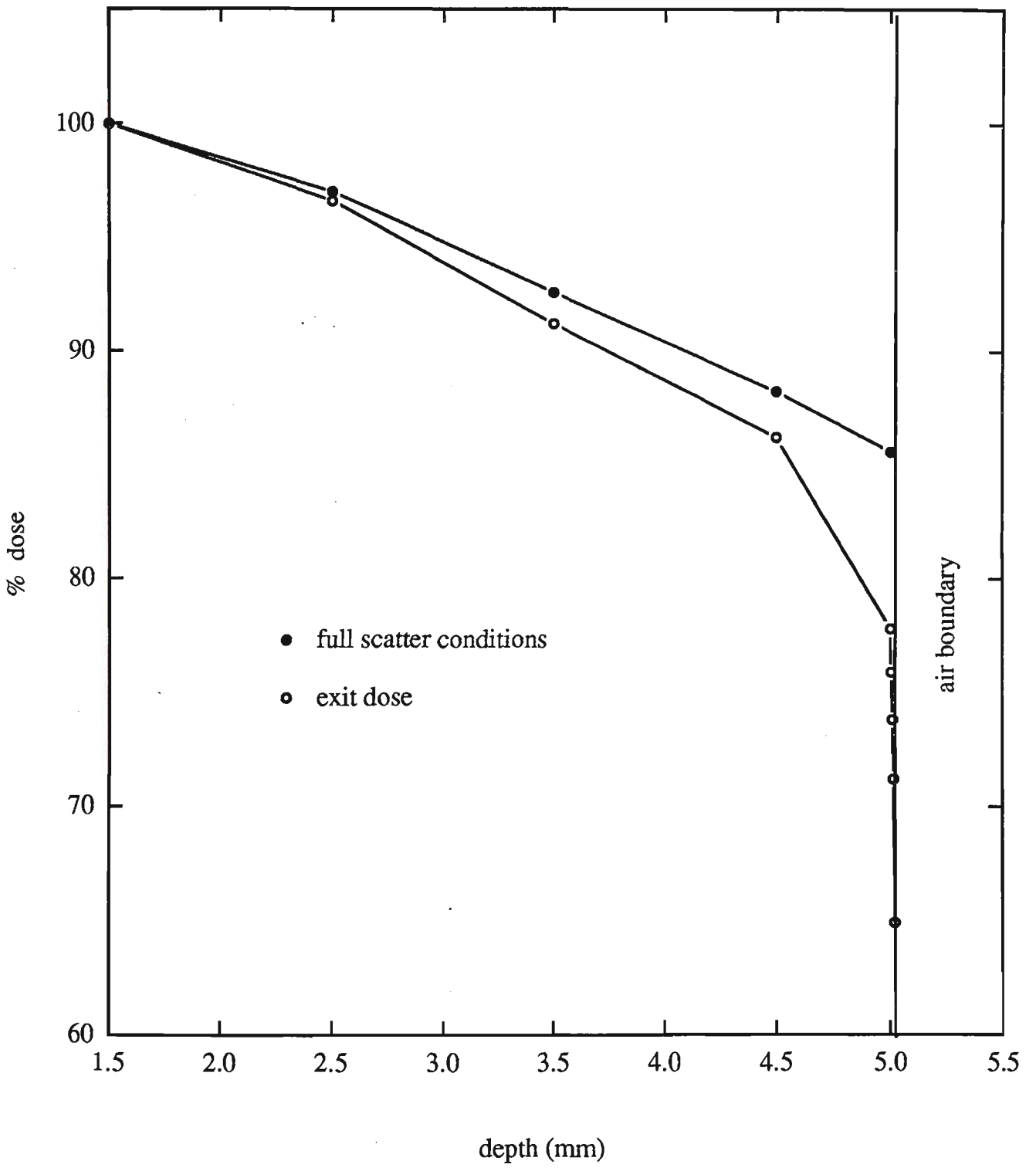

Figure 3.28 : Dose to skin due to exiting photon beams. A reduction in skin dose is seen in exiting beams due to the lack of backscatter. This effect reduces skin dose by approximately 15% compared to full scatter conditions.

3.7 Metal oxide semiconductor field effect transistors (MOSFET's) results

Surface and build up dose response

MOSFET's are small devices which only require a minimal potential difference to power them. Table 3.2 shows the surface dose results for MOSFET's compared to Attix ionisation chamber and TLD's at various field sizes and with the use of beam modifying devices. Results are normalised to 100% at d_{max}. Field size was varied between 2cm x 2cm and 40cm x 40cm.

Table 3.2 : Percentage surface doses from a Varian 2100C 6MV x-ray beam at 100cm SSD with various beam configurations.

field size (cm x cm)	beam modifier wedge/block tray	MOSFET (% of D_{max}) (±1%)	Attix (% of D_{max}) (±0.5%)	TLD's (% of D_{max}) (±2%)
2	none	6.5		
3		8		
5		10	10	10
10		16	16	17
15		22	21	22
20		27	27	25
25		32	32	31
30		37	37	35
35		39	39	40
40		42	42	43
5	10mm perspex block tray	10	10	11
10		18.5	19	18
15		26	26	27
20		34	33	34
30		49	49	48
40		59	60	59
5	15° wedge	10	9	9
10		15	14	15
20		23	23	22

Figure 3.29 shows a build up curve as measured with the MOSFET device compared to the Attix chamber. Results show the accuracy of the MOSFET for surface and skin dose measurements.

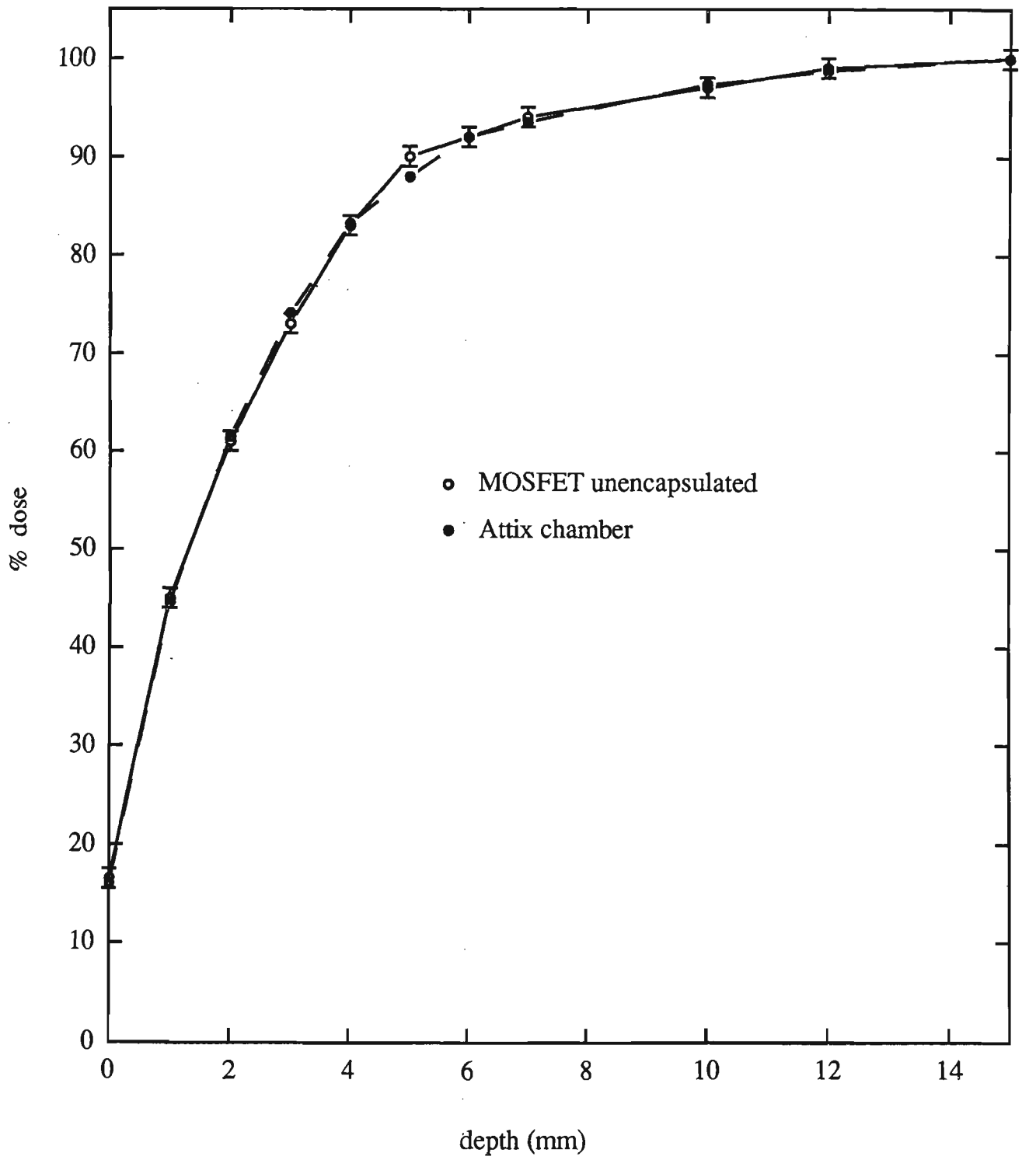

Figure 3.29 : Percentage dose build up measured with a MOSFET dosimeter compared to an Attix chamber. Good agreement is found for normally incident beams.

Table 3.3 shows percentage surface dose results for 18MV x-rays and various electron beam energies using the MOSFET's and Attix chamber.

Table 3.2 Percentage surface doses for 18MV x-ray and high energy electron beams.

Energy	MOSFET (±1%)	Attix (±0.5%)	TLD's (±2%)
6 MeV electron	82	80	83
9 MeV electron	85	85	87
12 MeV electron	90	89	92
16 MeV electron	91	91	93
20 MeV electron	95	94	94
18 MV x-ray	15	15	12

MOSFET's have previously been shown to be acceptable radiation dosimeters in both medical and non-medical applications (Hughes 1994). A simple change in design characteristics of a commercially available MOSFET was undertaken to improve there surface dose measurement capability. By removing the nickel casing, high density scattering and 'build up' material is eliminated and replaced with tissue equivalent solid water and wax. With the MOSFET totally encapsulated in its nickel casing, surface dose results were inaccurate with an over estimation of dose. That is, for a 10cm x 10cm open field at 100cm SSD for 6MV x-rays, the encapsulated MOSFET produced a percentage surface dose reading of 65% normalised to 100% at d_{max}. When just the top lid was removed so as to leave the nickel side walls, the percentage surface dose recorded was 35% of D_{max}. Totally uncovered and with wax used to fill the air cavities created by removing the casing, the percentage surface dose recorded was 16% of D_{max}. This value agreed with other detectors ie. Attix chamber, Markus chamber with Rawlinson correction and TLD extrapolation.

As shown in table 3.2, the MOSFET results agree well with percentage surface doses measured with the Attix chamber in measurements for open fields and with beam

modifying devices such as block trays and wedges. The MOSFET in each case has matched the Attix data for photon and electron beams. Photon beam percentage surface dose contributions are mainly supplied by electron contamination produced outside of the phantom. This is exaggerated at larger field sizes and with the use of perspex block trays. The MOSFET has accurately measured surface dose contributed by varying levels of contamination and photon in phantom scatter in this region of electronic disequilibrium. These results indicate that the uncovered MOSFET shows potential for skin dose assessment in-vivo on patients. The MOSFET's low power requirements mean that only a small dc battery is required to supply power during irradiation alleviating any electrical risks. The MOSFET can then be immediately read and compared to a standard for skin dose assessment. In-vivo surface and skin dose measurements are currently available through techniques such as TLD extrapolation where 3 thicknesses of TLD's are placed on the skin surface and dose recorded at the nominal centre of each TLD is extrapolated to zero thickness. However, the uncovered MOSFET has a few advantages over this system. These being :

i) immediate retrieval. Dose can be ascertained accurately after irradiation with as low as 10cGy of applied dose

ii) MOSFET's can be re-used again immediately. They do not require an anneal process after irradiation like TLD's

iii) inexpensive support equipment. They only require a small power source and voltmeter for data retrieval

iv) MOSFET's retain their dose history as information is not lost during the retrieval process

v) the precision of the reading is ±2% for two standard deviations whereas for thin TLD's the precision is ±5% for two standard deviations

All of the above properties make the uncovered MOSFET an attractive in-vivo dosimeter for skin dose measurements. The small wax mounting is primitive however and commercially available MOSFET's in a tissue type substrate would be ideal.

Conclusion

The uncovered MOSFET is an attractive alternative for in-vivo measurement of surface dose in clinical radiotherapy. The surface dose measurements for normally incident beams aligned closely to the well known Attix plane parallel ionisation chamber for normally incident beams.

Additional features include, immediate retrieval of information, accuracy at low applied doses, immediate reuse and its ability to record dose history. Using a small dc battery, the uncovered MOSFET can be used in-vivo for surface and skin dose measurements.

MOSFET's have only initially been tested at angle. The higher density base material may distort the accuracy of these devices at oblique angles of incidence. Initial tests performed by Perez (1995) showed a small angular response in results up to angles of 60°. Future tests should focus on the angular dependence of these detectors at very oblique incidence as this could be encountered in-vivo.

3.8 Radiochromic film results

Hypothesis

Data collected with other dosimeters produce point dose results, mainly located at the central axis. Gafchromic film would be a suitable in-vivo dosimeter for collecting off axis data concurrently with central axis data.

Accurate surface dose measurements covering the surface contours of a phantom or patient have been a tedious process in the past. Dosimeters such as extrapolation TLD's can be used however results are still point doses and accuracy depends on the quantity used. Gafchromic film along with several readout systems can be used for mapping the surface dose of an irradiated media. The low energy under response of MD-55-1 and MD-55-2 film (Kron et al 1998) should not cause significant disagreement in measured dose at linear accelerator energies.

Surface dose response

Surface dose response was measured with both MD-55-1 and MD-55-2 film. MD-55-1 was an attractive surface dose detector due to its active layer being 6μm thickness and located at the surface. Because MD-55-1 was less robust, it became commercially unavailable and was replaced by MD-55-2 which had two active layers located at approximately 100μm and 150μm. Table 3.4 shows the percentage 'surface' dose results for Gafchromic film along with the Attix chamber, TLD extrapolation, MOSFET and Radiographic film detector results. All readings were made for a 6MV x-ray beam at 100cm SSD normalised to 100% at d_{max}.

Table 3.4 : Comparison of dosimeter techniques for surface dose measurement.

Dosimeter	Field size (cm x cm)				
	5 x 5	10 x 10	20 x 20	30 x 30	40 x 40
Gafchromic MD-55-1	9±3	16	25	35	40
Gafchromic MD-55-2	12±3	20	31	41	46
MOSFET	9±1	16	27	37	42
Attix	9±0.5	16	27	37	42
TLD extrapolation	10±2	17	25	35	43
Radiographic X-omat V	31±2	36	46	57	63

Figure 3.29a shows the percentage surface dose profile for a 10cm x 10cm field, 6MV x-ray beam with a 45° steel wedge. Results are normalised to 100% at a depth of 1.5cm on the central axis. Results show increased percentage surface dose on the thin side of the wedge. The Markus chamber was placed perpendicular to the beam. As discussed previously in section 3.1, the dose averaging due to the spatial resolution would account for the larger surface penumbra seen with the Markus.

Discussion

For central axis surface dose measurements using the Java CCD system, a 2cm x 2cm piece of Gafchromic film is used and results are averaged over the entire area. The mean and standard error are quoted. Surface dose increases with field size are due to extra electron contamination and photon head scatter and is well documented (Sixel 1994). Table 3.4 shows the close agreement of Gafchromic film with other dosimeters except for radiographic film. Radiographic film's high energy response makes it

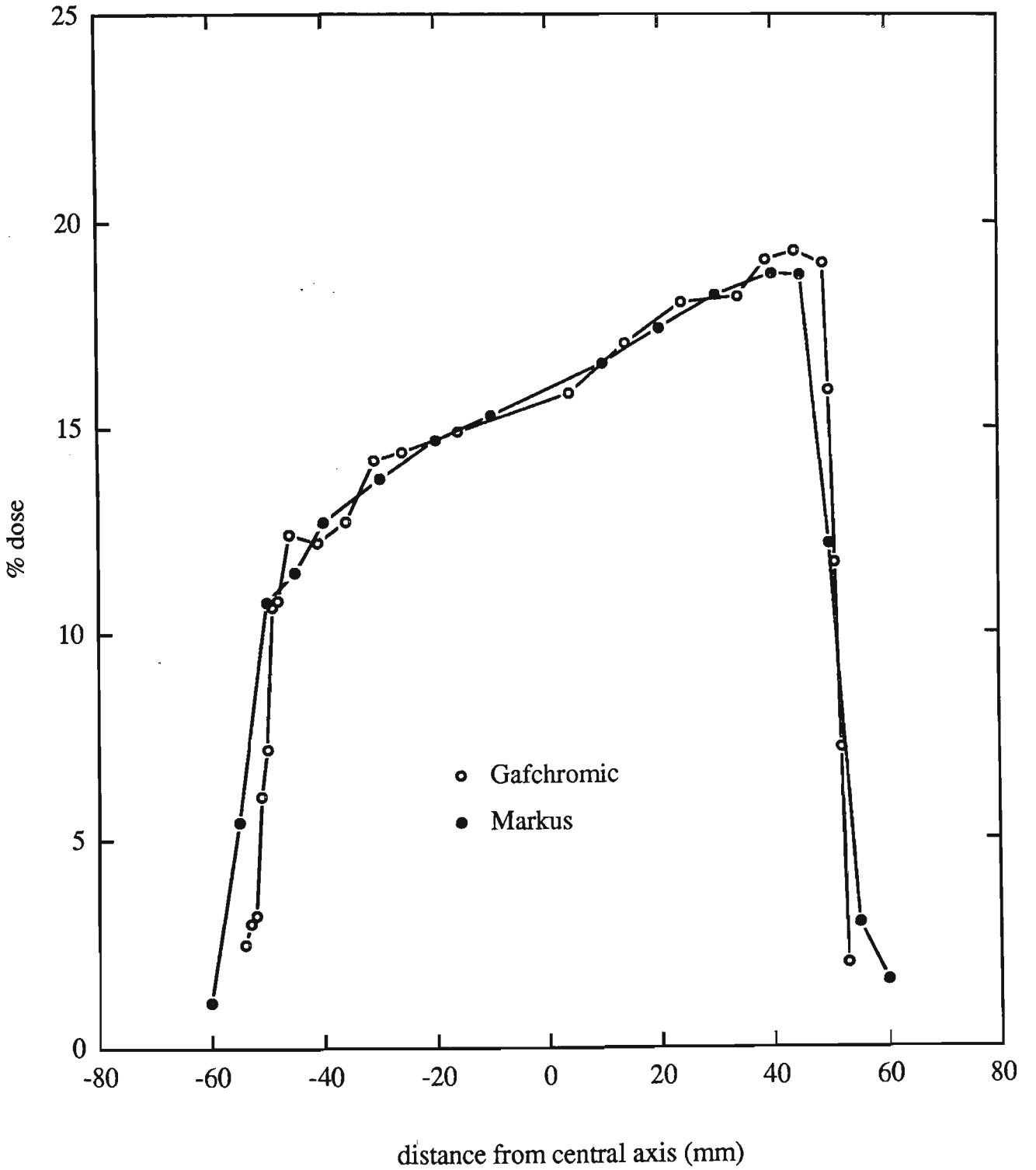
25
20
15
10
5
0
% dose
-80
-60
-40
-20
0
20
40
60
80
distance from central axis (mm)
Gafchromic
Markus

unsuitable as a surface dose detector where a large degree of low energy electron contamination and low energy head scattered photons are present.

Profiles have been measured as shown in figure 3.29a for a 45° wedged 6MV beam. When normalised to 100% at d_{max} on the central axis, a larger percentage dose is recorded on the thinner edge of the wedge. A significant contribution to this is the higher degree of attenuation of x-rays reducing the transmitted fluence through the thick end of the wedge. Low energy electron contamination and head scattered photons will also be attenuated more by the thicker end of the wedge. D_{max} profiles closely follow the wedge angle as measurements are not influenced by electron contamination at this depth.

Off axis measurements

Measurement of off-axis and peripheral skin dose (Fraass et al 1983, Kase et al 1983) with conventional detectors such as ionisation chambers (Mellenberg 1995) becomes a tedious task as dose integration is required at each position then the detector needs to be repositioned. The wide diameter of parallel plate ionisation chambers also provides poor spatial resolution in regions such as the penumbra and other high dose gradient areas. Extrapolation TLD's (Kron et al 1993) provide better spatial resolution however these require batch calibration and provide only point by point data. Radiochromic film provides a complete surface dose profile data set limited only by spatial resolution of the readout densitometer. This ensures very convenient collection of off-axis and peripheral skin doses in phantoms or in-vivo. Radiochromic film's near water equivalence also reduces the possible perturbations caused by primary and backscatter fluence. Measurements were also performed with MD-55-2 to assess skin dose off axis. Measurements were performed at 6MV, 10MV and 18MV. The film used was Gafchromic MD55-2 with batch number 970116. The film results were corrected for non-uniformity with a double exposure technique (Zhu et al). The film was analysed

with the 660nm Red GaAlAs ultra bright LED on a converted Scanditronix RFA300 densitometer (Carolan et al 1997). Results are compared to Attix ionisation chamber results at 0.15mm depth for skin dose analysis. The effective depth of measurement in MD55-2 was found to be 0.17±0.03mm water equivalent for high energy photon measurements by comparison of results to Attix ionisation chamber measurements. The Gafchromic film was placed perpendicular to the beams path on the surface of a solid water slab phantom. The film was cut into 1cm x 12cm strips and used to cover the beam profile. For larger field sizes, two strips were used to extend into the peripheral region. Errors associated with MD55-2 radiochromic film are mainly due to inherent variations in the film thickness and optical defects caused by scratches, finger prints and similar marks. Combination of these errors produce a standard error of measurement of approximately ±2% (one standard deviation) of D_{max} for measured dose.

Results

Figure 3.30a. shows the percentage skin dose normalised to 100% at Dmax measured using MD55-2 Gafchromic film placed on the surface of a solid water slab phantom at 6MV photon energy. The 10cm x 10cm field size and 30cm x 30cm field size shown are open fields without any beam modifying devices. Skin dose is greater for the larger field sizes at central axis and at all points inside and outside the field. The 20cm x 20cm field has a 6mm perspex block tray placed at 65.4 cm from the source. A 3cm wide by 8cm thick lead block is positioned on the block tray in an off axis position. The perspex block tray increases the skin dose and also produces a higher surface dose (approximately 7%) at the central axis compared to the field edge. Under the lead block, the skin dose reduces to approximately 20% of D_{max}.

Figures 3.30b. and 3.30c. show results for the experiment repeated for 10MV and 18MV photons. Results show that the reduction in skin dose under the block decreases

as beam energy increases. Reductions in dose under the lead block are approximately 10% ± 2% for 6MV, 7% ± 2% for 10MV and 3% ± 2% for 18MV.

Discussion

The finite thickness of MD-55-2 Gafchromic film influences the measurement of 'skin' dose to a certain depth, namely 0.17 ± 0.03mm. The skin region which extends within the first 1mm of depth has a large dose gradient with a change of up to 20% per mm occurring in this region. The measurement at 0.17mm from the Gafchromic film is the minimum depth of measurement attainable with this dosimeter and relates to a region just below the basal cell layer which is located at approximately 0.1mm depth.

The increase in percentage skin dose due to the perspex block tray is greater at central axis with an approximate reduction of 5-10% from the central axis out to the field edge. This may be explained by the lateral scatter of electron contamination from the block tray contributing a larger dose at the field centre compared to the off-axis and peripheral regions. This effect is seen for 6MV , 10MV and 18MV photons with the magnitude of dose decrease off-axis remaining similar.

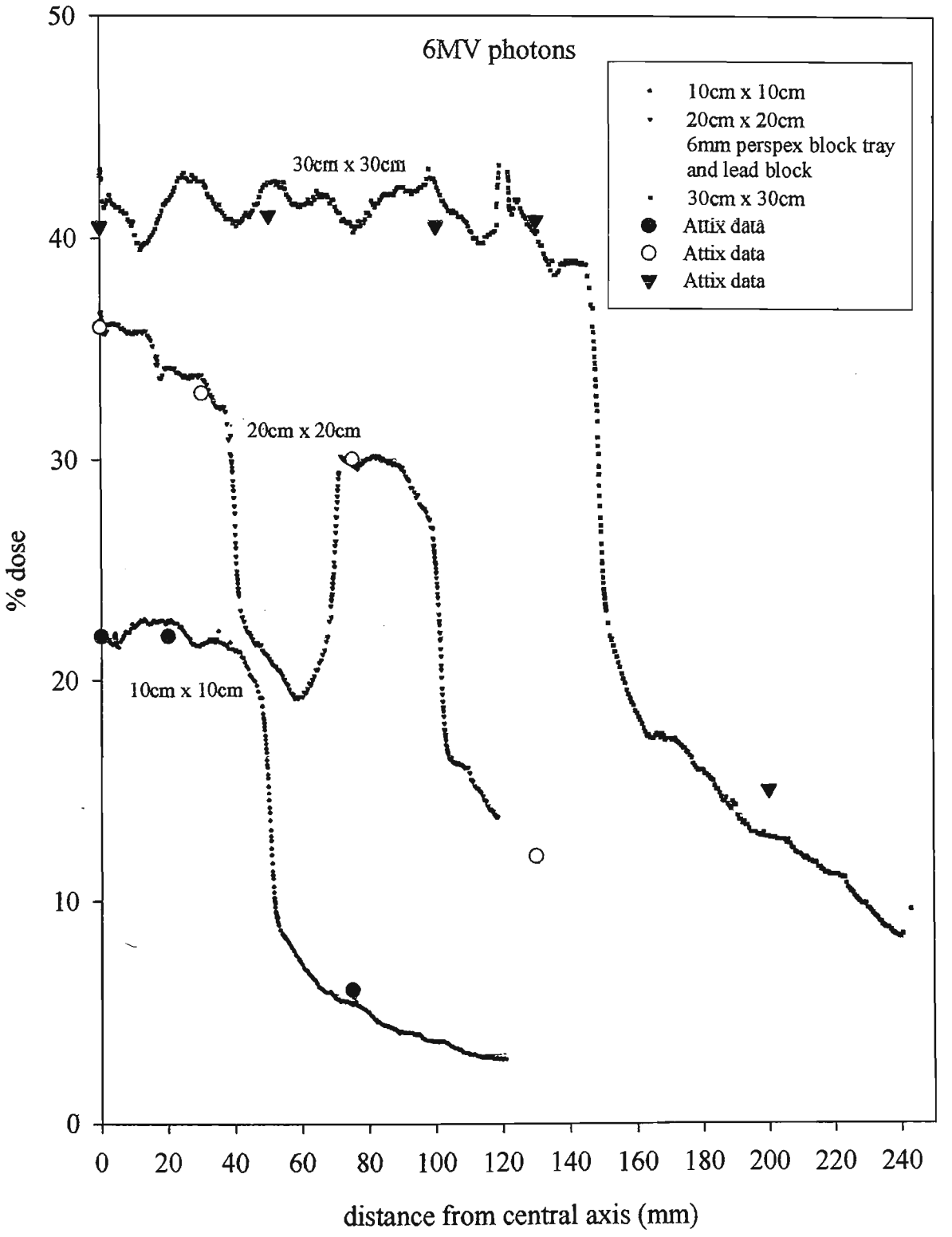

Figure 3.30a : Shows the off-axis and peripheral skin dose measured at 6MV energy. Several Attix chamber measurements made at 0.15mm depth are showed to compare with Gafchromic results.

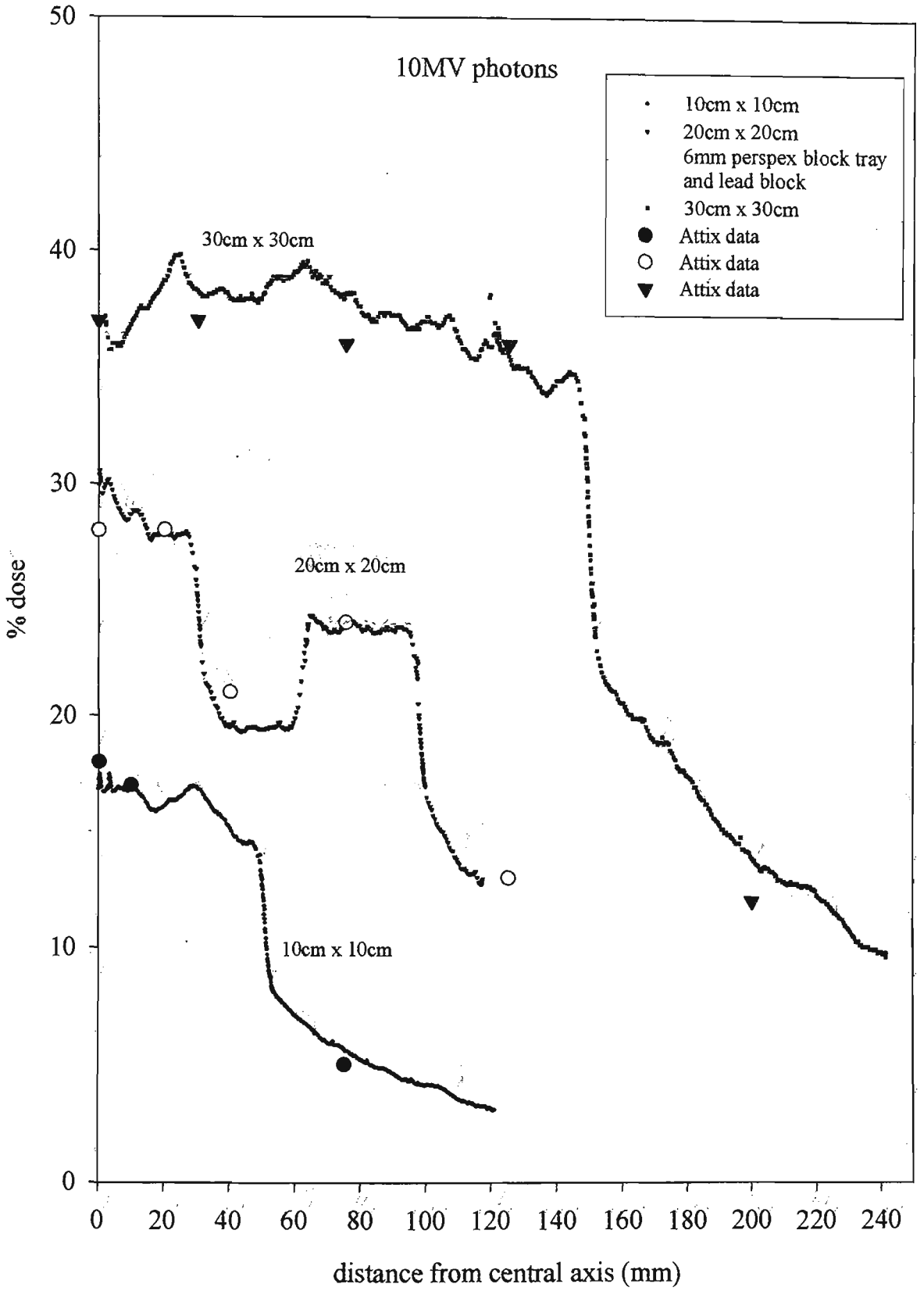

Figure 3.30b : Shows the off-axis and peripheral skin dose measured at 10MV energy. Several Attix chamber measurements made at 0.15mm depth are showed to compare with Gafchromic results.

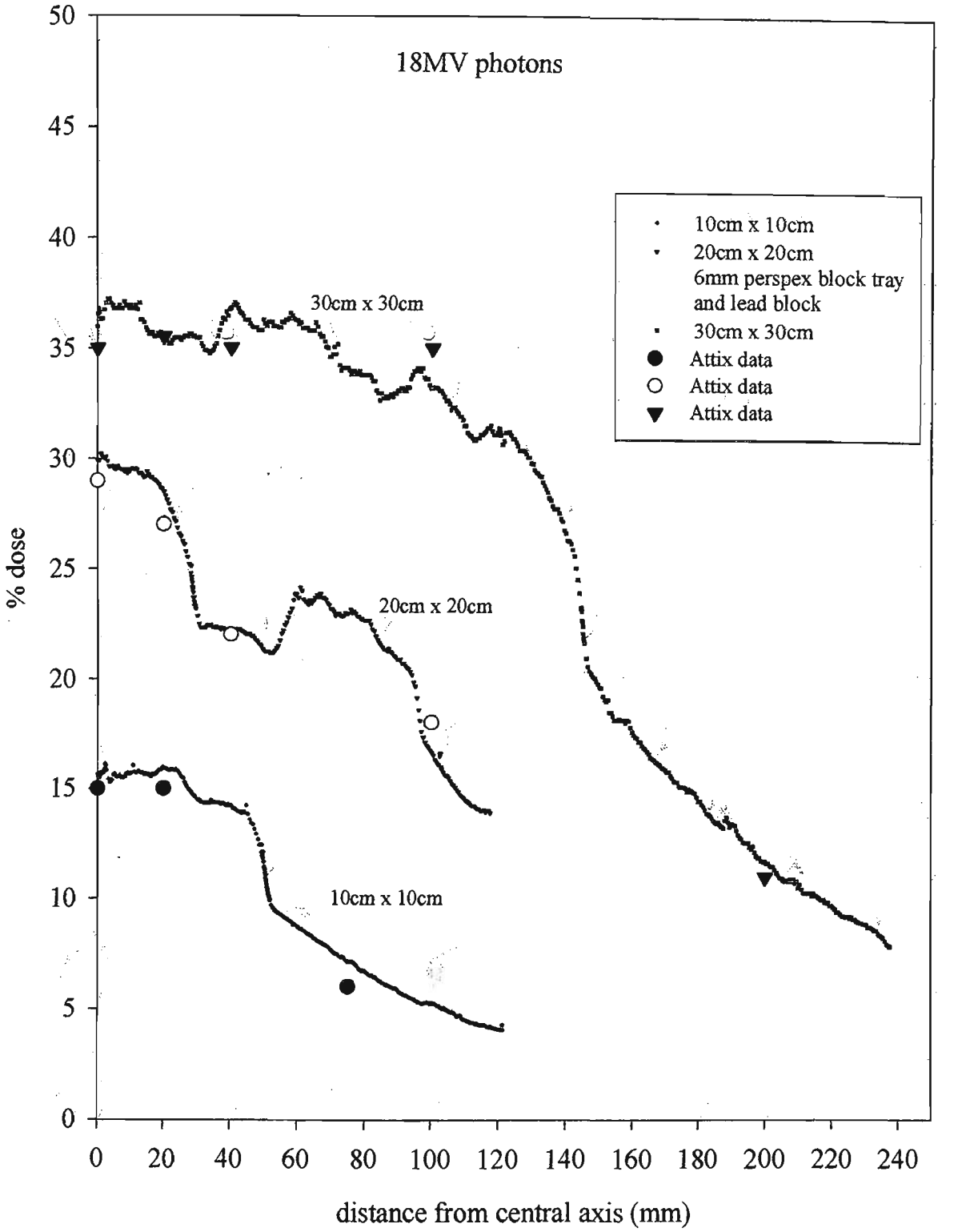

Figure 3.30c : Shows the off-axis and peripheral skin dose measured at 18MV energy. Several Attix chamber measurements made at 0.15mm depth are showed to compare with Gafchromic results.

A reduction in skin dose is seen directly under a lead block as shown in figure 3.30. This effect seems to be energy dependent with a larger reduction in skin dose seen with lower energy. The block was thick enough to ensure block transmission remained at less than 2% for all energies tested. The majority of dose deposited at the surface directly under the blocks therefore has been produced by electron contamination. Two important contributors to skin dose under blocks comes from the block tray and the air column. Nilsson (1985) and Yorke et al (1989) have shown that the air column has a much more significant effect on electron contamination at lower energies. This could explain the effect seen. By removing the photons in the air column directly under the blocks, we eliminate the production of electron contamination in this site. Thus a larger reduction in skin dose is seen at lower energies. For higher energies, the block tray produces the majority of electron contamination. As it is located approximately 35cm from the skin, the electron contamination produced at this site has enough longitudinal distance to scatter producing the higher skin dose under the blocked region.

Peripheral skin dose increases with field size. Measurements using the Attix chamber showed that less than 1% of peripheral dose is due to collimator transmission. Scattered electron contamination constitutes the rest of the percentage dose outside the field.

Conclusion

Gafchromic film shows potential as a very useful non intrusive detector for the measurement of skin dose especially in regions of high dose gradient such as the beam penumbra and under edges of blocks. Skin dose reductions under lead blocks are energy dependent with greater reductions seen at lower energy.

Extrapolation of surface dose with MD-55-2 film

The original MD-55-1 Gafchromic film had been used successfully to measure surface dose due to its single layer design which allowed the active layer to be positioned at the surface. Design changes of the new, more sensitive MD-55-2 Gafchromic film which effectively produced a two piece MD-55-1 sandwich moved the two active layers away from the surface. A simple extrapolation technique has been employed to estimate surface dose.

Measurements were performed at 6MV and 10MV. The film used was Gafchromic MD-55-2 with batch number 970116. The film results were analysed using a double exposure technique (Zhu et al 1997). This is performed by giving each film an initial dose of 5Gy to ascertain if any corrections are needed due to non-uniformity in dose response. A variation of 3% for 1 standard deviation was recorded in optical density for the films used in the experiment. The film was analysed with a 660nm, 3000mcd, GaAlAs ultra bright LED on a converted Scanditronix RFA300 densitometer (Carolan et al 1997). Negligible polarization effects (Klassen et al 1997) were observed using this densitometer. A set of standard films were irradiated to known doses in increments of 1 Gy to produce an optical density versus dose calibration. Results are compared to uncorrected Attix parallel plate ionization chamber results for surface ionisation analysis. Both Attix chamber and Gafchromic film experiments were performed in a RMI 30cm x 30cm solid water slab phantom at 100 cm source to surface distance.

The MD-55-2 Gafchromic film was tested for its thickness and physical density. The thickness was measured using digital callipers (Starrett) and was found to be 0.267 ± 0.005 mm. The films weight was measured using a micro balance (Mettler) and results were used to determine the physical density which was found to be 1.3 ± 0.5 mg/cm^3. Using these values an approximate effective water equivalent thickness of the Gafchromic film is calculated to be 0.35 ±0.015 mm.

The extrapolation technique was performed by irradiating a stack of 5 horizontal films, 1cm x 1cm pieces, placed on top of a solid water phantom. No scatter material was placed around the film during irradiation. In each case, the optical density was measured at the centre of each film piece to minimize the effects of variations in measured dose near the edge of the film. The experiments and film analysis were performed at a constant temperature of 22°C ± 1°C to reduce the effects of time and temperature dependent evolution (McLaughlin et al 1991) of Gafchromic film and the temperature dependent absorption spectra of the film. Gafchromic film was handled with tweezers to minimize scratching and fingerprints. The film was only removed from its light tight envelope during irradiation and readout to reduce the effects of ambient light (Butson et al 1998). All films were irradiated with an applied dose to D_{max} ranging from 40Gy to 80Gy . The exact dose depended on the field size and was designed to give the film a surface dose of approximately 15Gy to 20Gy.

Figure 3.31 shows the extrapolation technique used where 5 film layers are used to produce a central axis percentage build up dose measurement within the first few millimetres. Shown are results for 10cm x 10cm open field and 30cm x 30cm field size with a 10mm thick perspex block tray located at 65cm from the source for 6MV and 10MV photons. The active point of measurement was assumed to be at the centre of each film and thus the results for each film layer are quoted at half the water equivalent thickness, ie. 0.175mm. Dose was normalized to 100% at Dmax. Due to the non-linear nature of photon build up characteristics, a second order polynomial extrapolation was used as the line of best fit. Extrapolated surface dose for a 10cm x 10cm field at 6 MV is 15% ± 2% of Dmax compared to surface ionization of 16% ± 1% of Dmax as measured by the uncorrected Attix chamber.

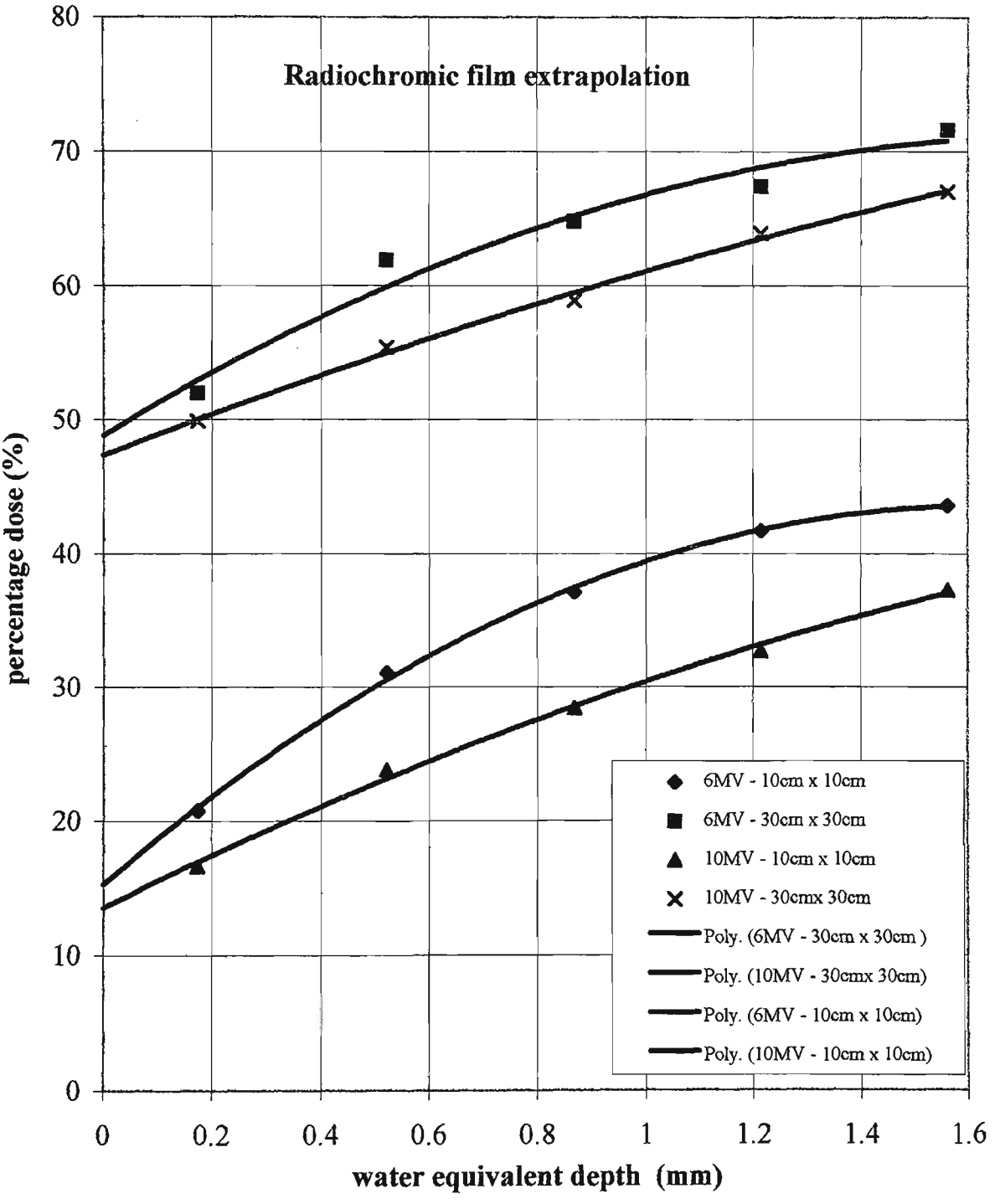

Figure 3.31 : The dose results for the extrapolation process where a 3rd order polynomial line of best fit is used to extrapolate to zero film thickness and thus produce an estimate of surface dose.

Figure 3.32a compares Gafchromic film extrapolated surface dose for open and blocked fields as a function of field size for 6MV photons to Attix chamber results. Surface doses matched to within 2% over all field sizes and energies. Figure 3.32b shows similar results for 10MV photons with open and blocked fields. Results agree within 2% of percentage surface dose. Gafchromic film extrapolation has produced an accurate surface dose assessment as well as produced dose measurements within the first 1 mm.

Its present relatively low dose sensitivity excludes Gafchromic film from in-vivo use for 1 fraction to assess entire treatment skin dose however if replaced every day on a patient or left on a head cast. In this way a record of integrated skin dose could be kept. This could be compared with patient skin damage as assessed by some other method. The necessary precautions needed to be taken to ensure the film is not damaged would include wrapping to prevent moisture or oil contamination, scratching and excess light exposure. Increased temperature during irradiation may also influence the dose response. The method presented shows that MD-55-2 Gafchromic film has a high spatial resolution for surface dose assessment and is a useful extrapolation device.

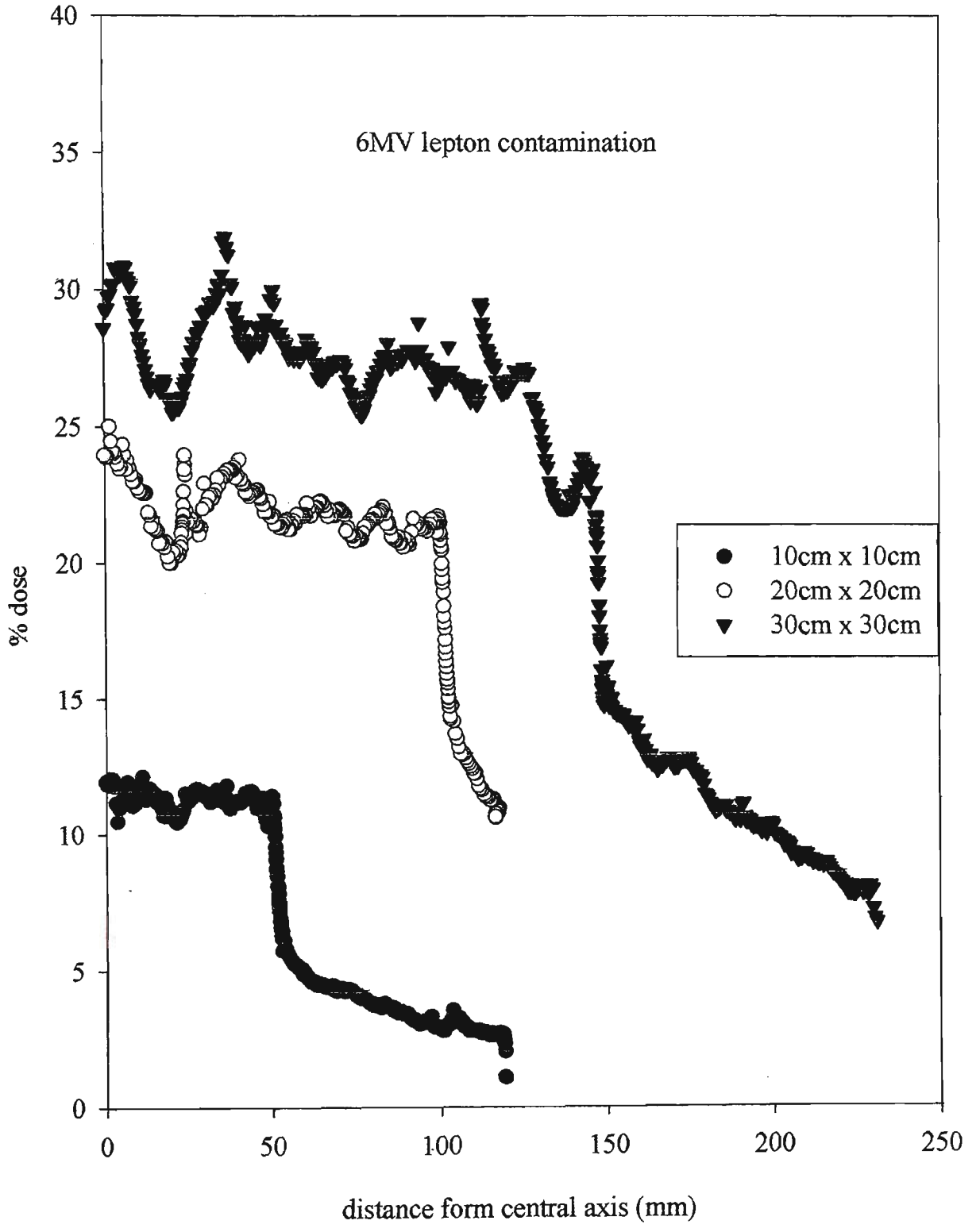

Figure 3.32a : The extrapolated electron contamination surface dose across a profile of a few typical clinical field sizes at 6MV x-ray energy.

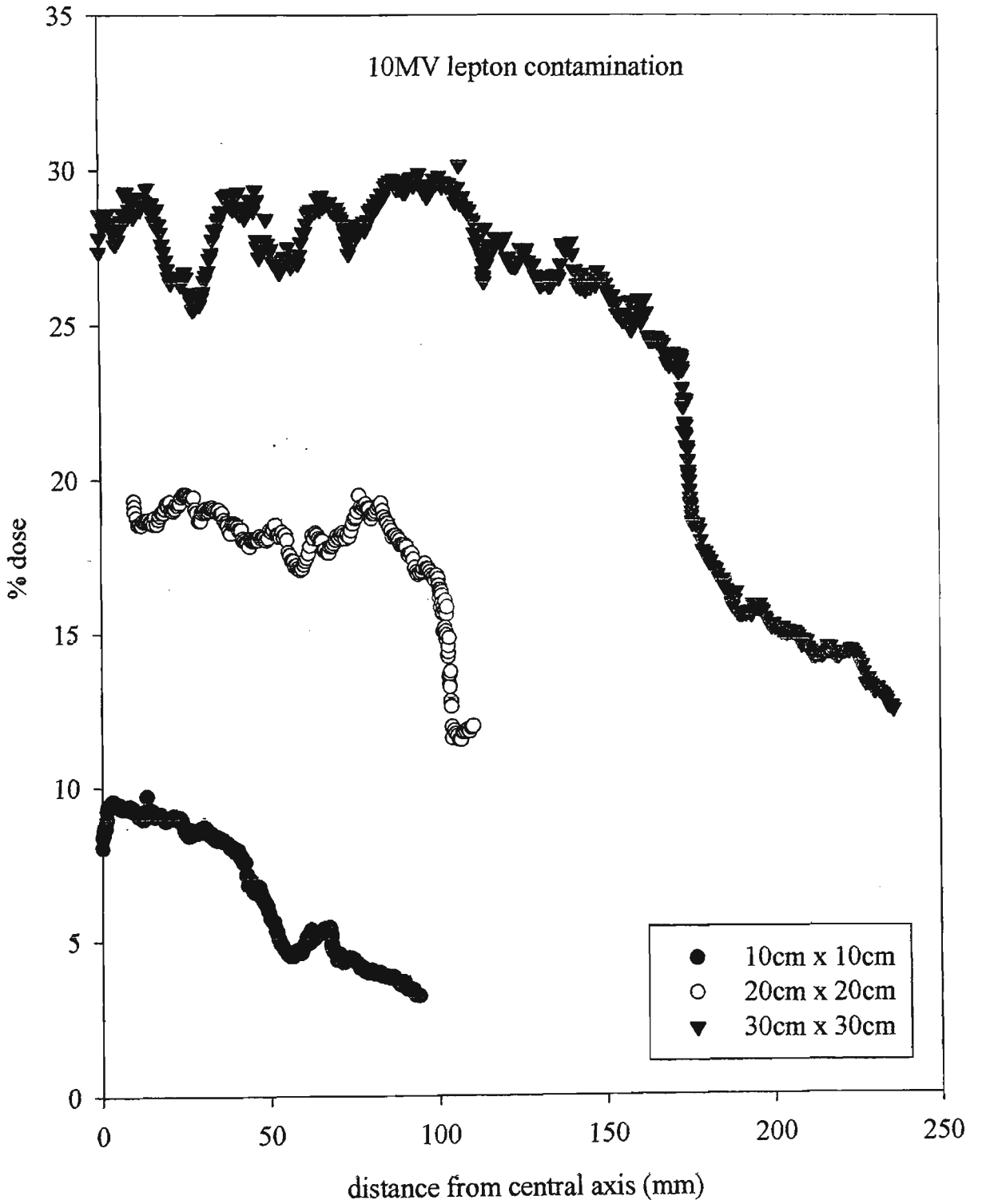

Figure 3.32b : The extrapolated surface dose across a profile of a few typical clinical field sizes at 10MV x-ray energy.

Measurement of electron contamination with Gafchromic film

In order to measure electron contamination, the film was suspended in air using a string brace which consisted of a 0.2mm thick string line attached to two points 60cm apart and stretched tightly.The side of the film was attached to the string thus negligible scatter material except the film itself was present. Three layers of Gafchromic film cut into 1.5cm x 13cm strips were stacked horizontally on top of each other to extrapolate to zero thickness to remove the incident dose due to phantom photon scatter. Results were measured along a profile of the beam for 6MV and 10MV x-rays.

Figure 3.33 shows the percentage dose results recorded in the first two layers of Gafchromic film and the extrapolated electron contamination dose derived by an extrapolation to zero film thickness. A linear extrapolation curve is used to derive the incident electron contamination dose. Figure 3.34a and 3.34b shows the extrapolated incident electron dose measured for various field sizes at 6MV and 10MV energy. Electron doses within the geometric field edge are relatively uniform for all field sizes with an increasing fluence with field size. A distinctive reduction in electron dose is seen in the penumbral region with a measurable dose recorded in the peripheral regions. Peripheral electron dose increases with field size. At 30cm x 30cm field size, electron contamination levels of 10% of applied dose are still measured up to 8cm outside the treatment field.

Gafchromic film has shown that the electron contamination produced in open fields is uniformly distributed across the entire treatment field. The extrapolation data shows that 60-70% of total incident surface dose is due to electron contamination at a 10cm x 10cm field size. As field size is increased this proportion increases. Peripheral dose due to electron contamination is also significant especially at larger field sizes. 10-15% of applied dose is delivered to the skin surface outside the treatment field due to electron

contamination. This is due to the lateral scatter of electron produced in the treatment head and air column.

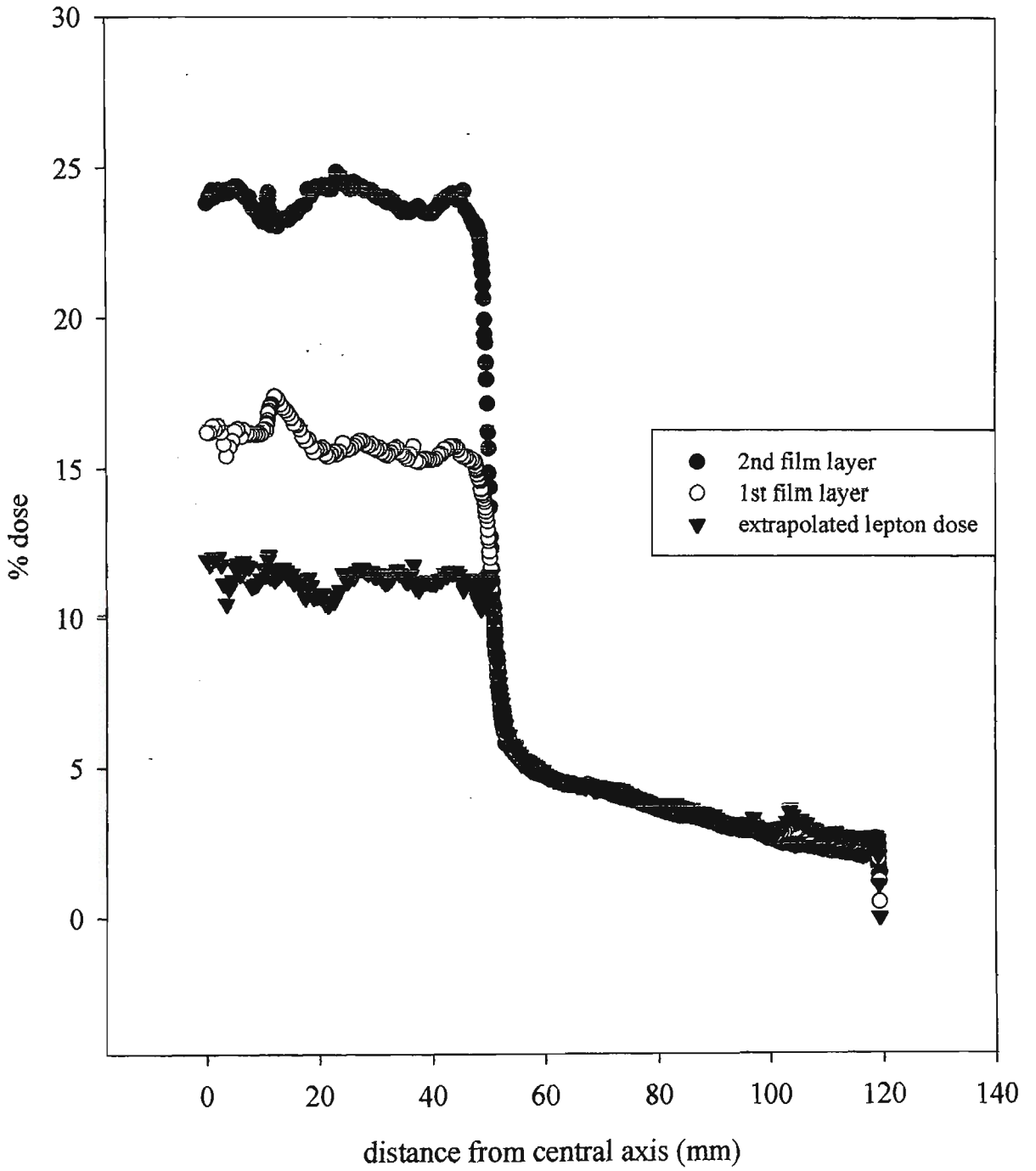

Figure 3.33 : The absorbed dose recorded with the first two films placed on the extrapolation stack and the extrapolated electron contamination dose measured using this technique at a 10cm x 10cm field size.

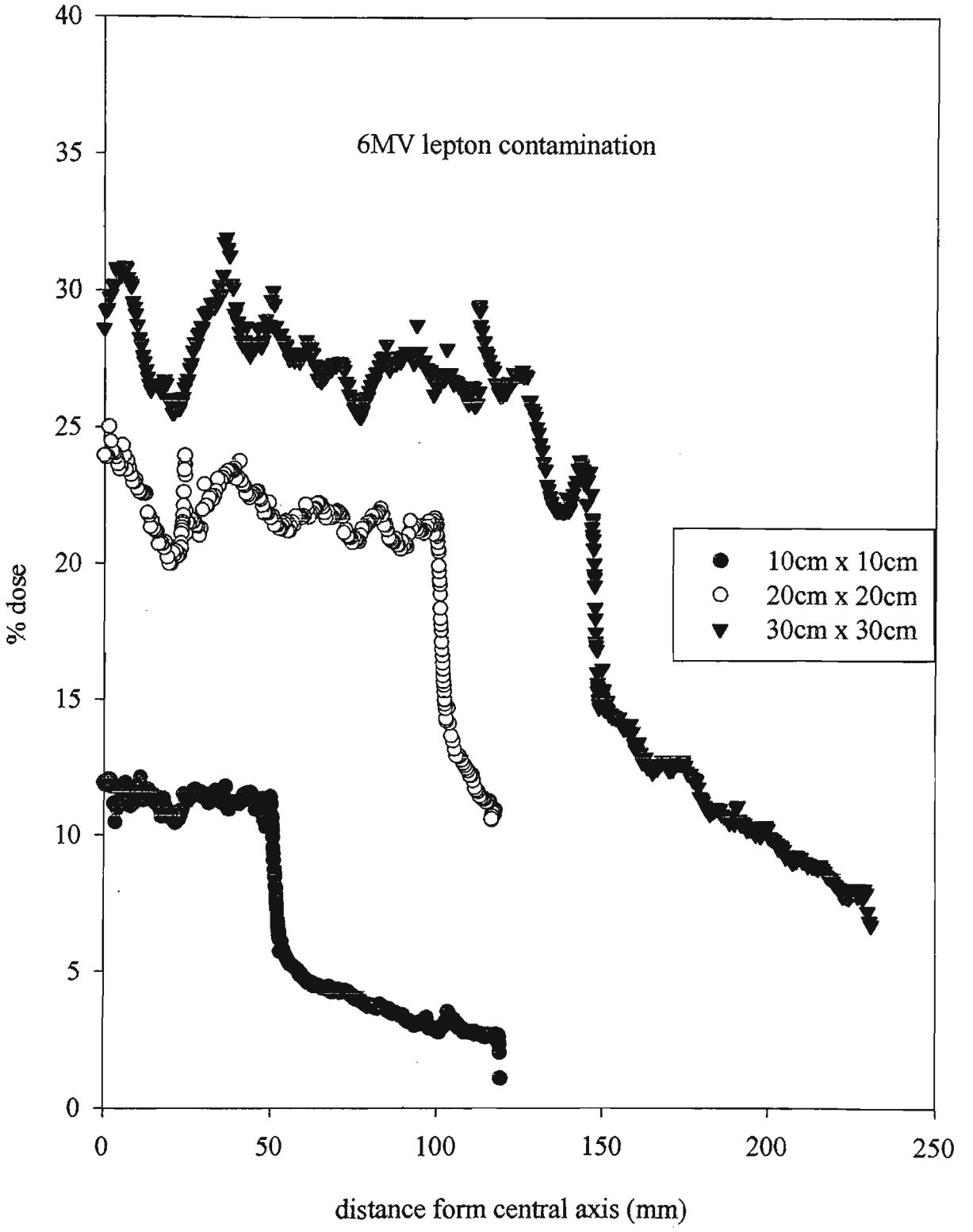

Figure 3.34a : The extrapolated electron contamination surface dose across a profile of a few typical clinical field sizes at 6MV x-ray energy.

There is NO p. 172 in original document

Fractionated treatment

Hypothesis

By placing Gafchromic film in the same position on the patient over the entire treatment, a dose record can be accrued by the time the patient has received a significant proportion of their treatment (ie. about 15Gy is required to produce a comparatively readable result). To achieve this aim, the film dose response needs to be linear over a range of doses given per fraction.

Table 3.5 shows the optical density/total dose obtained over various dose fractionation regimens to the same total dose. The films were irradiated to a total of 50Gy over a 4 week period in 20 x 2.5Gy. This typical clinical regimen was compared with 50Gy single exposure and other fractionated regimens. Results show that similar optical densities are achieved as a final result for all films. This investigation shows a constant response for this dosimeter which is independent of dose fraction size. This implies this dosimeter could be suitable as an in-vivo dosimeter used to integrate a dose record over several patient dose fractions. However, as mentioned in chapter two, the effects of temperature during irradiation which may be varied when used in-vivo could effect the accuracy of measured dose. Another important consideration would be to keep the film in a light tight envelope until the end of treatment to avoid effect due to ambient light.

As the dosimeter showed a constant response it was tested on an anthropomorphic phantom as an in-vivo skin dose monitor. Figure 3.35 shows a surface dose profile obtained when placed on a uvex head cast across the neck of an anthropomorphic phantom. A lateral field was applied. The surface dose profile follows the contour of the neck across the entry side and over to the exiting side of the beam. Results show an increasing surface dose as the angle of incidence to the neck increases.

Table 3.5 : Comparison of fractionated dose regimens on Gafchromic absorbed dose response.

Number of fractions	Dose per fraction (Gy)	Relative optical density	Absorbed dose (compared to 50Gy last day)
20	2.5	0.624	50.2
10	5	0.621	50.0
5	10	0.625	50.3
2	25	0.624	50.2
1	50 (first day)	0.625	50.3
1	50 (last day)	0.621	50.0

As the film passes over to the beam exiting side of the neck a substantial increase in skin dose is seen. This dose then falls off again as the amount of attenuating material increases with the thickness of the neck.

Conclusions

Gafchromic MD-55-1 film provides accurate measurements for surface dose in radiotherapy beams. Agreement with other dosimeters was found to within ± 3%. Film type MD-55-2 provides a measurement at an effective depth of approximately 0.15mm relating the measured dose to within the dermal layer. Gafchromic film provides a 2-D skin dose mapping tool and will be especially useful on curved surfaces where differences in absorbed dose are seen, ie. phantom breast, and head/neck treatments. The most viable option for this device appears to include mounting the film on a patient head cast in a light tight container, eg. a film envelope.

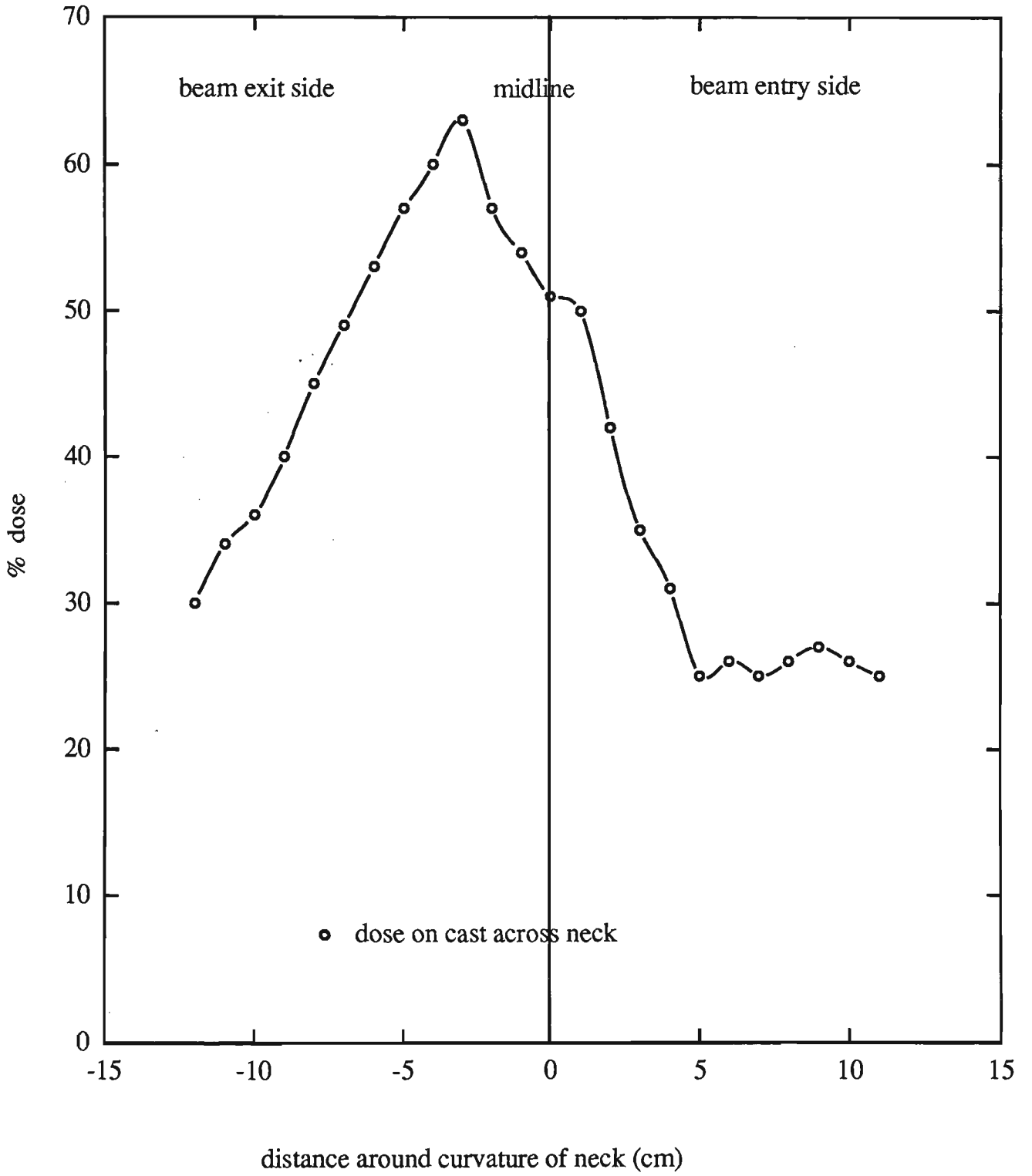

Figure 3.35 : A surface dose profile obtained with MD-55-2 film which is placed across the neck region of an anthropomorphic phantom. Note the incidence angle effect, where the surface dose increases with incident angle. When the film has passed the apex of the neck a reduction in dose is measured due to the exponential decay of the x-ray beam as it passes through the neck tissue.

3.9 Magnetic removal of linear accelerator contaminates

Rationale

It is sometimes desirable to reduce the electron contamination component of a medical linear accelerator x-ray beam from reaching the patient. Electron filtering using high atomic number attenuators is the subject of further investigation in appendix one of this thesis. Another method to achieve this is to apply a magnetic field to sweep contamination electrons away from the beam path. Electrons experience a force perpendicular to their direction of motion in the presence of a magnetic field. Thus electron contamination could be removed from an x-ray field.

Magnets

The aim of our study was to develop a very strong magnetic field which was not too heavy or cumbersome to be used in a clinical environment. To achieve this task, we decided to use permanent ceramic magnets. The magnetic characteristics of rare earth lanthanide inter metallic ions are very complex when compounded with transition metals such as iron. At sufficiently high temperatures above the curie temperature, they exhibit paramagnetic properties, ie. they are soft magnets and are only magnetic in the presence of another electromagnetic field. Upon cooling, the magnetic entropy is extracted and the material becomes 'hard' producing a permanent magnetic moment. The neodymium iron boron, NdFeB, compound used has a sufficiently high curie temperature (approx. 300° C) that it becomes permanently magnetised at room temperature. With an approximate percentage by weight of Neodymium 38%, Iron 60%, Boron 1% , the magnet exhibits Ferro and Ferri magnetic properties as well. These magnets exhibit a high magnetic flux, light weight and a high curie temperature.

Results

Figure 3.36 shows the magnetic field strength across the poles of the NdFeB magnetic deflector. Results were measured in planes across the magnet at the centre parallel to the main field direction. Field strengths up to 0.622 Tesla were recorded near the magnet faces with a pole separation of 6cm and reduced to a minimum of approximately 0.085 Tesla at the centre when the pole separation was 26cm.

As magnetic fields are dipole interactions, each pole strength is enhanced/diminished by its pole pair distance. This restricts the field strengths attainable for larger fields. Field strength variations measured with a magnetic flux meter in the axis normal to the pole faces is shown in figure 3.37. Field strengths with pole separations 6cm, 10cm, 15cm and 20cm are given. Zero centimetres on the x-axis refers to the plane across the central axis of the two magnetic poles with the positive and negative distance being above and below the magnet respectively. The magnetic field strength at the pole midpoint is greatest when the pole separation is the smallest. The magnetic field gradient is also the greatest at this pole separation when moving off axis. This relates to a higher flux density in this arrangement with the dipole lines of force not being allowed to spread away from the poles. This effect can produce a greater field strength for larger pole separations at small distance off axis.

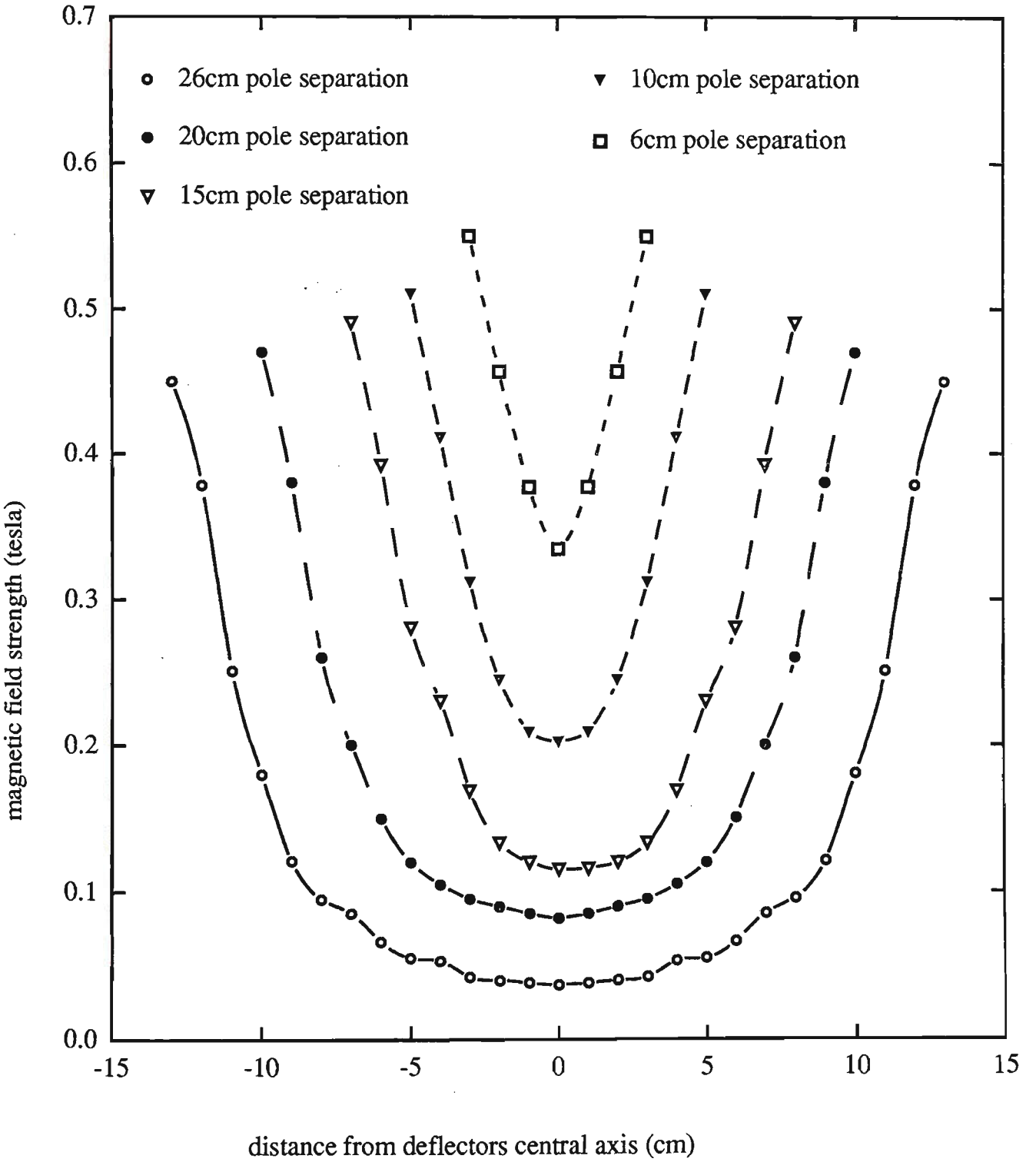

Figure 3.36 : Magnetic field strength across the plan of the electron deflector in various configurations. The magnetic field becomes stronger as the pole separation decreases.

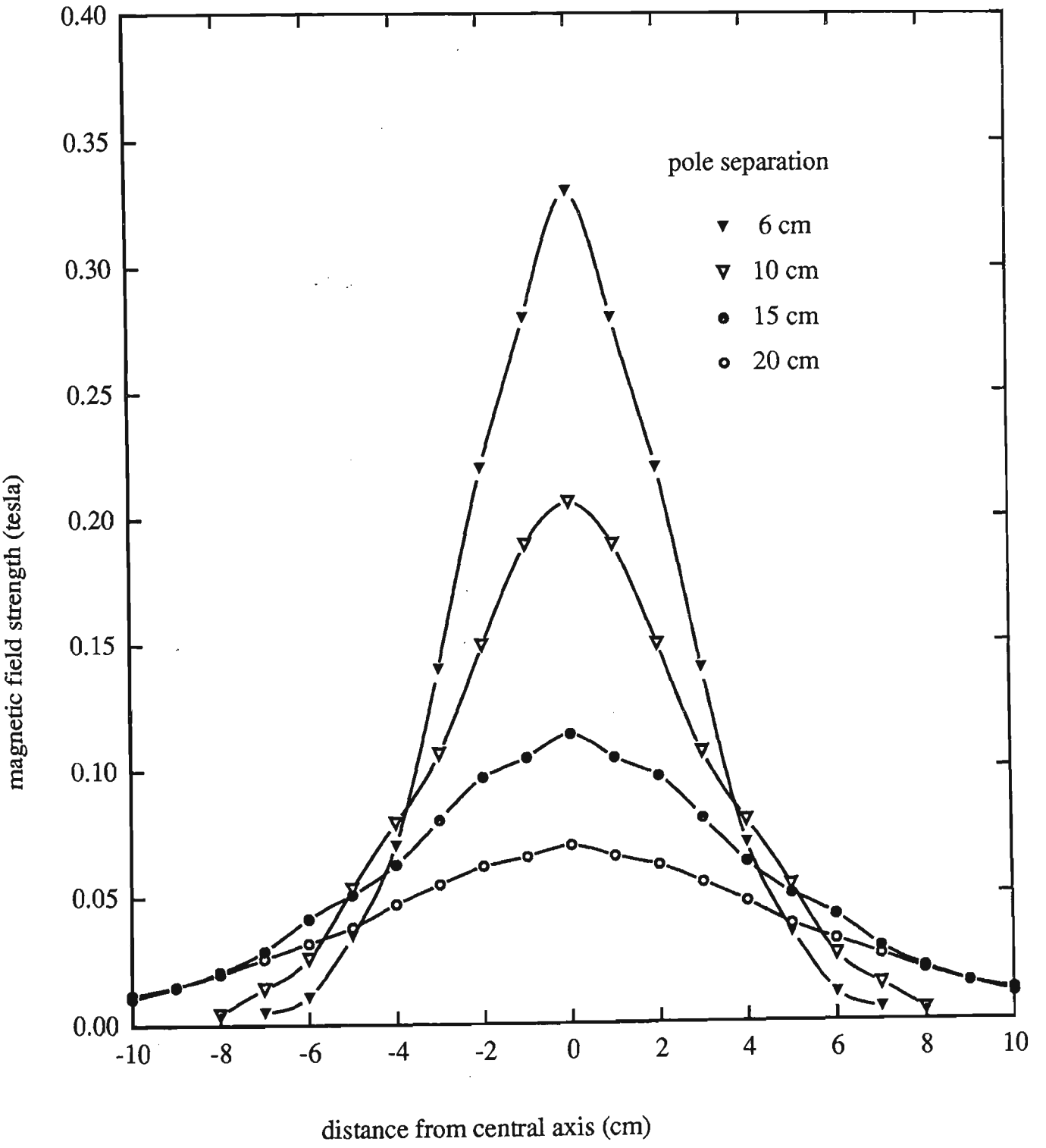

Figure 3.37 : Magnetic field strength perpendicular to the field direction for the magnetic deflector.

Figure 3.38 shows a computer enhanced x-ray image of a 10cm x 20cm 6MV x-ray beam at a position 6cm below the magnetic deflector holder position. The magnetic deflector was removed during this exposure. The Ag-Br Kodak X-OMAT V x-ray film was suspended in air. Shown are the x-ray interactions within the thin layer of film material and the Compton electron contamination incident producing a scattered dose distribution. Results were obtained with energy dependent film thus the film produces a qualitative result but gives no indication of actual dose deposition. Figure 3.39 shows another computer generated x-ray of the same field size and position of film with the NdFeB magnet in the block tray accessory mount. The magnetic field was perpendicular to the x-ray direction. Shown is the x-ray interactions and the swept electron contamination following a path relatively perpendicular to the magnetic field.

The x-ray images shown provide a qualitative picture of the presence of electron contamination and the effect of the magnetic field. Figure 3.38 shows the slightly ellipsoidal ring of electron contamination around the rectangular field size. Perhaps this pattern is produced by electrons scattering at large angles and spreading out past the last point of collimation which in this instance is the lower variable collimators. When the magnetic field is present the electrons are partially swept out of the treatment field via the Lorentz force as shown by figure 3.39. The electrons are bunched together as they are swept due to the magnetic gradient between the poles. The magnetic field is much stronger at the field edges (close to magnetic poles) than in the centre. Also it can be seen that a small percentage of particles are swept to the opposite side of the field. This would be due to two occurrences:

i) electrons that have performed a loop approaching 360° and then escaped the magnetic field to be projected to the opposite direction

ii) a small percentage of positrons produced via pair production and swept in the opposite direction to the electrons

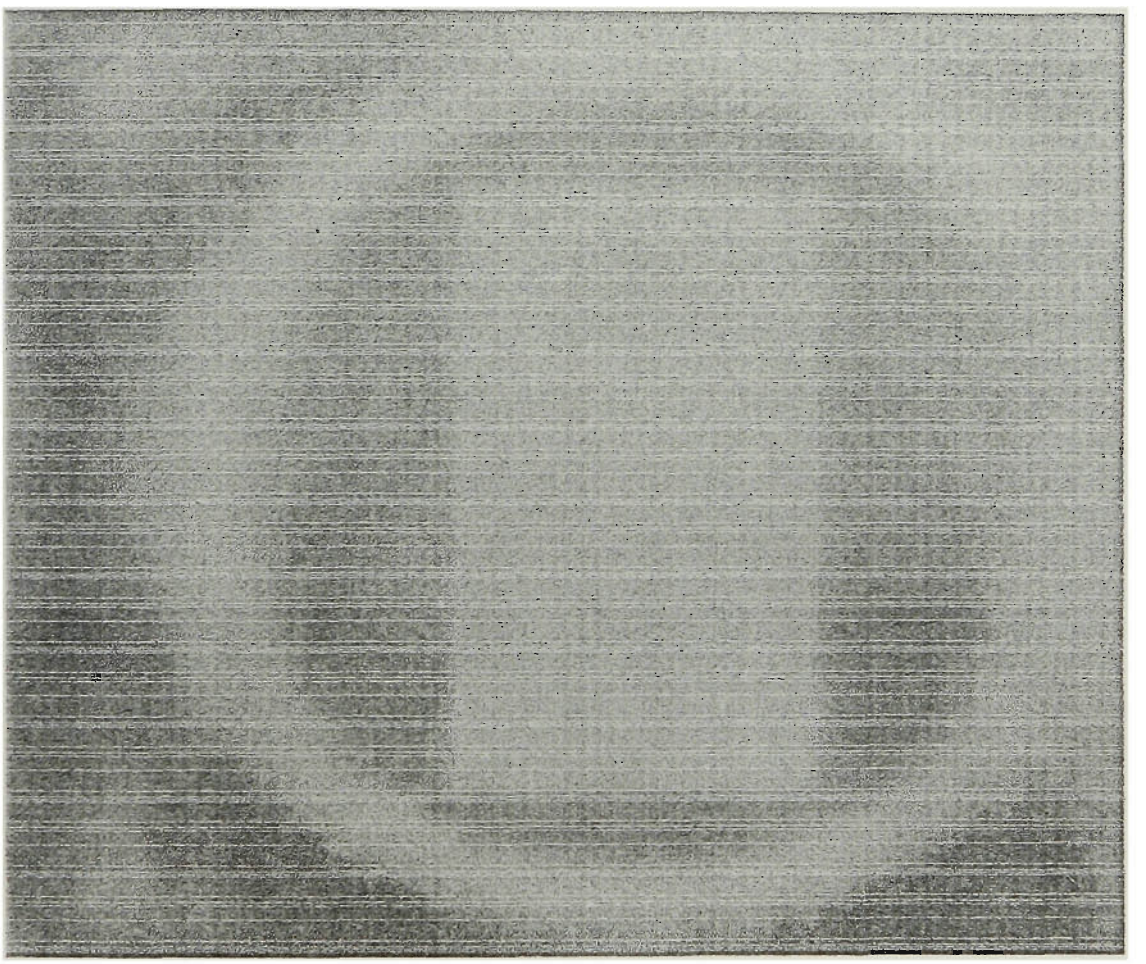

Figure 3.38 : Digitally enhanced radiographic image of an x-ray beam. Picture shows the rectangular x-ray beam and a ring of electron contamination.

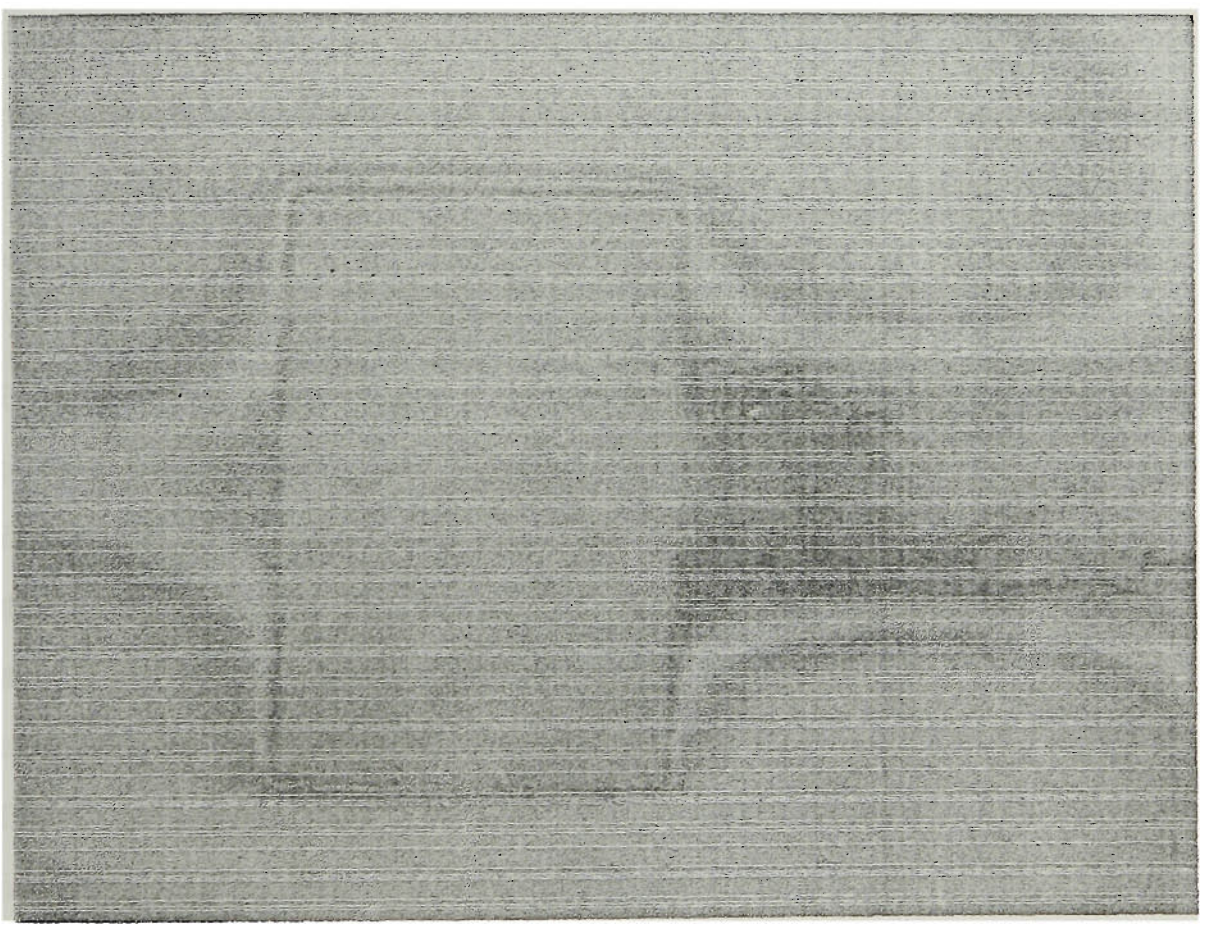

Figure 3.39 : Digitally enhanced radiographic image of an x-ray beam with the magnetic deflector attached to the linear accelerator. Shown is the unaffected rectangular x-ray beam and the electron contamination being swept away by the magnetic field.

Note that this is small compared to the levels swept on the other side. The magnetic field produced is non-uniform. If a uniform magnetic field strength existed then the electron would move in a circular path at right angles to the field and with a constant velocity parallel to the field. In a non-uniform field the electron experiences an increase and subsequent decrease in field strength as it passes through the deflector. In this situation the electrons path will be hyperbolic. It will start on a large radius of curvature with lower field strength which will narrow down until a maximum induction occurs followed by a broadening of curvature again as it passes by the poles to the other side.

Experiments to ascertain the magnetic devices ability to deflect electrons was performed with monoenergetic high energy electron beams. Electron energies ranging from 6MeV up to 20MeV were passed through the magnetic deflector to determine their deflection angles. A 1.0cm x 1.0cm monoenergetic electron beam was directed through the magnetic deflector with various pole separations. The lateral distance, the electron beam was deflected from the central axis was measured using radiographic film placed perpendicular to the beam axis. A deflection angle was calculated from trigonometry by the relationship of longitudinal and lateral travel.

The effect of magnetic field was measured for electrons ranging in energy from 6MeV to 20MeV. The electron contamination produced by x-ray interactions will be in the energy range of 0.5MeV to 3MeV. Therefore, the values for deflection angles by the magnetic field were extrapolated from the above measurements. A third order polynomial function was employed for this. Figure 3.40 shows the deflection angles as a function of energy at different field strengths attainable. This figure gives a guide for determining if electron contamination will still be present in the beam at various field sizes and field strengths. For example, with a 6MV x-ray beam of 10cm x 10cm field size. The field strength attainable by the magnetic deflector is 0.33 Tesla at the centre. If all electron contamination is less than 6MeV energy, the smallest deflection angle

would be approximately 45°. This is interpolated using figure 3.40. From simple geometry, this would relate to a deflection distance of approximately 30cm from the magnetic deflector (at 70cm from the source) to an SSD of 100cm. This would theoretically remove all contamination produced above the deflector. In the case of a 40cm x 40cm field size, the magnetic field would be approximately 0.085 Tesla. This would produce a maximum deflection angle of 30° and a minimum deflection angle of 20°. At 100cm SSD this relates to a deflection distance of 11cm to 17cm. Thus electron contamination is not totally removed from the beam. To remove all the electron contamination from the beam above the deflector a deflection angle of approximately 50° is required as a minimum. To achieve this deflection using this rationale, a field strength of approximately 0.35 Tesla is required. To perform this with a similar structured magnetic deflector as we have used, the field strength at the poles would have to be approximately 5 times larger than at the centre, or 1.5 Tesla. To theoretically produce this field strength, approximately 50-75kg of NeFeB material would be needed in the deflector. This would be too heavy for convenient placement and removal from the linac treatment head. An alternative might be to increase the effective strength of magnetic field. This could be achieved by placing another magnetic field closer to the x-ray source. This could be smaller in size as the divergence of the x-ray beam at this point would be smaller and the magnetic poles could be closer. It would 'start' the deflection process which would be finished by the second deflector. This feature is incorporated into the design of some racetrack microtrons.

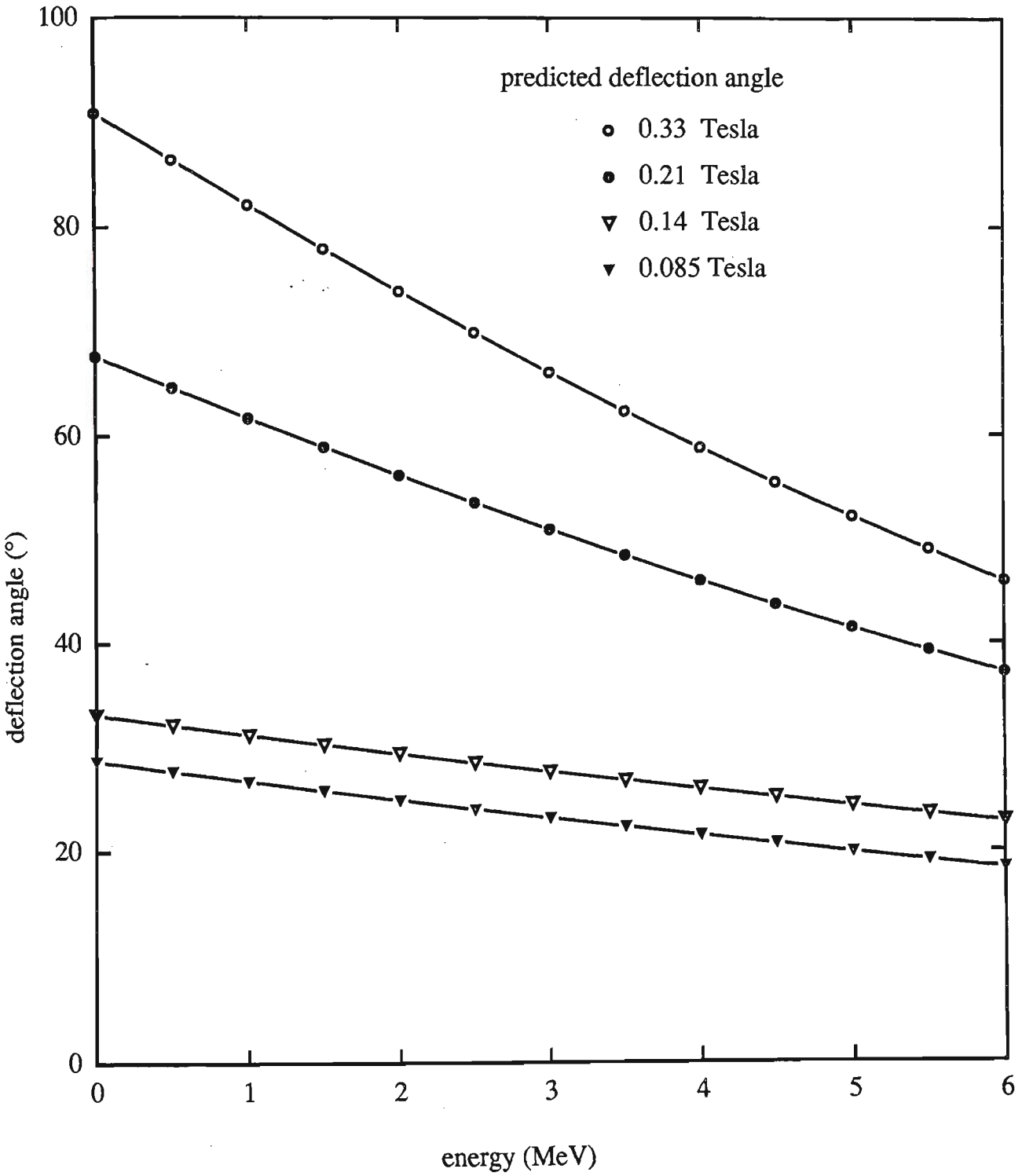

Figure 3.40 : Predicted deflection angles (for electrons) produced by the magnetic deflector. As the field strength increases the angular deflection increases.

Skin dose outside the field

One concern when dealing with sweeping electron contamination is the dose delivered off central axis. Figure 3.41 shows the off axis percentage surface dose profiles for a 20cm x 30cm (x,y) field size with and without the magnetic field. Scans were performed along the x and y axes of the beam from the central axis. Results showed a reduction in surface dose along both x and y profiles with the magnetic field. This reduction can vary for larger field sizes where the field strength attainable is not large enough to remove all contamination out of the treatment field. However an enhancement of dose is never seen. If contamination is swept to a position still on a patient, attenuation material such as 1.5cm blocks of wax or a thin sheet of lead could be placed next to a field to absorb the electron contamination.

Figure 3.42 shows dose build up curves for 6MV x-rays ranging from 10cm x 10cm up to 35cm x 35cm field sizes for open beams without the magnetic field. Surface doses range from 16% to 40% of D_{max} respectively. With the addition of the magnetic field the percentage dose build up curves for the same field sizes are shown in figure 3.43. Surface doses now range from 10% to 31% for 10cm x 10cm to 35cm x 35cm field sizes respectively. By subtracting the percentage dose results for the open field magnet results from no magnet results, differences which represent electron contamination swept off the central axis are also shown in figure 3.43. Surface dose differences range from 6% to 15%. Figure 3.44 shows the electron contamination left along the central axis with the use of the magnetic deflector. Results were obtained by a series of steps. Firstly Monte Carlo contamination free simulation results are subtracted from open field (ie. no magnet) results to obtain the electron contamination component. From this, the electron contamination swept away is subtracted to leave dose levels deposited by electron contamination when the magnetic field is present. Evaluation of this graph shows that a considerable portion of low energy electron contamination is still present, depositing dose near the surface.

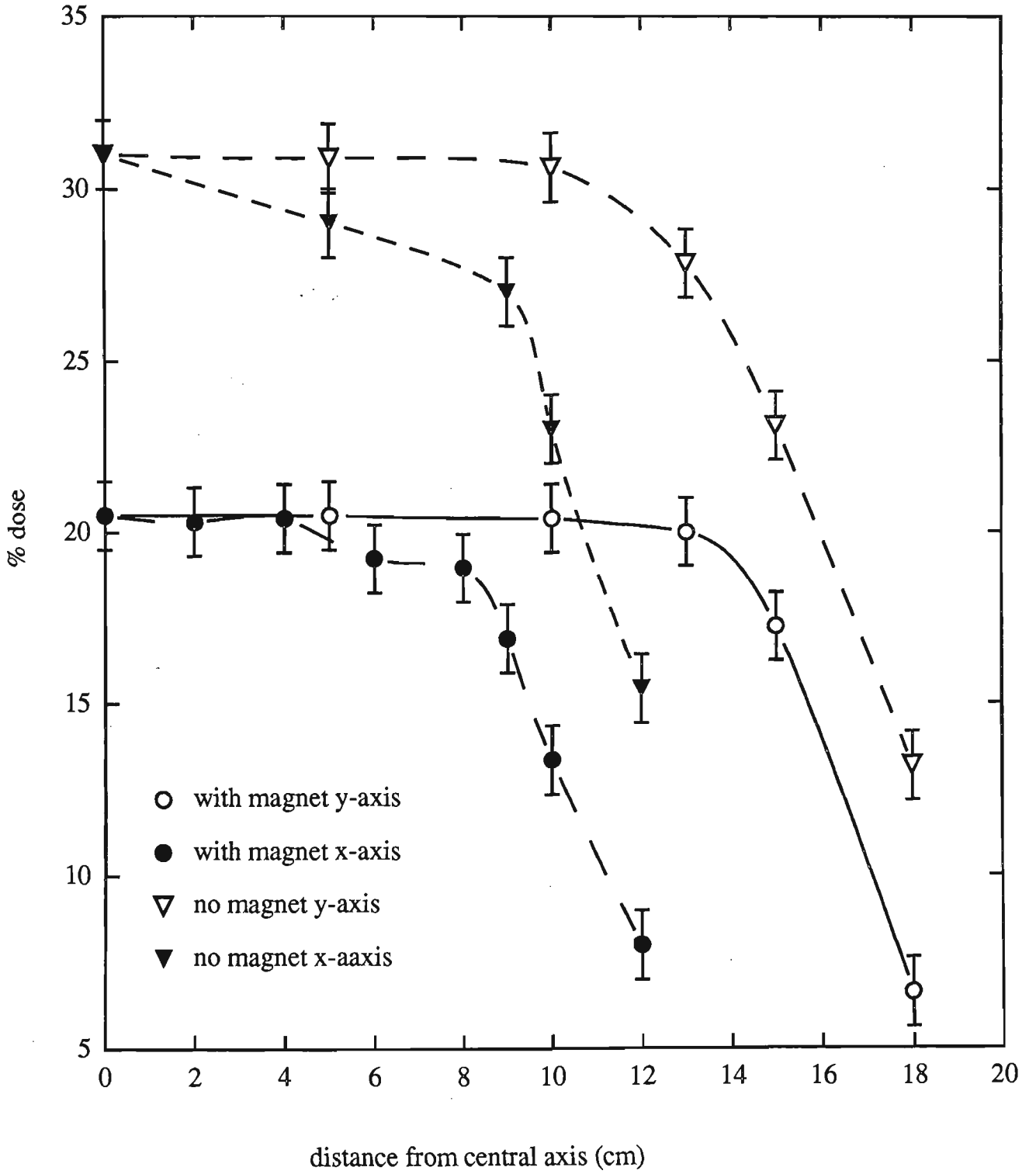

Figure 3.41 : Percentage surface dose measured off axis with and without the magnetic deflector. Reductions in dose are seen in all sights.

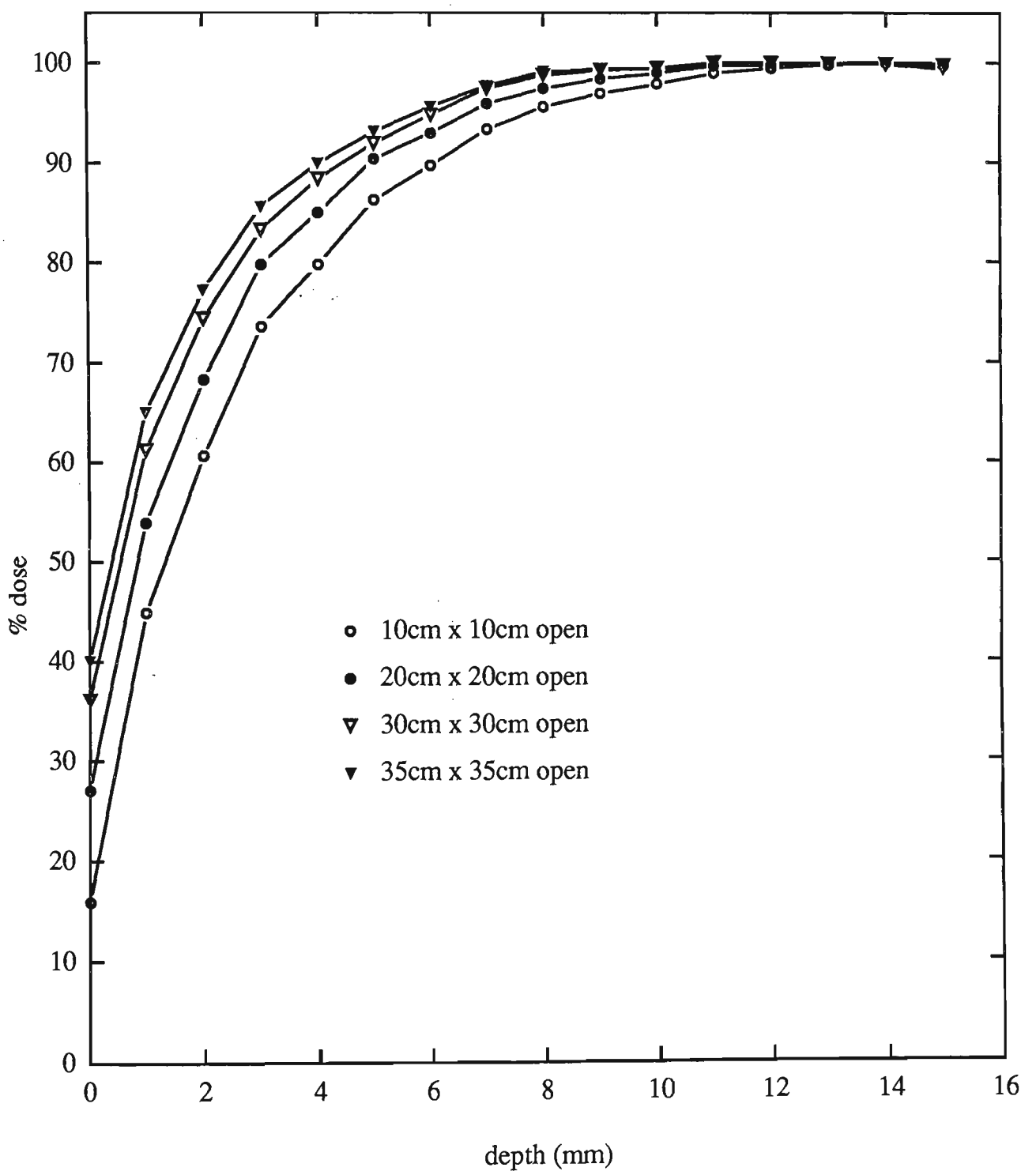

Figure 3.42 : Open field percentage dose build up without the magnetic deflector.

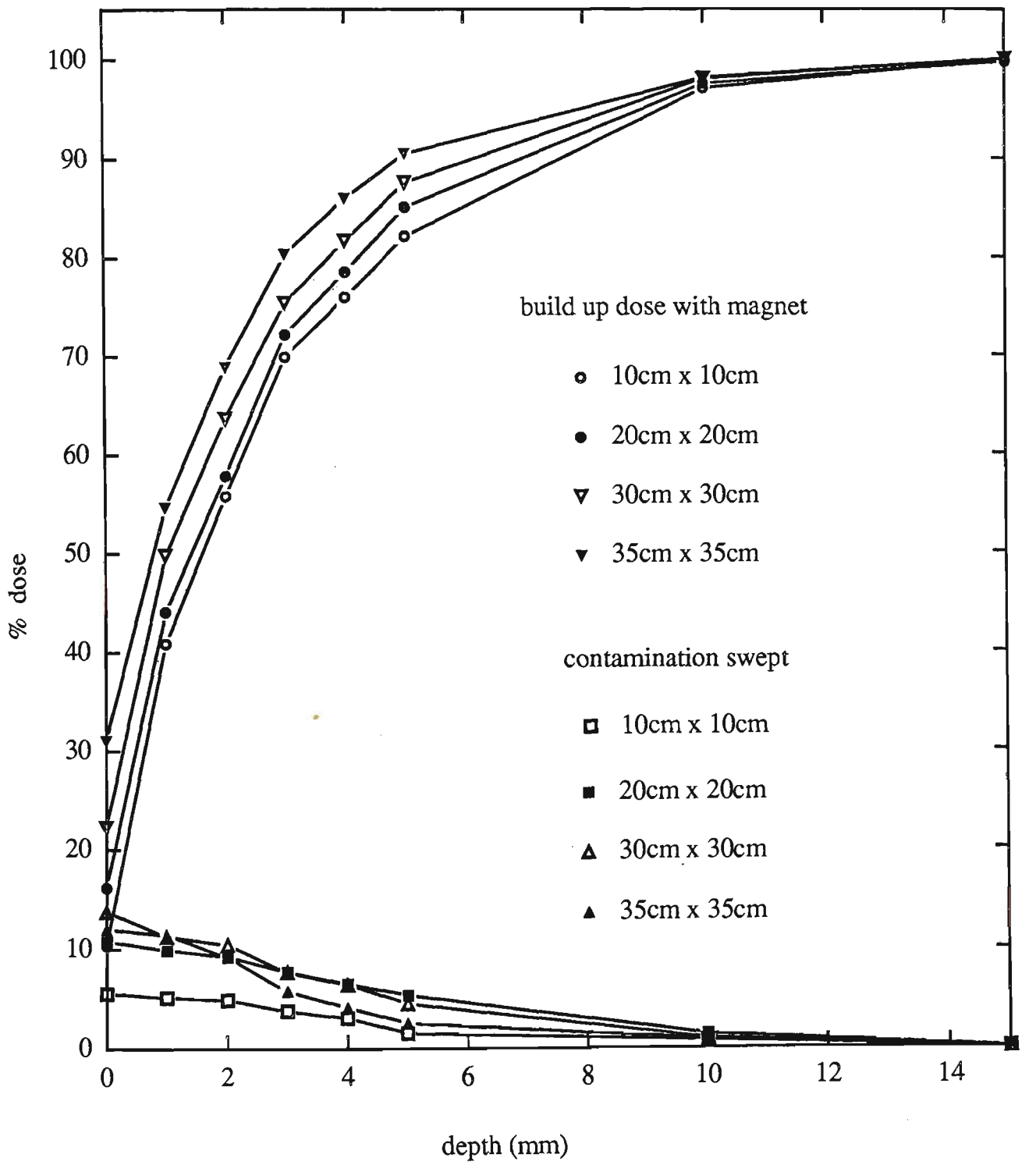

Figure 3.43 : Open field percentage dose build up with the magnetic deflector and the percentage dose from electron contamination swept away by this device.

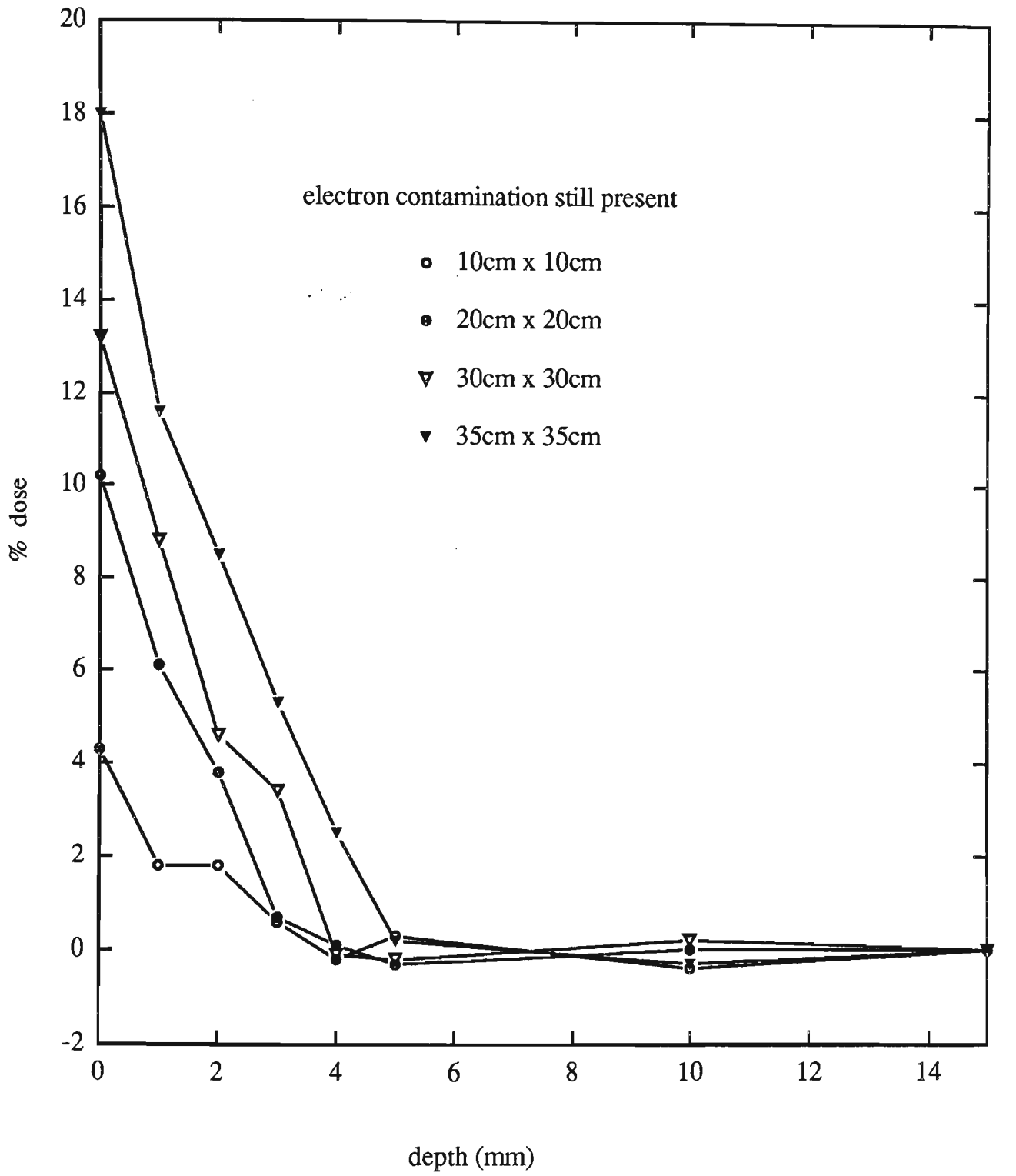

Figure 3.44 : Electron contamination still present in open fields with the magnetic deflector in place.

As the magnet is expected to sweep lower energy electrons to a greater extent than higher energy electrons it can be concluded that the majority of electron contamination still present must be produced after the magnetic deflectors position. The only material between the magnetic deflector and the patient/phantom surface is the air column. This consists of 35cm of air above the patient at 100cm SSD and is field size dependent. The effect of this air column will be examined in more detail in section 3.10.

Block trays

The magnetic deflectors effect on skin dose reduction was also measured for blocked fields. Figure 3.45 shows the percentage dose build up curves for a 20cm x 20cm field size with a 6mm perspex block tray for both magnetic field off and on. Also shown is the contamination swept away which is the difference of the two curves. Surface doses were 19% and 32% for magnetic field on/off respectively meaning 13% of surface dose is removed by the magnetic field on the central axis. Shown in figure 3.46 is the electron contamination dose present for a 20cm x 20cm field size with the 10mm perspex block tray for both magnetic field on/off. Results were obtained with the same procedure as for figure 3.43. Surface doses due to electron contamination were 13% and 27% respectively at this field size for magnetic field on/off. Essentially the magnetic deflector can remove the effects of increased skin dose produced by the use of a perspex block tray.

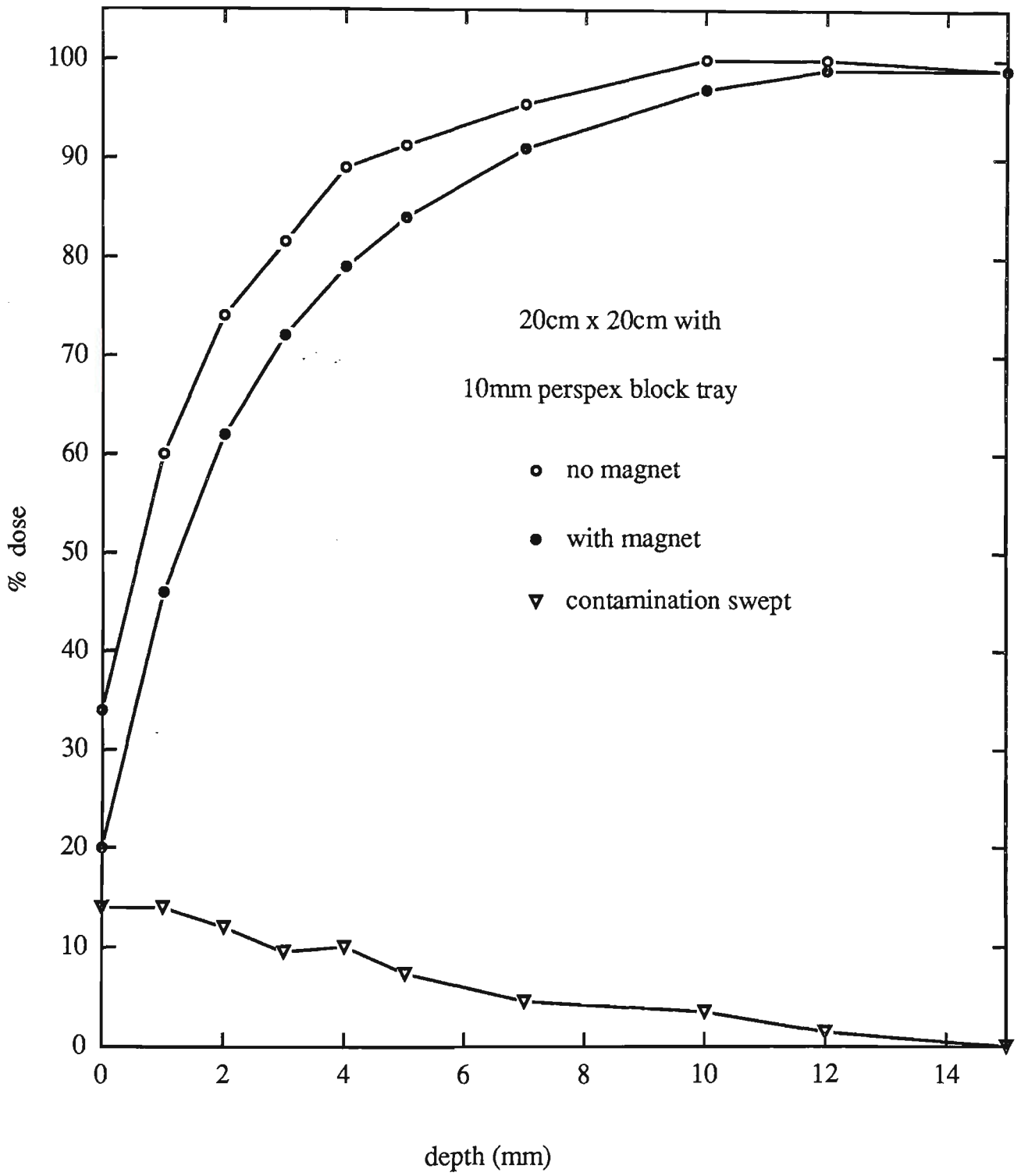

Figure 3.45 : Build up curves for photon fields with a 10mm perspex block tray with and without the magnetic deflector and the electron contamination swept away.

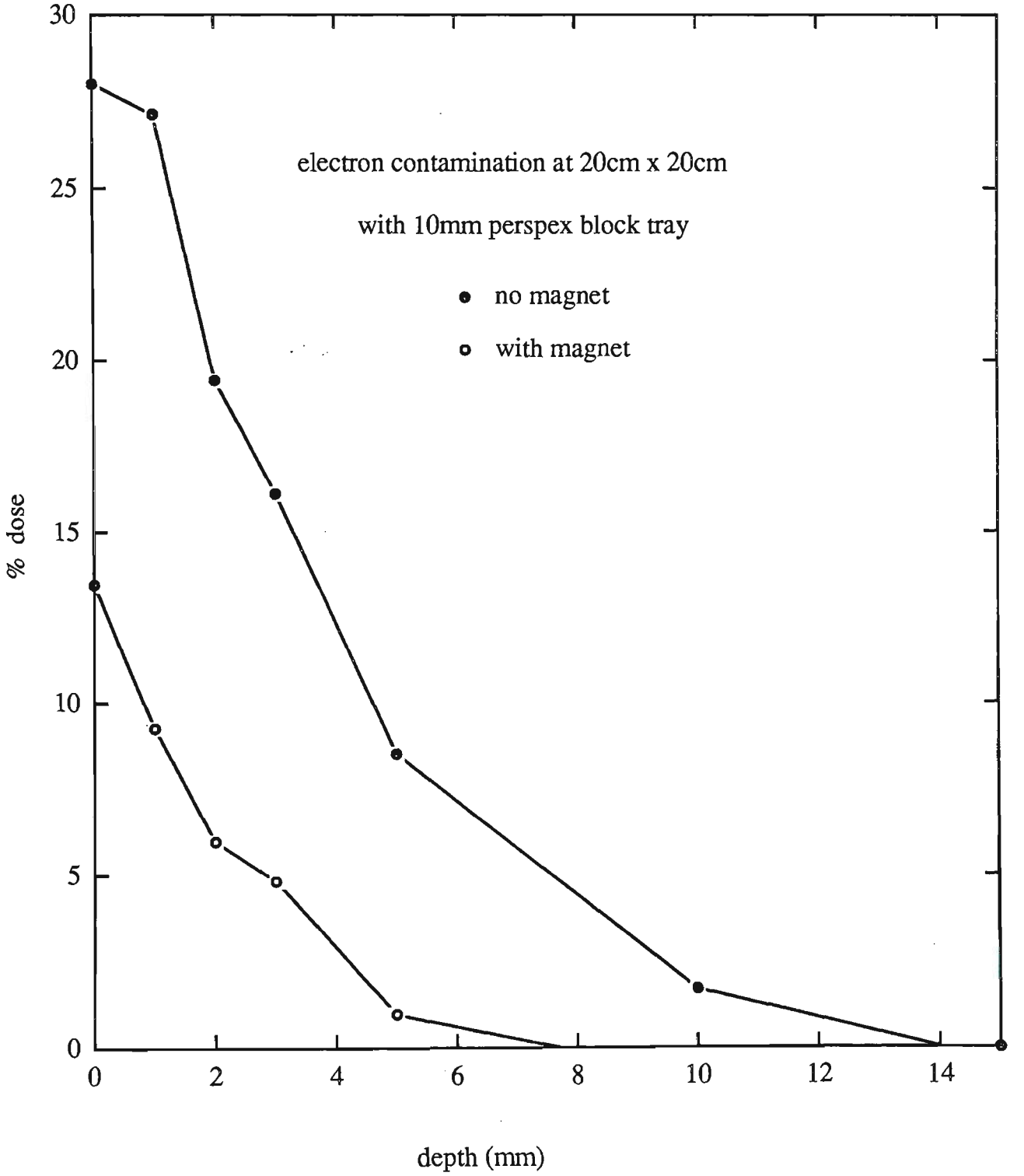

Figure 3.46 : Electron contamination present in a photon beam of 20cm x 20cm field size and a 10mm perspex block tray with and without the magnetic deflector.

Angle of incidence

Because the magnetic deflector removes most of the electron contamination the assumption that electron contamination has a minimal effect on the increase of skin dose with angle of incidence is examined. Figure 3.47 shows the percentage surface dose levels obtained for a 20cm x 20cm field size at oblique angle of incidence with and without the magnetic field present. Results are normalised to 100% at each individual D_{max} position. Subtraction of normal incidence percentage surface dose from oblique beam percentage surface dose for magnetic field on/off is given to show any irregularities in the incident angle effect by the removal of most of the electron contamination. This would also be shown by percentage dose differences recorded at the surface between the two experimental data values at various angles. No major variations were recorded at small angles. Similar results were obtained at depth within the build up region.

The percentage surface dose differences seen between various angles for a 20cm x 20cm field size with and without a magnet as shown in figure 3.47 are constant over the range of angles measured ie. (0-75°). There is a 10% difference which relates to the reduction in electron contamination produced from the introduction of the magnetic field. Its consistency over the range of angles measured points towards the assumption that electron contamination does not play a substantial role in the increase seen in percentage surface dose with angle of incidence. This agrees with analysis of the pure Monte Carlo simulations previously outlined.

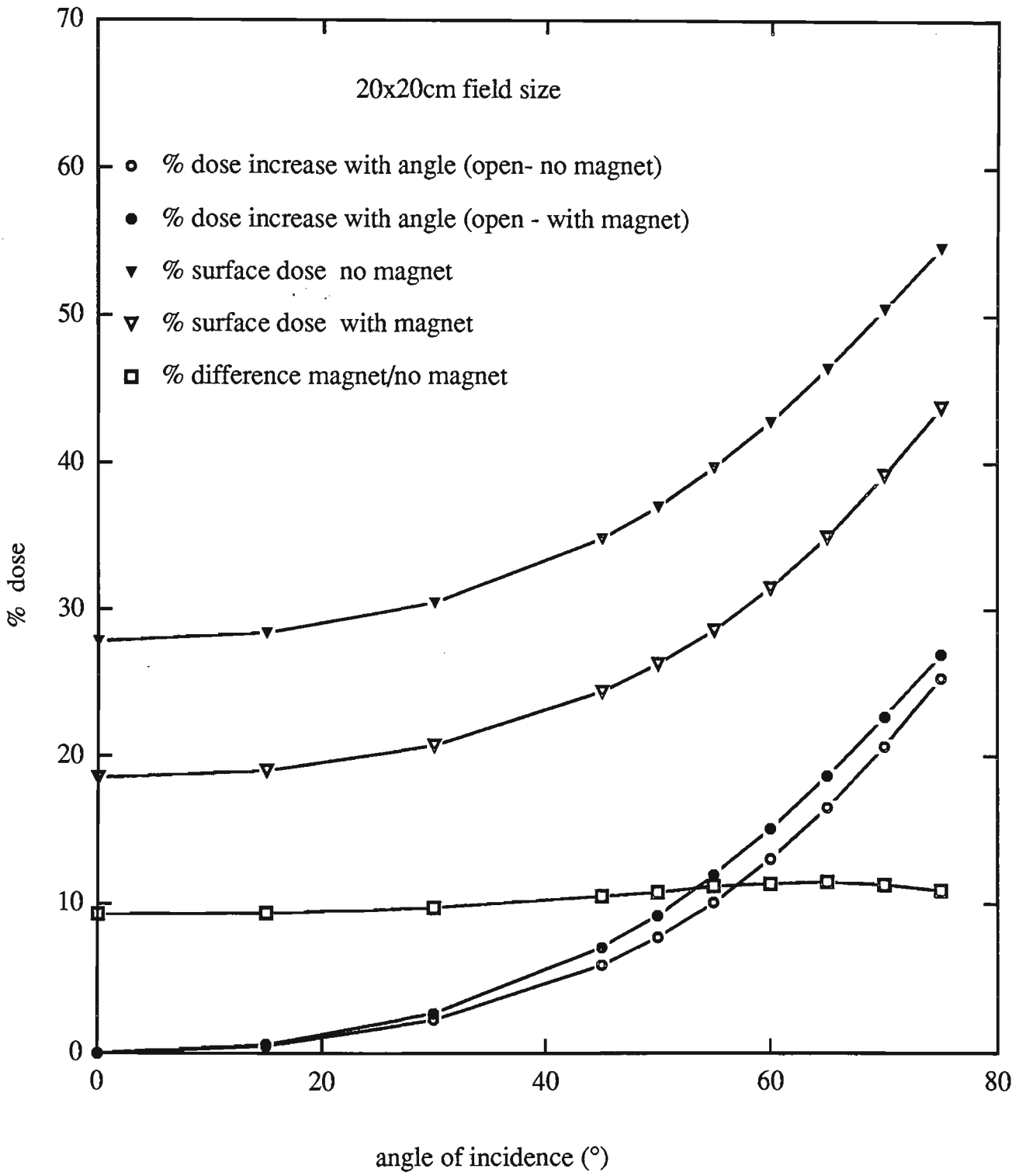

Figure 3.47 : Effects on percentage surface dose at oblique angles of incidence with and without the magnetic deflector.

Conclusions

Ceramic magnets such as the NdFeB magnets are a viable option for clinical use due to their size and weight. Light enough to be removed and replaced easily by one person, the ceramic magnet assembly can reduce skin dose by up to 30% of applied dose for the larger field sizes. This relates to a reduction of up to 60% of the original surface dose.

When the magnetic electron deflector is used clinically, certain considerations have to be accounted for. These being :

i) care must be taken when handling ferro magnetic objects such as cone plugs, metal rulers and iron edged lead blocks

ii) the magnet must be removed for electron treatment

iii) the magnetic device does not reduce dose deposition due to exiting opposed fields (eg. tangent breast fields) where approximately double the dose is deposited to the skin from the exit field as the entrance field (Kron et al 1995)

The NeFeB rare earth magnets have partially reduced the surface dose of the linac x-ray beam by sweeping the majority of the electron contamination away from the central axis. The ceramic magnets have been a useful experimental tool for removing electron contamination.

3.10 Removal of air generated electrons

Rationale

Helium is the closest inert gas available to produce near vacuum conditions. The contamination electrons normally produced in the air gap region directly between the magnetic deflector and the patient, will be significantly reduced with the introduction of helium. Production of a helium bag is a much simpler and cost effective way of removing electron contamination clinically as compared to a vacuum system.

Introduction

The Neodymium Iron Boron magnetic collimator produced a considerable reduction in dose to the build up region by sweeping the electron contamination away from the treatment field. However, on comparison of the percentage dose build up curve produced with the 'pure' photon incident Monte Carlo simulations it was noticed that the Monte Carlo results imply the magnetic device had not swept all (5-10% of D_{max}) of the low energy electron contamination. As the magnet should be more efficient at sweeping lower energy electrons it was possible that the extra electron contamination was due to the 35cm air column located below the magnetic collimator and above the phantom surface. Yorke et al (1989), had previously performed experiments and had shown that the air column above the phantom was capable of producing the electron contamination in question.

Materials and methods : Helium bag and Monte Carlo

The air volume directly below the magnetic deflector reintroduces electron contamination into the x-ray beam. The helium bag system was constructed from 0.02mm thick plastic with thin wire edges and a valve. As shown in figure 3.48 the bag has dimensions 40cm x 40cm x 25cm. Wire edges were inserted firstly to add weight to the device and secondly so the device could be moulded to form an irregular patient shape if required. A release valve was used to pump helium into the bag system. Experiments were performed with the helium flowing through the system and alternatively by injecting and corking the helium bag. Both methods produced similar results for skin dose reductions and thus the second method which reduced the amount of helium was employed.

The helium bag was positioned initially by itself and secondly in combination with the magnetic deflector under the Varian 2100C linear accelerator. Percentage dose build up curves were measured on the central axis for various beam configurations and energies. Results for contamination removed by the helium system alone are quoted along with the total reductions achievable with both systems.

With the helium bag, on top of the phantom, percentage dose build up results obtained are shown figure 3.49. By subtraction of these percentage dose curves from percentage dose build up curves for open fields the quantity of electron contamination removed by the system is attained as shown in figure 3.50. The dose removed is maximum at the surface and falls off quickly, at a depth of 4mm virtually no difference is seen. The short range of dose deposition implies the contamination electrons produced in the air volume directly above the patient are relatively low energy.

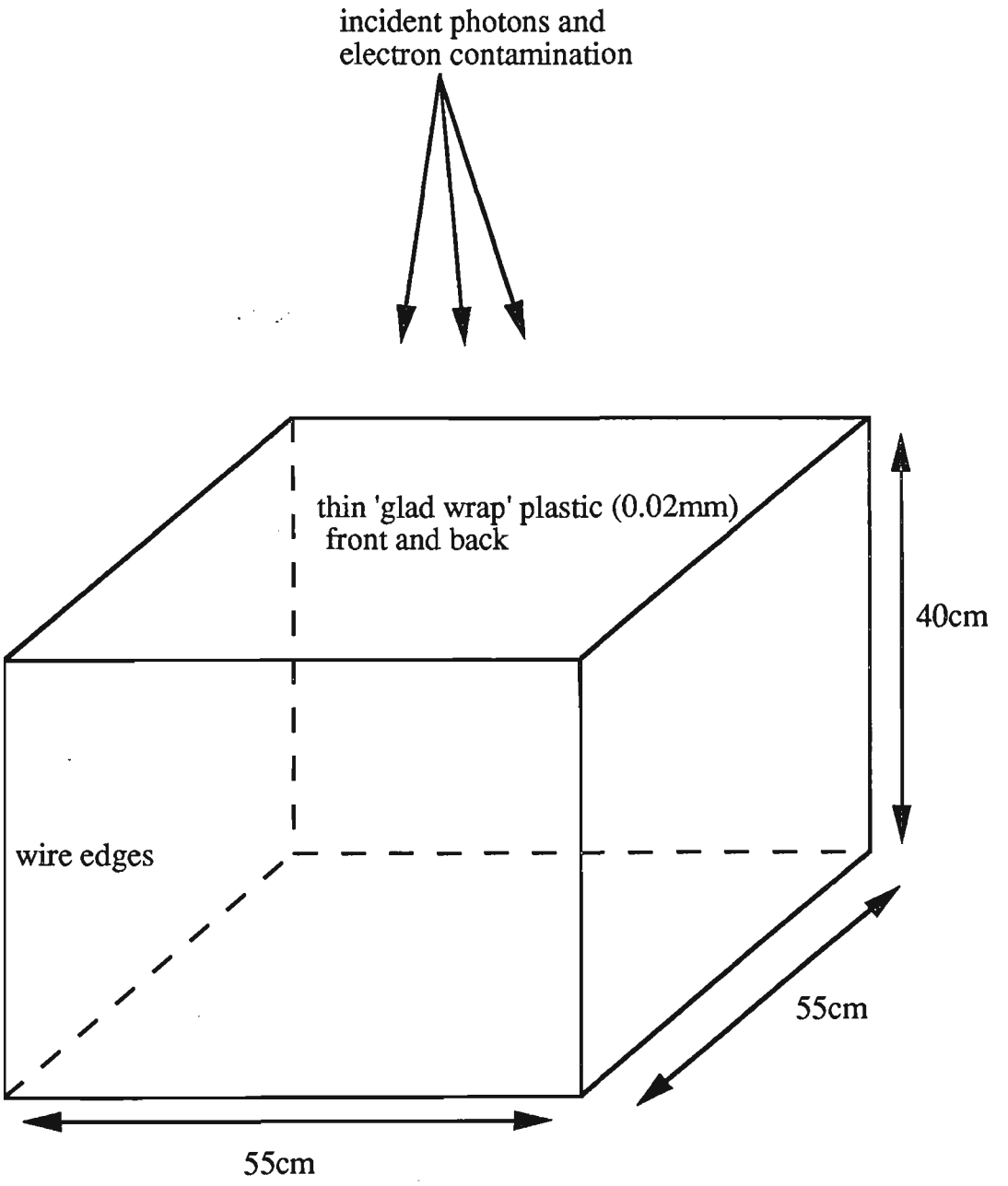

Figure 3.48 : Picture of helium bag system used to eliminate electron contamination produced by the air column.

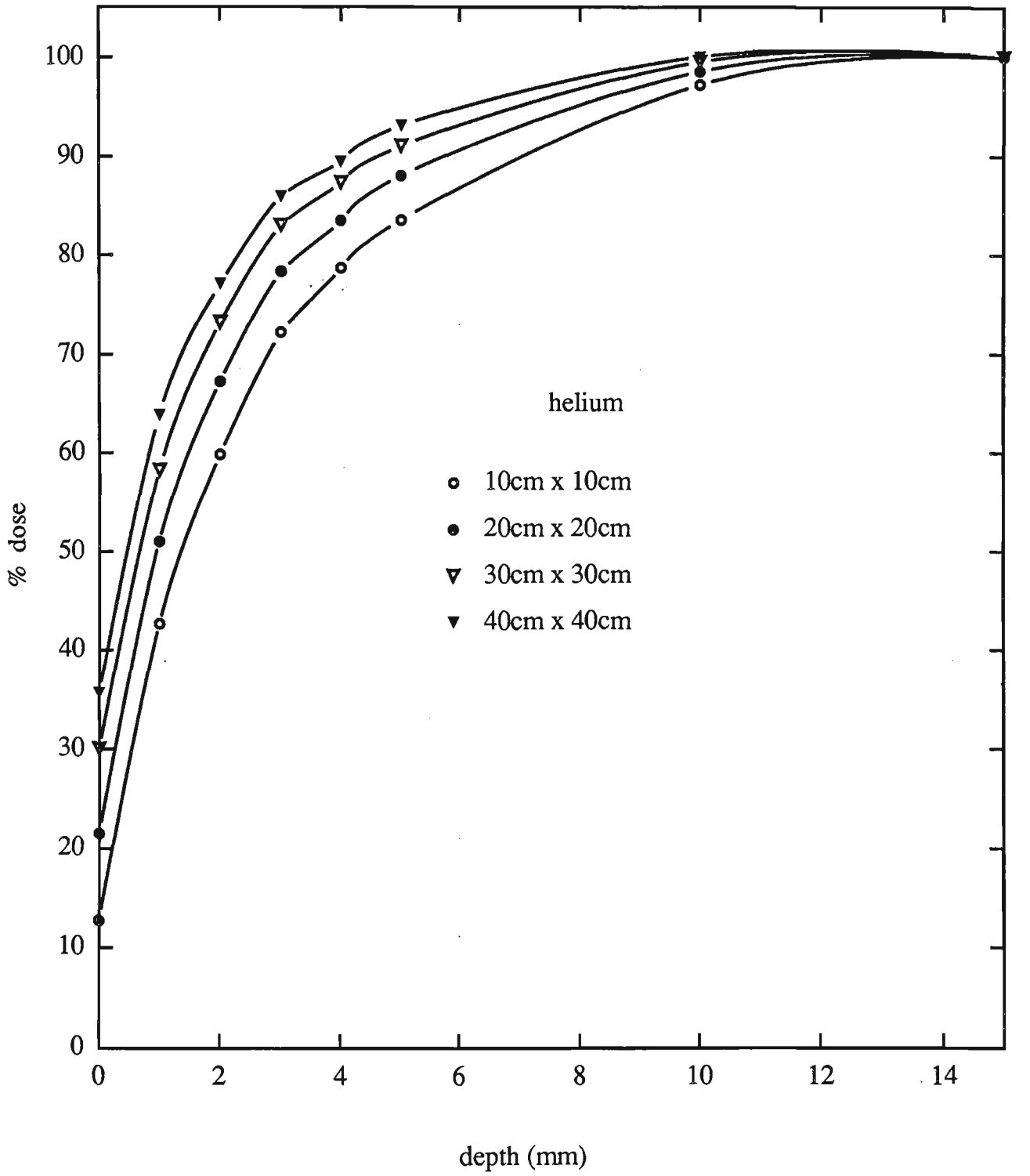

Figure 3.49 : Percentage dose build up produced for 6MV x-rays with the helium bag inserted into the beam

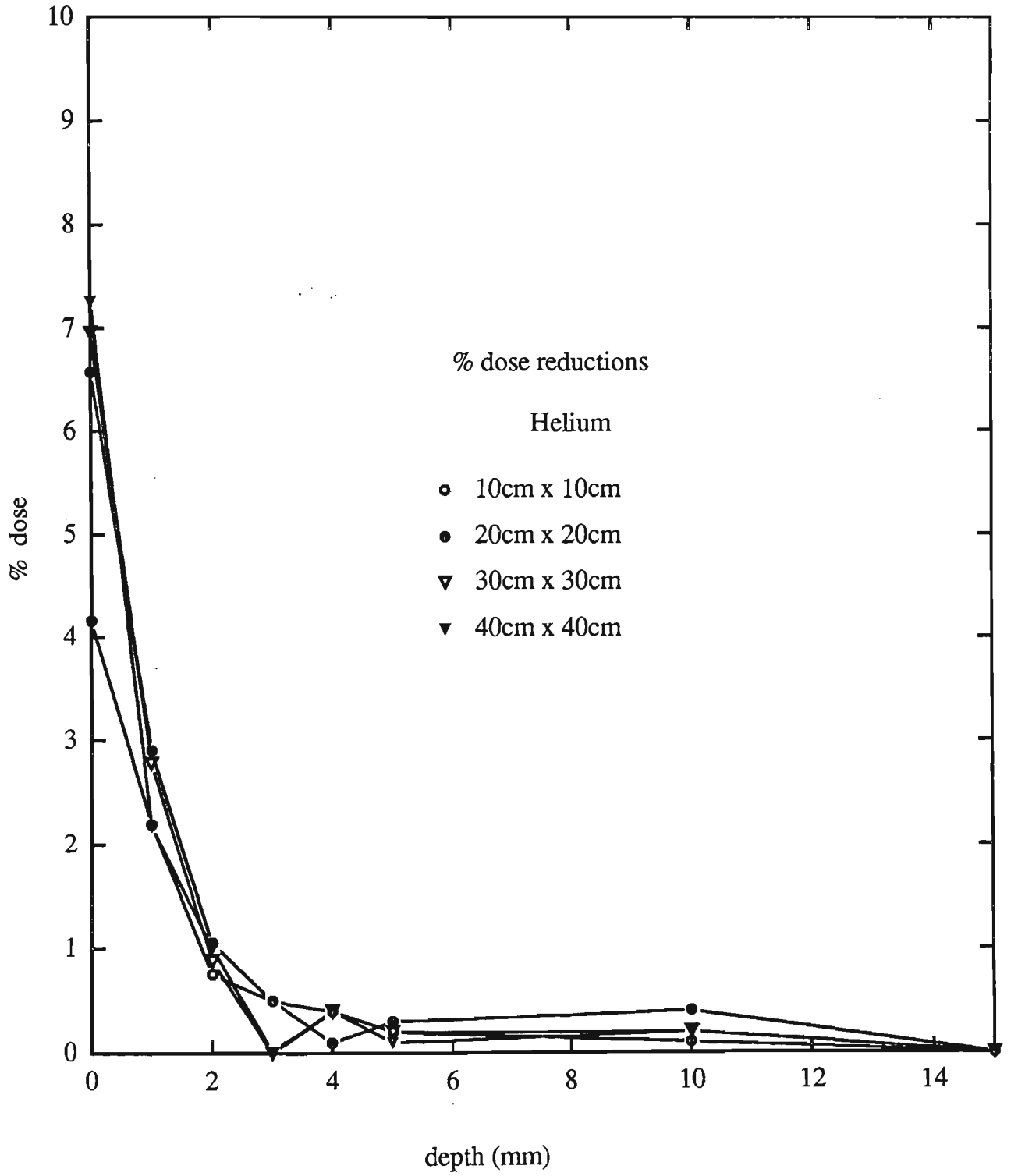

Figure 3.50 : Electron contamination eliminated by the replacement of air by helium.

Monte Carlo simulations were performed to simulate the dose deposition from the air column above the patient. The was performed using the Monte Carlo Neutron Photon (MCNP), Monte Carlo code. Varying volumes of the air column were simulated by changing the boundary conditions for the layer of air above the simulated water phantom. This approach would account for electrons generated directly by x-ray interactions with the air. It does not simulate accelerator head produced electron contamination or 'knock on' electrons produced in the air column by these head produced electrons.

The MCNP Monte Carlo input code for simulations were generated by Martin Carolan (private communication 1996) for this part of the analysis.

Figure 3.51 shows the first 2mm of percentage build up dose as the volume of air directly above the phantom was varied. All results were normalised to 100% at D_{max}. Results are for a 10cm x 10cm field size at 100cm SSD. An increase in extrapolated surface dose of approximately 4% was seen when the volume of air directly above the phantom was increased from 0cm to 20cm. A slight increase to approximately 5% was seen when the air volume was increased to cover the entire 100cm SSD. This is shown in figure 3.52 which also shows percentage dose at 0.3mm depth. A similar trend is seen with an increase in dose due to the air column. A negligible increase in percentage dose was recorded beyond 3mm depth with the MCNP simulations.

Percentage surface dose for experimental data, MCNP simulations with a vacuum and 100cm of air are shown in figure 3.53 as a function of field size. Percentage surface dose increases negligibly when only photon in-phantom scatter is considered. This is shown by the MCNP simulation with a vacuum. Approximately 4% to 5% of D_{max} is recorded at the surface for field sizes from 10cm x 10cm up to 25cm x 25cm.

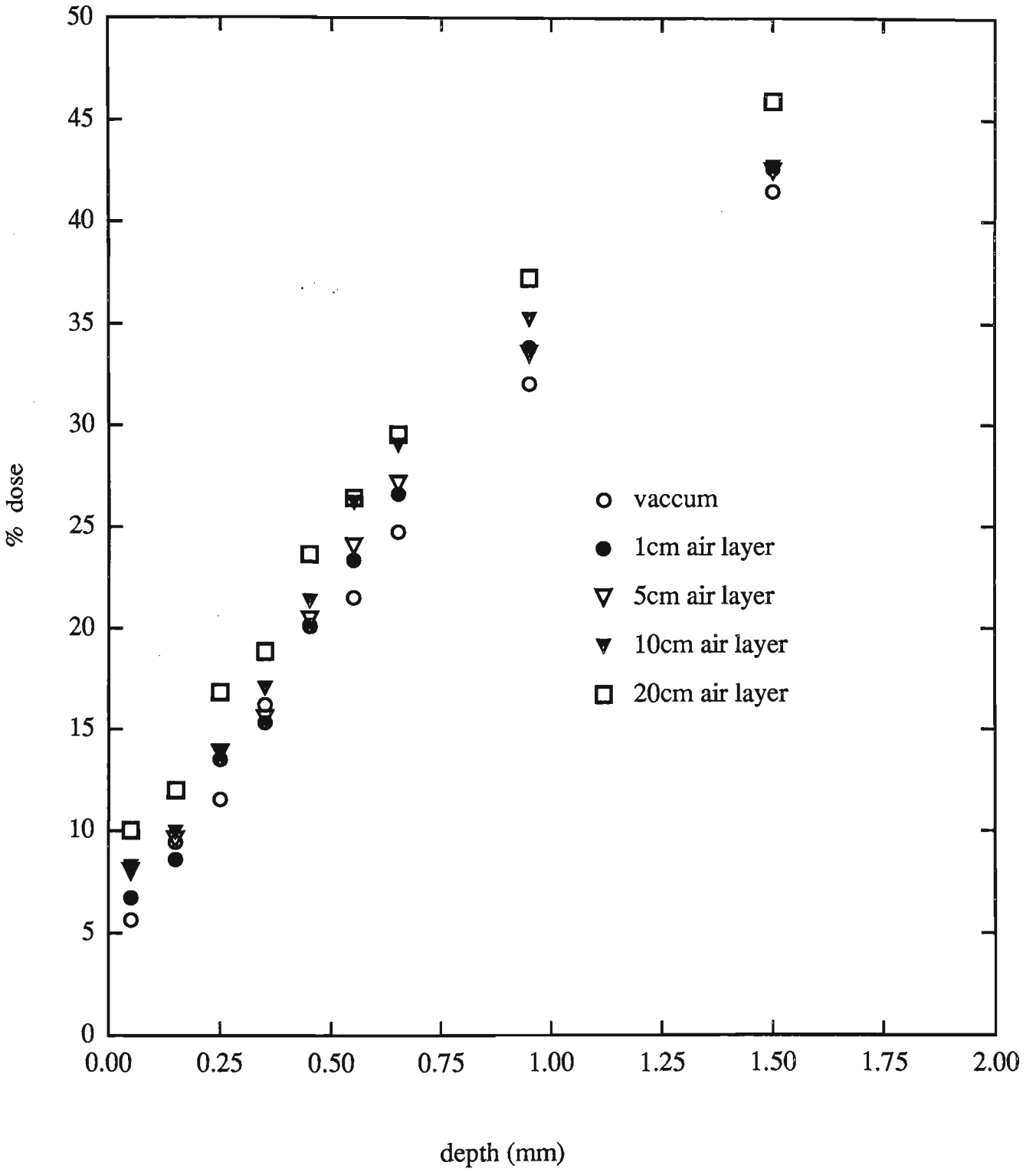

Figure 3.51 : Monte Carlo simulations of the first 2mm of dose build up with varying amounts of air directly above the phantom. As the air column increases so does the percentage dose near the surface.

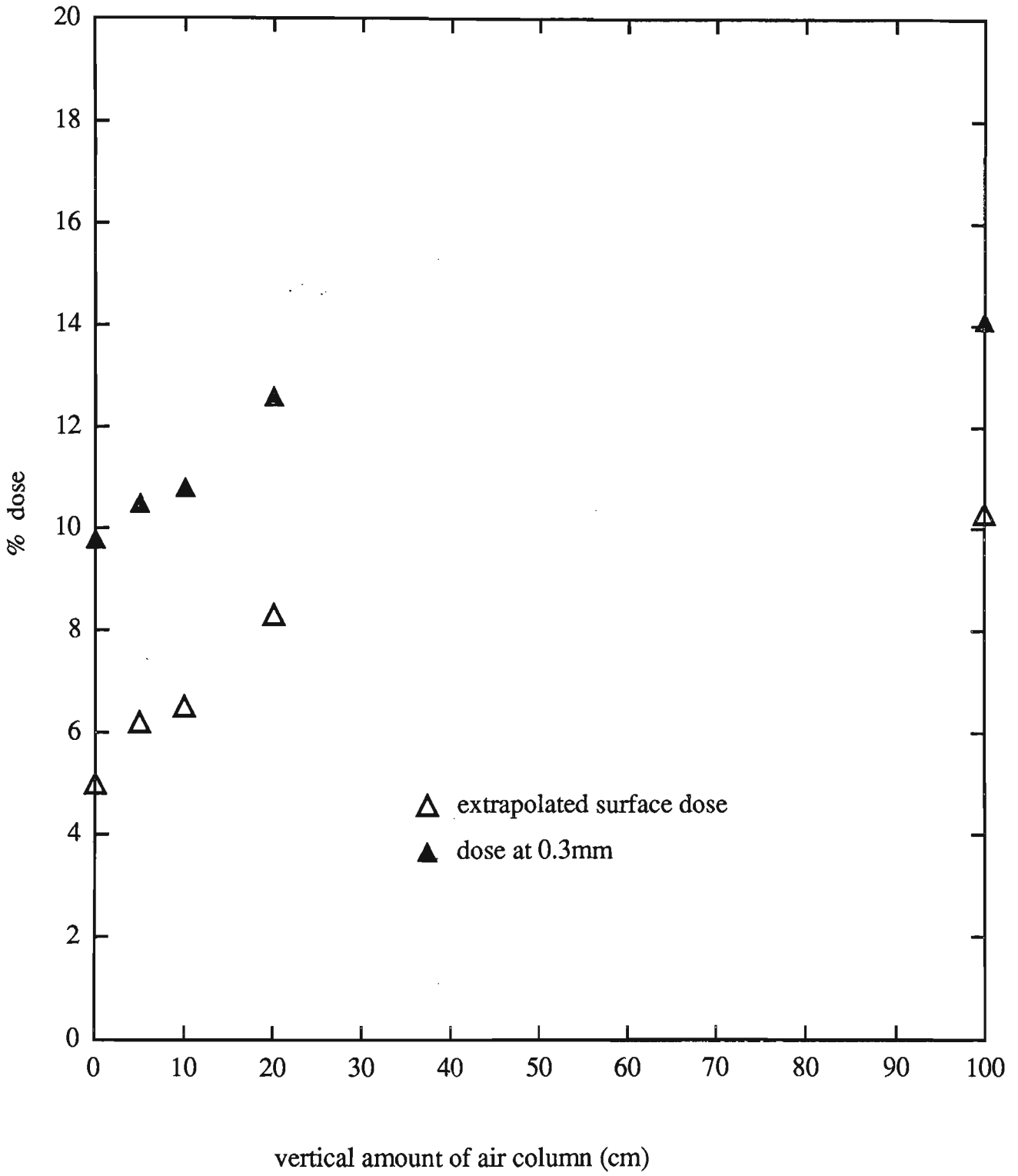

Figure 3.52 : Monte Carlo generated percentage surface dose and dose at 0.3mm as the air volume above the phantom is varied.

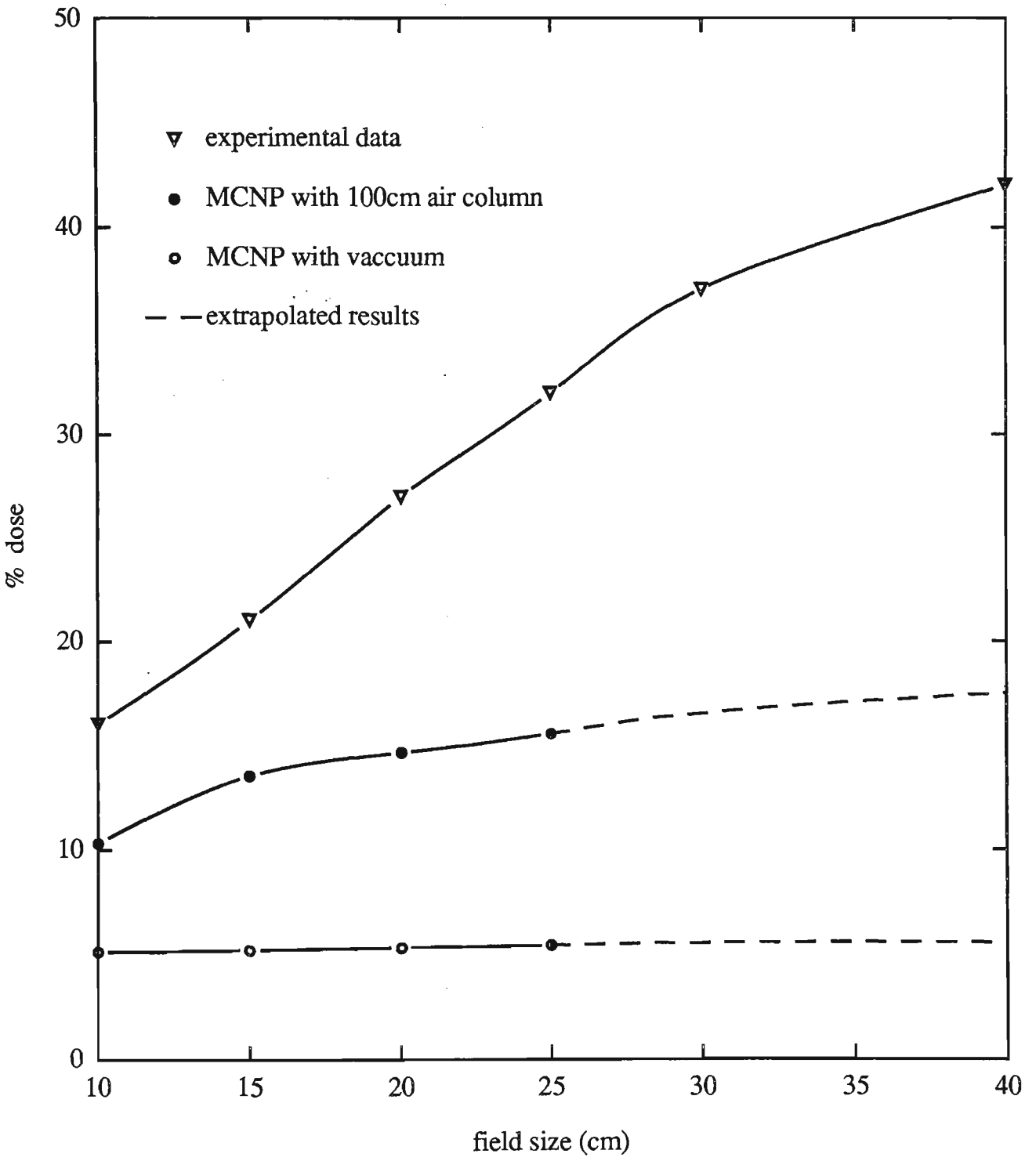

Figure 3.53 : Percentage surface dose for 6MV x-rays in three beam configurations. Experimental data shows large surface doses due to electron contamination. Monte Carlo generated results with an air column and vacuum have smaller surface doses.

Simulations with air show an increase in air contributed electrons as field size is increased. An increase from 10% to 14% is seen from field sizes 10cm x 10cm to 25cm x 25cm. By best fit extrapolation this would increase to 17-18% at a field size of 40cm x 40cm. Comparing these values to experimental helium data for 20cm of air removed shows a close match. Experimental contributions to surface dose from the air column are 4% for 10cm x 10cm, 6% for 20cm x 20cm and 7.5% for 40cm x 40cm. These values are 4%, 7% and 9% respectively for MCNP simulations with the same configuration of air column. The helium is expected to contribute a small amount to the production of electrons due to its density. However its density compared to air is 6.8 times less dense than air. This is expected to produce an approximate 15% difference compared to the simulated vacuum results.

The physical density of air at NTP is 1.205kg/m^3, compared to 1000kg/m^3 for water. The relative electron density is 0.0012, thus the range of electrons in air is approximately 3 orders of magnitude larger than their range in water. That is, an electron with a range of 1m in air has a range in the order of millimetres in water. Monte Carlo simulations predict that the last 20cm of air produces approximately 70% of dose due to the entire air column. Thus statistically, 30% of the electrons produced should have a range in air greater than 20cm or 0.2mm in water. Experimental results show 35-40% of the dose at the surface is measured at 1mm depth. This constitutes a slightly larger proportion of dose at depth. Experimentally, air is still present above the helium layer and electrons generated here would travel a greater distance due to the presence of helium instead of air.

The density of helium at RTP is 0.178 kg/m^3, ie. approximately 14% the density of air, thus it probably removes 86% of the 'air' column particles for interaction. At megavoltage energies, the spectrum of electron energies produced by the helium atoms will not differ significantly from air particles due to the low energies needed to ionise the electron clouds surrounding these low atomic number atoms or molecules. Another

significant difference between simulation and experiment would be the production of 'knock on' electrons in the air column by higher energy electron contamination. These electrons could have a higher energy and thus deposit their dose at a deeper depth than photon induced air interactions.

Helium bag and magnetic deflector

Experiments were performed with the helium bag combined with the magnetic electron deflector. Figure 3.54 shows percentage dose build up curves for the combined magnet/helium bag system and the electron contamination removed by the system. The contamination removed was calculated by subtraction of the magnet/helium build up data from open field data. Results shown are for 6MV x-rays at 100cm SSD with a 10mm perspex block tray inserted at 65cm distance from the source. Reductions up to 30% of applied dose are achievable at this energy.

Contribution to surface dose by each component

By comparing the percentage doses due to photon in-phantom dose, air generated electrons and head generated electrons, figures 3.55 and 3.56 were produced. They show the percentage by ratio contribution to surface dose and dose at 1mm by each component. At the surface, only a small contribution is deposited by photons and the majority by head and air generated electrons. At 1mm, phantom scatter deposits the majority of dose however at larger field sizes, head generated electrons deposit comparable dose to phantom scatter.

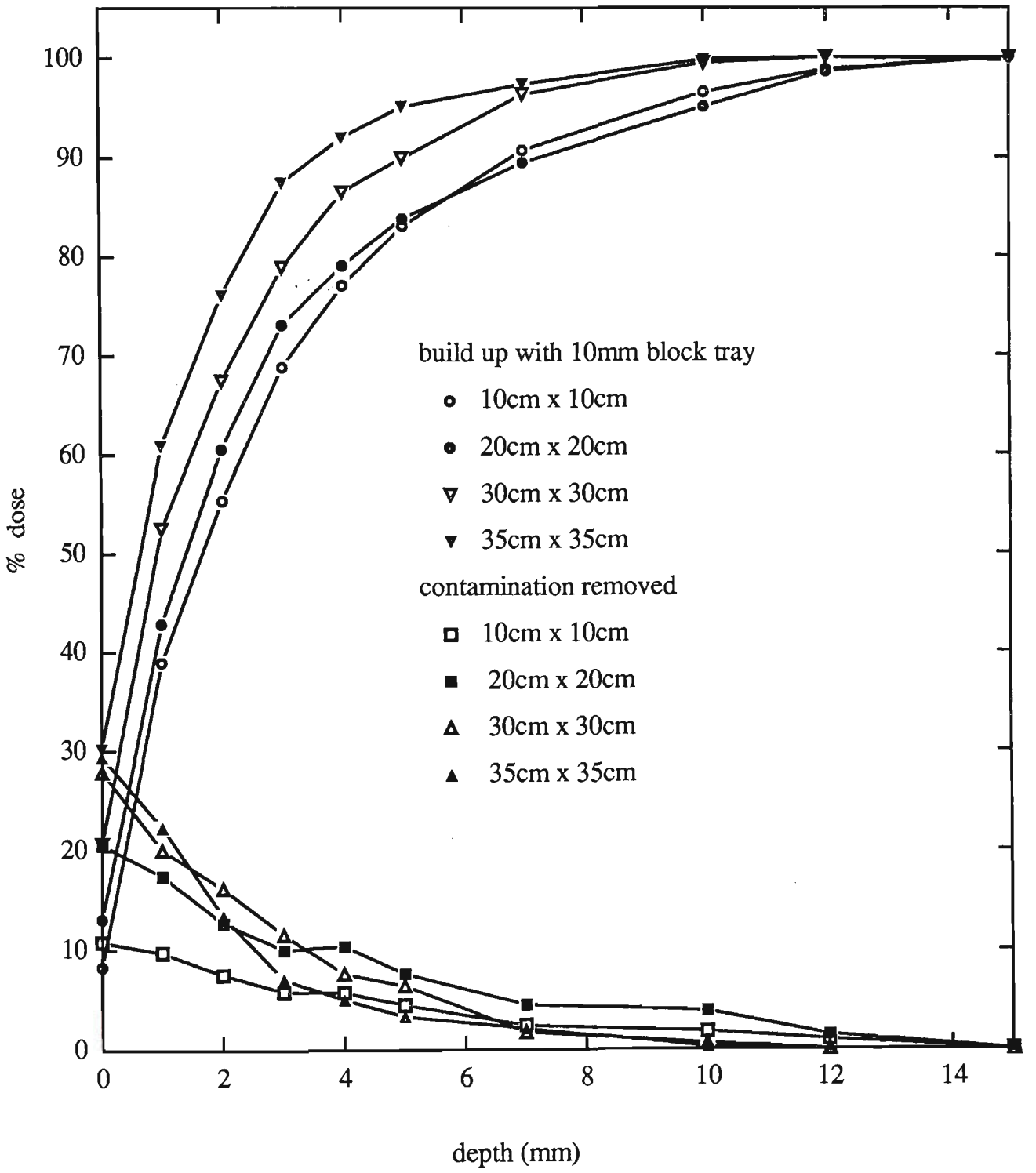

Figure 3.54 Dose build up curves measured with the combination of the magnetic deflector and the helium bag system. A reduction of up to 70% of initial surface dose is seen for this treatment configuration.

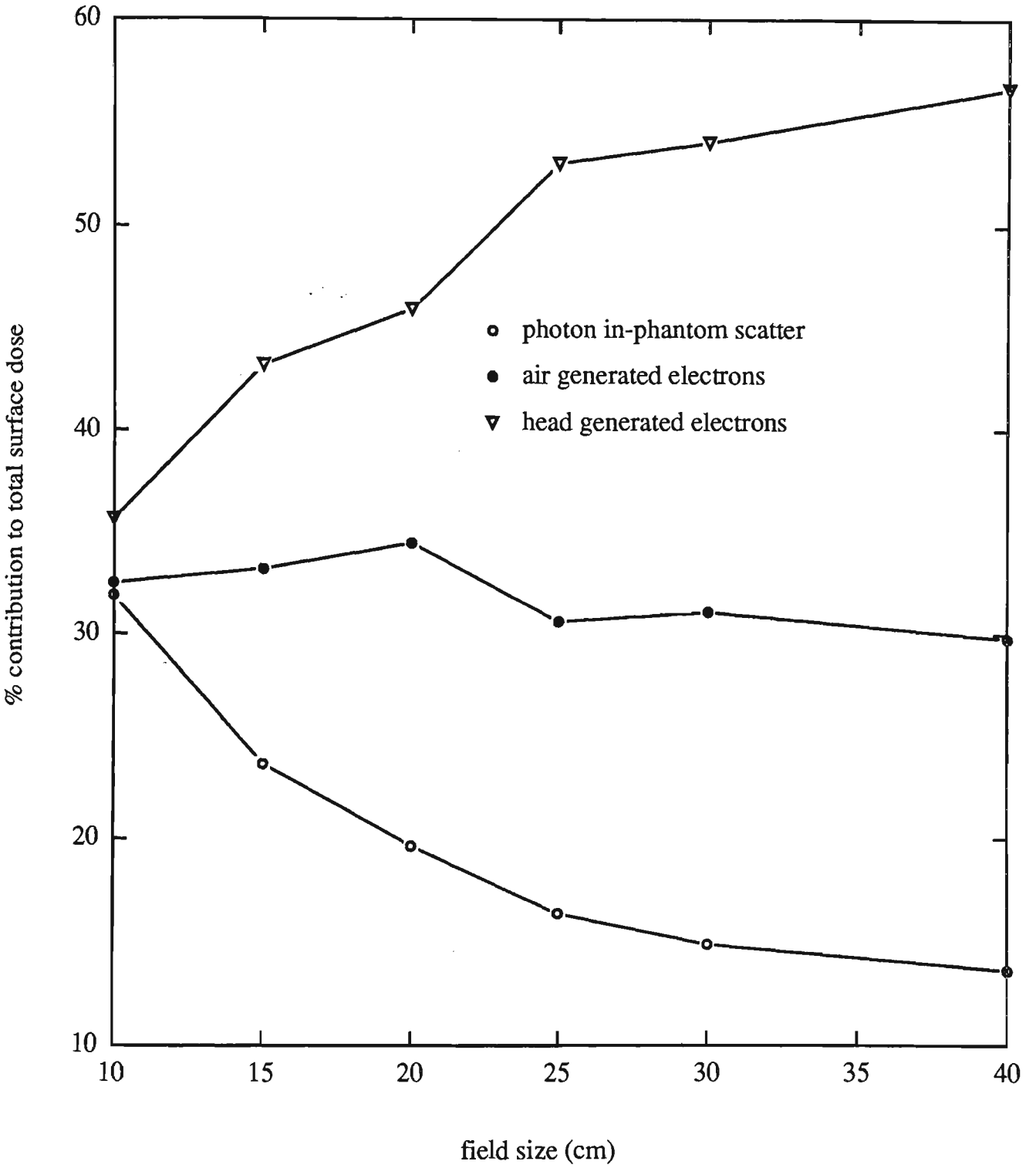

Figure 3.55 : Percentage contribution to surface dose from photon interactions, head generated electrons and air column generated electrons.

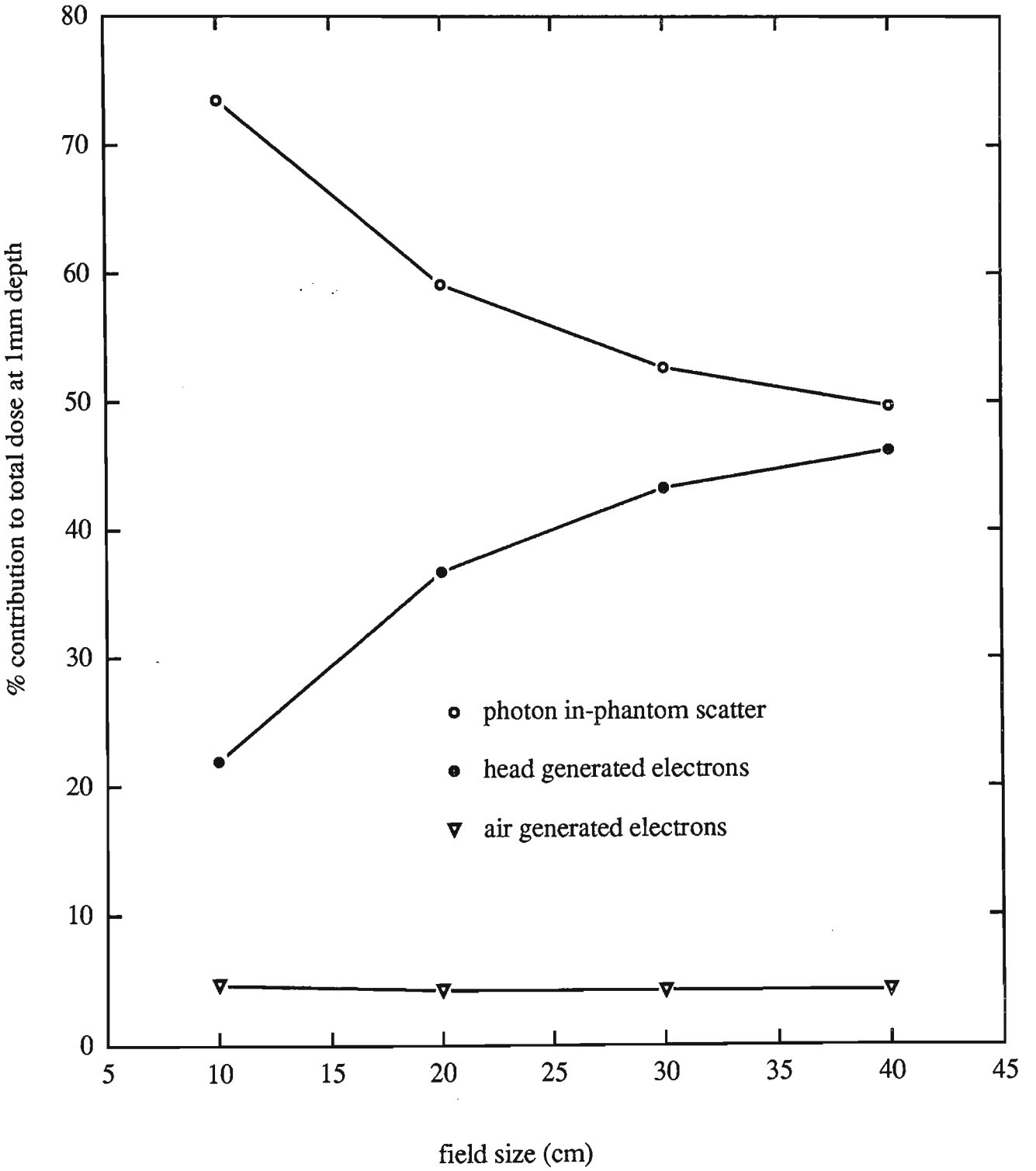

Figure 3.56 : Percentage contribution to dermal layer (1mm) dose from photon interactions, head generated electrons and air column generated electrons.

Chapter 4 6MV dose build up modelling

4.1 A new analytical model for calculation of dose build up

Using the information presented in chapter 3, a quantitative empirical model has been formulated to predict entrance dose deposition in the build up region from photon phantom scatter radiation, open field electron contamination and changes associated with beam modifying devices. With this modelling system open fields, block trays and wedges can be modelled as well as SSD changes, patient geometry and beam incident angle.

Most equations were fitted from experimental data using the Marquardt-Levenberg algorithm (Marquardt et al 1963). This is a regression procedure using values for one or more independent variables to predict other dependent variables. The Marquardt-Levenberg algorithm is used to find the coefficients of the independent variables that give the 'best fit' between the equation and the experimental data. Thus the algorithm looks for the parameters to minimize the sum of the least squared differences (SS) such that,

$$SS = \sum_{i=1}^{n} (y_i - \bar{y}_i)^2 \qquad 4\text{-}1$$

where y_i is the observed and $\bar{y}_i$ is the predicted value of the dependent variable. An iterative procedure is followed to reduce the residual sum of the squares to a negligible amount.

Equivalent square calculations

To enable accurate dose calculation in the build up region for rectangular and irregular field sizes, an estimate of equivalent square field size for the irregular field size is required. The introduction of lead blocks into the x-ray beams path shields both primary photons, head scatter and electron contamination. This section shows models to convert a rectangular or irregular field size to equivalent square size estimation for build up dose modelling.

For a rectangular field, a modified Sterlings formula was used as follows :

$$ESQ_{rect} = \frac{2xy}{x+y} + \frac{a}{4b} - 0.25 \qquad 4\text{-}2$$

where : x = x direction field size in cm, y = y direction field size in cm , a = larger of x or y in cm, b = smaller of x or y in cm. Note, the first term on the right is Sterling formula.

Figure 4.1 shows model fits and experimental data for equivalent square field sizes at the surface for y= 5cm, 15cm and 30cm with the x-axis varying. The standard deviation of the model over measured data points was 0.2cm.

Figure 4.2 shows the percentage surface dose recorded for blocked fields and open square fields at an initial 30cm x 30cm collimator field size. Results were obtained by placing cerrobend blocks on a block tray and equating surface dose on central axis or in an open part of the beam. Results show that surface dose from blocked fields follows a similar response in surface dose for square fields of the same area.

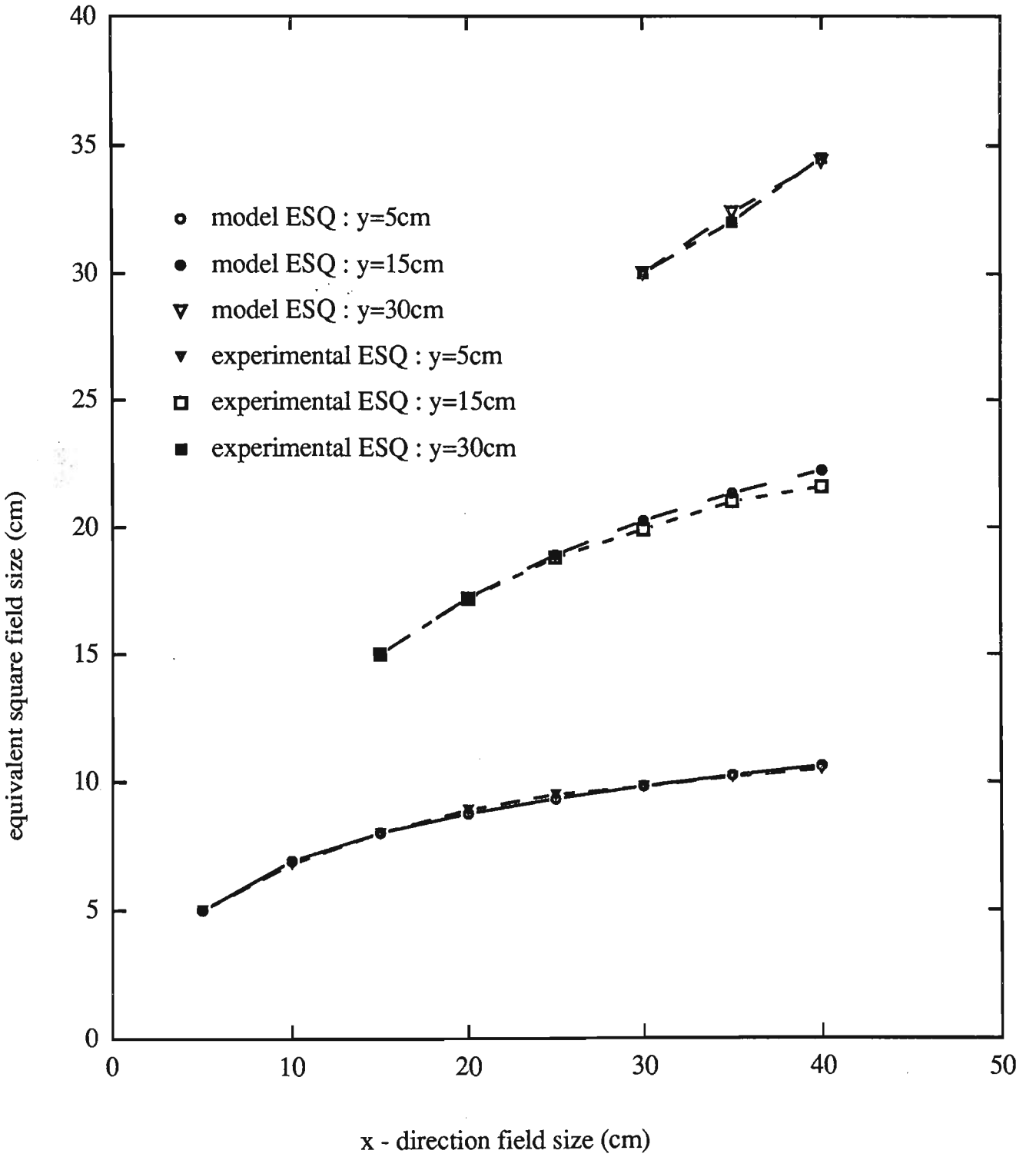

Figure 4.1 : Model fits to data for the equivalent square calculation

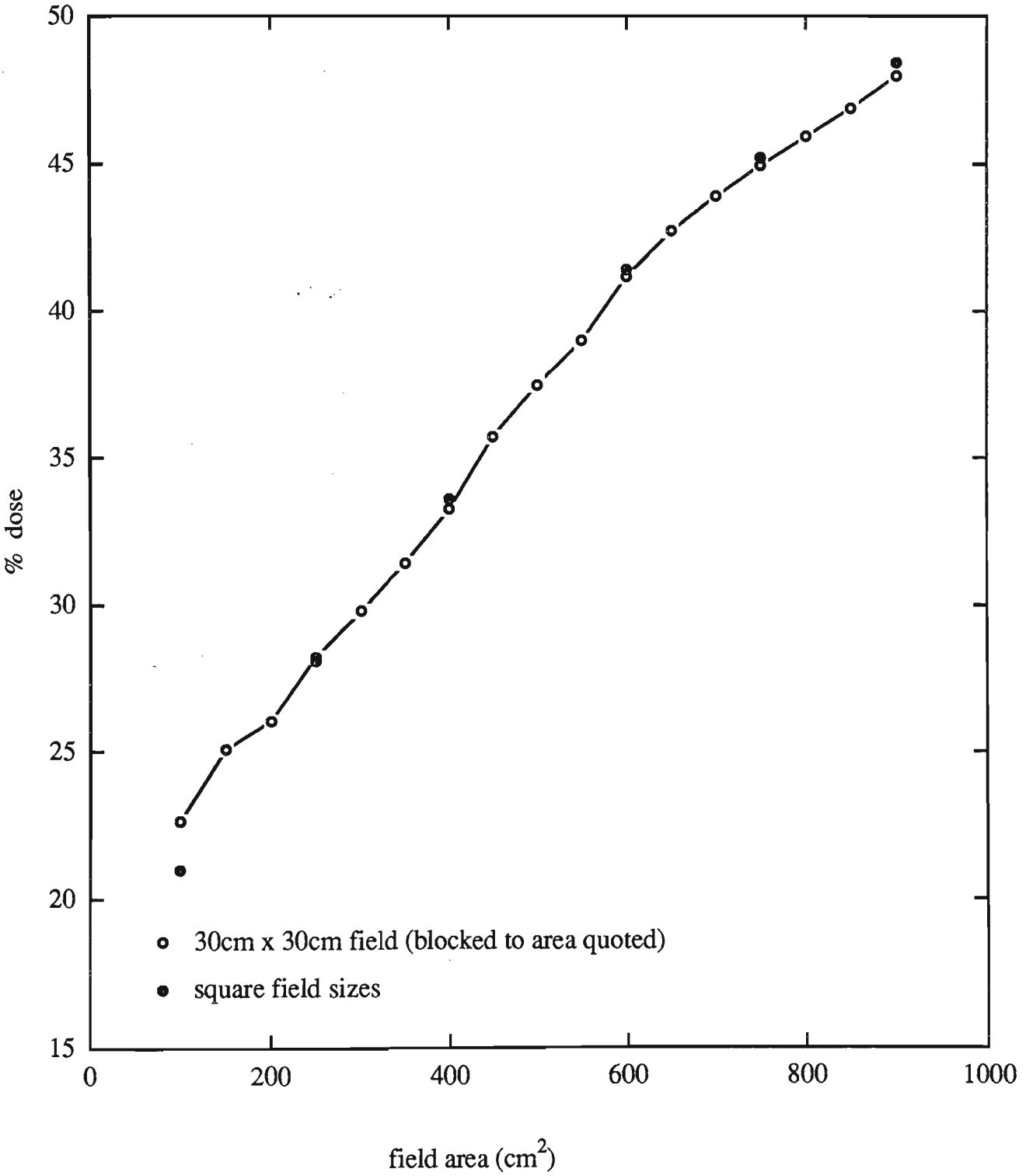

Figure 4.2 : Experimental validation data for the equivalent square calculation for irregular field shapes.

Thus for irregular shaped blocked field :

$$ESQ_{irreg} = \sqrt{ESQ_{rect}^{\ 2} - area(cm^2).of.blocks} \qquad 4\text{-}3$$

Discussion

Surface dose equivalent field sizes were seen to be relatively collimator independent, ie. a 10cm x 40cm field size is equivalent to a 40cm x 10cm field. This is attributed to the electron contamination producing the majority of the dose in this region. The symmetrical design of the accelerator treatment head contributes to this collimator independence. There is a small difference in exposure of the flattening filter due to the difference in height of the two sets of collimators. This does affect collimator output factors but is not a large enough effect to be apparent for surface dose measurements.

Large discrepancies in calculated equivalent square field sizes can occur if part of the beam is blocked producing irregular shaped fields, ie. the surface dose ESQ field size for a typical inverted Y treatment calculated with Sterling's 4 x Area/Perimeter formula would be $13cm^2$ where as experimentally it is $20cm^2$. In evaluating surface dose equivalent square field sizes of irregular shaped fields with large blocked areas, errors could occur if only Sterling's 4 x Area/Perimeter model was used. Thus a model is introduced which accounts for these variations. It accounts for both, variations from Sterling's model for rectangular fields and changes in equivalent square field size from irregular shaped blocked fields. This model is incorporated with analytical models for build up dose to enhance the calculation of surface and build up dose for patients before treatment begins.

Methods have been developed by other scientists to calculate equivalent squares from irregular shaped fields such as :

i) geometric approximation method where rectangular portions are selected which contain most of the irradiated areas and excludes only that which is remote from this point (Khan 1992).

ii) the Clarkson method which separates the primary and scattered components of dose at a point in the phantom (Clarkson 1941).

iii) sector integration to calculate the equivalent area of the scatter component (Cunningham J, et al 1972).

These methods however have been developed with dose at depth in mind with in-phantom scatter as the important variables. The simple area method explained in this paper gives adequate results with regards to surface dose. Foremost is that calculating an equivalent square field size for irregular shaped patient fields is a very convenient way to calculate the field size. More detailed analysis of accuracy of the equivalent square method is given in appendix 2.

The photon in -phantom component

Build up dose is contributed to by photon in-phantom scatter produced by x-ray interactions occurring within the patient and by electron contamination which is produced by x-ray interactions outside the patient. This model deals with these components separately. Each additional change in build up dose associated with the addition or removal of a certain treatment procedure such as the use of block trays or a change in angle of incidence is then included.

Photon in-phantom scatter radiation is modelled by :

$$\%D_{photon} = 100 - (100 - S)e^{-\alpha x} \qquad 4\text{-}4$$

where S is the photon component surface dose, x is the depth in water (mm) and α is the empirical value which defines the curvature. For a 6MV x-ray beam :

$$\alpha = 0.352 + 6.37 \times 10^{-4} s \qquad 4\text{-}5$$

where s is the equivalent square field size in centimetres and is calculated using equations 4-1 and 4-2.

Figure 4.3 shows the results of applying the empirical fits for the photon in-phantom scatter model or $\%D_{photon}$ in the build up region for a 20cm x 20cm field size at 100cm SSD.

Electron contamination and head scatter

Open field contamination is modelled by the empirical formula :

(Range of validity 0-1mm)

$$\%D_{cont} = \beta e^{-\gamma x} - \psi(s)(1-x) \qquad 4\text{-}6$$

(Range of validity 1-15mm)

$$\%D_{cont} = \beta e^{-\gamma x} \qquad 4\text{-}7$$

where $\beta = \delta + \varepsilon s + \zeta s^2$ 4-8

$$\gamma = \eta + \iota s \qquad 4\text{-}9$$

$$\psi(s) = \kappa + \lambda s + \mu s^2 \qquad 4\text{-}10$$

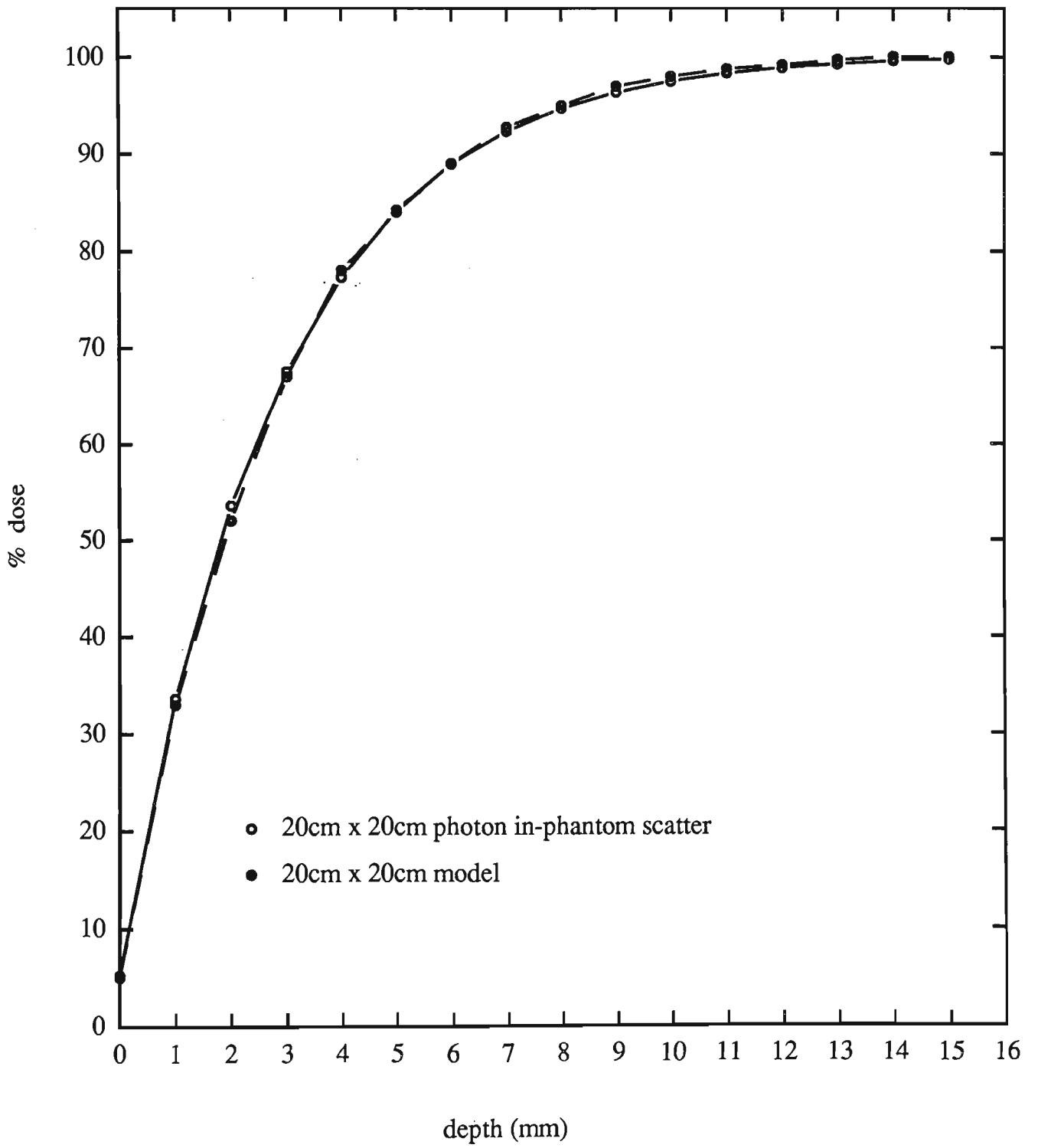

Figure 4.3 : Model fits to data for the photon in-phantom scatter calculation. Photon in phantom scatter is generated using Monte Carlo methods.

where x is the depth in water (mm), δ= -3.637, ε = 2.014, ζ = -0.01832, η= 0.2798, ι = 0.00208, κ = -0.577, λ = 0.4, μ = -0.003175.

Figure 4.4 shows the results of applying the empirical fits for the open field electron contamination produced or $\%D_{cont}$ in the build up region for field sizes between 10cm x 10cm and 40cm x 40cm.

Beam modifying device : block trays

The change in percentage dose for the addition of a block tray (for 6mm perspex) is modelled by the equation:

(Range of validity 0-1mm)

$$\%D_{tray} = \xi e^{-\nu x} - \Omega(s)(1-x) \qquad 0 \le x \le 1\text{mm} \qquad 4\text{-}11$$

(Range of validity 1-15mm)

$$\%D_{cont} = \beta e^{-\gamma x} \qquad x > 1\text{mm} \qquad 4\text{-}12$$

$$\xi = o + \pi s + \rho s^2 \qquad 4\text{-}13$$

$$\nu = \sigma + \tau s \qquad 4\text{-}14$$

$$\Omega(s) = \upsilon + \phi s + \chi s^2 + \psi s^3 \qquad 4\text{-}15$$

where o=.512, π =-.01102, ρ= 0.0001748, σ=-0.877, τ=0.6123, υ=1.28, ϕ=0.190, χ=0.0037, ψ= -0.000103

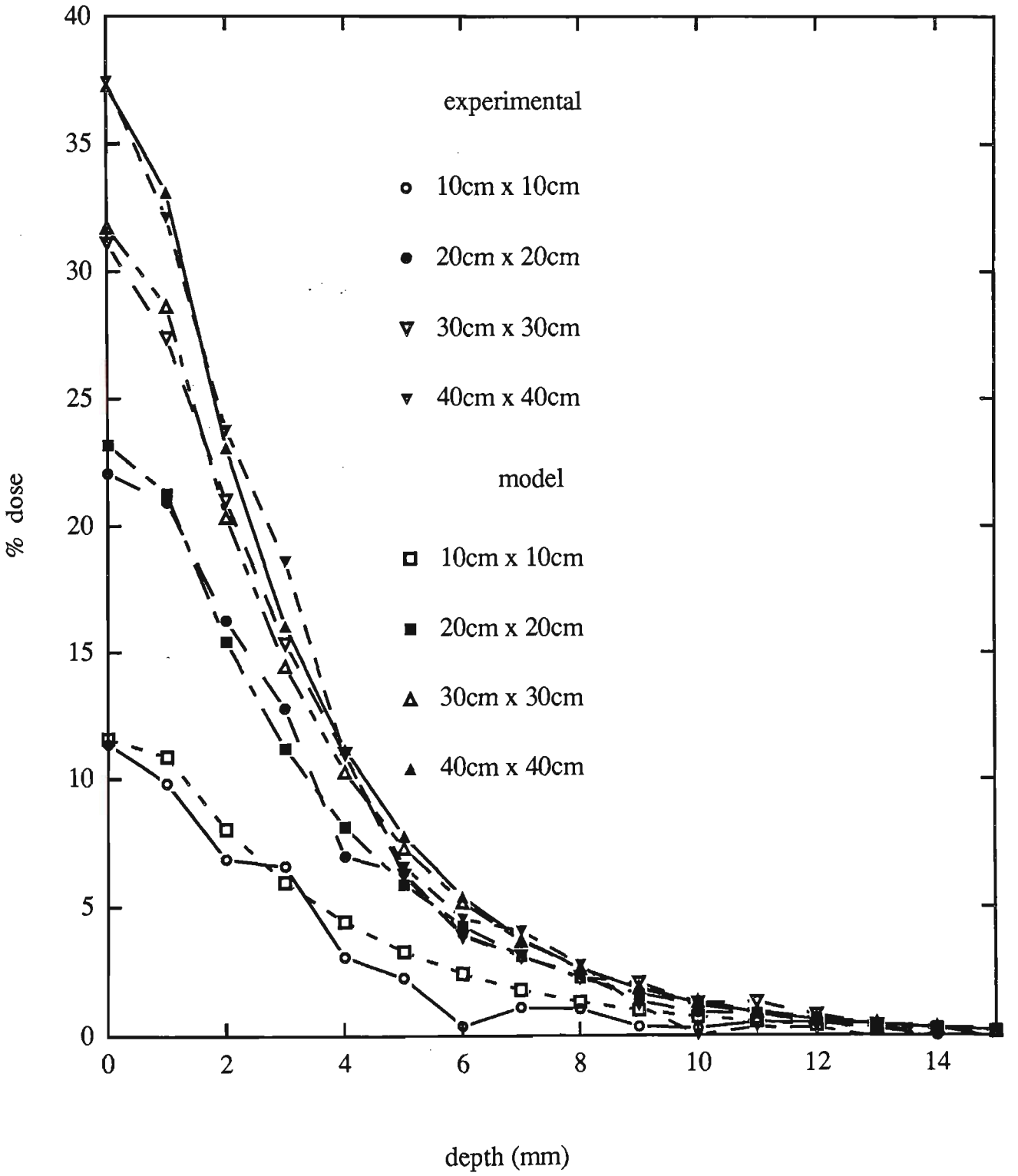

Figure 4.4 : Model fits to data for the electron contamination calculation.

Figure 4.5 shows the results of applying the empirical fits for the change in percentage build up dose through the introduction of a 6mm perspex block tray at 10cm x 10cm and 30cm x 30cm field sizes compared to experimental results.

Beam modifying device : wedges

The change in percentage dose with the introduction of a 15° wedge is modelled by the equation :

(Range of validity 0-6mm)

$$\%D_{wedge} = \alpha + \beta x + \gamma x^2 \qquad 4\text{-}16$$

(Range of validity 6-15mm)

$$\%D_{wedge} = \%D(6mm) - 0.643x + 2.94 \times 10^{-2} x^2 \qquad x > 6\text{mm} \qquad 4\text{-}17$$

$$\alpha = \delta + \varepsilon s + \zeta s^2 \qquad 4\text{-}18$$

$$\beta = \eta + \iota s + \kappa s^2 \qquad 4\text{-}19$$

$$\gamma = \lambda + \mu s + \nu s^2 \qquad 4\text{-}20$$

where δ=-4.378, ε=0.9648, ζ=-0.02637, λ=-0.01591, μ=0.006046, ν=-0.0008548, η=1.401, ι=-0.1938, κ=0.009235

Figure 4.6 shows the results of applying the empirical fits for the change in percentage build up dose through the introduction of a 15° wedge at 7cm x 7cm, 14cm x 14cm and 20cm x 20cm field sizes compared to experimental results.

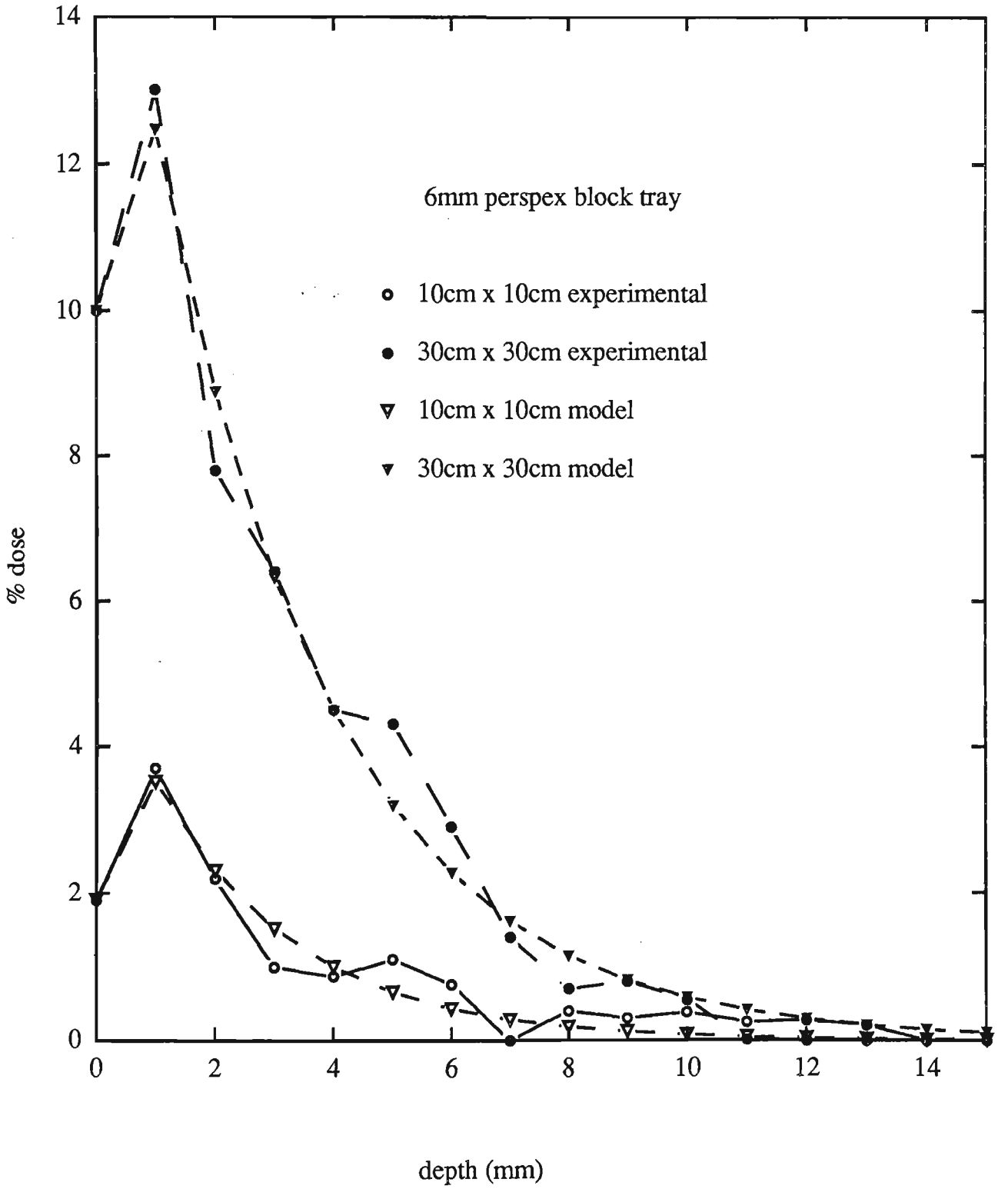

Figure 4.5 : Model fits to data for the change in dose due to block tray calculation.

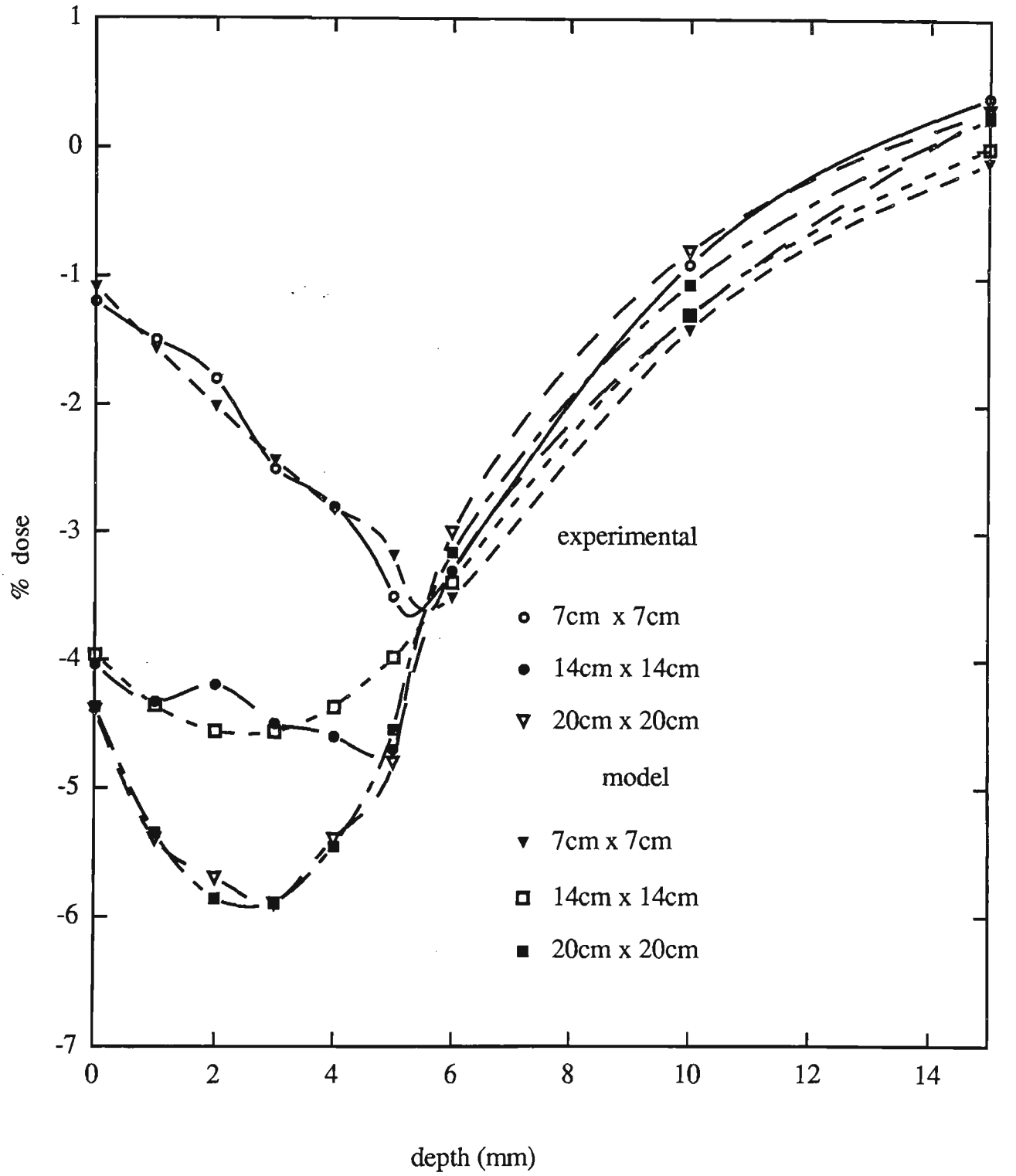

Figure 4.6 : Model fits to data for the change in dose due to the inclusion of wedge calculation.

Beam angle of incidence

The change in percentage dose build up produced by the beam angle of incidence is modelled by:

(Range of validity 0-1mm)

$$\Delta\%D_{angle} = b(\theta) + (f(s)b + g(\theta))x \qquad 4\text{-}21$$

(Range of validity 1-12mm)

$$\Delta\%D_{angle} = a(\theta) + b(\theta)(x-1) + c(\theta)(x-1)^2 \qquad 4\text{-}22$$

where x = depth(mm), s = equivalent square field size(cm), b = surface dose at 0° incidence, θ= angle of incidence, a(θ) = dose at 1mm and

$$f(s) = 0.8 - 0.2f \qquad 4\text{-}23$$

$$b(\theta) = me^{n\theta} \qquad 4\text{-}24$$

m = 0.6797 , n = 0.05055

$$g(\theta) = c - (d\theta - e)^2 \qquad 4\text{-}25$$

c=1.352, d = 0.03212, e = 1.116

$$b(\theta) = p(s)e^{q\theta} \qquad 4\text{-}26$$

q = 0.04944

$$p(s) = g + hs + is^2 \qquad 4\text{-}27$$

s= field size(cm), g = -0.206

h = 2.32 x 10^{-3}, i = -2 x 10^{-5}

$$c(\theta) = re^{t\theta} \qquad 4\text{-}28$$

r = 0.003168, t = 0.06076

No correction is need to dose after 12mm depth due to the agreement of results . Figure 4.7 shows the results of comparing the model and experimental results for beam angle of incidence.

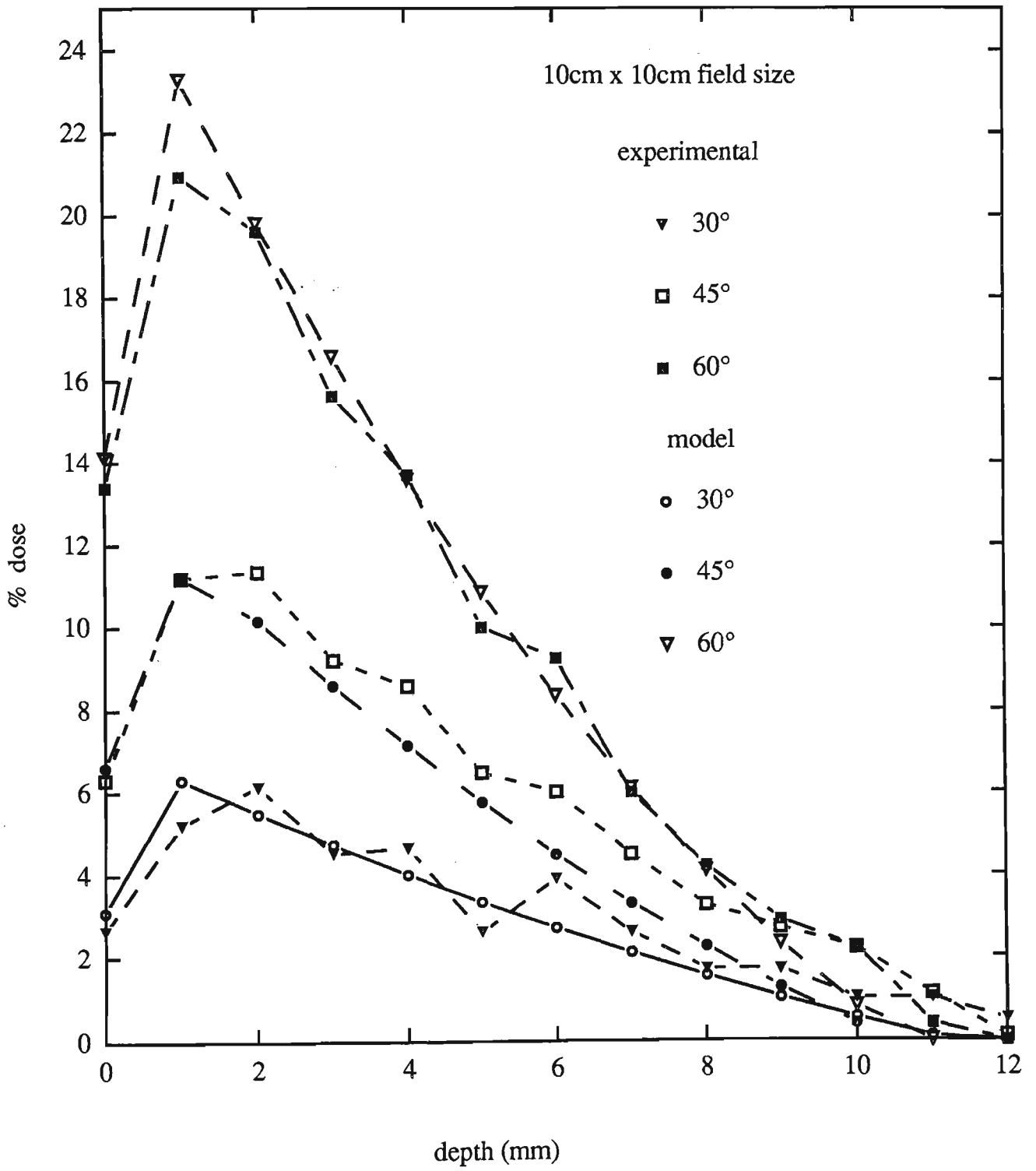

Figure 4.7 : Model fits to data for the change in dose due to the beam angle of incidence calculation.

Source surface distance

The effect of the source surface distance is negligible when open fields are used. This is related to the field size being quoted at the isocentre and thus the collimators remain unmoved.

The effect of SSD is significant when using a block tray. This is likely to be due to the large angle scattering of the electron contamination being rapidly reduced as distance from the block tray increases. Changes in percentage dose build up (for 6mm perspex block tray) are modelled by :

$$\xi = \gamma \exp(-\omega x) \qquad 4\text{-}29$$

where x = depth (mm)

$$\gamma = \alpha s + \beta s^2 \qquad 4\text{-}30$$

where s is the deviation from 100cm SSD (cm).

$$\alpha = 0.6501 + 0.0017 f - 0.0002 f^2 \qquad 4\text{-}31$$

$$\beta = 0.0119 - 9x10^{-6} f + 4x10^{-7} f^2 \qquad 4\text{-}32$$

where f = field size (cm)

ω is separated into two equations for SSD's smaller and larger than 100cm. For smaller SSD's the value of change in SSD is given by a negative distance. For SSD's greater than 100cm the distance is positive.

(Range of validity SSD<100cm)

$$\omega = \chi + \delta s \qquad 4\text{-}33$$

where s = deviation from 100cm SSD in centimetres.

$$\chi = 0.16,\ \delta = 0.0018 - 0.0013f + 0.0525f^2 \qquad 4\text{-}34$$

f is field size in metres.

(Range of validity SSD>100cm)

$$\omega = \chi + \delta s \qquad 4\text{-}35$$

where s = deviation from 100cm SSD in centimetres, $\chi = 0.1$, $\delta = 0.0075f$, where f is field size in metres.

Figure 4.8 shows the comparison of model and experimental results for the SSD effect.

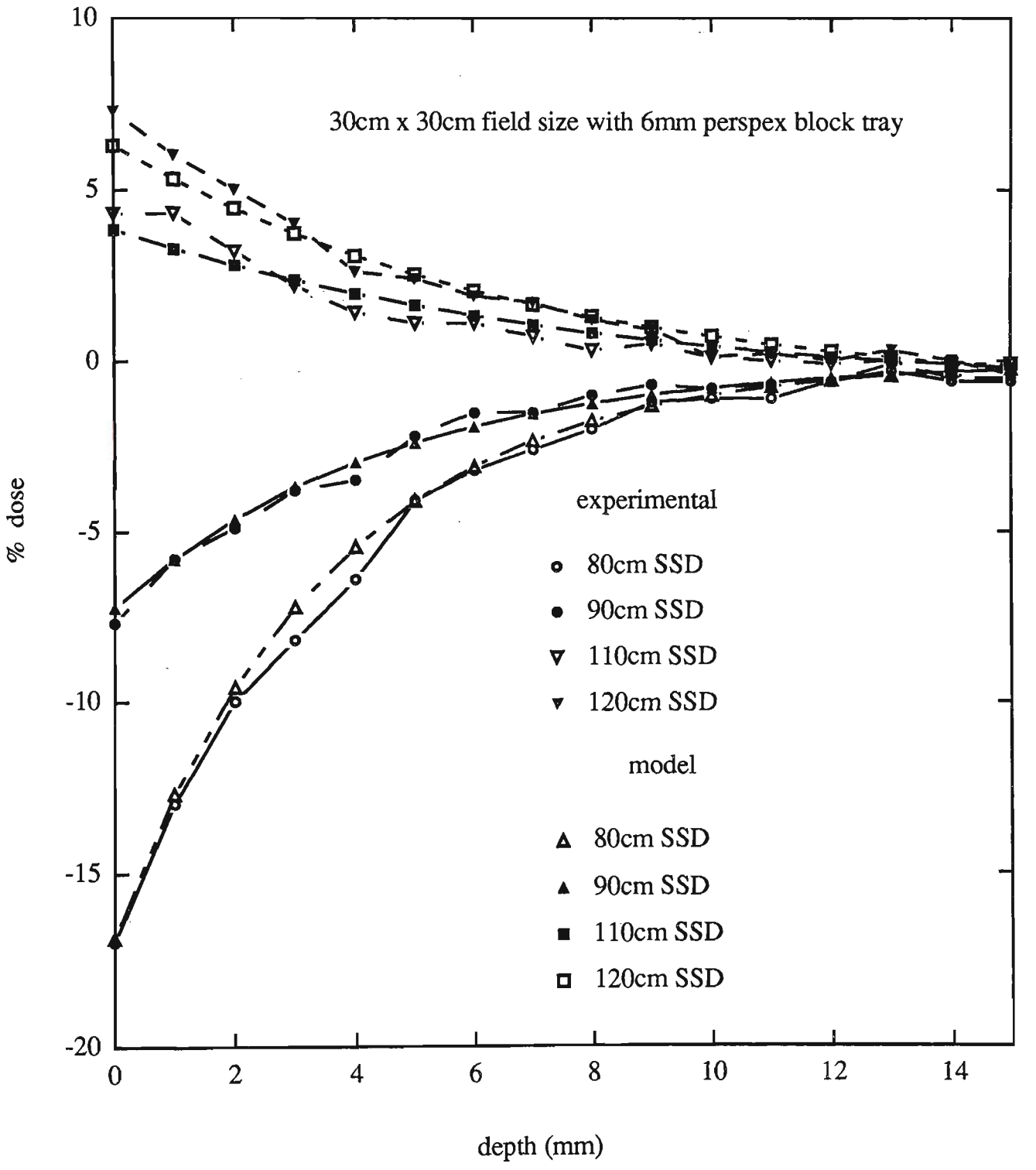

Figure 4.8 : Model fits to data for the change in dose due to the SSD effect with block trays calculation included.

4.2 Clinical dose estimates

Software program and data input

The 6MV empirical equations are stored in a Microsoft EXCEL program spreadsheet as individual functions. Each part of the equation (eg. in-phantom photon scatter, open field electron contamination) is stored independently and a percentage dose contribution is given individually. Dose is shown from the surface to 15mm depth (D_{max} position) in 1mm intervals with the inclusion of dose at 0.07mm equivalent to the basal cell layer. If warranted, extra depths can be included to study dose at a particular depth. Each section is summed appropriately if needed. An input table is provided to enter treatment parameters such as the collimator field size, blocked field size, SSD, angle of incidence, and the use of beam modifying devices. Each dose section is then summed in the spread sheet to give total entrance build up dose. The system also graphically presents the entrance build up dose curve for the treatment procedure. To get a total skin dose, the exit dose can also be added from an opposing beam. Figure 4.9 shows the input table and dose columns for the planning system with patient data entered. Figure 4.10 shows the entrance build up dose curve produced for these parameters.

The complete calculation is given by:

$$\%D_{total} = \%D_{photon} + \%D_{cont} + \%D_{tray} + \%D_{wedge} + \%D_{aoi} + \%D_{SSD} + \%D_{exit} \qquad 4.36$$

where each section is defined earlier. Each section is used depending on the patients specific treatment parameters.

6MV x-ray skin dose planning system									
x-field (cm)	25		eq square =	17.33603239					
y field (cm)	13								
block tray	yes	1							
wedge	no	0							
AOI	1	45							
SSD(cm)	117				% Dose entrance (components)				
					Electron	Photon	Block	Wedge	Angle of
					contamination	in-phantom	tray	correction	incidence
					and head	scatter	correction		correction
depth (mm)	% Dose entrance (total)			depth(mm)	scatter				
0	32.73739281			0	20.36870798	4.5	6.148902816	-4.422616488	6.610413743
0.1	41.19780809			0.1	20.10772115	7.904881266	6.150805956	-4.502619178	7.034399713
1	69.91936475			1	18.79190698	33.57435546	6.702828862	-5.07217577	10.85027344
2	81.42300522			2	13.70234999	53.79721202	4.613739441	-5.387362558	9.309703779
3	88.89704256			3	9.991236938	67.86335109	3.175762363	-5.368176852	7.866692172
4	93.63958085			4	7.285233238	77.64714537	2.185963624	-5.014618653	6.521238622
5	96.54244568			5	5.312117374	84.45232695	1.504658226	-4.32668796	5.273343129
6	98.21781371			6	3.873395686	89.18571515	1.035697188	-3.304384773	4.123005692
7	99.08551296			7	2.824334081	92.47805402	0.712898548	-2.690784773	3.070226312
8	99.43317204			8	2.059397915	94.76806167	0.490707464	-2.135984773	2.115004989
9	99.45763568			9	1.501635306	96.36089136	0.337767296	-1.639984773	1.257341723
10	99.29346115			10	1.094935843	97.46879437	0.232494418	-1.202784773	0.497236513
11	99.03251103			11	0.79838593	98.23940351	0.160032232	-0.824384773	0.21
12	99.46771314			12	0.582152916	98.77540569	0.110154539	-0.504784773	0
13	99.6485318			13	0.424483955	99.14822548	0.075822366	-0.243984773	0
14	99.769251			14	0.309517694	99.40754271	0.052190597	-0.041984773	0

Figure 4.9 : Input data table for the build up dose planning equation.

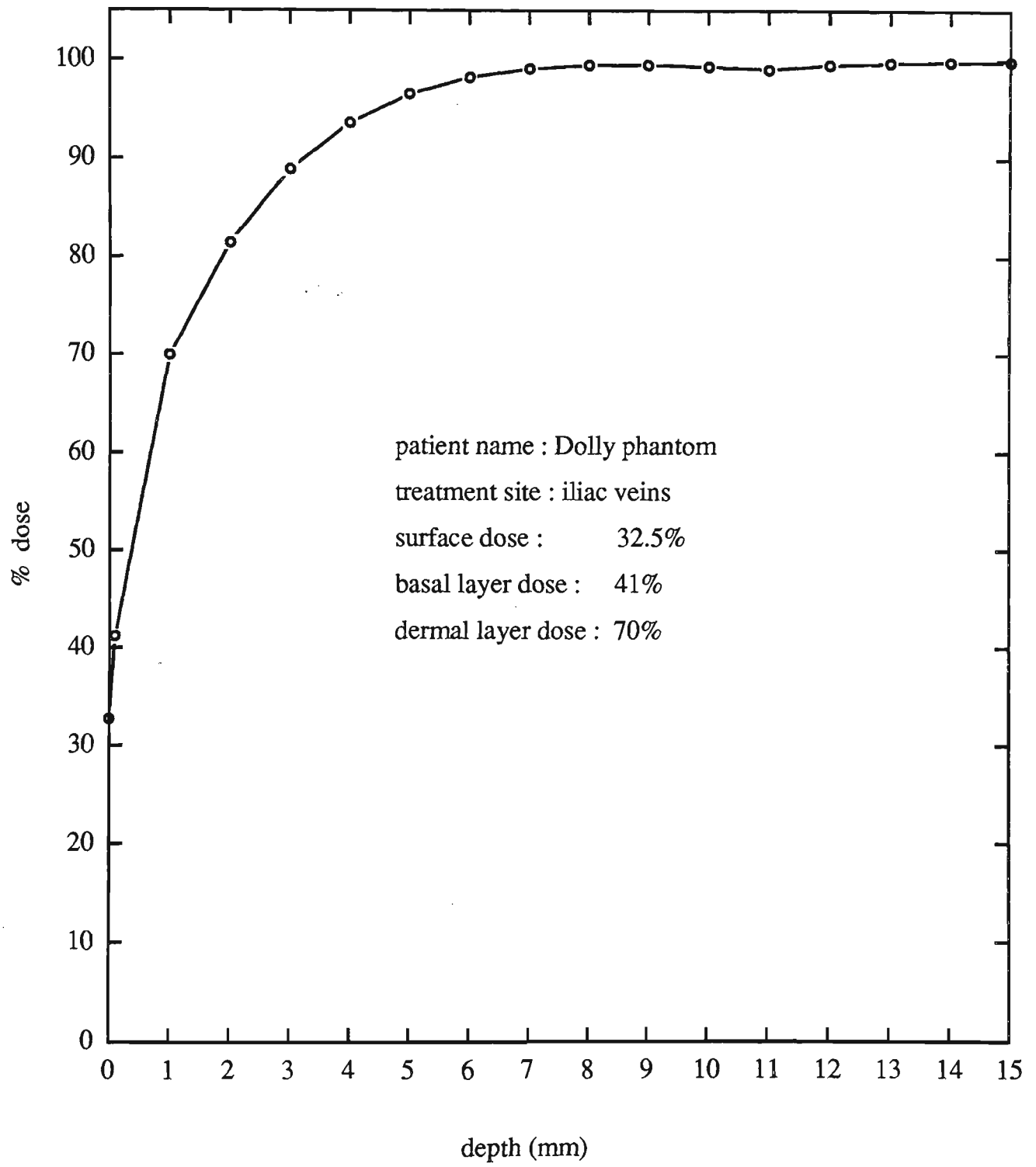

Figure 4.10 : Calculated dose build up curve using equations for typical patient parameters.

Examples of dose fits to model

Measurements to validate the accuracy of the planning system were performed in

i) solid water slab phantom

ii) in-vivo patient measurements

The solid water slab phantom trials were used to measure dose over the whole build up region. Surface, basal cell and dermal layer doses were measurable in-vivo using extrapolation TLD's.

Slab phantom results

Figure 4.11 shows the comparison of the mathematical model fit to experimental data for the differences in normally incident beams and at an angle of 37° for an open 23cm x 9cm field size beam at 100cm SSD. Two standard deviations over all angles and data points measured was calculated as 1.9%.

In-vivo results

Clinical measurements have been performed as part of a breast skin dose study. A sample of 18 patients undergoing parallel opposed tangential fields of 6MV x-rays have been examined. All patients gave their informed consent to participate in the study. A dose of 2Gy was prescribed per fraction to the tumour/target volume. This covered the whole breast excluding approximately a 1cm margin around the breast skin surface. A fixed SSD of 100cm was used and in some cases, wedges were used to improve the dose homogeneity across the target volume. Measurements were performed using the TLD extrapolation technique. Measurements were performed on the central axis of the fields in the entrance and exit locations for the tangential fields. Other parameters measured include, field size, angle of incidence, use of block trays and wedges and the

separation for the exit dose determination. In-vivo results are compared to predicted calculations for accuracy.

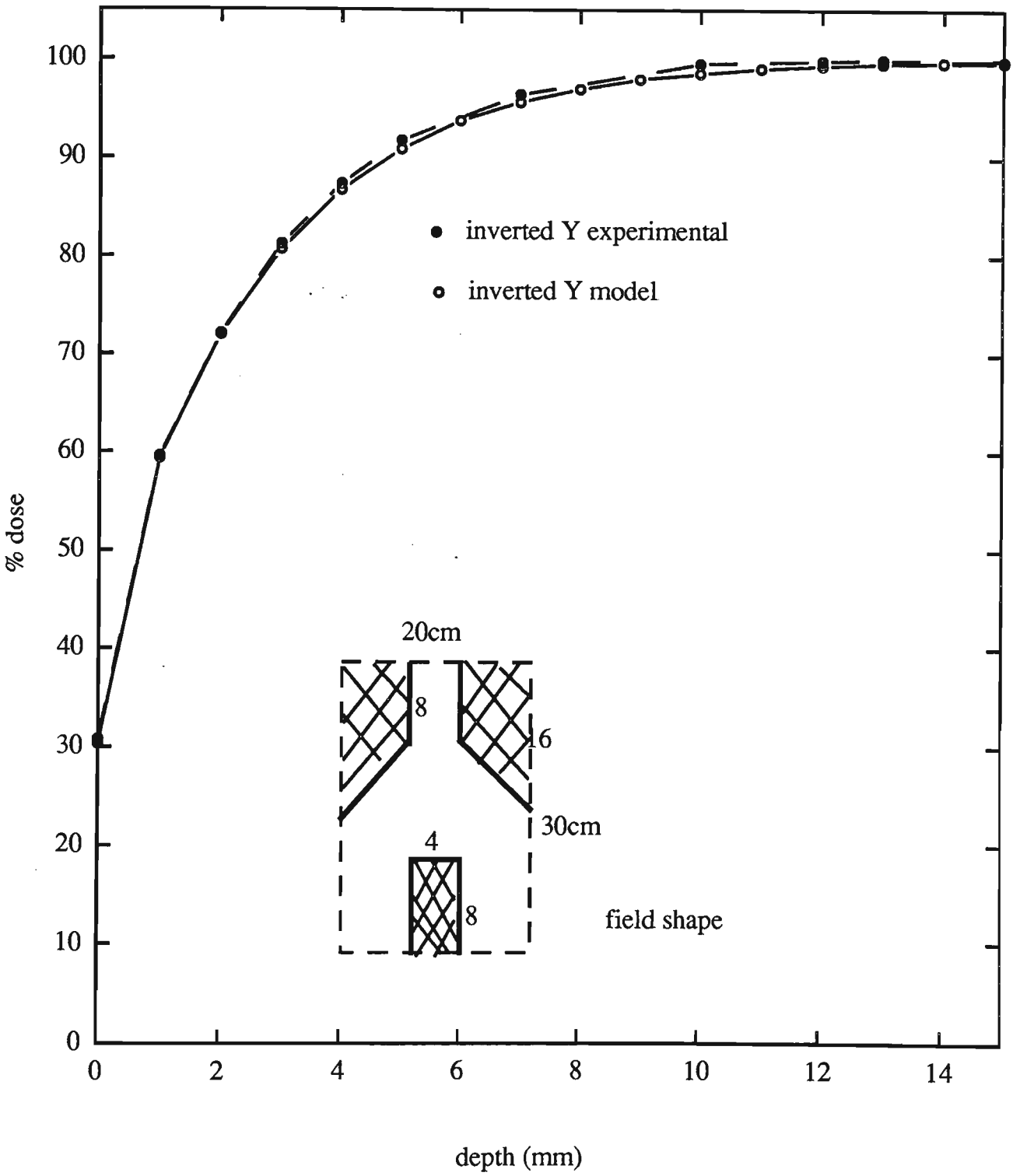

Figure 4.11 : Model fits to data for the total build up dose calculated compared to experimental data. Surface doses are 30%- model and 31% - experimental.

Figure 4.12 shows the 18 patients entrance dose as measured by TLD extrapolation. Also shown are the calculated skin dose results for each treatment. Surface dose results for this group of patients ranged from 21% to 43% of applied dose. The average difference between in-vivo measured results and the calculated results was 32cGy. As a percentage of applied dose, the deviations between measured and calculated dose was 2.5% and in terms of a surface dose, the deviation was 9.5%. Figure 4.13 shows the results for total skin dose which includes both entrance and exit dose. The standard deviation between calculated and measured results is 2.1cGy which relates to a percentage deviation of 3.5%.

Adaptability to other machines

The model was originally created using data collected from a Varian 2100C linear accelerator with serial number 142. This machine is approximately 8 years old and its head design includes only single asymmetric jaws. The second Varian 2100C linear accelerator available for use at the Illawarra Cancer Care Centre, serial number 1050, has dual asymmetric collimators and perhaps some small undefined differences in head design.

Table 4.1 quotes surface dose and dose at 1mm depth for various configurations on the old and new Varian 2100C as a percentage of D_{max}. Also quoted is a percentage difference from the model in the dose at these points. These results show an agreement of within 3% at 0 and 1mm for the new Varian machine. If these differences were considered a problem by a centre, variations to the models could be simply performed. Assuming, by physical principles, that the shape of each dose component would be similar, a limited set of data could be collected to reproduce the parameters needed to reshape each mathematical equation.

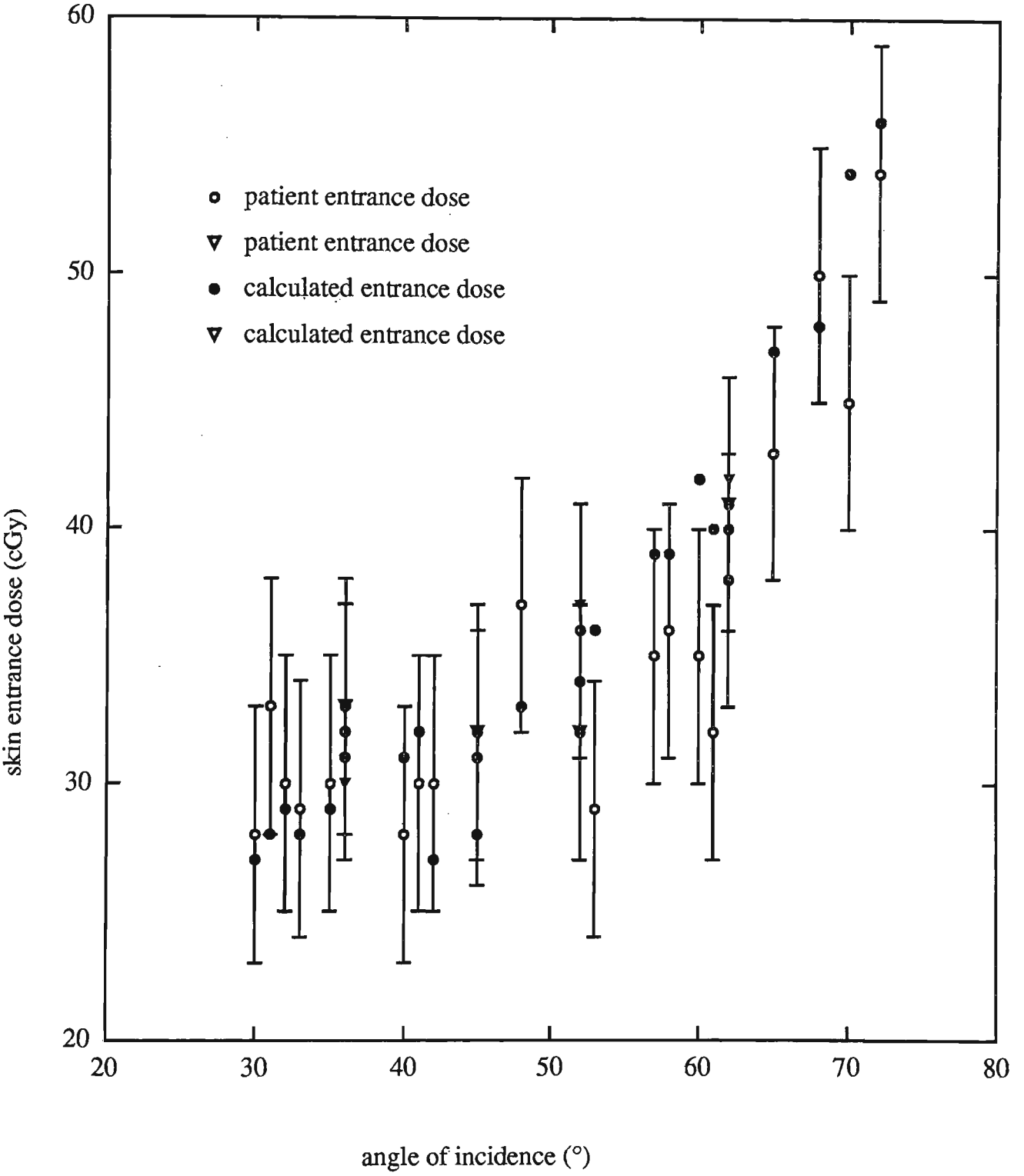

Figure 4.12 : In-vivo patient data for patient surface dose compared to calculated skin dose for entrance beams.

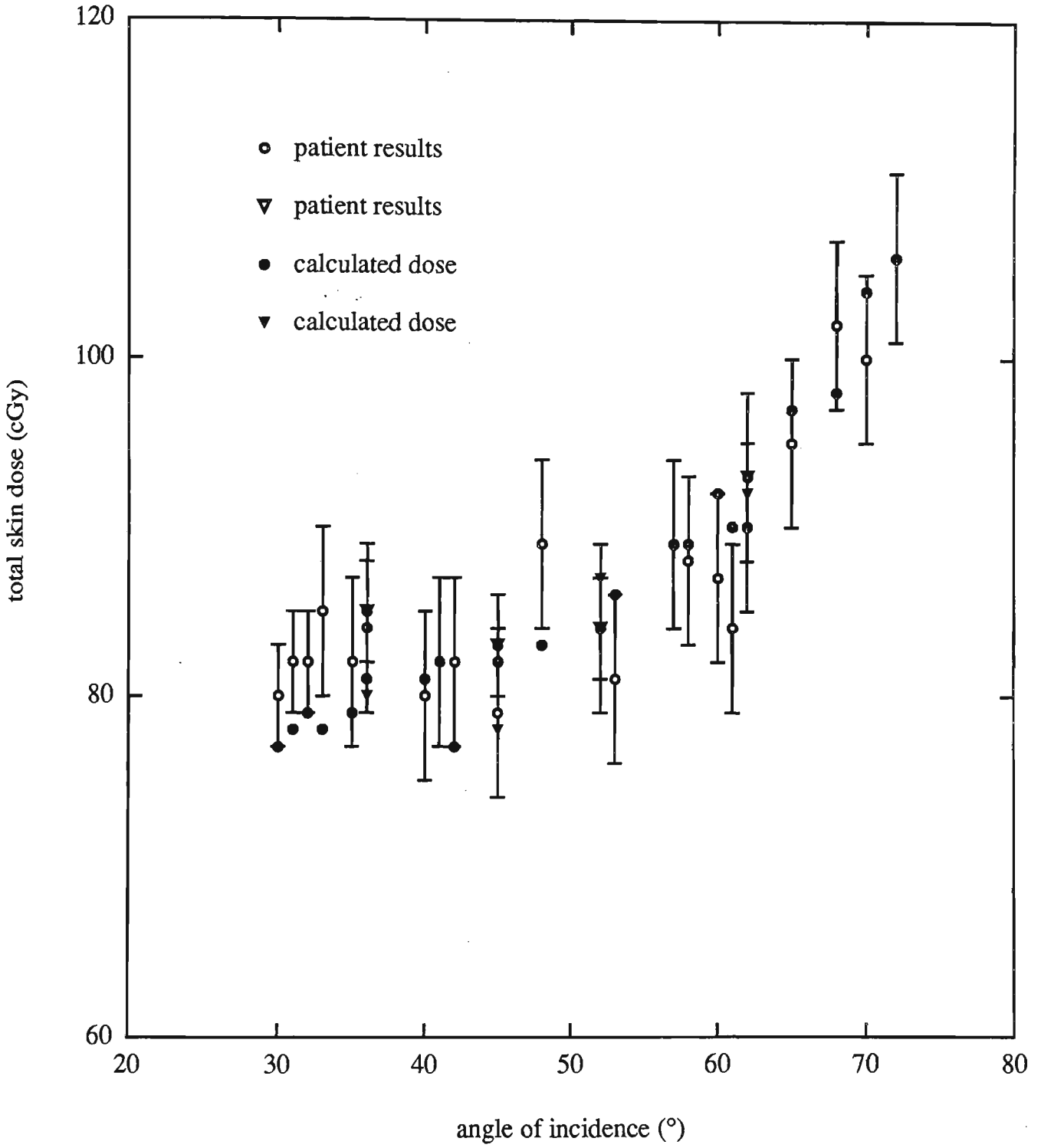

Figure 4.13 : In-vivo patient surface dose compared to calculated total skin dose (entrance + exit dose).

4.3 Spectral analysis of the electron contamination

The relative fluence of each electron contamination energy component can be approximated by correlation of the percentage attenuation of the beam in the build up region to the electron ranges of monoenergetic beams. The percentage attenuation of contamination electrons from depth d_i to d_{i+1} corresponds to the relative abundance of electron contamination with energy range from E_i to E_{i+1} having electron range from R_i to R_{i+1}. Therefore by comparison of these two quantities an approximate energy spectrum can be ascertained.

Assuming a parallel incident beam of electrons, secondary electrons undergo multiple random scattering which causes their ranges to vary slightly. In terms of mass stopping power, the range R, in the continuous slowing down approximation can be estimated by

$$R = \int_0^{E_o} \left(\frac{dE}{\rho dx} \right)^{-1} dE \qquad 4\text{-}37$$

where E_0 is the incident energy of the electrons in the phantom and ρ is the density of the target material. $dE/\rho dx$ is the mass stopping power in MeV cm^2/g. With equation 4.37, the approximate range for electrons with different energies can be determined. The range is defined well enough to produce a coarse estimate of each spectral components value.

Figure 4.14 shows Monte Carlo generated monoenergetic low energy electrons beams over the first 15mm depth. A slowly increasing range is seen with beam energy. The build up region of electron beams increases with beam energy.

Figure 4.15 shows the energy spectrum calculated to match this data by the means described above. Each energy bin is 0.25 MeV wide. Results show a high proportion of low energy contamination with quite a long tail out to 3.75MeV.

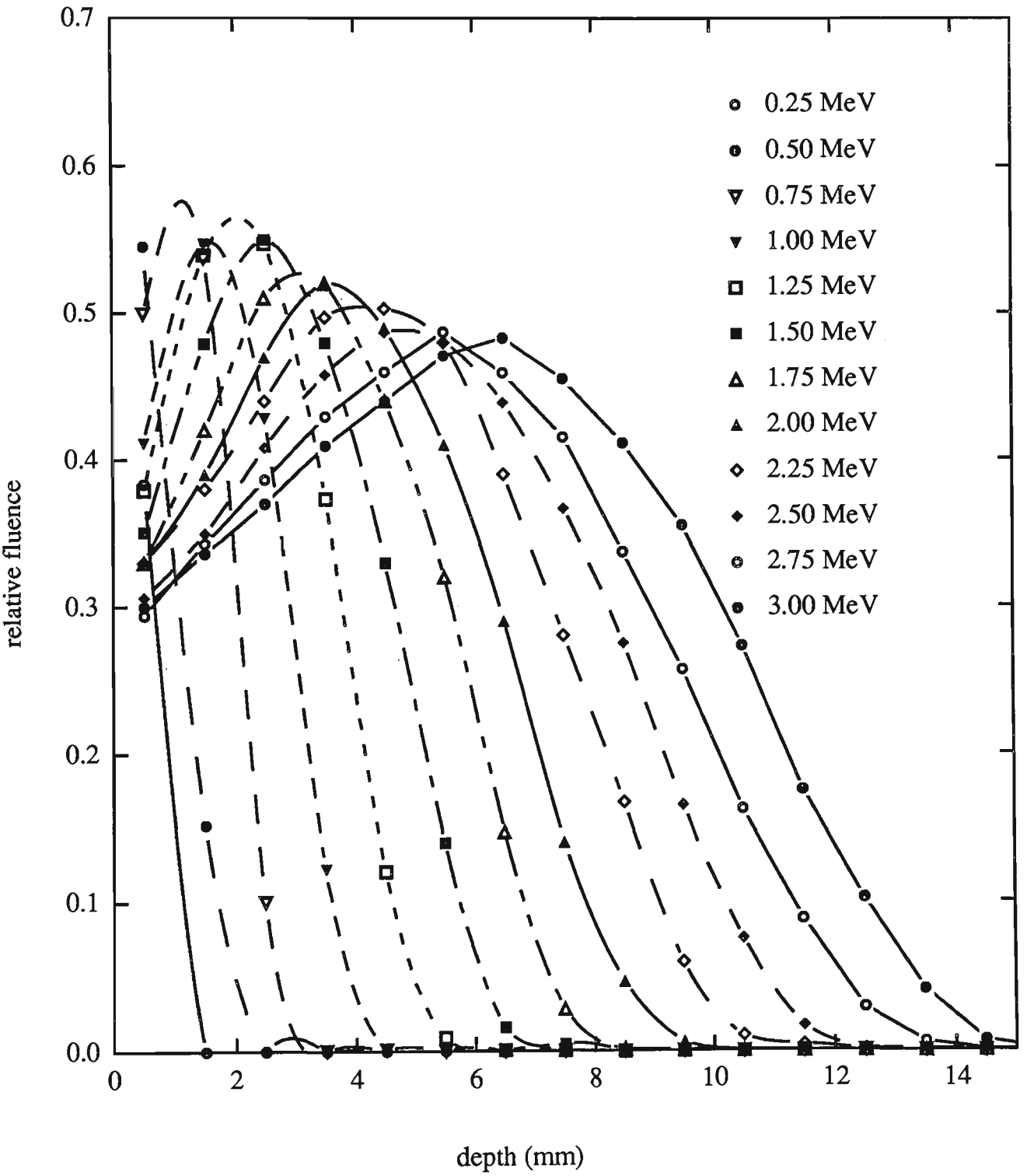

Figure 4.14 : Monte Carlo generated monoenergetic dose curves for electrons ranging from 0.25MeV up to 3MeV.

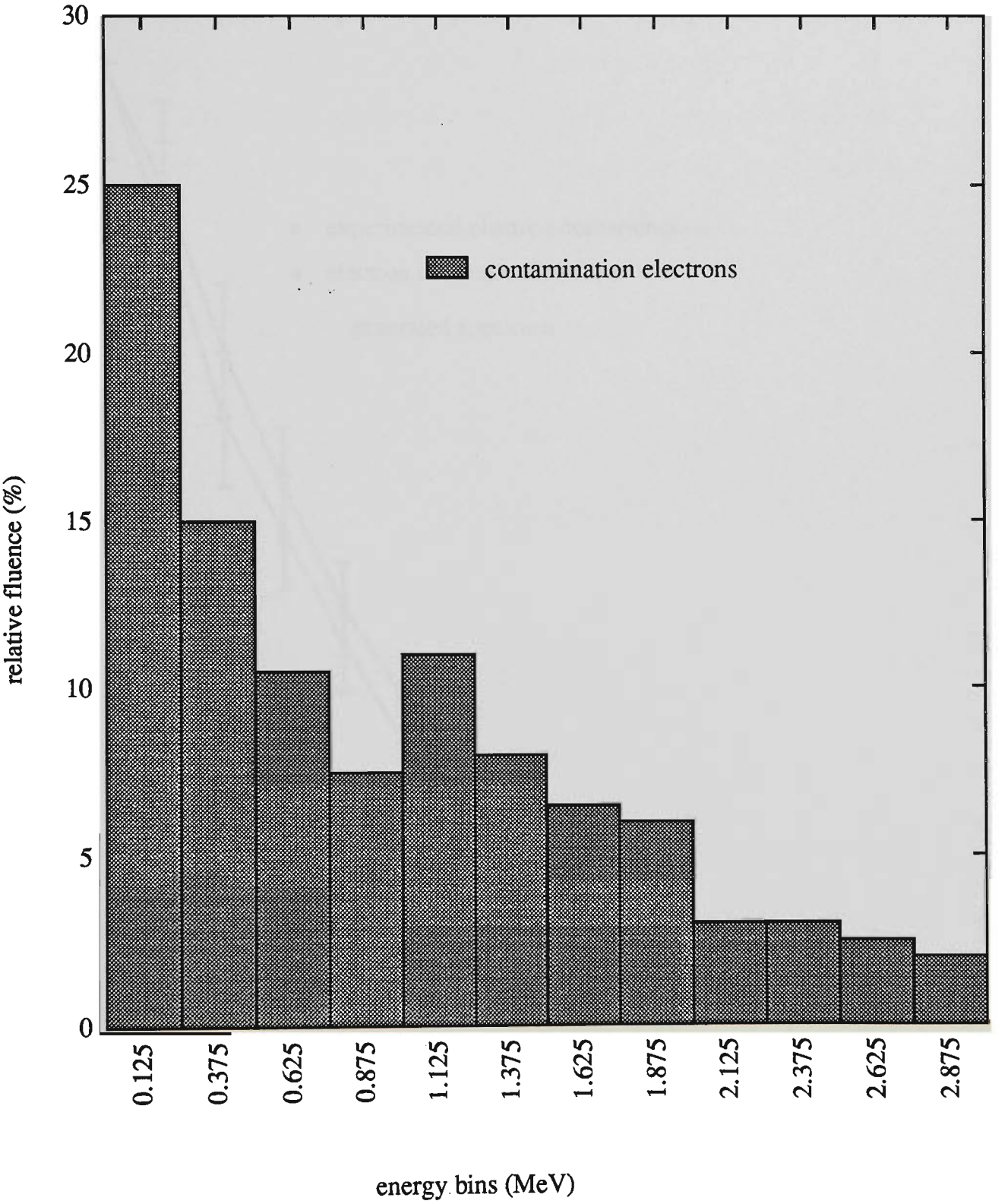

Figure 4.15 : Reconstructed energy spectrum for the 6MV electron contamination spectrum at 10cm x 10cm field size.

Figure 4.16 shows the simulated depth dose produced by this spectrum from EGS4 Monte Carlo in water compared to the measured contamination levels.

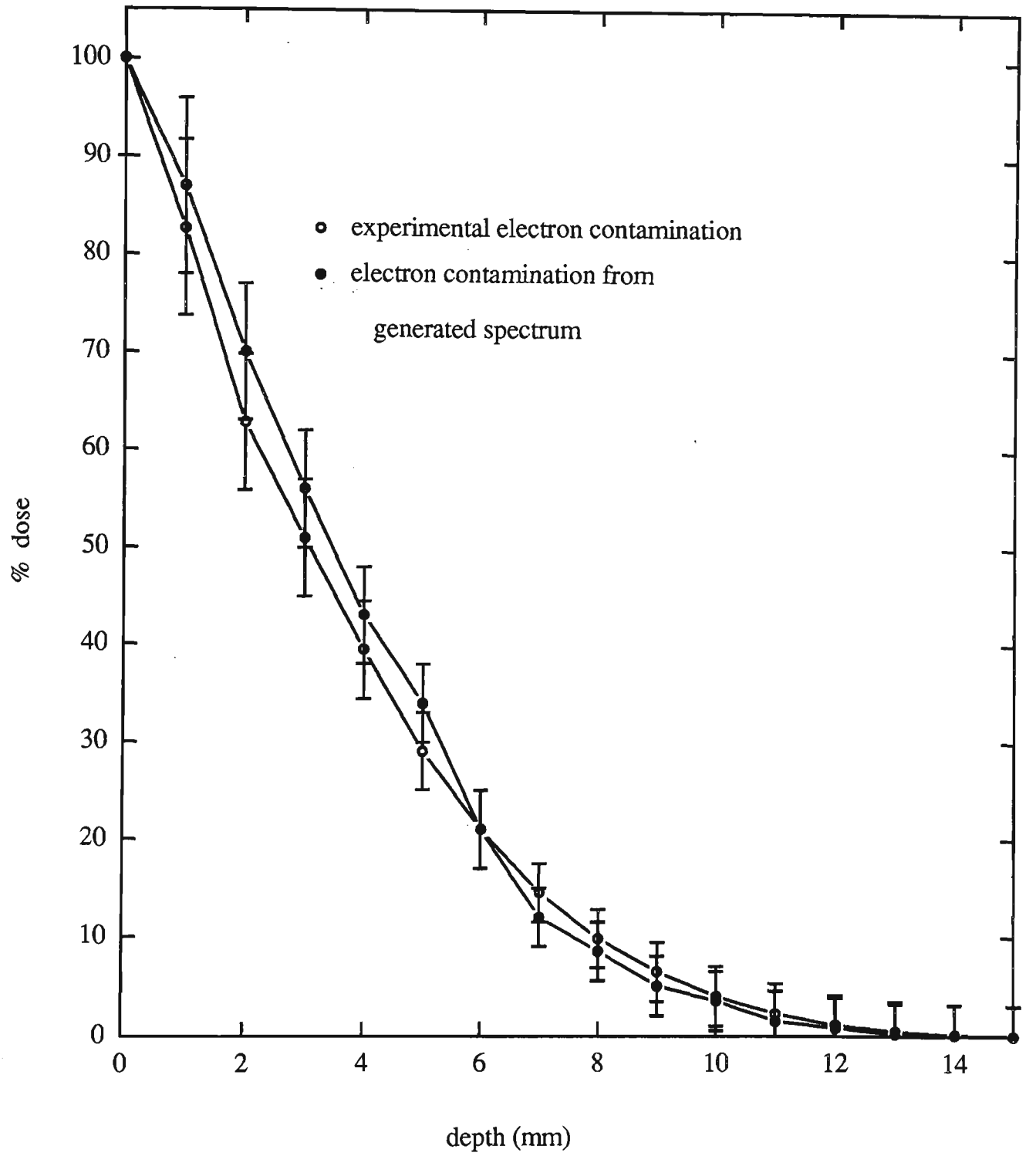

Figure 4.16 : Experimental and simulated depth dose curves to verify the energy spectrum generated. for contamination electrons.

Chapter 5 High skin dose modalities

5.1 Introduction

Enhanced dose is sometimes prescribed for skin cancers or to reduce near surface recurrence at other sites (eg. breast). Three methods of increasing skin dose are outlined in this chapter. These include the use of kV x-rays, electron/x-ray mixes and bolus techniques.

5.2 Skin dose from an orthovoltage x-ray machine

Rationale

Orthovoltage and superficial x-ray machines produce a much higher skin dose than megavoltage machines. The contributions to this dose from electrons and low energy photons was examined.

Mini methods

Detailed skin dose experiments are reported at 250kV filtration (0.3mmSn+0.5mmCu+1.5mmAl), (HVL 2.3mm Cu) for a 10cm x 10cm field size at 50cm FSD unless otherwise stated. This field size was accomplished by the use of the 10cm x 10cm cone in various configurations and with a variable collimator as shown in figure 5.1. Surface doses were recorded with the cone having :

i) intact perspex front and side plates

ii) no perspex plate

iii) lead side plate

iv) cone lead lined without plates

v) magnetic field

The lead was added to the cone to mimic the behaviour of previous designs which used lead glass . To accomplish this, 0.45 mm copperised lead was placed inside the cone to simulate a lead cone. Skin dose measurements were taken at central axis unless otherwise stated. Experiments to ascertain the contribution from low energy contamination electrons and photons produced within the cone were performed. These included measurements using the lead lined cone at extended FSD, surface dose measurements across the field at 50cm FSD to measure surface dose closer to the wall of the cone, plus the introduction of a magnetic field below the bottom of the cone to sweep away low energy electrons produced within the cone.

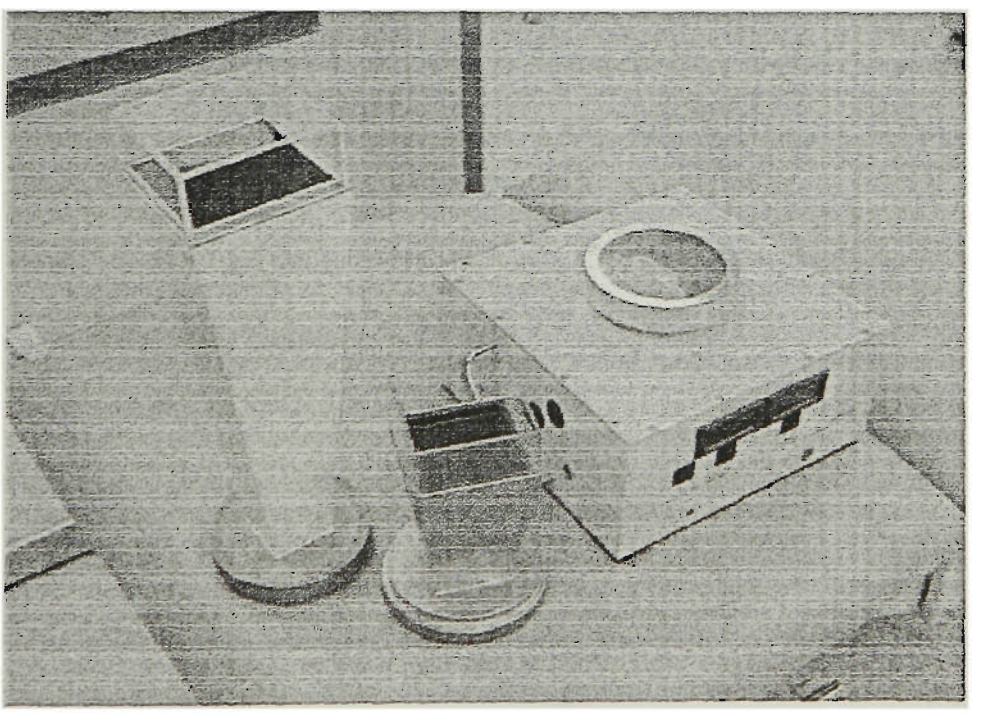

Figure 5.1 : Picture of the orthovoltage cones and variable collimator used in the experiments.

Results and discussion

Figure 5.2 shows the surface/near surface dose obtained at 250kV 10cm x 10cm field size, 50cm FSD, for various cone configurations and the collimators as measured by the Attix chamber. The results were normalised to 100% at the 'flat' beginning of the beams characteristic depth dose. That is, at 0.3mm depth in solid water for the cone and at 1mm depth in solid water for the collimator. Results for depth ionisation were also obtained with a Markus chamber. The percentage ionisation and percentage dose was assumed to be the same for these results. A comparison is given in table 5.1.

Table 5.2 shows results for experiments undertaken with the perspex cover removed from the 50cm FSD cone at 250kVp. Percentage surface doses are quoted for the 10cm x 10cm lead lined cone as the chamber is moved across the umbra closer to the wall. Results are normalised to 100% at the central axis with the percentage dose at the wall as measured by the Markus chamber being 113%. Table 5.3 shows the percentage surface dose for the lead lined cone as the FSD is changed to increase the distance between the lead material and the collecting chamber. Results are normalised to 100% at 1mm depth. At 50cm FSD the surface dose was 127% and at 55cm FSD 112% measured by Attix chamber.

Table 5.1 : Percentage doses for various orthovoltage cone/collimator configurations.

configuration	Attix	Markus
cone closed with perspex	100	100
cone open	110	109
cone with lead sides	113	111
cone lead lined	127	120
collimator	98	98

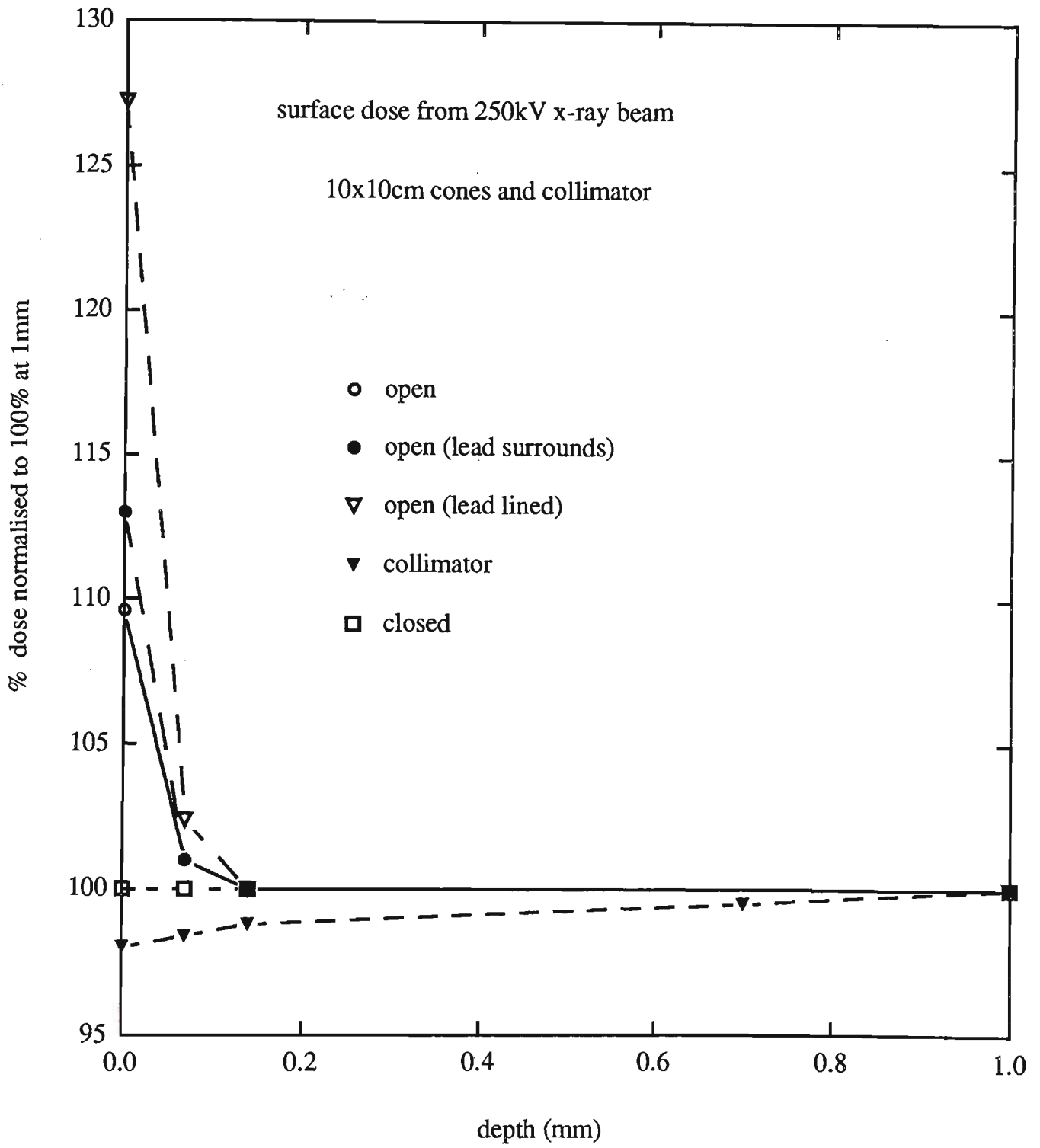

Figure 5.2 : Surface dose produced by an orthovoltage machine. High surface doses are measured when there is no front perspex plate to absorb low energy electron contamination.

Table 5.2 : Dose for 50cm and 45cm FSD at surface normalised to 100% central axis.

distance from central axis (cm)	50cm FSD (% dose)	45cm FSD (% dose)
0	100	100
3	103	106
5	107	113

Table 5.3 : Range of surface dose contamination at extended FSD's.

FSD (cm)	50	51	52	53	54	55
% dose	127	127	123	119	115	112

As shown in figure 5.2 the highest surface dose at central axis for the 10cm x 10cm cone was obtained when the cone was lined with 0.45mm thick copperised lead and the front perspex plate removed. The surface dose increased to 127.5% of dose when normalised to 100% at 1mm as measured by the Attix chamber and 120% as measured by the Markus chamber. The differences measured are possibly due to the Markus' front window thickness being larger and therefore not allowing as many low energy electrons to pass through and be collected. With just the sides near the ends being lead and no perspex over the front of the collimator, surface dose was measured as 113% with the Attix chamber and 111% with the Markus chamber. The open cone was 110% (Attix) and 109% (Markus). These results point towards both low energy secondary photons and electrons being produced within the cone through photon interactions.

To test the hypothesis of the extra surface dose being low energy electrons and photons three tests were carried out.

i) Source of extra surface dose

As the chamber was moved closer to the edge of the cone at 50cm FSD the surface dose increased to 107% normalized to the central axis dose of 100%. This indicated that the contamination was produced by the wall material as measured charge increased close to it. This effect was seen in every direction towards the walls. This was expected as lead produces both low energy photons and electrons.

ii) Energy of electrons and photons

The FSD was increased, thus increasing the distance between the photon/electron producing material and the collecting chamber. Results showed a drop in surface dose from 127% at 50cm FSD to 112% at 55cm FSD. The range of electrons produced has been calculated in order to ascertain if this drop is consistent with low energy photons or electrons or a mixture of both.

Lead has its K-shell binding energy at 88keV. Below this level the photon has insufficient energy to eject the k-shell electron. Other shells occur at 15.8keV (LI) , 15.2keV (LII) down to very low energies. If the 250kVp (maximum likely energy) beam produces a k-shell photo-electron from the lead material inside the cone this will produce a spectrum of electron energies from 0 to 162keV. Equating from stopping powers, an electron with energy 162keV has a range of approximately 0.032g/cm^2 in water which is equivalent to 0.32mm depth and approximately 0.036g/cm^2 in air. This relates to a range at normal temperature and pressure of 30cm in air. The half value layer of the 250kV beam using filter 7 is 2.3mm Cu. This equates to an effective energy of 125keV. This energy x-ray could produce a k-shell photo-electron at 37keV. For a k-shell photoelectron at this energy, from stopping powers, its range is 0.0025g/cm^2 = 0.025mm in water and 0.0029g/cm^2 = 2.4 cm in air.

The ratio of photoelectric to Compton interactions varies greatly as a function of energy. In the case of water, the ratio of Compton scattering to photoelectric effect at 250keV and 125keV respectively is 99% : 0.2% and 96% : 1%. However as the atomic number increases, so do the ratio's. For lead the Compton to photoelectric ratio at 250keV is 10% : 90% and 125keV is 3% : 97% respectively. As the copperised lead is more than 95% lead the photoelectric effect is the dominant interaction at the energies used on the orthovoltage machine. Thus the range of electrons could be up to 30cm with the majority being of the order 0-10cm around the effective energy of the x-ray beam.

iii) Differentiating electrons and photons.

A set of NdFeB ceramic magnets (5cm x 5cm x 2cm) were placed underneath the cone to sweep away the electrons produced via the Lorentz force. This was a smaller version of the magnetic electron deflector discussed in chapters 2 and 3. Results showed that surface dose at 50cm FSD was reduced from 110% to 102% with the use of the magnets. This shows that the majority of the dose enhancement at the surface is indeed contamination electrons produced from the side wall material of the cone. With the 10cm cone, the ceramic magnets had a pole separation of 12cm. The magnetic field strength was measured with a Hall effect probe. At 2cm distance from the poles, the field strength was approximately 0.1 Tesla. This point corresponds to a point 1cm in from the wall of the cone and thus a position where the majority of contamination electrons would be. At the centre of the cone, the magnetic field strength was 0.034 Tesla.

Combining the Lorentz force equation $\mathbf{F} = q\mathbf{V} \times \mathbf{B}$ and centrifugal force equation $F = mv^2/r$, the relativistic velocity of an electron with kinetic energy 250keV in a magnetic field strength of 0.1 Tesla can be calculated. The result gives us a radius of curvature for this electron to be 1.26cm. In the centre of the cone where magnetic field

strength is 0.034 Tesla the radius of curvature of the same electron would be 3.72cm. As the cone was 5cm above the phantom, this should include nearly all electrons produced from the lead. Note, only a small percentage of low energy photons and some electrons that were not totally deflected by the magnetic field are still present. However these results indicate that the extra surface dose is due mainly to the effects of electron contamination produced by the lead material placed on the inside wall of the cone.

Conclusion

The perspex front plate attached to the orthovoltage 50cm FSD cones absorb the electron contamination produced within the cone and thus give the basal cell layer a skin sparing effect. The contamination is only low energy and was mostly absorbed by 0.1mm of solid water. This shows that a thin film of low density material could be painted over the inside of the cone to eliminate the electron contamination if the front perspex plate needed to be removed for any clinical reason. A consequence also of the photoelectrons produced with the cone by the lead material is the dose incident on the patient from lead shielding. The same copperised lead is used for shielding purposes on patients which could increase the surface dose quite considerably at the boundary of the lead causing large basal cell doses to occur. With consideration of this in hand, lead edges should be painted or covered with a thin layer of wax to reduce the contamination ejected from them.

The magnetic device proved a useful tool in differentiating the electron contribution from the x-ray contribution. It was however no more useful in reducing surface dose than the perspex end plate provided. This is due to the low energy and short range of these electrons. In this respect, the skin dose provided by orthovoltage machines remains dose limiting in some cases, unlike megavoltage machines which provide skin dose sparing.

5.3 Build up characteristics of electron beams

Rationale

Electrons are often used to boost areas where there is a probability of near surface recurrence. The boost dose is generally 1/6th of the total dose eg. 10Gy boost on top of 50Gy x-ray dose. The skin dose properties of electron beams are therefore of particular significance when the contribution to total dose from both modalities is considered.

Open fields

Percentage ionisation distributions for electron energies 6, 9, 12, 16 and 20 MeV were measured by the Markus chamber in the build up region. Results are shown in figure 5.3 for a 10cm x 10cm electron applicator. All data is for the 2100C type I applicators. It is acknowledged that type II applicators will give slightly lower surface doses due to less electron scatter.

These results were in agreement with build up results obtained with a diode detector in water. Because the dose gradient near the surface for electron beams is small compared to x-ray beams, then detectors such as the scanditronix diodes used (which have a 1mm epoxy overlay above the detector) do give reasonably accurate surface dose measurements. The Markus data was applied together with fall off characteristics previously measured with diodes to produce complete data for depth dose curves as shown in figure 5.4. These results were then combined with x-ray results to analyse photon/electron beam weighting's for point dose optimisation.

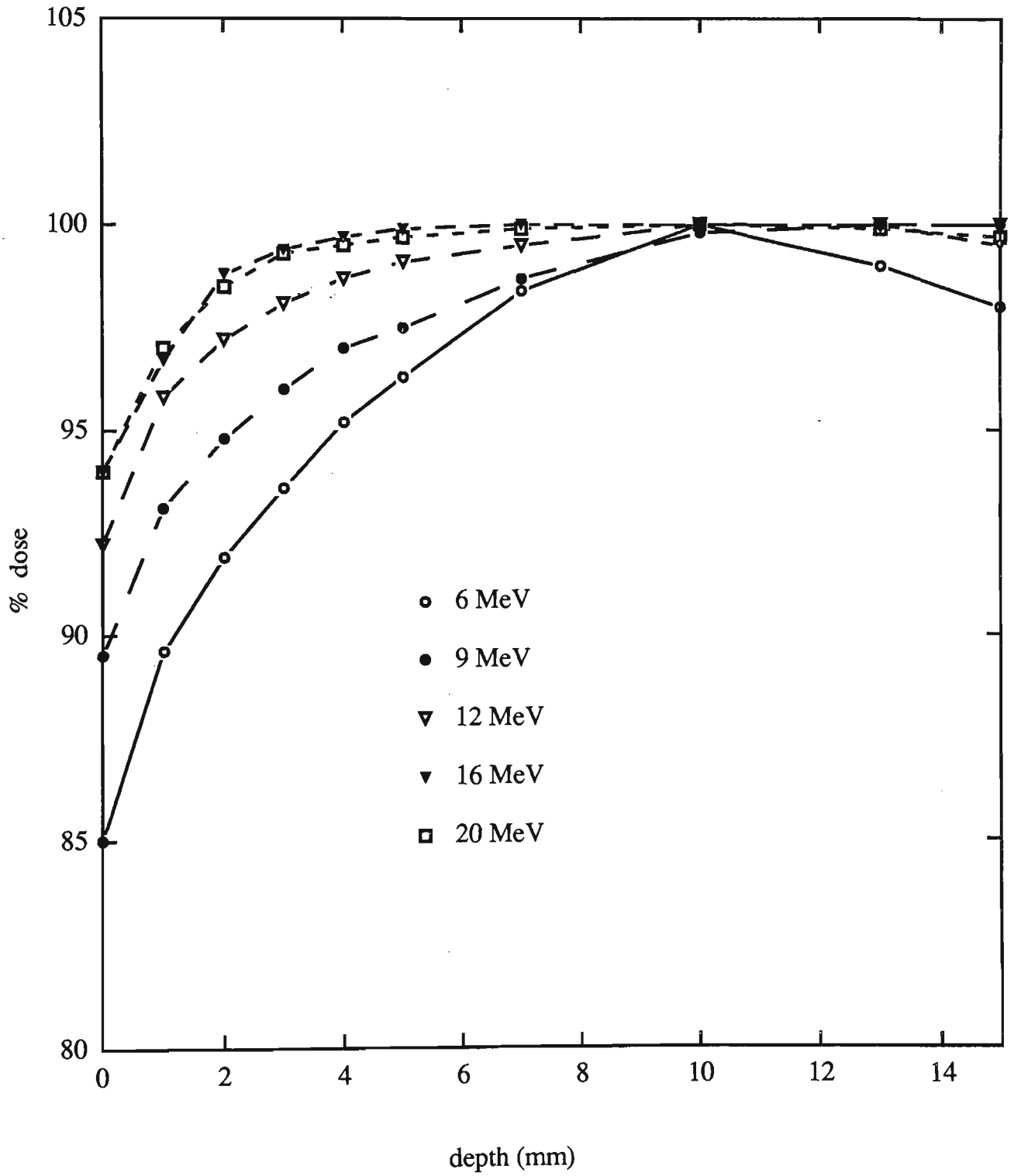

Figure 5.3 : Dose build up for a clinical electron beam using a type I 10cm x 10cm electron applicator.

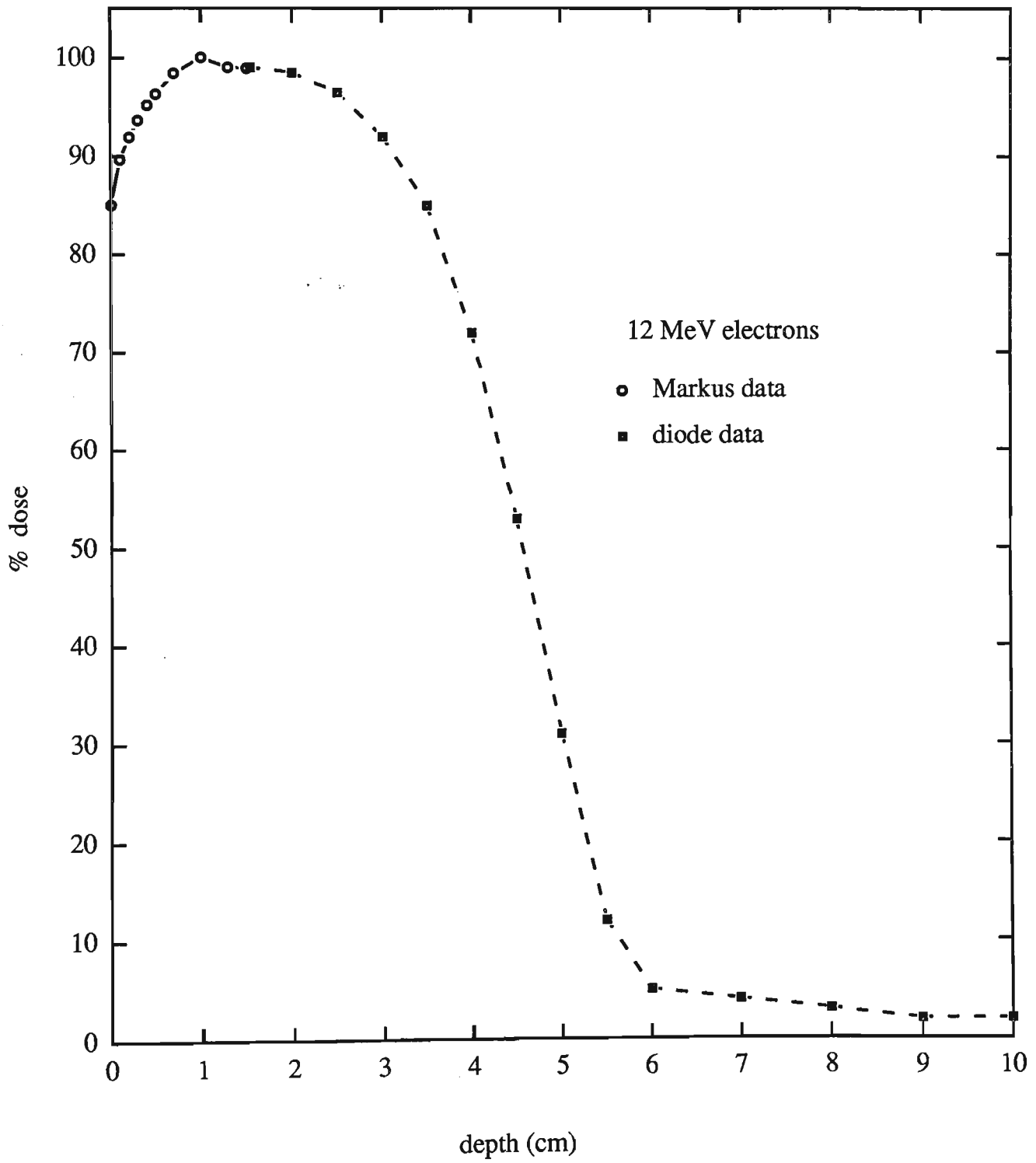

Figure 5.4 : Measured percentage depth dose for a 12MeV electron beam.

Assumptions

i) no Rawlinson correction for Markus over response was applied to electron data because TLD and diode results closely matched the raw Markus data. The nominal electron energy is high compared with x-rays and scattering power reduces with energy. The surface dose is so high that it masks the need for a chamber wall in scatter correction.

ii) the data in the build up region has been re normalised to account for air to water stopping power because the air to water stopping power ratio has a small energy dependence. This is performed as the chamber is air filled which produces slight discrepancies in measured dose and absorbed dose.

iii) no depth ionisation to depth dose correction has been performed on the diode data. This is because the stopping power ratio of silicon to water is relatively energy independent.

Table 5.5 displays the surface dose and position of maximum dose for the various applicator and energy configurations. In general surface dose increases for increasing energy.

Results show an increase in surface dose as beam energy increases for electron beams. The depth of maximum dose does not follow any systematic pattern. The size of the applicator seems to have a nominal effect. The jaw settings for different applicators change and this may have some impact on surface dose. Each energy has a different type of foil which may also influence the surface dose with energy. No information concerning electron beam build up is given in detail as this lies outside the scope of this thesis. However basic build up characteristics are needed for photon/electron beam weight optimisation.

Table 5.4 : Surface dose for megavoltage electron beams.

applicator size (cm)	beam energy (MeV)	surface dose (%)	depth of maximum (mm)
10cm x 10cm	6	85	16
	9	89	20
	12	92	30
	16	94	28
	20	94	24
20cm x 20cm	6	84	16
	9	90	20
	12	94	30
	16	95	28
	20	95	24

Dual modality treatment

By mixing the photon and electron beams together by selected ratios, a combined percentage depth dose curve can be produced. The combined percentage dose was produced by manipulating the raw data on a spreadsheet. The percentage depth dose data of the beams were multiplied by selected ratios to produce the required percentage depth dose. ie. for 60% x-ray and 40% electrons, the weighted depth dose curve was calculated by adding, 0.6 times the x-ray dose to 0.4 times the electron dose at the required depths. The calculated build up curves always lie in between the x-ray and electron 100% weighted depth dose curves and follow the general trend in shape of these two curves. A calculated beam with a higher x-ray weighting will more closely resemble the x-ray depth dose and a higher electron weighted beam will have a shape more closely resembling a pure electron depth dose curve. Figure 5.5 shows results of

weighting the 6MV x-ray and 12MeV electron beams to ratios of 100X/0E, 60X/40E, 50X/50E, 40X/60E, 0X/100E.

Shown as a convenient summary in table 5.6 are the results for surface dose, dose at 20cm, the 90% dose levels and the 70% dose levels for these selected ratios. It can be seen that as the weighting of the x-ray beam is increased, the surface dose decreases and as the weighting of the electron beam is increased, the dose at 20cm decreases. However, the depth of 90% dose shows very little variation over the entire range. From below 4mm and above 30mm for 40X/60E compared to below 6mm and above 30mm for 60X/40E shows that the 90% level is relatively unaffected by the beam weighting's.

Virtually any percentage depth dose curve could be produced inside the total x-ray and electron beams with a given weighting. However, increased electron weighting leads to higher skin dose with less dose at d_{20}. Increased x-ray weighting decreases skin dose but increases dose at depth , d_{20}.

Table 5.5 : Dose parameters for dual modality treatments.

weight 6MV x-rays (%)	weight 12MeV electrons (%)	surface dose (%) of D_{max}	dose at 20cm (%) of D_{max}	90% level depth (cm)	70% level depth (cm)
100	0	16	38.6	0.7-4.0	0.3-9.0
0	100	92	1	0.0-3.5	0.0-4.5
60	40	46	23	0.4-3.5	0.2-5.0
40	60	61	15	0.4-3.5	0.1-4.5
50	50	53	19	0.4-3.5	0.2-4.5

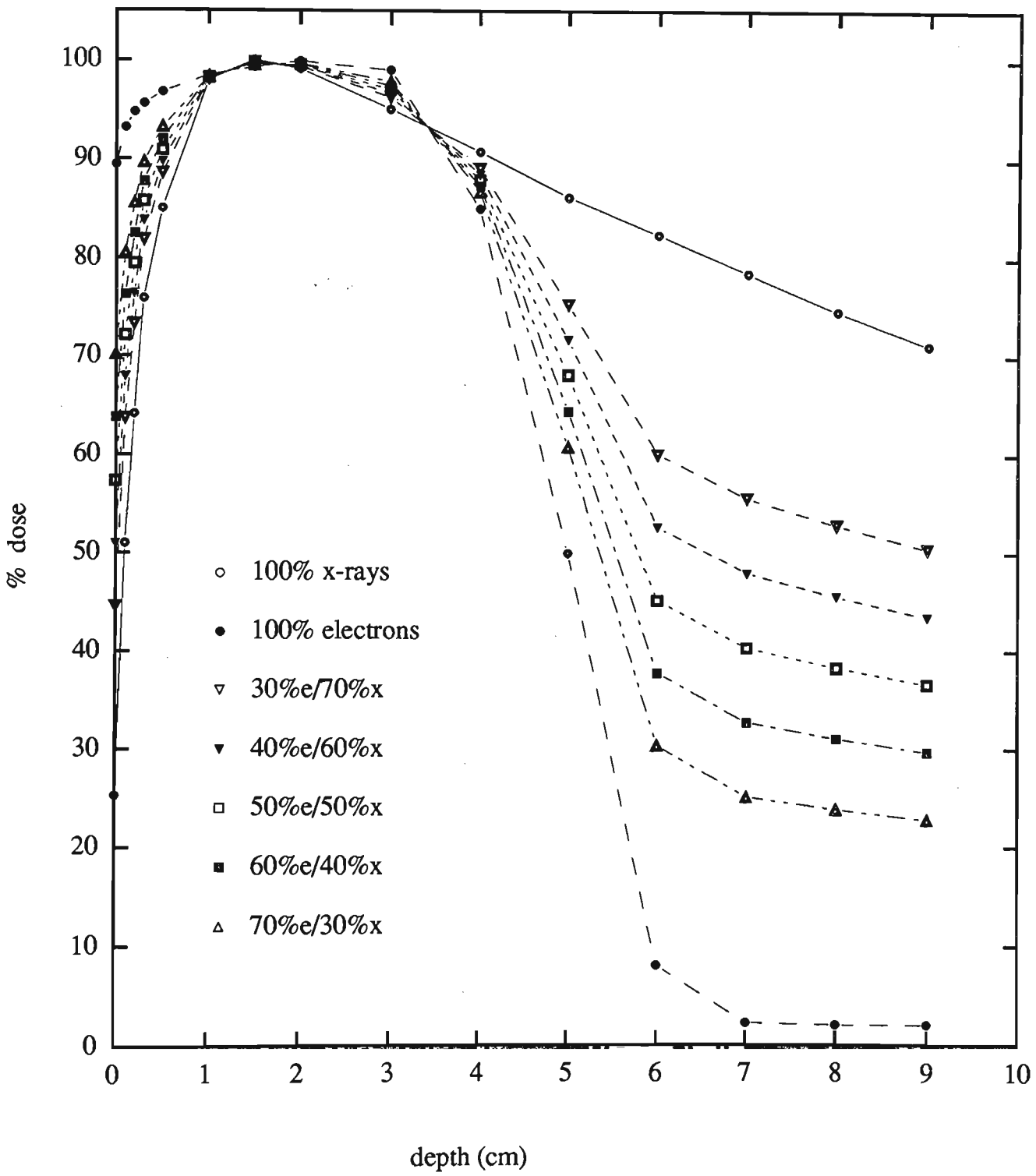

Figure 5.5 : Calculated percentage depth dose curves for various photon electron beam weights using 6MV x-rays and 12 MeV electrons.

Note, as many electron doses are prescribed to the 90% , it is misleading to assume that weight change within a reasonable range will significantly affect the depth of this 90% level.

Discussion

Skin dose to a patient by the use of photon/electron mixes can be controlled and kept to an optimum level whilst still taking into consideration other necessary effects, eg. spinal cord dose. There are many factors that can influence the x-ray beam surface dose component of the mixed modality treatment. As mentioned earlier, the depth dose characteristics of photon beams is influenced by beam characteristics and other settings such as field size and the use of block trays. These parameters vary from patient to patient. The field size, block trays and beam angle have a significant impact on the depth dose build up characteristics of photon beams and thus the dose to skin during treatment. These effects should also be taken into account when dual modality treatments are used for skin sparing.

Conclusion

The photon/electron weighting's can be optimised for a certain clinical treatment due to individual patient requirements.

This data is important from a clinical point of view. It shows that the 90% level of radiation does not vary in depth significantly within a wide range of photon and electron weights. This means that dual modality is not useful in shifting the area of treatment in accordance with depth but has the ability to control dose to skin and vital organs to produce the optimal level for both areas whilst still delivering the required tumour dose.

This data is useful for assessing patient skin and vital organ dose and a data set containing these types of graphs contain an effective guideline in terms of optimising beam weighting. This data can be used in conjunction with isodose plans which generally do not effectively show the surface dose in sufficient detail.

A simple protocol has been presented here where predicted central axis dose for co-incident x-ray and electron beams can be calculated. The ability to formulate depth dose curves along a ray with electron and x-ray beams incident at different angles would be an excellent future enhancement.

5.4 Bolus

Bolusing is performed to increase the dose to the skin of a patient whilst receiving radiotherapy. X-ray beams produce a significant build up region or a large skin sparing effect. Measurements were performed to ascertain if the effect of bolus was compromised when small air gaps inadvertently arise in between the bolus material and the patients skin. In some instances, due to the shaping ability of the bolus material, small air gaps of the order of a few millimetres might occur in certain regions of the treatment field. This section examines whether these air gaps compromise the dose given to the skin during radiotherapy. Electron beams are not considered in this analysis.

Mini-methods

Measurements were performed under a Varian 2100C linear accelerator. Photon beam measurements were made using an Attix Model 449 parallel plate ionisation chamber, in a solid water stack phantom. The chamber was connected via a triaxial cable to a Keithley model 2540 electrometer at 300V bias voltage. Results were obtained with various field sizes, differing amounts of bolus material and various air gaps. The bolus materials investigated were wax and super flab. The air gaps were introduced by placed small plastic blocks on the edge of the solid water phantom and placing the bolus on top of it. Results quoted are for 6MV x-rays with wax bolus however similar results were recorded for other experimental configurations (ie. super flab).

Results

Figure 5.6 shows a typical build up curve for a 6MV x-ray beam at 100cm SSD. Two field sizes are shown, 10cm x 10cm and 30cm x 30cm. Surface doses are 16% and 37% respectively for the two beams showing the variability of surface and skin dose

associated with patient specific parameters. With the use of block trays and with varying beam angle of incidence the values for surface dose at 6MV x-rays can reach 70%. If some cancerous cells were expected to be located near the surface then a bolus material would be needed to increase the dose to the skin to close to that of the tumour dose.

Figure 5.7 shows the same two build up curves and the influence on the curves with the introduction of bolus and air gaps. Results are quoted for two field sizes and with three different air gap distances. The x-axis quotes the distance from the isocentre which is at 100cm from the source. The experiments were performed with the top surface being kept at 100cm SSD. Thus as the air gap increases, the distance from the isocentre of the skin also increases as a constant 10mm of bolus is placed on top. Results show that for small air gaps of only a few millimetres a negligible decrease in skin dose is observed. If the air gap is 10mm a noticeable decrease in dose to the skin surface is seen with a drop of 6% for a 10cm x 10cm field size however this has increased back to maximum dose within 2mm.

By subtracting the percentage dose results beyond the air gap from percentage dose results without an air gap, the reduction in dose delivered to the skin can be seen. Figure 5.8 shows these results for a 6MV x-ray beam, 10mm of wax bolus at 10cm x 10cm and 30cm x 30cm field sizes with different air gaps. A negligible result is seen for a 2mm air gap. Less than 2% difference is seen for all air gaps at the larger field sizes. For a 10cm x 10cm field size a difference of 6% at the surface was seen for the air gap of 10mm. This value dropped to 2% after 2mm depth. This 2% was mainly due to the inverse square law effect with the changing distance to the measurement chamber.

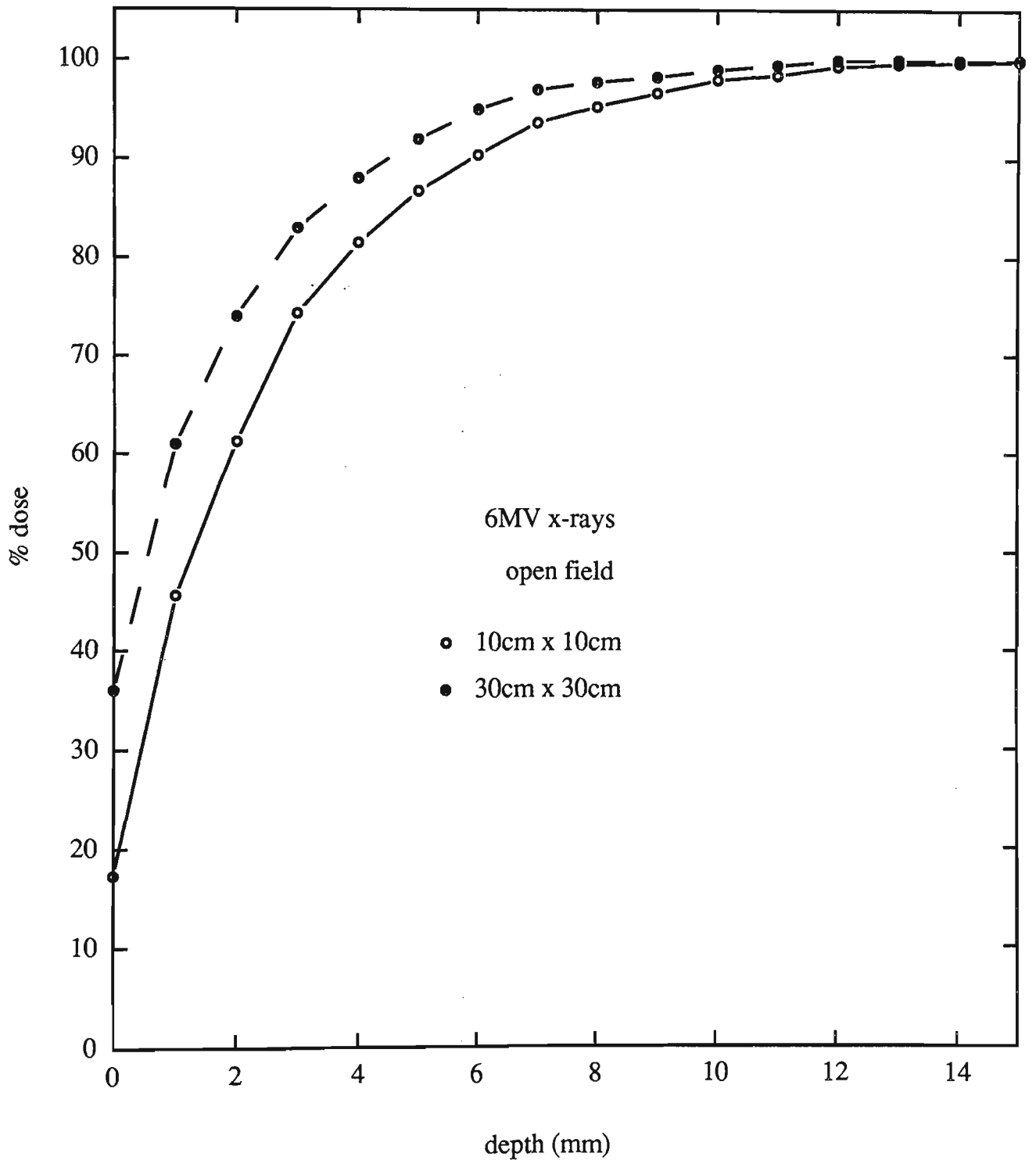

Figure 5.6 : Open field percentage dose build up curves for 6MV x-rays.

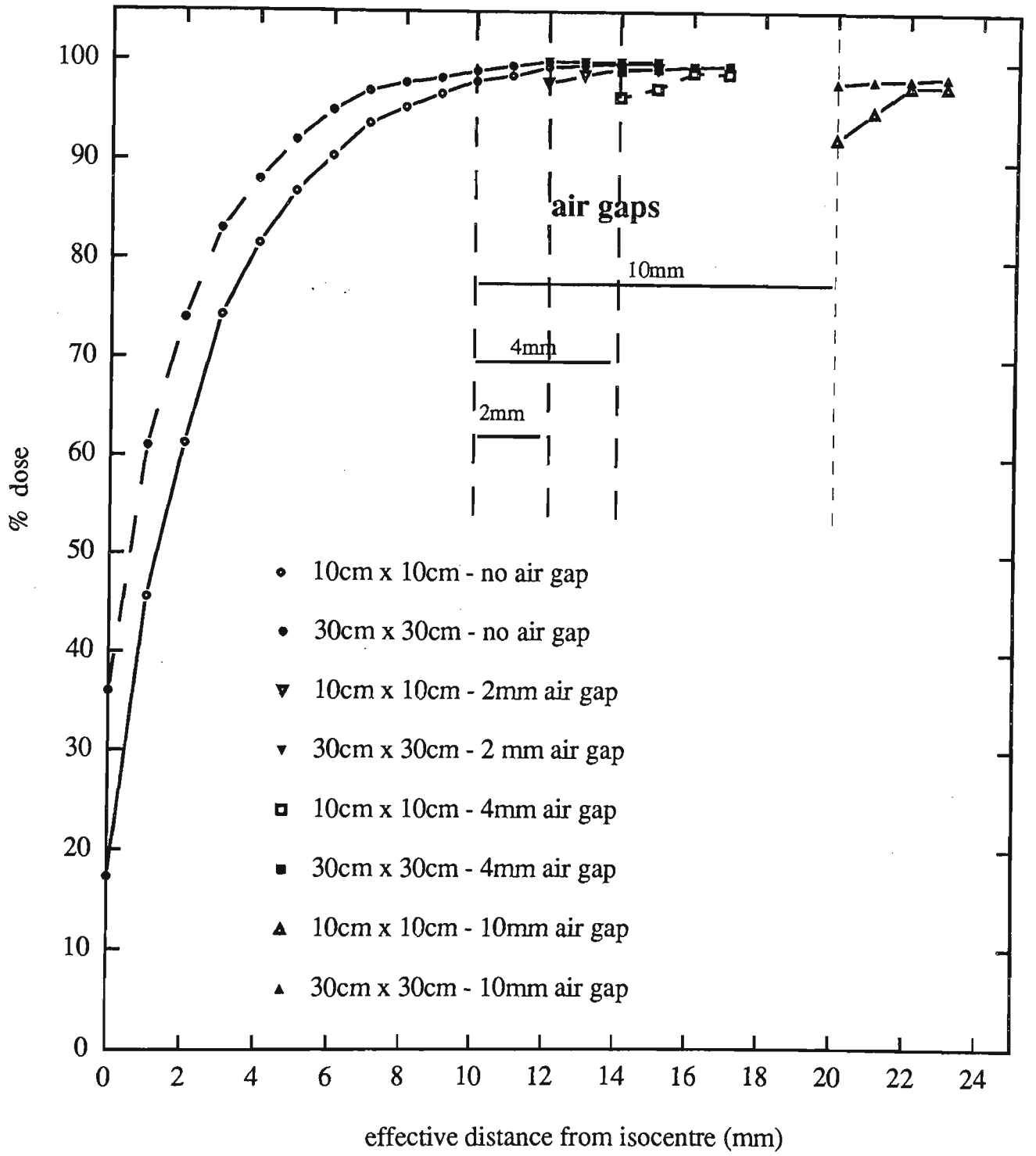

Figure 5.7 : The impact of air gaps on the build up characteristics of 6MV x-rays. Small air gaps produce a negligible effect. Once the air gaps reach a size of 10mm, a noticeable decrease in dose is seen due to redevelopment of longitudinal electron disequilibrium.

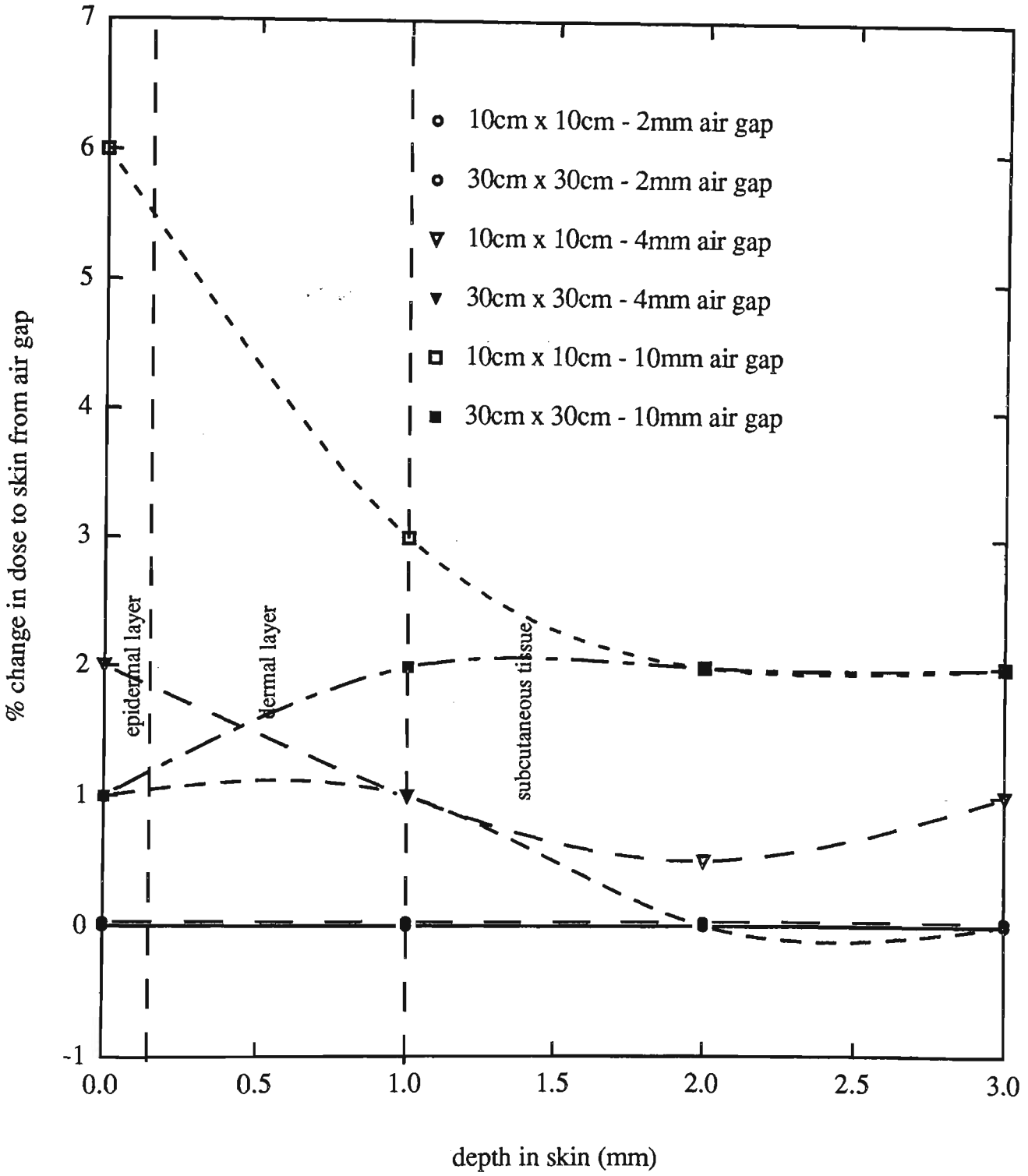

Figure 5.8 : Percentage dose differences delivered to the skin with varying sizes of air gap.

Discussion

Bolus material is often placed on a patients skin during radiotherapy thus effectively removing the build up effect of photon beams. Treatments for breast carcinoma (Muller-Sievers et al 1992) or maxillary sinus carcinoma (Janjan et al 1991) are examples of treatments where bolus material is used to increase the skin dose. Unfortunately due to insufficient malleability of bolus material small air gaps can be generated.

The significance of the air gap effect was considered as electronic disequilibrium would be regenerated in the secondary build up region and this could have caused the dose directly to the patient skin to decrease. This is seen in the case of air cavities such as the nasophrynax or oesophagus (Wong et al 1992). These cavities are however a larger size (of the order of centimetres). Results here using small air gaps of less than 1cm show that no significant reduction in skin dose results. Clinical air gaps are expected to be discontinuous, being mostly small air pockets whereas these results are for continuous air gaps produced by a flat sheet and therefore represent the maximum likely reduction in dose. The small reductions seen are due to the forward scattering of electrons produced by the high energy photon beams. Electrons generated in the bolus material are mostly forward scattered. They are therefore likely to exit the bolus material and pass through the small air gap to reach the skin surface and deposit dose. A small percentage will be scattered and a small percentage will not be generated from side scattered interactions. This can be seen as a field size dependent effect where a smaller 5cm x 5cm field has a larger reduction due to lateral electron disequilibrium than the 30cm x 30cm field.

Higher energy beams are not frequently used with bolus due to the nature of the treatment site, however a similar effect would be expected as the electron scattering patterns at high energies are similar. Experiments with larger air gaps at high energy

show a small secondary build up with the valley to peak dose only differing by a few percent. This difference increases slightly with increasing energy in the primary build up region (Wong et al 1992).

Conclusion

The effects of small air gaps under bolus material have been shown to produce only small decreases in skin dose for radiotherapy x-ray treatment fields. Air gaps should be minimised under bolus however though, the introduction of small air gaps does not significantly reduce skin dose.

Chapter 6 Summary

Predicted clinical results with magnet and helium system

The clinical use of the magnet and helium bag system, discussed in chapter 3 could reduce the dose delivered to skin if needed. Predicted results are shown below.

Table 6.1 below shows a list of various patient treatments at our centre. Quoted are the treatment site, tumour dose, applied dose per field, and the predicted basal layer skin dose (depth 0.07mm) with and without the skin sparing system and finally the predicted reduction in basal cell layer skin dose. Table 6.2 provides data for the same patients however predicted skin doses are quoted at a depth of 1mm relating to the dermal layer. Results were obtained using phantom data collected in this research as clinical trials have not begun as yet. Patients have not yet been treated using either of these clinical devices in place. The clinical use of the magnet electron deflector is envisaged on patients requiring low skin dose provided ethical questions about the implementation can be worked through.

Table 6.1: Predicted basal layer (0.07mm) skin dose reductions achievable clinically.

treatment site	tumour dose	applied dose per field	basal dose without magnet	basal dose with magnet	reduction in basal dose
	(Gy)	(Gy)	(Gy)	(Gy)	(Gy)
supra/clav	50	50	12.5	7	5.5
larynx	62.5	32.5	6.8	3.5	3.3
breast	50	30	10.5	5.7	4.8
hip/pelvis	40	32.7	16	6.9	9.1
mantle	35	25.5	15.3	7.4	7.9

Table 6.2: Predicted dermal layer (1mm) skin dose reductions achievable clinically.

treatment site	tumour dose (Gy)	applied dose per field (Gy)	basal dose without magnet (Gy)	basal dose with magnet (Gy)	reduction in basal dose (Gy)
supra/clav	50	50	27.5	20	7.5
larynx	62.5	32.5	16	12.7	3.3
breast	50	30	16.8	11.7	4.3
hip/pelvis	40	32.7	24.5	17.6	6.9
mantle	35	25.5	21.7	15.5	6.2

As can be seen in tables 6.1 and 6.2 significant reductions are achievable clinically with the integral skin dose reduction system. An important consideration when dealing with skin reactions is also the exit dose from opposing fields. For example with the breast treatment mentioned above, a relatively low entrance skin dose is recorded. We see a reduction from 10.5Gy down to 5.7Gy. A dose of 10.5Gy to the basal layer may not produce any harmful effects alone but skin dose is also deposited from the exiting beam by the parallel opposed tangent field. A basal layer skin dose of 23Gy would be given from the opposing field. Thus initially total basal layer dose is 33.5Gy.

Studies by Turesson (12) have shown clinical normal tissue complication probability (NTCP) curves for erythema/telangectasia reactions in skin. Results show a sharp increase in likelihood of reactions for erythema at approximately 30-35Gy. Similarly, telangectasia which could be considered to occur from dose deposited at 1mm depth has a sharp increase in NTCP at around 40Gy. Predicted dose results at 1mm show that dose initially would be (considering entrance and exit dose) 39.5 Gy which would be reduced to 35Gy by the use of the magnets and helium bag. In this case, a small reduction in skin dose could significantly reduce the patients NTCP.

Conclusion

The practicality of the above system makes it feasible for clinical use where skin dose needs to be reduced. The magnetic deflector weighs approximately 15kg and is easily attachable to the treatment head of the accelerator. It can also be easily removed like a block tray if the device is not needed. The helium bags could be made in different sizes and shapes to suit typical treatment sites and field sizes. The bag could be easily inflated and placed on the patients skin during treatment. There would realistically be opposition to its use around the head/neck region due to initial safety precautions but other areas would be clinically useable, with a small time penalty.

Basal cell layer dose was reduced by up to 30% of applied dose for 6MV photons, this equates to up to 70% of initial skin dose. The two piece system (magnets and helium) can be easily attached and removed from the accelerator and produced no change to tumour dose whilst removing unwanted skin dose caused by electron contamination.

Clinical implementations of the magnetic electron deflector and helium bag system will be investigated. Studies into the effects of other overlaying materials such as burn retention tapes will be investigated.

Reliable in-vivo techniques which measure skin dose have been established as reported here. These include extrapolation TLD's, MOSFET's and Radiochromic film. This report shows that accurate skin dose assessment can be performed in the radiotherapy clinic. The correlation bewteen skin dose and skin reactions is not yet an exact science and should be the subject of further investigation.

Appendix 1 Electron filters in radiotherapy

Electron contamination which reaches a patient skin can be reduced by the use of electron filters. These devices are normally constructed from either medium atomic number materials for lower energy photons (Khan 1984) through to a low/high combination atomic number filters for higher energy photons (Nilsson 1985). They primarily reduce the amount of forward scattered electrons. As shown in figure A1.1, adapted from Khan (1984), Tin was found to be an optimum electron contamination filter in 10MV x-ray beams. For higher energy beams such as 25MV, a combination aluminium lead filter was found to be optimum for electron contamination removal. These results however vary greatly depending on the position of the filter in relation to the phantom, the thickness of the filter material and spectrum of the x-ray machine. In general the thickness of an electron filter in theory should be at least equal to the maximum range of secondary electrons produced. This would relate to a thickness of 0.9mm ($0.5gm/cm^2$) for tin in a cobalt-60 beam. However this thickness must be tailored to produce a negligible effect on the depth characteristics of the x-ray beam (ie. beam hardening) and to provide a respectable output (similar to a wedge) due to the attenuation of the primary beam by such a device.

Mini-methods

Filtering of electron contamination produced from the head of the linear accelerator was performed with a series of elements with different atomic numbers. Materials used included aluminium, copper, zinc, and lead. All these materials were placed at 65cm from the source in the block tray accessory mount to determine the effective filtering properties of each material. Table A1.1 gives the atomic details of each filter used.

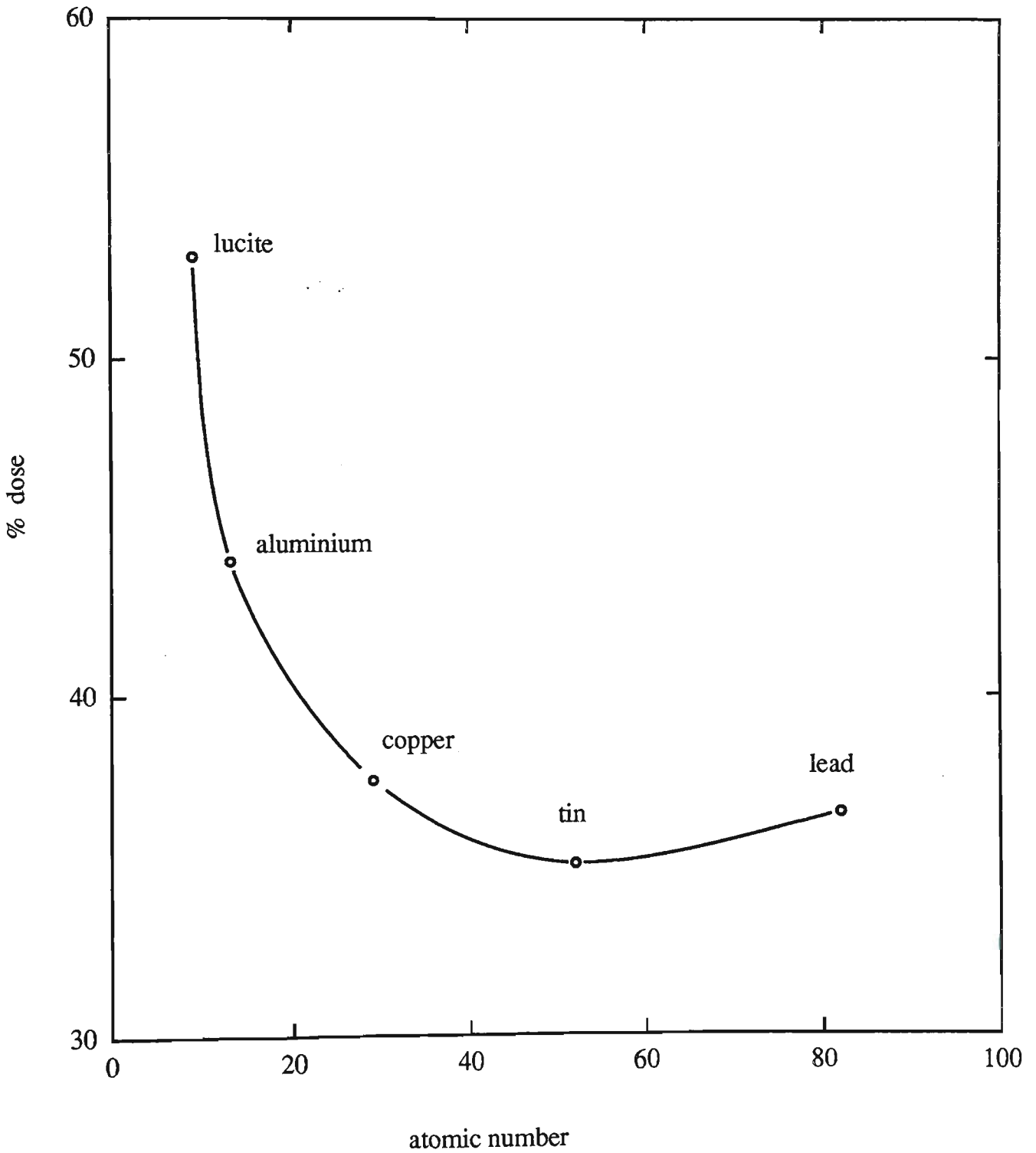

Figure A1.1 : Electron filtering capabilities of various absorbers at 10MV x-ray energy. Tin was found to be the optimum electron filter at this energy.

Table A1.1 Atomic number and physical density of electron filter materials.

material	aluminium	copper	zinc	lead
atomic number	13	29	30	82
physical density	2.7	8.93	7.1	11.35

Results

Electron contamination produced by the treatment head of the linear accelerator can be removed by placing an electron filter in the beams path. Figure A1.2 briefly demonstrates the reduction in surface dose achievable by using electron filters. Reductions up to 5% in surface dose are achievable. At 6MV, lead was shown to be marginally better at reducing surface dose than Aluminium, Copper and Zinc. There seemed to be only a small (<1%) change in surface dose when the thickness of filtering material placed in the beams path was increased or decreased from approximately 0.2mm to 1mm.

Clinical use of electron filters are hindered by two factors. Firstly their opaqueness means the filter must not be in place during patient setup. Secondly, the filters attenuation properties would require an attenuation factor to be used. If the filter was accidentally left out then a correction would be needed. Beam hardening could also be an issue in effecting the depth dose characteristics. Electron filters can be used clinically to reduce skin dose however the magnetic electron deflector and/or helium bag system were able to remove more electron contamination.

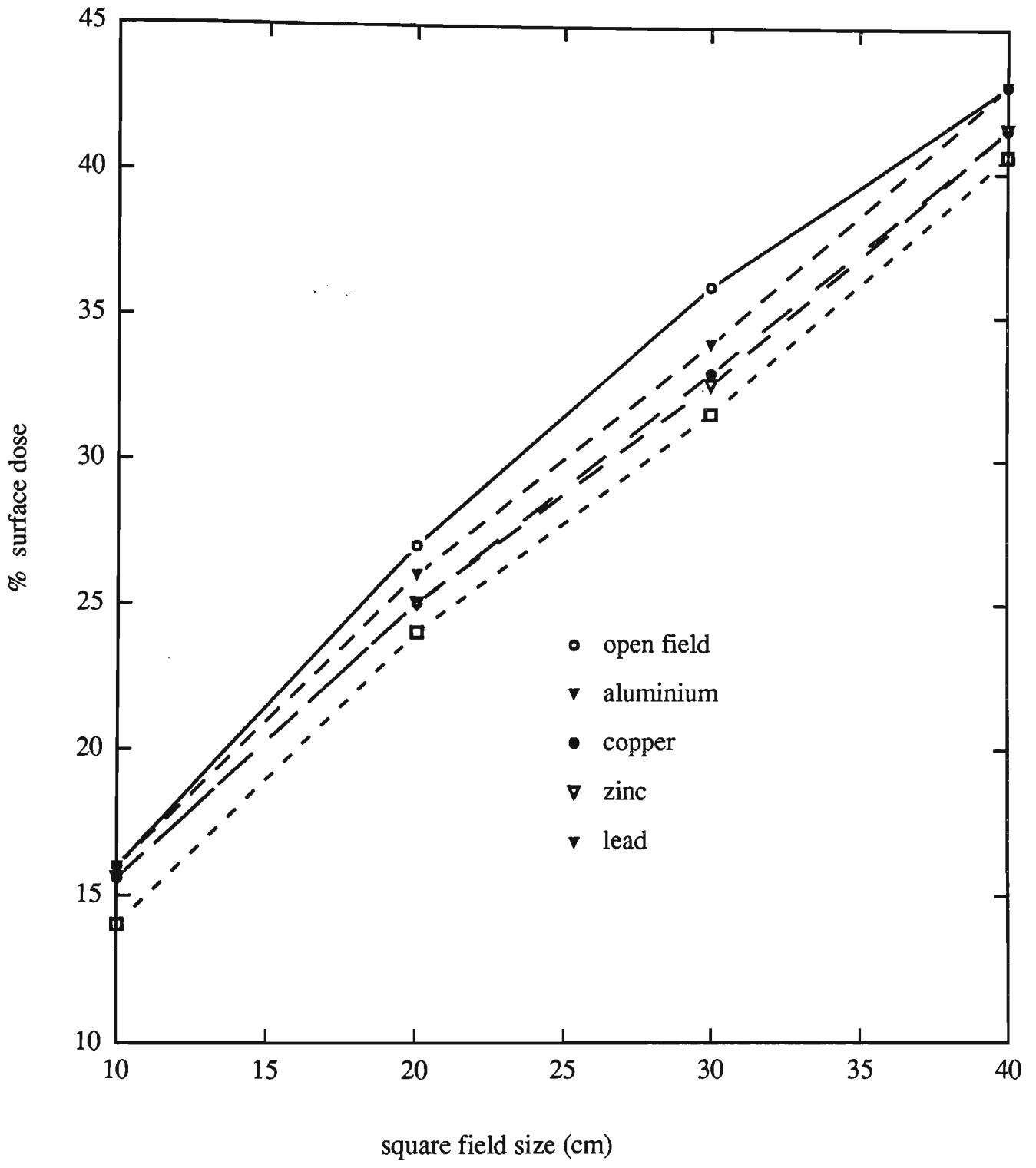

Figure A1.2 : Percentage surface dose measured as a function of field size for various electron filters at 6MV x-ray energy.

Appendix 2 Equivalent square calculation

Introduction

To enable correct dose calculation in the build up region for irregular patient field sizes, an estimate of equivalent square field size for the irregular patient field size is required. The introduction of lead blocks into the x-ray beams path shields both primary photons, head scatter and electron contamination. This section briefly reports data on irregular fields and their effect on surface and build up dose in terms of equivalent square size estimation.

Materials and methods

Measurements were taken in most cases on the central axis of the x-ray beam. When the blocked area measured infringed upon or became close to the Attix chamber it was moved to the most open area in the irregular field chosen. Rectangular and square field sizes from x = 5cm, y = 5cm to x = 40cm, y = 40cm in 2.5cm intervals were measured for charge at the surface and at depth. Equivalent square field sizes were obtained by linear interpolation between measured square field sizes. From these results, equations were modelled and reported in chapter 4 using the Marquardt iteration algorithm. For irregular fields, lead and cerrobend blocks were placed on a 6mm perspex block tray in the accessory mount of the linac to reduce the original field size. Surface dose measurements were obtained to ascertain the reductions introduced by this shielding.

Results

Table A2.1 shows the surface equivalent square field sizes for rectangular fields between 5cm x 5cm and 40cm x 40cm. Results were obtained through linear interpolation between measured square field sizes. Unlike dose at depth, no significant

jaw dependent readings were observed, eg. 5cm x 40cm, 40cm x 5cm gave the same results. As stated in chapter 4, results show that Sterling's 4xA/P equation underestimates the equivalent square surface doses by up to $2cm^2$ for long narrow rectangular fields.

Table A2.1 : Equivalent square field sizes for rectangular fields.

field sizes (cm)	5	10	15	20	25	30	35	40
5	5	6.8	8	8.9	9.5	9.8	10.2	10.5
10		10	12.2	13.6	14.8	15.6	16.4	16.8
15			15	17.2	18.8	19.9	21	21.6
20				20	21.7	23.7	25.3	26.5
25					25	27.5	29	30.5
30						30	32	34.5
35							35	37.5
40								40

Irregular fields in patient treatment can be dealt with in two sections.

i) rectangular fields where the machines collimators are the only form of shielding

ii) blocked fields where lead or cerrobend is placed on a block tray to shield an organ or some irregular shape

When dealing with rectangular fields no additional material is placed in the beams path to attenuate or produce existing electron contamination. Thus the calculation of an equivalent square field size gives a good match to surface dose due to contamination electrons. For an irregular field, additional material is placed in the beams path by the

insertion of a block tray and the lead blocks. Two effects arise from their introduction. The area of block tray which could produce electron contamination will be reduced by the virtual elimination of x-rays interacting in the block region. This will impact on the block tray effect in the build up region with field size. Secondly, the lead blocks can interact to produce electron contamination especially from their side walls. These blocks will impact on the homogeneity of electron contamination delivered to the patients skin. In these situations the equivalent square calculation is still an adequate approximation (ie. within ±5% for most blocked fields).

References

Ahnesjo A, Andreo P 1989 Determination of effective bremsstrahlung spectra and electron contamination for photon dose calculations *Phys M ed. Biol.* **34** 1451-1464

Aldrich J E Meng J, Andrew J 1992 The surface doses from orthovoltage x-ray treatments. *Medical Dosimetry* **17** 69-72

Andreo P 1985 The interaction of electrons with matter: II scattering. The Computation of dose distributions in electron beam radiotherapy pg 56 Umea Sweden.

Biggs P J, Russell M D 1983 An investigation into the presence of secondary electrons in mega voltage photon beams *Phys. Med. Biol.* **28** 1033-1043

Biggs P J, Ling C 1979 Electrons as the cause of the observed shift with field size in high energy photon beams *Med. Phys* **6** 291-295

Bragg W H 1912 *Studies in Radioactivity.* New York Macmillian. *as cited by Khan.*

Butson M, Yu P, Metcalfe P 1998 Effects of readout light sources and ambient light on radiochromic film. *Phys Med Biol* **43** 2407-2412

Carolan M, Butson M, Herrmann K, Mathur J, Metcalfe P 1997 Conversion of an infrared densitometer for radiochromic film analysis *Australas Phys Eng Sci Med* **20** 183-185

Chaney E, Cullip T, Gabriel T 1994 A Monte Carlo study of accelerator head scatter *Med. Phys.* **21** 1383-1390

Cheung Y, Yu P, Young E, Chan C, Ng M, Tang F, Wong T 1997 The electron dose distribution surrounding an 192Ir wire brachytherapy source investigated using EGS4 simulation and Gafchromic film *Appl Radiat Isot* **48** 985-990

Clarkson J 1941 A note on depth doses in fields of irregular shape *Br. J. Radiol.* **14** 265

Clifton Ling C, Biggs P 1979 Improving the build up and depth dose characteristics of high energy photon beams by using electron filters *Med. Phys.* **6** 296-301

Constantinou C, Attix F H, Paliwal B R 1982 A solid water phantom material for radiotherapy X-ray and gamma ray beam ray calculations *Med. Phys.* **9** 436-441

Constantinou C 1978 Tissue Substitutes for Particulate Radiations and their use in Radiation Dosimetry and Radiotherapy *PhD Thesis* University of London

Cunningham J, Shrivastava P, Wilkinson J 1972 Program Irreg - Calculation of Dose from Irregularly Shaped Radiation Beams, *Computer Programs in Biomedicine.* **9** 192-199

Dupont S, Rosenwald J, Beauvais H 1994 Convolution calculations of dose in the build up region for high energy photon beams obliquely incident *Med Phys* **21** 1391-1400

Faddegon B, Ross C, van de Zwan L, Rogers D 1988 Measurement of megavoltage bremsstrahlung spectra from a linear accelerator *Med.Phys.* **25** 800-805

Fiorino C, Cattaneo G M, Vecchio A D, Longgobardi B, Signorotto P, Calandrino R, Fossati V, Volterrani F 1992 Skin dose measurements for head and neck radiotherapy *Med. Phys* . 19 1263-1266

Fraass B, van de Geijn J 1983 Peripheral dose from megavolt beams *Med Phys* **10** 809-818

Gagnon W F, Grant III W 1975 Surface dose from megavoltage therapy machines *Radiation Physics* 'Radiology 117 December ' 705-708

Gerbi B J, Khan F 1990 Measurement of dose in the build up region using fixed-separation plane parallel ionization chambers *Med. Phys*. 17

Gerbi B J, Meigooni A, Khan F 1987 Dose build up for obliquely incident photon beams *Med. Phys*. 14 393-399

Gill P, Murray W, Wright M 1990 Numerical linear algebra and optimization Addison Wesley Publishing Company 215-325

Gray L H 1936 An ionisation method for the absolute measurement of gamma ray energy. *Proc R Soc* A156 578 (*as cited by Khan*).

Harper N, Metcalfe P, Hoban P, Round W 1991 Electron contamination in 4MV and 10MV radiotherapy X-ray beams *Australasian Physical and Engineering Sciences in Medicine* **14** 141-145

Hamilton C, Denham J, OBrien M, Ostwald P, Kron T, Wright S, Drr W Underprediction of human skin erythema at low doses per fraction by the linear quadratic model *Radiother. Oncol* . **40** 23-30

Howarth J L 1951 *Br. J. Radiol*. **24** 671-675

Hughes R, Huffman D, Snelling J, Zipperian T, Ricco A, Kelsey C 1988 Minature radiation dosimeter for in-vivo radiation measurements *Int J Radiat Oncol Biol Phys* **14** 963-967

Jackson W 1971 Surface effects of high energy x-rays at oblique incidence *British Journal of Radiology* **44** 109-115

Janjan N, Zellmer D, Gillin M, Kengchon W, Cambell B 1991 Measurement of skin dose in primary irradiation of maxillary sinus carcinoma *Med. Dosim.* **16** 33-36.

Jani S K, Pennington E, Wacha J, Anderson K 1988 Effect of collimator setting on the output of rectangular fields from linear accelerators *Medical Dosimetry* **13** 73-75

Johns H E and Cunningham J R 1983 The physics of Radiology 4th Ed Charles C Thomas

Jones L 1996 Radiobiological calculations of fractionated radiotherapy *Honours thesis* University of Wollongong

Kallman P 1995 Serial and parallel structures in radiobiology *PhD thesis* Karolinska Institute/ University of Stockholm

Kase K, Svensson G, Wolbarst A, Marks M 1983 Measurements of dose from secondary radiation outside a treatment field *Int J Radiat Oncol Biol Phys* **9** 1177-1183

Khan F M 1992 The Physics of Radiation Therapy 2nd Edition Williams and Wilkins London.

Klassen N, van der Zwan L, Cygler J 1997 Gafchromic MD-55 : investigated as a precison dosimeter *Med Phys* **24** 1924-1934

Klein E E, Purdy J A 1993 Entrance and exit dose regions for a clinac 2100C *Int .J. Rad. Onc. Biol.Phys.* **27** 429-435

Klein O.and Nishina Y 1929 *Z..Physik .* **52** 853 *as cited by Siegbahn*

Klevenhagen S C 1991 Complications in low energy x-ray dosimetry caused by electron contamination *Phys Med Biol* **36**

Klevenhagen S C 1985 Physics of electron beam therapy First edition Adam Hilger Ltd Bristol UK 1985

Krithivas G, Rao S N 1985 A study of the characteristics of radiation contaminants within a clinically useful photon beam *Med. Phys.* **12** 764-768

Kron T, Elliott A, Wong T, Showell G, Clubb B, Metcalfe P 1993 X-ray surface dose measurements using TLD extrapolation *Med. Phys.* **20** 703-711

Kron T, Ostwald P 1995 Skin exit dose in megavoltage x-ray beams determined by means of a plane parallel ionization chamber (Attix chamber) *Med Phys* **22** 577-578

Kron T, Butson M, Hunt F, Denham J, 1996 TLD extrapolation for skin dose detyermination in vivo, *Radiother Oncol* 41 119-123.

Ling C C, Biggs P 1979 Improving the build up and depth dose characteristics of high energy photon beams by using electron filters *Med. Phys.* **6** 296-301

Lovelock D, Chui C, Mohan R 1995 A Monte Carlo model of photon beams used in radiation therapy *Med. Phys.* **22** 1387-1394

McGervey John D 1983 Introduction to Modern Physics 2nd Edition Acedemic Press Inc.

McLaughlin, Chen Yun-Dong, Soares 1991 Sensitometry of the response of a new radiochromic film dosimeter to gamma radiation and electron beams *Nuclear Instruments and Methods in Research* **A302** 165-176

McParland B J 1991 The effects of a universal wedge and beam obliquity upon the central axis dose buildup for 6MV x-rays *Med. Phys.* **18** 740-743

Marquardt D 1963 An algorithm for least squares estimation for non-linear parameters *J. Soc. Ind. Appl .Math.* **11** 431-441

Mellenberg D E Determination of build up region over response corrections for a Markus type chamber *Med. Phys.* **17** 1041-1044

Meigooni A, Sanders M, Ibbott G, Szeglin S 1996 Dosimetric characteristics of an improved radiochromic film *Med Phys* **23** 1883-1888

Metcalfe P, Kron T, Hoban P 1997 The physics of Radiotherapy X-rays from linear accelerators Medical physics publishing Madison Wisconsin U.S.A

Metcalfe P 1990 X-ray Beam Modelling in Radiotherapy: The effect of lung Inhomogeneities *PhD Thesis* University of Waikato New Zealand

Mohan R, Chui C, Lidofsky L 1985 Energy and angular distribution of photons from medical linear accelerators *Med. Phys.* **12** 592-597

Muench P, Meigooni A, Nath R, McLaughlin W 1991 Photon energy dependance of the sensitivity of radiochromic film and comparison with silver halide and LiF TLD's used for brachytherapy dosimetry *Med. Phys.* **18** 769-775

Muller-Sievers K, Kober B, Semrau C 1992 The surface doseage in the radiotherapy of a small breast carcinoma with 6MV x-rays. A contribution to quality assurance in radiotherapy. *Strahlenther. Onkol.* **168** 291-296

Murray D 1990 Using EGS4 Monte Carlo in medical radiation physics *Austral. Phys. Eng. Sci. Med.* **13** 132-147

Nelson, Hirayama, Rogers 1985 The EGS4 Code System Stanford Linear Accelerator Center Report SLAC - 265

Newcomb C, van Dyk J, Hill R 1993 Evaluation of isoeffect formulae for predicting radiation-induced lung damage *Radiotherapy and Oncology* **26** 51-63

Nilsson B, Sorcini B, 1989 Surface dose measurements in clinical photon beams *Acta. Oncologica.* **28** 537-542

Nilsson B 1985 Electron contamination from different materials in high energy photon beams *Phys. Med. Biol.* **30**

Orton C, Seibert J 1972 Depth dose in skin for obliquely incident Co60 radiation *B.J.R.* **45** 271-275

Parthasaradhi K, Rao B M, Prasad S G, Lee Y, Ruparel R, Garces R 1989 Investigation on the reduction of electron contamination with a 6MV X-ray beam *Med. Phys.* **16** 123-125

Perez M D, 1996. Analysis of high energy x-ray angle of incidence with MOSFET detectors. *Honours Thesis* , University of Wollongong.

Podgorsak MB 1990 Surface dose in intracavitary orthovoltage radiotherapy *Med. Phys.* **17**

Pointon R 1991The Radiotherapy of Malignant Disease 2nd Edition. Springer- Verlag

Perez C, Brady L 1992 Principles and practice of Radiatio Oncology Second edition J.B.Lippincott company

Rao B M, Prasad S G, Parthasaradhi K, Lee Y, Ruparel R, Garces R 1988 Investigations on the near surface dose for three 10MV X-ray beam accelerators with emphasis on the reduction of electron contamination *Med. Phys.* **15** 246-249

Rawlinson J A 1992 Design of parallel plate ion chambers for build up measurements in mega voltage photon beams *Med. Phys.* **19** 641-648

Reinstein L, Gluckman G 1997 Comparison of dose response of radiochromic ilm measured with He-Ne laser, broadband, and filtered light densitometers *Med Phys* **24** 1531-1533

Rogers D, Faddegon B, Ding G, Ma C, Wei J, Mackie T 1995 BEAM : A Monte Carlo code to simulate radiotherapy treatment units *Med. Phys.* **22** 503-524

Sauer O, Neumann M 1990 Reconstruction of high energy bremsstrahlung spectra by numerical analysis of depth dose data *Rad. Oncol.* **18** 39-47

Siegbahn K 1965 Alpha Beta and Gamma Ray Spectroscopy. North Holland Publishing Company

Sixel K E, Podgorsak E 1994 Build up region and depth of dose maximum of megavolatge x-ray beams *Med. Phys.* **21** 411-416

Spencer L V, Attix F H 1955 A theory of cavity Ionisation *Radiation Res.* **3:239** (*as cited by Khan*)

Steel G G, McMillan T J, Peacock J H 1989 The 5 R's of radiotherapy *Int J. Radiat. Oncol. Biol. Phys.* **56** 1045-1048

Stevens M, Turner J, Hugtenburg R, Butler P 1996 High resolution dosimetry using radiochromic film and a document scanner *Phys Med BiolPhys Med Biol* **41** 2357-2365

Stirling T, Perry H, Katz L 1964 Automation of Radiation treatment planning *Brit . J. Radiol.* **37** 5434-550

Suchowerska N, Davison A, Drew J, Metcalfe P 1997 The validity of using radiographic film for radiotherapy dosimetry *Australas Phys Eng Sci Med* **20** 20-26

Svensson G 1977 Superficial doses in treatment of breast with tangential fields using 4MV x-rays *Int .J .Rad. Onc. Biol. Phys.* **2** 705-710

Tabata T, Ito R 1974 *Nucl. Sci. Eng.* **53** 226

Thames H D, Hendry J H 1987 Fractionation of Radiotherapy, *Taylor and Francis London* 1987.

Turesson I, Thames H 1989 Repair capacity and kinetics of human skin during fractionated radiotherapy : erythema, desquamation, and telangiectasia after 3 and 5 year's follow up. *Radiotherapy and Oncology* **15** 169-188

Velkley D E, Manson D J, Purdy J A, Oliver Jr G D 1975 Build up region of mega voltage photon radiation sources *Med. Phys.* **2** 14-19

Wallace W E Rare Earth Intermetallics. Acedemic Press New York 1973

Weidner R T, Sells R L 1980 Elementary Modern Physics 3rd edition Allyn Bacon Inc.

Wellhofer Dosimetrie 1986 *Markus Electron Chamber* Schwarzenbruck D-8501

Werner B L, Khan F M, Deibel F C 1982 A model for calculation electron beam scattering in treatment planning *Med. Phys.* **9** 180-187

Wierzbicki W, Sixel K, Podgorsak E 1993 An analytical resresentation of radiosurgical depth-dose data *Phys. Med. Biol.* 38 1351-1358

Williams, Warwick, Dyson and Bannister 1989 Gray's Anatomy 37th Edition. Churchill Livingston

Withers H R 1975 The four R's of radiotherapy *Adv. M. Radiat. Biol.* 5 241-247

Wong T, Metcalfe P, Kron T, Emilius G 1992 Radiotherapy X-ray Dose Distribution beyond Air cavities *Aust. Phys. Eng. Sci. Med.* **15** 138 -146

Woodard H, White D 1986 The composition of bodsy tissues *Brit. J. Rad.* **59** 1209-1219

Yip T C and Ege G N 1985 Depth distribution of internal mamary lymph nodes on lateral Lymphaseimtigraphy *Clinical Radiology* **6** 149-152

Yorke E, Ling C, Rustgi S 1985 Air generated electron contamination of 4 and 10MV photon beams: a comparison of theory and experiment *Phys. Med. Biol.* **30** 1305-1314

Zhu Y, Kirov A, Mishra V, Meigooni A, Williamson J 1997 Quantitative evaluation of radiochromic film response for two-dimensional dosimetry *Med Phys* **24** 223-231